Universitat Politècnica de Catalunya
Institut d'Estudis Espacials de Catalunya

Magnetic Diagnostics Algorithms for LISA Pathfinder: System Identification and Data Analysis

by

Marc Díaz-Aguiló

A thesis submitted for the degree of

Doctor of Philosophy

Advisors:
Prof. Enrique García–Berro Montilla
Prof. Alberto Lobo Gutiérrez

Barcelona, 2011

Every honest researcher I know admits he's just a professional amateur.
He's doing whatever he's doing for the first time. That makes him an amateur.
He has sense enough to know that he's going to have a lot of trouble, so that makes him a professional.

Charles Franklin Kettering (1876-1958) U. S. Engineer and Inventor.

Contents

Acknowledgements **v**

List of Figures **ix**

List of Tables **xiii**

Acronyms list **xv**

1 Introduction **1**
1.1 Physics of gravitational waves 2
1.2 Gravitational wave detectors 3
1.2.1 Ground-based detectors 3
1.2.2 Space-based detectors: The LISA mission 7
1.2.3 Technology demonstrator: The LISA Pathfinder mission . . . 12
1.3 Thesis objectives and outline 13

2 LISA Pathfinder and the Magnetic Diagnostics Subsystem **15**
2.1 The LISA Pathfinder mission 15
2.1.1 Mission rationale 17
2.1.2 LTP basic design and mission subsystems 19
2.2 Noise measurement breakdown in LTP 22
2.2.1 Noise breakdown 24
2.3 The diagnostics subsystem onboard LISA Pathfinder 28
2.4 Magnetic acceleration noise in LTP 31
2.4.1 Magnetic noise quantitative breakdown 34
2.5 The LTP Magnetic diagnostic subsystem 39
2.5.1 Magnetic coils description 40
2.5.2 Magnetometers description 43

3 Magnetic experiments onboard LISA Pathfinder **47**
3.1 Introduction 47
3.2 Experiment description 49

3.3 Forces and torques . . . 52
3.4 Modeling of the noise sources . . . 53
3.4.1 Magnetic hardware noise . . . 54
3.5 Results . . . 57
3.6 Conclusions . . . 60

4 Optimization of inflight magnetic estimations 63
4.1 Introduction . . . 63
4.2 Experiment overview . . . 64
4.2.1 The injected magnetic fields . . . 65
4.3 Dynamic model . . . 68
4.4 Estimation model . . . 71
4.4.1 Estimation procedure and bias correction . . . 72
4.4.2 Whitening and splitting . . . 73
4.5 An analysis of the uncertainties . . . 75
4.5.1 The capacitive actuator gain . . . 75
4.6 The optimal frequency . . . 76
4.7 Robustness of the estimates . . . 80
4.8 Summary and conclusions . . . 83

5 Interpolation of the magnetic field 85
5.1 General description of the problem . . . 87
5.2 Multipole interpolation . . . 89
5.2.1 Numerical simulations . . . 91
5.3 A novel alternative approach: neural networks . . . 95
5.3.1 Neuron model . . . 96
5.3.2 Neural network architecture . . . 96
5.3.3 Learning paradigms and learning/training algorithms . . . 97
5.3.4 Performance assessment . . . 98
5.4 Results . . . 99
5.4.1 Field estimation . . . 100
5.4.2 Gradient interpolation . . . 100
5.4.3 Statistical analysis . . . 101
5.5 Conclusions . . . 102

6 The robustness of the magnetic field interpolation method 105
6.1 Introduction . . . 105
6.2 The neural network architecture . . . 107
6.2.1 The fiducial neural network architecture . . . 107
6.2.2 Training and testing . . . 109
6.2.3 Varying the number of neurons . . . 111
6.2.4 Changing the type of neuron . . . 112

6.2.5 Underlying structures . . . 113
6.3 Variations in the magnetic dipoles . . . 114
6.4 Offsets in the magnetometers . . . 116
6.5 Precision of the position of the magnetometers . . . 117
6.6 Varying environmental conditions . . . 119
6.7 Hybrid interpolation system . . . 122
6.7.1 Architecture of the hybrid interpolation system . . . 123
6.7.2 Results of the hybrid interpolation architecture . . . 125
6.8 Summary and conclusions . . . 126

7 LISA Pathfinder simulator 129
7.1 LTPDA toolbox: Data Analysis toolbox for LISA Pathfinder . . . 130
7.2 State Space Model class . . . 131
7.2.1 State space representation . . . 131
7.2.2 Requirements on the state space architecture . . . 131
7.2.3 Model library and class methods . . . 133
7.3 LISA Technology Package subblock modeling . . . 135
7.3.1 Equations of motion . . . 136
7.3.2 Sensing mechanisms . . . 136
7.3.3 Delays . . . 138
7.3.4 Controllers . . . 139
7.3.5 Actuators . . . 140
7.3.6 Noise sources . . . 141
7.4 Simulations . . . 144
7.5 Conclusions . . . 144

8 Summary and Conclusions 147
8.1 Summary of the thesis . . . 147
8.2 Conclusions . . . 148
8.3 Future work . . . 152

A Reference frames and coordinate definitions for LTP 153
A.1 Reference Frames . . . 153
A.2 Coordinate Definitions . . . 157

B Magnetic data from the ACE mission 159
B.1 ACE magnetic experiment description . . . 159

C Calculation of the magnetic field produced by the LTP coils 163
C.1 Magnetic field calculation . . . 163
C.2 Gradient calculation . . . 164

D Estimation of parameters using linear least squares **167**
D.1 Least square theory 167
D.2 One amplitude parameter and one single channel reception 169
D.3 Two amplitude parameters and one single channel reception 169

E Magnetic moments of satellite subsystems **171**

F Neural network principles: theory and application **173**
F.1 Introduction to feedforward neural networks 173
F.2 Neuron model 174
F.3 Neural network architecture 175
F.3.1 What is the best network architecture? 176
F.4 Selection of input data 176
F.5 Learning paradigms and learning-training algorithms 177
F.5.1 Learning paradigms 177
F.5.2 Learning algorithms 178
F.5.3 Learning rate 179
F.5.4 The early stopping technique 179
F.5.5 Estimating variances of the weights of neural networks 180

Bibliography **181**

Acknowledgements

La tesi és un viatge llarg. Un viatge que comença en forma d'il·lusió i de repte, que transcorre per un camí que combina dificultats i satisfaccions i que, finalment, arriba a un final necessari de retrospecció i conclusions. Un viatge per l'aprenentatge, la ciència i el treball ben fet que no hagués estat possible sense l'ajuda, col·laboració i empenta dels meus dos directors: l'Enrique i l'Alberto. Entre els tres, en la pluja d'idees de les reunions dels divendres tarda, modestament crec que hem aconseguit tirar endavant un conjunt d'estudis molt interessants. Moltes gràcies Alberto per la teva rigorositat i mètode a l'hora de *fer ciència*. Amb aquests anys m'has mostrat la importància de no només ser conscient de que estem solucionant un problema, sinó també la necessitat de ser rigorosos amb el *com* i el *perquè* de la solució. Gràcies Alberto per ajudar-me a ser més "científic" i menys "enginyer". Moltes gràcies també per la teva immensa força, ajuda i amistat. Has estat un guia excel·lent. Moltes gràcies Enrique per les inacabables ganes de treballar, la teva constància i la teva dedicació. Moltes gràcies per treure temps de qualsevol banda i seguir fent ciència de manera tant eficient. Gràcies per ser una *màquina* de treballar i sempre tirar endavant la feina amb rigorositat. La teva empenta i la teva gran energia han estat uns elements claus i imprescindibles d'aquesta experiència. Realment imprescindibles. Moltes gràcies també per la teva gran determinació, per tenir les idees tan clares i pel teu incansable suport, consell i amistat. Ha estat un plaer treballar amb vosaltres. Gràcies per creure en mi i per valorar el meu treball.

També vull agrair tots aquests anys a tot el grup LTP, la convivència i feina conjunta que hem fet durant aquests anys. Molts dinars al Nexus, moltes intenses tardes de treball i grans converses. Unes gràcies especials al Nacho i al Pep per engrescar-me amb el projecte des d'un bon començament, gràcies per estar sempre disposats a resoldre'm qualsevol dubte i ensenyar-me com començar a *navegar* pel projecte. Un agraïment especial pel nostre gran viatge a New York. Gràcies Pep per involucrar-me al LTP team, per compartir els primers meetings i per introduir-me una nova manera de pensar. Gràcies Nacho per un constant positivisme i per saber transmetre-me'l. Gràcies per la teva amistat i confiança. Moltes gràcies també als altres *group members* per fer-me la vida més fàcil i per remar en la mateixa direcció. Gràcies al Lluis, a l'Aleix, a l'Ivan, al Carlos, a la Pris, i també als nouvinguts, Ferran, Nikkos i Victor. Gràcies Ferran per la gran companyia als viatges de Darmstadt i

Paris, gràcies per disfrutar d'unes bones caminades. Nacho, Pep, Ferran, gràcies per les ones de San Francisco. Un agraïment molt especial al Miquel, per tenir una gran passió pel projecte i per engrescar-me en el projecte LTPDA. T'estic profundament agraït que propiciessis les meves estades a Hannover, ha estat una manera òptima de descobrir noves maneres de treballar i d'endinsar-me en el Data Analysis team. Gràcies Miquel per obrir-me aquesta porta. Moltes gràcies Alberto pel positivisme constant, per unes converses inoblidables al Nexus i per un espectacular viatge a Corea. Thank you Markus for your humour and your lessons about Sweden. Thank you for feeling so comfortable among us and for making us feel so comfortable with you. Gràcies Eva, Anna i Pilar per tot el suport. També voldria agrair els bons moments a tots els companys de despatx de l'UPC, gràcies Isabel, Fran, Roger, Victor, Aracel·li i Estel, pels dinars de *tupper* tan especials. Un agraïment molt gran també a tots els *aeros* de l'Escola de Castelldefels per acollir-me al vostre equip. Especialment Pep, Xevi i Adeline gràcies per fer-me fàcil i agradable el meu començament en el món de la docència i al Santi per aguantar-me al despatx. Gràcies Adeline per tot el suport i consell en aquesta recta final i per compartir *Control* amb mi.

I would like to express my most sincere gratitude to the whole LTPDA team for giving me the opportunity to work within this project, to contribute and start to see that many things were moving in the right direction. I would like to thank especially Martin Hewitson, for introducing me in the SSM team and believing in my work. Thank you very much for hosting me at the AEI and for being always so encouraging, efficient and grateful. I would also like to thank Adrien and Boutheina for doing the SSM collaboration a dynamic and interesting activity. It has been a pleasure to learn from you two. Thanks to Ingo for sharing the office during my Hannover stay and for being so efficient and helpful. Thank you very much Luigi for your collaborative effort, your tireless work and your efficient help. Thank you Mauro for being always so grateful and so helpful with the magnetic analysis. Thank you very much Eric for being so hard-working and for your valuable input in the SSM effort. Thank you Anneke & Frank for being so helpful during my stay in Hannover. Thank you Guiseppe, Prof. Stefano Vitale, Prof. Karsten Danzmann, Michele, Fabrizio, Heather & Antonio for all your effort and your inexhaustible help and collaboration.

Als amics de Tarragona, tot i no haver estat molt per la ciutat últimament, gràcies pels grans moments de la infància. Especialment, gràcies Ivan, Manel, Rotger, Aleix, Pablo i Arnau. Pedro i Virgili, gràcies per sempre preocupar-vos per mi i sempre fer-me riure. Gràcies Joan Manel per creure en els grans reptes i valorar-los. Gràcies Gerard i Laura per fer les estades a Hannover molt més agradables, els partidets de tennis i els sopars plegats estan en la meva memòria. Gràcies Cris, Laura i Marta per seguir sent les grans amigues de Boston i seguir en contacte. Gràcies Andrea per donar-me energia durant el meu primer any de tesi. Gràcies Jordi, Pere i Diego per ser els de sempre, per compartir la vida amb mi i per sempre tenir ganes d'estar

junts. Trobar-vos, tenir-vos, anar al gimnàs, anar a córrer, jugar a pàdel, a futbol, fer soparets i riure junts ha estat una vital font d'energia per tirar endavant. En tots aquests soparets, Jara, Anna i Maria també heu estat una font de rialles, de converses i de benestar importantissim i essencial. Gràcies a tots.

Un agraïment sense dimensions pels meus pares. Sempre m'heu prestat un suport i una estimació incondicional. Gràcies per ser qui sou, per estimar-me tant i per preocupar-vos sempre per a què tot anés en la direcció correcta. Gràcies per haver-me educat així com ho heu fet, amb això m'heu donat el millor dels tresors. Sempre el guardaré amb mi. Tot l'esforç que he ficat en aquesta tesi és en gran part gràcies a vosaltres. Sou essencials en aquesta tesi i en la meva vida. No tinc paraules tampoc per l'amor i l'amistat que em dóna l'Ariadna. Una germana inigualable, una amiga increïble, una persona clau en la meva vida, clau en la meva existència, i, per tant, clau també en aquesta tesi. Siguis on siguis, sempre et tinc el cap, sempre et tinc al cor.

Júlia, ets *ella*. Has estat l'estrella més brillant de totes, has estat la meva llum durant tot aquest temps i ets la meva il·lusió pel futur. Aquesta tesi ha estat molt més fàcil al teu costat. Va ser molt bonic trobar-te, ha estat extraordinari conèixer-te i és felicitat compartir amb tu els camins d'aquesta vida. Ara se n'acaba un, però ens en queden molts per començar.

Barcelona, Juliol de 2011

List of Figures

1.1 Gravitational wave polarizations. 4
1.2 Noise curves of LISA, LIGO and the PPTA project, and some of the gravitational wave sources that they expect to detect 6
1.3 Best strain sensitivities for the LIGO detectors 7
1.4 Current design of the LISA mission orbit and its 1 year evolution . . 9
1.5 Triangular LISA constellation formed by the three LISA spacecraft. 10
1.6 Expected noise curve for LISA: influence of force perturbations, shot noise, and antenna transfer function 12

2.1 Artistic view of the LPF spacecraft with its propulsion module . . . 16
2.2 Schematic view of the payload of LPF, the LTP 18
2.3 General view of the LPF spacecraft 22
2.4 View of the LCA hardware already placed within the LPF spacecraft 23
2.5 Coordinate reference frame centered at the positions of the coils. . . 40
2.6 Technical drawing and picture of the onboard magnetometers 44

3.1 Artistic view of the LTP: representation of the two GRSs, the optical bench and the inductions coils 48
3.2 Coordinate reference frame of the experiment. This reference frame is centered at the position of the coils (see Appendix A). 49
3.3 Control system architecture of LISA Pathfinder. 51
3.4 The three components of the magnetic force acting on test mass 1 when coil number 1 is on. 52
3.5 Three components of the magnetic torque acting on test mass 1 when coil number 1 is on. 53
3.6 Block diagram of the current source of the coils. 54
3.7 Noise spectral density of the sinusoidal current circulating through the onboard coils. 55
3.8 Relative displacements and rotations of the test masses due to the magnetic excitations produced by coil number 1. 56
3.9 Breakdown of the noise contributions to the total displacement signal when a current of 1 mA and 1 mHz is circulating in coil 1. 58

4.1 Schematic view of LPF, showing the inertial sensors, magnetometers and induction coils. 65
4.2 Control system architecture of LPF. 71
4.3 Amplitude of the differential displacement channel of the interferometer and its corresponding whitened signal. 74
4.4 Error of the modulus and phase differences of the transfer function $H^b_{F_x \to x_{12}}$ with respect to its nominal behavior. 77
4.5 SNR as a function of frequency for each of the received signals for the magnetic experiments. 78
4.6 Time series responses and its corresponding Fourier domain analysis for 4 different excitation currents 79
4.7 Global error functions of each of the magnetic parameters with respect to the excitation frequency. 80
4.8 Statistical distributions of the estimates for the 5 magnetic parameters of the test masses for 3 different simulations. 81

5.1 Artist view of the LISA Pathfinder spacecraft. The LCA is in the center and the 4 magnetometers are indicated by the arrows 86
5.2 Conceptual diagram showing the position of the magnetic sources, of the test masses, and of the magnetometers 88
5.3 Magnetic field contour plots in the LCA region for a given source dipole configuration. 93
5.4 Binned errors of the estimated modulus of the magnetic field and of its x component by classical interpolation methods 94
5.5 Neural network architecture: magnetometers readings are the inputs and estimates of fields and gradients at the test masses are the outputs 95
5.6 Error distributions for each field component at the position of test mass 1 and test mass 2 output by the neural network interpolation algorithm 99
5.7 Input-Output correlation coefficients learned by the neural network . 101
5.8 Probability density function of the errors distribution for the three components of $\boldsymbol{\nabla} B_x$ 102

6.1 Schematic view of the payload of LISA Pathfinder, the LTP 106
6.2 Neural network architecture used for interpolating the magnetic field readings in LPF 108
6.3 Quality of the estimate as a function of the number of neurons in the hidden layer 110
6.4 Quality of the estimate as a function of relative error between the real field and the training field (on-ground measurements) 115
6.5 Quality of the estimate as a function of the offset in all 4 magnetometers117

6.6 Quality of the estimate (mean error) due to the mechanical uncertainty in the precise position of the magnetometers. 118
6.7 Spectrum of fluctuations of the magnetic field at the position of the test masses. 119
6.8 Temporal realization of the magnetic field and its interpolation at the position of the test mass 1 120
6.9 Spectral density of the magnetic field and its interpolation at the position of test mass 1. 121
6.10 Hybrid interpolation system for magnetic field inference 124
6.11 Classification algorithm output for 3 different magnetic configurations 125

7.1 Diagram of the control system architecture for LISA Pathfinder . . . 137
7.2 Transfer functions of the two main control loops governing LPF . . . 140
7.3 Acceleration noise breakdown simulations for the absolute and the differential displacement channels 143

A.1 Coil reference frame: coordinate reference frame centered at the position of the coils 155
A.2 Attitude parametrization. 157

B.1 Time series of the magnetic field measured by the ACE mission . . . 160

C.1 Coordinate reference frame for the magnetic field calculation. 164

F.1 Schematics of the operations performed by an artificial neuron. . . . 174
F.2 Feed forward neural network architecture 175

List of Tables

1.1 Sensitivities of the ground based detectors. 6

2.1 Apportionment of the DC forces onto the x-axis acceleration reading. 26
2.2 Apportioning of the different perturbations expected in the x-axis acceleration reading in the MBW. 29
2.3 Test mass properties. 34
2.4 Other constants needed for the calculation of the magnetic contributions. 35
2.5 Magnetic field figures expected during mission operations. 35
2.6 Contribution of the magnetic field effects to the total acceleration noise. 40
2.7 Positions of the test masses. 41
2.8 Positions of the coils. 41
2.9 Field and gradient produced by the coils at the positions of the test masses. 43
2.10 Positions of the magnetometers. 44

3.1 Preliminary assessment of the errors in the estimates of the magnetic properties for each individual noise source and for all sources combined together. 60

4.1 Standard deviations of the estimated parameters for different estimation scenarios. 83

5.1 Estimation errors in the components of the magnetic field and of its modulus using classical interpolation methods 94
5.2 Statistical properties of the distribution of errors of the interpolated magnetic field. 103

6.1 Positions of the test masses and positions of the magnetometers . . . 109
6.2 Quality of the estimate for the most common neuron activation functions. 112
6.3 Input-output relationship learned by the network. 114
6.4 Standard deviation of the error output by the network 122

7.1 Principal *ssm* methods grouped by functionality. 134

8.1 Uncertainty of the determination of each magnetic contribution. . . 151

E.1 List of subsystems units and their dipole magnetic moment. 171

Acronyms list

ACE	Advanced Composition Explorer
ADC	Analog-to-Digital Converter
AGAUR	Agencia de Gestió d'Ajuts Universitaris i de Recerca
ASD	Amplitude Spectral Density
BMU	Best Matching Unit
COM	Center of Mass
CPU	Central Processing Unit
CRB	Crámer-Rao bound
CSIC	Consejo Superior de Investigaciones Científicas
DAC	Digital to Analog Converter
DAU	Data Acquisition Unit
DDS	Data management and Diagnostic Subsystem
DFACS	Drag Free Attitude Control System
DMU	Data Management Unit
DPU	Data Processing Unit
EETAC	Escola d'Enginyeria de Telecomunicació i Aeroespacial de Castelldefels
EH	Electrode Housing
EHF	Electrode Housing Frame
EM	Engineering Model
ESA	European Space Agency
ESAC	European Space Astronomy Centre

ESTEC	European Space Research and Technology Centre
EGO	European Gravitational-wave Observatory
FEE	Front End Electronics
FEEP	Field-Emission Electric Propulsion
FIR	Finite Impulse Response
FM	Flight Model
ICE	Institut de Ciències de l'Espai (Barcelona)
IEEC	Institut d'Estudis Espacials de Catalunya (Barcelona)
IIR	Infinite Impulse Response
IS	Inertial Sensor
GRS	Gravitational Reference Sensor
LCA	LTP Core Assembly
LIGO	Laser Interferometer Gravitational-wave Observatory
LISA	Laser Interferometer Space Antenna
LPF	LISA Pathfinder
LTP	LISA Technology Package
LTPDA	LISA Technology Package Data Analysis
MBW	Measurement Bandwidth
MDS	Magnetic Diagnostic Subsystem
MEC	Ministerio de Educación y Ciencia
MICINN	Ministerio de Ciencia e Innovación
MSE	Mean Squared Error
NASA	National Aeronautics and Space Administration
NN	Neural Network
NTC	Negative Temperature Coefficient
OB	Optical Bench
OBC	Onboard Computer
OMS	Optical Metrology System
OW	Optical Window

PCU	Power Control Unit
PDU	Power Distribution Unit
PSD	Power Spectral Density
PTA	Pulsar Timing Array
PPTA	Parkes Pulsar Timing Array
SC	Spacecraft
SNR	Signal-to-Noise Ratio (also denoted SN and S/N)
SOM	Self-Organizing Map
SSM	State Space Model
TM	Test Mass
TM_1	Test Mass 1
TM_2	Test Mass 2
TMS	Temperature Measurement Subsystem
UPC	Universitat Politècnica de Catalunya
VE	Vacuum Enclosure

Chapter 1

Introduction

This thesis is conceived within the definition, design, and execution of LISA Pathfinder, however it focuses on a very specific topic: data analysis of the magnetic effects in the frequency range of the milli-Herz. These data analysis activities are necessary as a part of the scientific efforts intended to test key technologies for gravitational wave detection in space. LISA Pathfinder (LPF) is the mission intended to test vital technologies for the LISA mission (Laser Interferometer Space Antenna). The latter will be a space-based gravitational wave detector with the main goal of detecting and observing gravitational waves within the frequency range between 0.1 mHz to 0.1 Hz. The detection of gravitational waves at low frequency requires differential measurements of distances of the order of pico-meters between two bodies separated by 5 million kilometers. Due to the demanding requirements of LISA, the European Space Agency (ESA) started a precursor mission, LISA Pathfinder. This mission is mainly developed by ESA, with NASA (National Aeronautics and Space Administration) contributing with some specific subsystems. In this effort, several new hardware subsystems never flown before, have been developed for LISA Pathfinder.

The task of testing new technology in space, combined with the stringent requirements of both LISA and LISA Pathfinder, entails an important data analysis effort. The activities of data analysis, prior to launch, are devoted to the validation of the correct behavior of all subsystems and to the design of the experiments needed to be performed inflight. During mission operations, data analysis activities will focus mainly on the detailed analysis of the correct operation of the satellite, on the estimation of its most important characteristics and on the processing of all telemetry data to achieve mission requirements. The work presented in this thesis is devoted mainly to the data analysis algorithms related to estimate the contribution of the magnetic perturbations to the measurement of the total differential acceleration between the two test masses of LISA Pathfinder. Nevertheless, as the motivation for LISA and LISA Pathfinder is the observations of gravitational waves,

in this first chapter, we give a brief introduction to gravitational waves, its nature and the efforts made towards their detection. We also give a brief overview of the concept and status of the main ground based-detectors, and of the space missions, LISA and LPF.

1.1 Physics of gravitational waves

In the gravitation theory of Newton, gravitational fields propagate instantly. This effect is not realistic, because it does not comply with the laws of causality. A consistent alternative to this theory is the General Theory of Relativity introduced by Einstein in 1916. In this theory, Einstein presents gravitational waves to describe the propagation of gravitational fields. These waves are originated in a source of gravitational field whose structure varies with time. Then, the gravitational field variation triggered by this source propagates away into the surrounding space at some finite speed. As a consequence, another body at a certain distance feels such variation after a finite amount of time. Gravitational perturbations travel as ripples of the spacetime geometry, meaning that they cause distortion in this geometry. The aforementioned space-time geometry is determined from the distribution of mass and energy. Gravitational waves travel through empty space at the speed of light. They have two polarization modes, the plus-polarization, $+$, and the cross-polarization, $\times$. These waves are transverse to the propagation direction (Misner et al., 1973). As a consequence, the distance metric between freely falling bodies changes in the perpendicular direction to the traveling gravitational wave in 2 different polarizations (Fig. 1.1). This particularity constitutes the key characteristic of gravitational waves and can be used to measure them. Gravitational wave effects were first discovered by Hulse and Taylor by measuring the decrease of the rotation period of a binary pulsar (Hulse & Taylor, 1975; Taylor et al., 1979). They attributed this observed loss of energy to gravitational wave radiation (Taylor & Weisberg, 1982).

The relative change in distance between freely floating bodies due to the distortion of the space time geometry caused by gravitational waves is very small at positions close to the Earth, where detectors can be located. The amplitude of a gravitational wave is usually represented by the strain, h, which represents the relative change in distance between two test bodies separated initially by a distance L. Thus, it is defined as:

$$h = \frac{1}{2}\frac{\Delta L}{L}. \tag{1.1}$$

Particularly, for gravitationally bounded systems, we can estimate the value of the strain as[1]

[1]This is an approximation of the order of magnitude of the strain. More specifically, it is proportional to the quadrupole moment acceleration of the source, $\ddot{Q}_{ij}(t)$.

$$h \sim \frac{l}{R}\left(\frac{GM}{lc^2}\right)^2 \tag{1.2}$$

where M is the mass of the source, R is the distance from the source to the test bodies, l is the linear size of the source, and $G = 6.67 \times 10^{-11}\mathrm{m}^3\ \ \mathrm{kg}^{-1}\mathrm{s}^{-2}$ and $c = 3 \times 10^8$ m s^{-1} are, respectively, the gravitational constant and the speed of light (Schutz, 1984). If we assume that the free floating test bodies are located at a distance of $L = 1$ km, the change in distance is around of 5×10^{-18} m, 1 000th of a nucleus.

The spectrum of gravitational waves covers a wide range of frequencies, from 10^{-16} Hz to 10^4 Hz. Part of this spectrum, with the exception of the cosmic microwave background (located at frequencies around 10^{-16}, as $10^{-16} \sim 1/t_{\mathrm{U}}$, where t_{U} is the age of the Universe), is shown in Fig. 1.2. The detection of gravitational waves in the high frequency band is intended to be covered by the on-ground detectors (see section 1.2.1). These instruments are designed to detect emissions by rotating neutron stars, about $1\,M_\odot$ massive objects like binary systems of neutron stars or black holes (specially, the ones in their last epoch of the inspiral process) and supernova explosions (Hughes, 2003). The very low frequency band is covered by Pulsar Timing arrays projects such as the PPTA (Parkes Pulsar Timing Array). On the other hand, the low frequency band is planned to be covered by the first envisioned space-based gravitational wave detector: the Laser Interferometer Space Antenna (LISA) — section 1.2.2. If the design sensitivity planned for LISA is achieved, this detector will collect signals from the binary systems known as the verification binaries (Stroeer & Vecchio, 2006). Moreover, LISA is expected to detect large amount of white dwarf binaries (Stroeer & Vecchio, 2006), super massive black holes, SMBHs, (Berti et al., 2005), and extreme mass ratio inspirals, EMRIs (Gair et al., 2004).

1.2 Gravitational wave detectors

1.2.1 Ground-based detectors

Nowadays, three different detector technologies are used for the detection of gravitational waves. Resonant mass detectors and the interferometric detectors intend to detect gravitational wave sources in the high frequency band and the Pulsar Timing Array projects intend to detect gravitational waves in the very low frequency band.

Resonant mass detectors

In 1960, Weber initiated his work to detect gravitational waves by means of resonant mass detectors (Weber, 1960, 1969). This research interest in developing such detectors has continued until the present date, with an enhancement of their sensitivity by

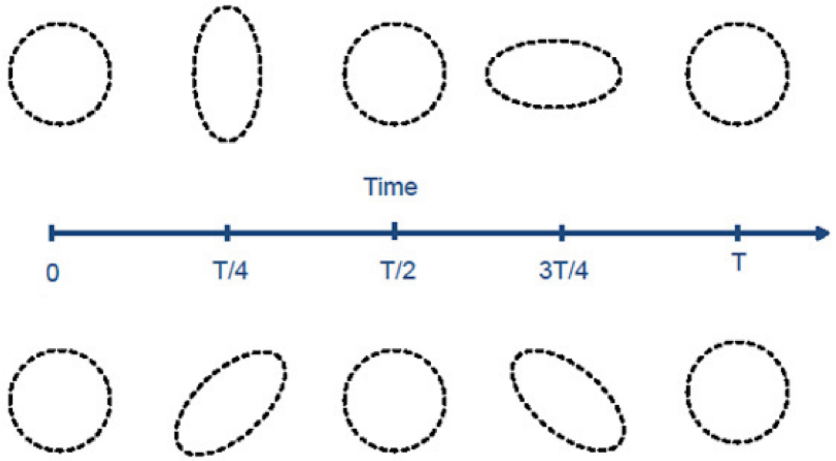

Figure 1.1: Gravitational wave polarizations. Representation of the interaction of free falling macroscopic bodies disposed within a circle with a traversing gravitational wave. The gravitational wave travels perpendicularly to the plane of the circles. The space-time geometry is changed in time depending on the polarization of the wave. The top row shows the plus polarization and the bottom row shows the cross polarization.

almost three orders of magnitude (in amplitude). Resonant mass detectors consist of solid bodies (cylinders or spheres) with a very high Q mechanical resonator (Frossati, 2003; Fafone, 2004). This resonator is excited by the gravitational wave crossing the detector. The most relevant resonant mass detectors are Allegro (Heng et al., 2002) in North America, Auriga (Zendri et al., 2002) in Italy, Explorer (Astone et al., 2002) in Switzerland, Nautilus (Astone et al., 1997) in Italy, Niobe (Blair et al., 1995) in Australia, MiniGRAIL (de Waard A., 2005) in the Netherlands, and Mario Schenberg (Aguiar et al., 2002) in Brazil. They reach impressive strain sensitivities of $\sim 10^{-21}$ $\mathrm{Hz}^{-1/2}$ ($\sim 6 \times 10^{-21}$ m $\mathrm{Hz}^{-1/2}$ in distance, since they are approximately 3 meters long) at the kilo-Hertz frequency range with a bandwidth of tens of Hertz.

Interferometric detectors

Around the late 70s, new investigations started as an alternative method to detect gravitational waves. At that moment, this method was based on laser interferometry and, more specifically, in the classical Michelson interferometer. These detectors were named interferometric detectors, and they represent the base design for the future gravitational wave detectors. They measure the phase differences between two laser beams reflected on two bodies. These phase differences are expected to occur by the change in the distance between the two bodies when the gravitational wave traverses the detector. The change of phase, $\delta\phi$, in a Michelson interferometer of arm-length L is

$$\delta\phi = 2\,\frac{\omega_l}{\omega_{\rm GW}}\,h_+ \sin\frac{\omega_{\rm GW}\tau}{2}, \tag{1.3}$$

where ω_l is the angular frequency of the laser light, $\omega_{\rm GW}$ is the angular frequency of the gravitational wave, and τ is the round-trip time experienced by the laser beam, $\tau = 2L/c$, and L the arm-length of the interferometer (Lobo, 1992). The optimum arm-length is

$$L = \frac{\pi c}{2\omega_{\rm GW}} = \frac{\lambda_{\rm GW}}{4}, \tag{1.4}$$

where $\lambda_{\rm GW}$, is the wavelength of the gravitational wave. The design of the interferometric detectors is complicated by the high sensitivity required. Therefore, more involved interferometric designs have been implemented in current designs. Usually, the configurations adopted are the power-recycled Michelson interferometer with Fabry-Perot cavities in the arms (Acernese et al., 2007; Abramovici et al., 1992; Danzmann, 1992), and the dual recycling technique (Lück et al., 2006; Meers, 1988). The use of these techniques increases the interaction time between the light and the gravitational wave and, as a consequence, overcomes the photon shot noise in a certain band.

The sensitivity of ground-based interferometric detectors is limited by different sources of noise. Among these sources the most relevant are the seismic noise, the thermal noise, the photoelectron shot noise, the gravity gradient noise, and quantum effects. They are relevant in different bands. This is shown in Fig. 1.3. The gravity gradient and seismic noise prevent the detection of gravitational waves in the low frequency range. Nevertheless, at high frequency, the dominant noise source is the shot noise (Lyons et al., 2000). The most important ground based detectors that are currently operative are listed in Table 1.1, along with their arm-length and best strain sensitivity. GEO600 is located in Hannover, Germany (Lück et al., 2006) and it is a German-British collaboration for gravitational wave detection. On the other hand, the LIGO collaboration (Sigg & the LIGO Scientific Collaboration, 2008), which is funded by the US, has two detectors, one located in Hanford (Washington) and another in Livingston (Louisiana). VIRGO is a gravitational wave detector located in Italy, within the site of EGO (European Gravitational Observatory) at Cascina (Acernese et al., 2007). Finally, TAMA 300 is a gravitational wave detector located at the Mitaka campus (Tokyo) of the National Astronomical Observatory of Japan (Takahashi & the TAMA Collaboration, 2004). The LIGO collaboration has planned the implementation of the third generation instruments for the LIGO detector (Advanced LIGO team, 2008). These changes promise an order of magnitude increase in broadband strain sensitivity. This means reducing the sensitivity down to $\sim 2 \times 10^{-24}$ Hz$^{-1/2}$. This enhancement of performance would imply an increase of a factor of 1 000 in probability of detection of gravitational waves.

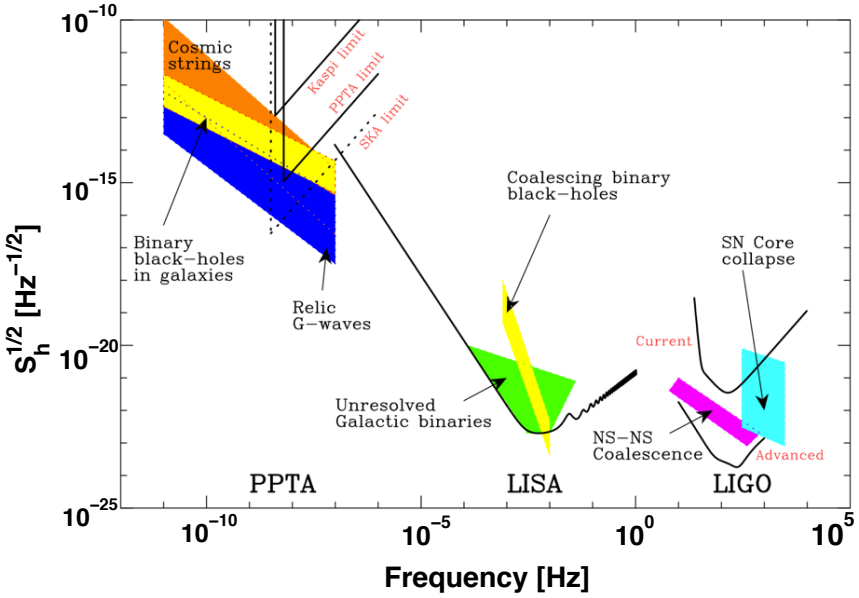

Figure 1.2: Expected noise curves for LIGO (right curve), LISA (middle curve) and some of the PTA projects (left curve), and the expected sources of gravitational waves at different frequencies. LISA or the PTA projects seem to be noisier than LIGO, but what matters is the signals that each detector can actually sense.

Table 1.1: Sensitivities of the ground based detectors.

Detector	Arm-length [km]	Strain sensitivity [Hz^{-1}]
GEO600	0.6	7×10^{-22}
LIGO Hanford	2	4×10^{-23}
LIGO Hanford	4	2×10^{-23}
LIGO Livingston	4	2×10^{-23}
TAMA300	0.3	3×10^{-21}
VIRGO	3	5×10^{-23}

Pulsar Timing Arrays

A Pulsar Timing Array uses a set of millisecond pulsars to detect and analyze gravitational waves. This detection would originate from a detailed investigation of the arrival times of pulses emitted by these millisecond pulsars spread over the celestial sphere and detected using one or more radio telescopes. This millisecond pulsars are used because they appear not to be prone to the starquakes and accretion events

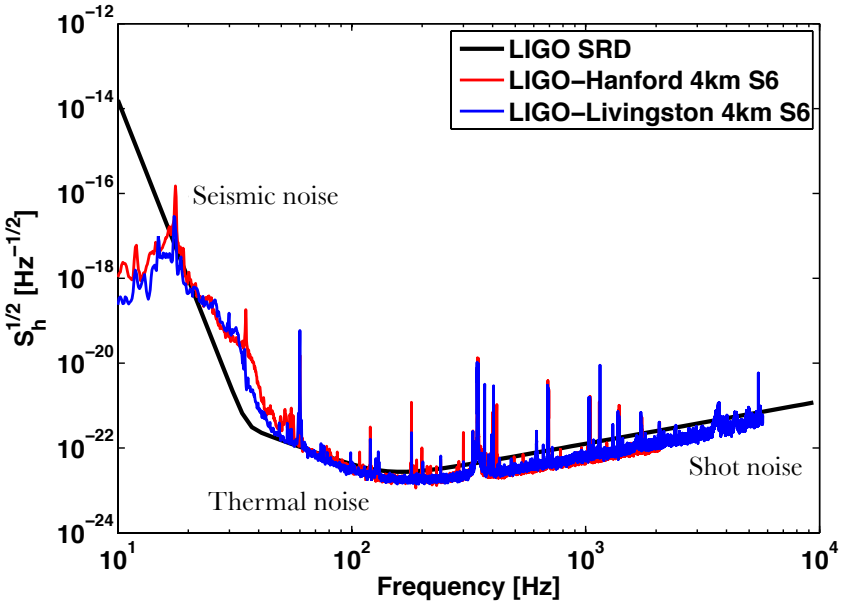

Figure 1.3: Best strain sensitivities for the LIGO detectors. This figure shows the requirement for the strain sensitivity for the LIGO instrument (black line), the strain sensitivity curve for the Science Run 6 (S6) for the LIGO instrument located at Hanford (red curve), and the strain sensitivity for S6 for the LIGO instrument located at Livingston (blue curve) (Sigg & the LIGO Scientific Collaboration, 2008). The low-frequency branch of these curves is limited by seismic noise, the central region of the frequency range is limited by thermal noise, and finally the high-frequency portion is limited by shot noise.

which can affect the period of classical pulsars. A Pulsar Timing Array is sensitive to perturbations on timescales ranging from days to decades, therefore it aims to detect gravitational waves with a frequency from 10^{-9} to 10^{-6} Hz. Thus, the expected astrophysical sources of such gravitational waves are massive black hole binaries in the centers of merging galaxies, where tens of millions of solar masses are in orbit with a period between months and a few years (Hobbs, 2010). Currently, there exist three active pulsar timing projects: The Parkes Pulsar Timing Array, PPTA (Yardley et al., 2010), the European Pulsar Timing Array (Janssen et al., 2008), and the North American Nanohertz Gravitational Wave Observatory (Jenet et al., 2009). These three projects have begun collaborating under the title of the International Pulsar Timing Array project (Hobbs et al., 2010).

1.2.2 Space-based detectors: The LISA mission

The high frequency band of the gravitational wave spectrum is being scanned or will be scanned by the ground-based detectors. The very low frequency band will be cov-

ered by the PTA projects, and the low frequency range remains still uncovered since the local noise noise does not allow the ground-based detections at frequencies below 1 Hz. This local noise is produced by moving objects, seismic movements, gravity gradient noise or meteorological phenomena. Hence, the solution envisioned by the science community to overcome such limitations is to place an interferometric gravitational wave detector in space. In this environment, the seismic noise does not exist, and moreover, the gravity noise is strongly reduced. At the same time, the length of the arm can be orders of magnitude longer than in Earth. The mission that is planned to be the first space-based interferometric detector is LISA, which stands for Laser Interferometry Space Antenna. This mission requires the testing and validation of never-flown key technologies. To this end, the European Space Agency, with some NASA contributions, have implemented of LISA Pathfinder, LISA's precursor mission.

One of the main goals of the LISA mission[2] is to detect gravitational waves originated from massive black holes and galactic binaries in the low frequency range, that is, from 0.1 mHz to 0.1 Hz (Bender, 1998). More specifically, the main purpose of the mission is to learn about the formation, growth, density, and surroundings of massive black holes (from $10^5 M_\odot$ to $10^8 M_\odot$). The observation of these sources would provide unique new information about these objects, and would test General Relativity to unprecedented accuracy. The low frequency range is particularly interesting since it spans the most certain and powerful sources of gravitational wave radiation. Typically, this is because large scale mass motions imply long time scales. Figure 1.2 shows the detection spectrum for LISA and LIGO and the expected sources for each of the missions.

The present design for LISA consists in three identical spacecraft separated by 5×10^6 km, forming an equilateral triangle. The distances between the satellites are the arm-length of the detector. This arm-length has to be of the order of $\lambda_{\mathrm{GW}}/4$, where λ_{GW} is the wavelength of the gravitational wave. This triangular constellation will be placed in an Earth-like orbit 20° behind the Earth, and it will therefore orbit the Sun. In the current design, the plane of this triangle has an inclination of 60° with respect to the ecliptic to provide the most stable size of the triangle. This orbit configuration can be seen in Fig. 1.4. Figure 1.5 shows the triangle formation of the three spacecraft, with the distances between the vertexes of the equilateral triangle formed by the three satellites of LISA. Note that these distances are not constant since the LISA constellation is affected by the gravitational field of the Solar System. Actually, the arm-lengths of the triangle will have variations of $\sim$ 60 000 km and angle variations of 1% per year, respectively. This angle and length variations are expected to occur in time scales of months, but LISA is conceived to detect length variations in time scales of hours. Therefore, this will not represent a limitation to detect gravitational waves within its sensitivity frequency band. Also, Doppler shifts

[2] `http://list.caltech.edu/doku.php?id=start`

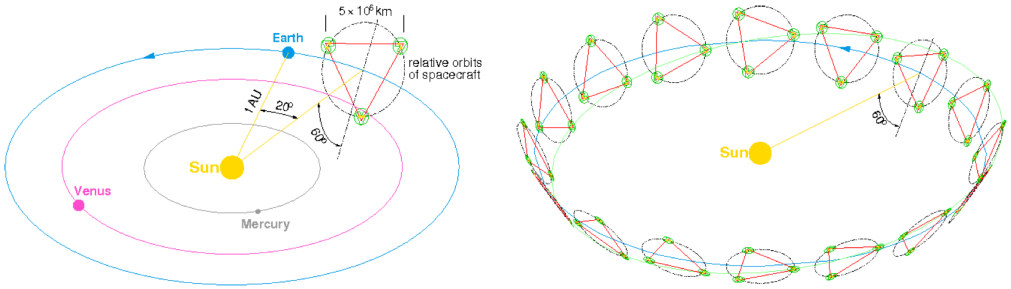

Figure 1.4: Left panel: Scheme of the current design of the orbit of the three LISA spacecraft and their relative position with respect to the Earth's orbit and to the ecliptic plane. Note the tilt of the triangle plane relative to the ecliptic (60°) and the trailing angle behind the Earth (20°). Right panel: Evolution of the LISA constellation during one year. Note that the normal to LISA's plane describes a cone in the sky once a year, while the three satellites rotate clockwise around the barycenter of the triangle, also once per year.

will require laser modulations up to a few MHz. Basically, LISA is a giant Michelson interferometer with an extra arm added to give independent information on the polarization of the gravitational wave, and also for redundancy. Each of the three spacecraft contains two optical assemblies. The two assemblies in one spacecraft are each pointing towards an identical assembly on each of the other two spacecraft to form a pseudo-Michelson interferometer (see Fig. 1.5). In the milli-Hertz frequency range, LISA strain sensitivity must be at least of $\sim 10^{-20}$ $\mathrm{Hz}^{-1/2}$, therefore the interferometric system must measure the differences in the round trip path length between the two arms with a noise below ~ 40 pm $\mathrm{Hz}^{-1/2}$. Each spacecraft contains two vacuum enclosures housing a platinum-gold cube of 46 mm in size. These cubes are known as the test masses and are in nominally perfect free fall. They serve as an optical reference or mirror for the light beams of the interferometer. A hypothetical gravitational wave traversing the constellations will vary the length of the optical path between the test masses of one arm relative to the other arms, and this will trigger a gravitational wave detection.

The spacecraft cannot maintain its motion along the geodesic because it will be subject to important perturbations resulting from solar radiation pressure and the solar wind. Therefore, the main goal of the satellite is to isolate the test masses from the environment and to maintain them in perfect geodesic motion or free fall. Thus the spacecraft position does not directly translate into the gravitational wave signal, however, it is totally necessary to keep the spacecraft well centered on their respective test masses to reduce spurious local noise forces and, obviously, to avoid the test mass crashing into the inner walls of the spacecraft. To this end, the relative motion of the spacecraft with respect to the test masses is precisely measured by means of a capacitive sensor that measures the change in the electrical capacitance

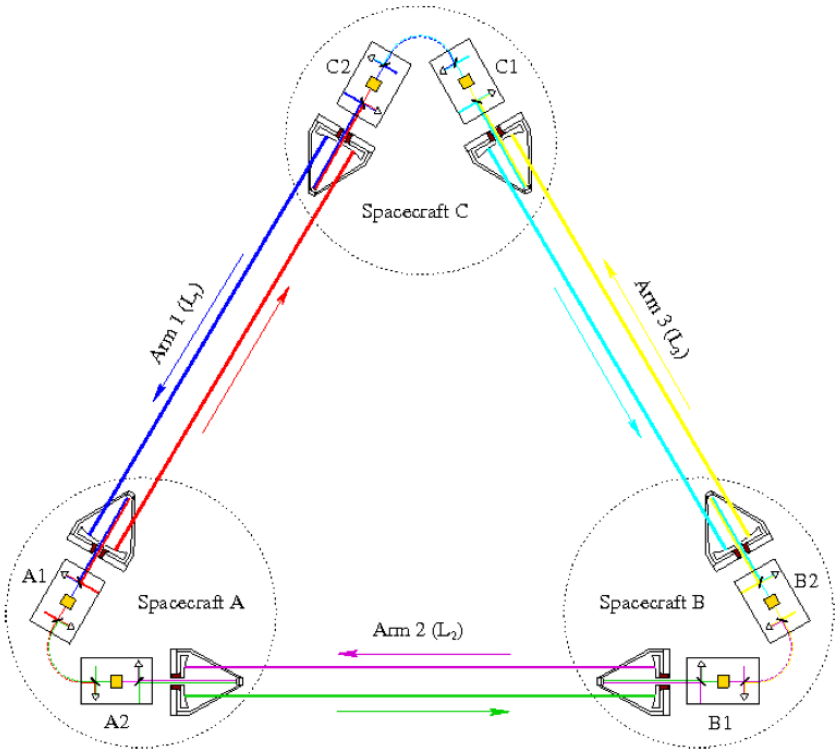

Figure 1.5: Triangular constellation formed by the three LISA spacecraft. Each of the satellite harbors two test masses in nominally geodesic motion. The distance between each pair of spacecraft is 5 million kilometers, which corresponds to a gravitational wave frequency of 15 mHz — as $L = \lambda_{\rm GW}/4$. The relative distance variations in a frequency band around 1 mHz between corresponding test masses in remote spacecraft is measured to picometer precision by means of laser interferometry.

between the test mass and a set of electrodes that surrounds it. These electrodes are obviously fixed to the spacecraft. This measurement is then converted into a force-command which activates a set of micro-thrusters that exert forces on the spacecraft. This technique is known as *drag-free control* (Lange, 1964). The required resolution of the capacitive sensors is ~ 10 nm Hz$^{-1/2}$ and the disturbing accelerations induced by the sensor back-action and by the parasitic forces on the test masses must be lower than 3 fm s^{-2} Hz$^{-1/2}$, in the frequency range of 0.1 mHz to 0.1 Hz (Bender, 1998).

In Michelson interferometers a single light source is split and recombined after traveling identical path lengths. Therefore, when they are combined and measured by the photodetector the noise is rejected since it is common to both laser beams. On the contrary, LISA uses six different light sources: one per test mass (see Fig. 1.5). In this case, the noise from the light sources is uncorrelated and the time for a

photon to travel from one spacecraft to another is $\sim$ 15 s. In this situation, the uncorrelated noise of the lasers, together with its frequency noise, dominate the measurement of the distance between the test masses, thus disabling the detection of gravitational waves. However, time-delay interferometry techniques succeed in eliminating the laser phase noise. These techniques are based on the formation of different combinations of different phasemeter outputs from different optical benches with suitable time delays in order to create correlated signals to cancel the noise. In order to generate the appropriate time-delayed copies of the phasemeter signals, these techniques require accurate knowledge of the distance between the spacecraft (Tinto et al., 2003).

In the current design of LISA, the sensitivity limiting noise effects (Bender, 1998; Danzmann & Rüdiger, 2003; Schumaker, 2003) are grouped in : (1) shot noise and (2) acceleration noise. The shot noise is the effect of spurious path difference inversely proportional to the square root of the received laser power. Due to the low level of light power received by the interferometer telescopes, the shot noise plays a major role in the total noise budget of spurious displacements. This noise defines the flat center band of the LISA sensitivity curve (see Fig. 1.6). The acceleration noise is the dominating noise source below 1 mHz. This noise is due to the acceleration of the test masses that cannot be shielded by the drag free control. These accelerations comprise those caused by temperature and magnetic field fluctuations, charge fluctuations of the test masses due to cosmic and solar radiation, microgravity effects, and other. Residual noise accelerations have a rather white spectral distribution, which results in position errors increasing approximately as ω^{-2}. This is because the position spectral density relates to the acceleration spectral density as

$$S_{\Delta x}^{1/2} = \frac{S_{\Delta F}^{1/2}}{m_{\rm TM}\,\omega^2}, \tag{1.5}$$

where $m_{\rm TM}$ is the mass of each test mass and $\omega = 2\pi f$. On the other hand, the LISA antenna response decreases as $(f\tau)^{-1}$ at frequencies above the inverse of the round-trip time τ. Thus, above certain frequencies the sensitivity decreases proportionally to ω^{-1}. Figure 1.6 shows the LISA noise curve, where the aforementioned noise sources and the frequency dependence of the LISA interferometer response have been taken into account.

Low frequency stray forces inside the spacecraft tend to move the test masses away from their geodesics and, therefore, they prevent to put them in perfect free fall. A residual noisy acceleration can be converted to strain noise as

$$S_{\Delta F}^{1/2}(\omega) \xrightarrow{1/m} S_{\Delta a}^{1/2}(\omega) \xrightarrow{1/\omega^2} S_{\Delta x}^{1/2}(\omega) \xrightarrow{2/L} S_{h}^{1/2}(\omega), \tag{1.6}$$

That is:

$$S_{h}^{1/2}(\omega) = \frac{2}{m_{TM}\,L\,\omega^2} S_{\Delta F}^{1/2}(\omega). \tag{1.7}$$

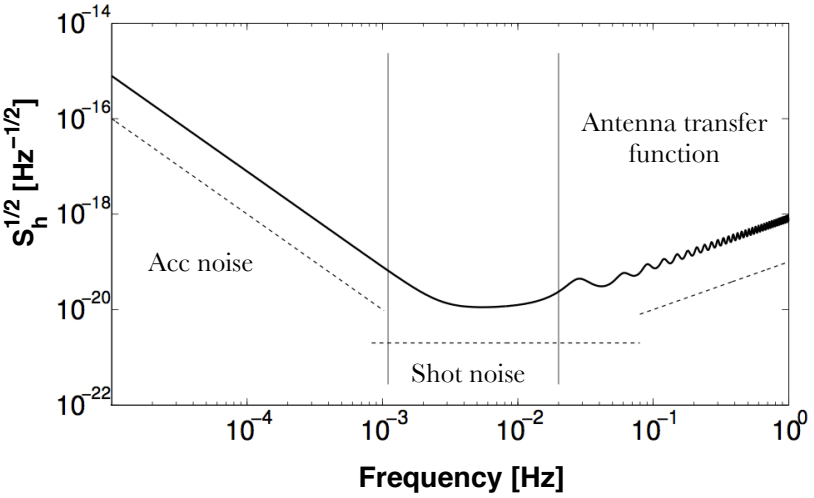

Figure 1.6: Expected noise curve for LISA. Noise related to force perturbations acting on the test masses such as magnetic field or thermal fluctuations are proportional to ω^{-2} and are relevant in the lower LISA band (up to 1 mHz). The shot noise defines the noise plateau in the center of the band. Finally, the high frequency noise is due to the antenna transfer function and increases proportionally to ω.

In this case, as the effect decays with ω^2, above ~ 3 mHz the performance of LISA is expected to be dominated by the shot noise of the laser interferometer, which is expected to be ~ 40 pm Hz$^{-1/2}$. This is true only if stray forces have a power spectral density

$$S_{\Delta a}^{1/2}(\omega) = \frac{S_{\Delta F}^{1/2}(\omega)}{m_{\mathrm{TM}}} \leq 3 \times 10^{-15} \sqrt{1 + \left(\frac{f}{8\,\mathrm{mHz}}\right)^4} \sqrt{1 + \frac{0.1\,\mathrm{mHz}}{f}} \mathrm{ms}^{-2}\mathrm{Hz}^{-1/2} \quad (1.8)$$

down to a frequency of 0.1 mHz. This residual noise determines the free fall accuracy required for LISA.

1.2.3 Technology demonstrator: The LISA Pathfinder mission

The technologies required for the LISA mission are therefore many and challenging. At the same time, some flight hardware cannot be tested on ground. For instance, free fall conditions can not be maintained during periods of hours, such as required to make sub-milliHertz measurements. This led to set up a technology demonstrator to

test critical LISA technologies in a flight environment. This precursor mission, called LISA Pathfinder (LPF), is framed within the Scientific Program of the European Space Agency (ESA). The idea of LISA Pathfinder is to mimic the behavior of one of the LISA arms, squeezing it from five million kilometers to 35 centimeters. This enables to place both test masses in a single spacecraft. The key technologies to be submitted to test in LISA Pathfinder are the drag-free concept and the Optical Metrology Subsystem (OMS). The first consists of a Gravitational Reference Sensor (GRS), which uses a set of electrodes to determine by capacitance measurements the position of the test masses with respect to the spacecraft to nanometer precision. Then it sends signals to a set of micro-thrusters which are ignited to relocate the spacecraft so that the test mass remains in its centered position, thereby preserving the free fall motion of the latter. Secondly, the OMS provides picometer precision measurements of the relative position/acceleration of the two test masses, using precise interferometry.

As it has been detailed for LISA, there are some internal forces that can not be eliminated by the drag free mechanism. Among them, the main contributions are the temperature and magnetic field fluctuations inside the satellite and the charge fluctuations of the test masses. Each of these perturbations have an effect on the acceleration noise of the test masses, thus are detected by the interferometric readings. To achieve maximum efficiency of the instrument, these contributions have to be identified and subtracted. To this end, LISA Pathfinder is endowed (Cañizares et al., 2009) with the Data management and Diagnostics Subsystem (DDS). The DDS is conformed by a set of hardware units intended to measure the relevant physical magnitudes inside the satellite, and can be split into three subsystems: the magnetic diagnostics unit, the thermal diagnostics subsystem, and the radiation monitor. The first of these three subsystems is the unit under analysis in this thesis.

1.3 Thesis objectives and outline

This thesis is focused on the study of the Magnetic Diagnostics Subsystem and its related data analysis algorithms. The ultimate objective is to determine the contribution of the magnetic effects to the main science reading of the LISA Technology Package instrument. Moreover, the precision of such estimate must be determined. To this end, this thesis undertakes two complementary tasks. First, we estimate the magnetic properties of the test masses, namely, their remanent magnetic moment and their magnetic susceptibility. Second, we estimate the magnetic field and its gradient at the position of the test masses from the readings of the four onboard magnetometers. Concerning the first task, there is a necessity to assess the kinematic response of the LTP instrument to the specific magnetic signal injections. For this reason and for other needs of the mission, the LTP Data Analysis team has a dedicated research line intended to develop a complete, fast, accurate, and realis-

tic LISA Pathfinder simulator. As part of this thesis we have contributed to the modeling of some subsystems and the integration of the whole simulator. Once this kinematic response is modeled, the response to the test masses to specific magnetic injection to determine their magnetic properties must be analyzed. On the other hand, to achieve the second task, since classic methods failed to deliver precise estimates, alternative interpolation architectures to estimate the magnetic field at the positions of the test masses must be developed.

From the list of the primary objectives of the thesis, this study can be split into three major sections. First, the design and analysis of the magnetic experiments to determine the magnetic properties of the test masses. In a second step the estimation of the magnetic field and its gradient out of the readings of the triaxial onboard magnetometers onboard LISA Pathfinder must be done. Finally, a third task consists in the contribution to the collaborative effort of developing a complete LISA Technology Package simulator within the LTP Data Analysis software. According to these considerations this work is organized as follows. Chapter 2 introduces the main goals and characteristics of the LISA Pathfinder mission and it describes the Diagnostics Subsystem onboard LPF. Among the main important features of the diagnostics units, we focus on the characteristics of the hardware related to the magnetic diagnostics unit. These hardware pieces are the most used by the data analysis algorithms presented throughout this thesis. Chapter 3 is mainly devoted to the design of the magnetic experiment to be performed in flight in order to estimate the magnetic properties of the test masses. Chapter 4 is an extension of Chapter 3 since it presents specific data analysis processing steps and procedures to estimate precisely and robustly the magnetic properties of the test masses. Chapter 5 focuses on the estimation of the magnetic field and its gradient at the positions of the test masses. To this end, we use an alternative to classic interpolation methods based on neural networks. Chapter 6 analyses the robustness of the neural network interpolation scheme in various mission circumstances. We present also some of the limitations of the method and our vision to the LISA scenario. Finally, Chapter 7 presents the LTP Data Analysis simulator. We present an overview of the entire development of the Data Analysis tools and, specifically, the complete LTP simulator. This is the result of the collaborative work of a large group of scientists within the LTP Data Analysis team, however, it is briefly presented in this manuscript since the dynamic response of the complete instrument to specific inputs is of relevant importance to the thesis. The final chapter summarizes the main contributions of the present work. We also present the future studies needed on this topic and how we plan to organize the data analysis activities of the magnetic data during science operations.

Chapter 2

LISA Pathfinder and the Magnetic Diagnostics Subsystem

In this chapter we present an overview of the LISA Pathfinder mission, its main characteristics and its objectives. We also describe the main science measurement to be performed in flight and the influence of various noise sources to this measurement. Finally, we present the contribution of the different identified magnetic effects and we stress the need for the Magnetic Diagnostics module. We also present the hardware contained within this module and we put forward the necessity of performing two tasks: estimate the magnetic properties of the test masses and infer the magnetic field at the test masses. These two tasks are the main objectives of this thesis.

2.1 The LISA Pathfinder mission

LISA raises many new technological challenges and a handful of the most critical ones can not be tested on ground. For instance, the impossibility of testing accurate free fall trajectories for long periods of time (in the order of hours). Therefore, ESA decided that a technological precursor mission was needed. This mission was called LISA Pathfinder. The idea of this mission is to reproduce the behavior of one only LISA arm, but reducing it from five million kilometers to 37.6 centimeters. This enables the possibility of placing both test masses of the LISA-link in a single spacecraft. Of course, such a reduction of the arm length prevents LPF from detecting gravitational waves, and converts it into a technological test bench of the different subsystems to be used by LISA. At the same time, the stringent requirements of LISA are somewhat reduced for LISA Pathfinder, both regarding the frequency range and the sensitivity of the measurement. Actually, the measurement bandwidth for LISA Pathfinder is restricted from 1 mHz up to 30 mHz, and the dif-

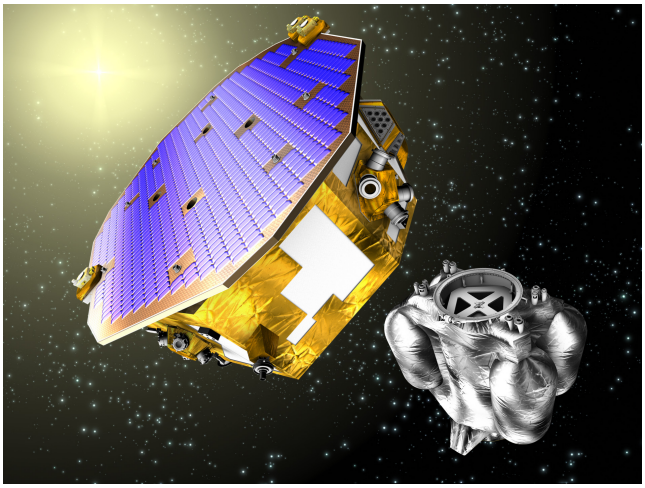

Figure 2.1: Artistic view of the LISA Pathfinder spacecraft after the separation from its propulsion module that will inject it in the Lagrangian point L1, 1.5 million km away from the Earth.

ferential acceleration noise requirement is set to 3×10^{-14} m s^{-2} Hz$^{-1/2}$. This means that both requirements have been relaxed one order of magnitude with respect to those of LISA.

LISA Pathfinder includes two science modules: the LISA Technology Package — also known as the LTP (Vitale, 2005; Anza et al., 2005) — which is the European Space Agency (ESA) science module, and the Disturbance Reduction System — known as DRS (Folkner et al., 2003) — which is the science module contributed by the National Aeronautics and Space Administration (NASA). Its main components are the key technologies to be tested for LISA, which are: the Gravitational Reference Sensors (GRS) — also known as Inertial Sensors (IS) — coupled with the drag free concept and the interferometric measuring system. The two GRSs are the two large vertical cylinders — see Fig. 2.2, where the two test masses are hosted. The two gold-platinum test masses freely float at the center of each of these cylinders. The center position of these cylinders are separated by the above mentioned 37.6 cm. The relative position/acceleration between the two test masses is measured by the onboard interferometer. This interferometer has also a channel that measures the position of test mass 1 with respect to the spacecraft. On the other hand, the positions and rotation of the test masses with respect to the Electrode Housing reference frame are measured by the gravitational reference sensor (see Appendix A for specific details). These measurements are then fed to the onboard control system. This control architecture ensures a drag free behavior of one of the test masses by means of an ultra precise micro-Newton propulsion system, that is, the spacecraft isolates the test mass from the perturbations coming from outer space. In this case,

the test mass follows a geodesic motion and the satellite is maintained centered with respect to this test mass. For this purpose, the mission uses a set of FEEP thrusters (Field Emission Electric Propulsion). On the other hand, the other test mass is controlled by a Low Frequency controller and follows the first test mass. This second control loop uses the electrodes as the main actuation system and prevents the second test mass to crash with the spacecraft walls. It is important to note that the Low Frequency Control does not act within the frequency band of interest of LPF, therefore test mass 2 also follows a quasi-free fall trajectory within this band. The main science measurement is the differential displacement between both test masses and it is delivered by the onboard interferometer.

The requirement for the LTP instrument is formulated in terms of spectral density of differential acceleration noise as:

$$S_{\delta a}^{1/2} = \frac{S_{\delta F}^{1/2}}{m_{\mathrm{TM}}} \leq 3 \times 10^{-14} \left[1 + \left(\frac{\omega/2\pi}{3\ \mathrm{mHz}}\right)^2\right]\ \mathrm{m\,s^{-2}\,Hz^{-1/2}} \tag{2.1}$$

within the band ranging from 1 mHz up to 30 mHz. The main objective of LISA Pathfinder is to demonstrate that this residual differential acceleration noise requirement can be achieved. In this case, LPF will verify the ability to place a test mass in purely gravitational free fall and measure the relative distance to another free falling object.

2.1.1 Mission rationale

LISA Pathfinder will operate in a Lissajous orbit around the Lagrange point L1 of the Sun-Earth system, an environment similar to that where the LISA constellation is expected to operate. Briefly, LISA Pathfinder will demonstrate the possibility of building an inertial frame within a spacecraft orbiting the Sun on the scale of the meter in space and on the scale of a few hours in time at the level of Eq. (2.1).

The mission programme in performing this demonstration is scheduled in two differentiated steps:

1. An expected noise model for the specific orbit and for the specific characteristics of the spacecraft is derived. Then, the mission is designed to ensure that any differential residual acceleration noise of the test masses is kept below the requirements.

2. Once LPF is in orbit, the differential residual acceleration noise between the two test masses is measured. Then, the noise model for LISA is validated following these iterative steps:

   (a) One noise contribution to the main acceleration measurement is identified.

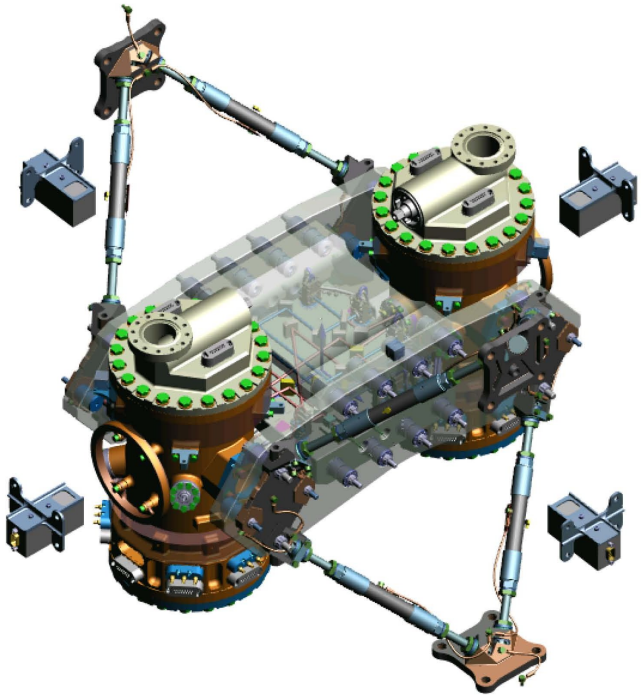

Figure 2.2: A schematic view of the payload of LPF, the LISA Technology Package (LTP). The grey floating boxes represent the four tri-axial fluxgate magnetometers, which are attached to the LCA walls (not seen in the picture). The circular induction coils are observed in copper color, close to each of the two GRS towers.

(b) We determine whether its effects can be subtracted adjusting the specific instrument parameters, or we can estimate its contribution.

(c) In the first case, we upload the new instrument parameters and we remeasure the acceleration noise. We check if this noise contribution has been eliminated.

(d) In the second case, we estimate this contribution and we suppress its contribution from the main acceleration data stream (see section 2.4.1).

(e) We schedule this procedure for each identified noise source.

This iterative process is based on the fact that the noise model expects that the contributions to the total power spectral density fall into three categories:

1. Noise sources whose effect can be identified and suppressed by a proper adjustment of selected instrument parameters. For instance, the force due to residual coupling of test masses to the spacecraft (Vitale, 2005).

2. Noise forces related to measurable fluctuations of some physical parameter. For instance, forces due to thermal gradients or to magnetic fields. The LTP includes sensors to measure the above physical disturbances (Cañizares et al., 2009). At the same time, in order to identify the system properties, it also includes heaters to induce thermal gradients, and magnetic coils to induce large magnetic fields. With this information, we solve a system identification problem and we reproduce the expected acceleration noise data stream due to these effects. Then, we subtract them from the main acceleration measurement.

3. Noise sources that cannot be removed by any of the above methods. In this group, for instance, we find the charged particle flux due to cosmic rays and solar radiation. These noise sources will be also measured in order to compare them with the predicted noise models. If the preliminary noise model is correct, these noise sources must have a contribution below the mission requirements. If not, we will be in front of unforeseen sources of disturbance, and new procedures will have to be investigated.

If the procedure described above is successful, the noise model for LISA will be validated and the technological ability to place a test mass in purely gravitational free fall will be demonstrated.

2.1.2 LTP basic design and mission subsystems

The design of the LTP has its core component in the two free-floating test masses separated by 376 mm. These two test masses are cubes made of an alloy of Pt (27%) and Au (73%), have a mass of 1.96 kg and a side size of 46 mm. They are both hosted within a single spacecraft. The relative motion along the common x- sensitive axis, is measured by means of a laser interferometer. At the same time, each of the two test masses are surrounded by their position sensing electrodes. These electrodes provide positioning information of both test masses relative to the housing frames (Vitale, 2005). The information of the laser and the sensing electrodes is fed to the control system that commands the position of the spacecraft and of the test masses. The drag-free control law commands the micro-Newtown thrusters to keep the spacecraft centered with respect to a reference point (the position of test mass 1). The low frequency control law commands the electrode actuation system to force test mass 2 to follow test mass 1. This is done out of band and only along the sensitive axis. In order to accomplish all these tasks, the LTP possesses several subsystems.

1. *Gravitational Reference Sensor (GRS)*: This subsystem is also known as the Inertial Sensor (IS). There exist two GRSs in LTP, one for each test mass. In Fig. 2.2, the GRS are the two brown towers at the center of the payload scheme. Each of these sensors are formed by a set of electrodes that surround each test mass. The electrodes, hosted by the housing, form a set of variable

capacitors with the test mass (Dolesi et al., 2003). The variation of capacitance of these capacitors, due to motion of the test mass, is used to detect it via a set of parametric-bridge based differential capacimeters. This mechanism allows for the reading of the position of the test mass and their orientation with respect to the spacecraft. The variable capacitance of electrodes is also used to apply forces to the test mass, using selected voltages. The front-end electronics is in charge of providing the readout of the capacitive sensing and also apply the requested voltages for actuation (Hueller, 2003). The sensitivity of the measurements of the GRS for the x-axis is on the order of 1.8 nm $\mathrm{Hz}^{-1/2}$ for displacement at 1 mHz and on the order of 200 nrad $\mathrm{Hz}^{-1/2}$ for angular excursions (Vitale, 2005). Moreover, each of the test masses is held inside a high-vacuum chamber. This vacuum chamber has a residual pressure requirement of 10^{-5} Pa and should guarantee the proper vacuum during science operations and during integrations and testing. At the same time, this chamber carries the mechanical interfaces between the GRS and the optical bench. The caging mechanism that should hold the test mass during launch is also mounted inside the vacuum enclosure (Bortoluzzi et al., 2003). Finally, in the GRS we have also the CMS (Charge Management System) that forces the discharge of the test mass by means of ultraviolet light units (ULU). It also contains getter pumps that provide the requested high vacuum around the test mass (Vitale, 2002). In summary, each of the two GRS is formed by one test mass, a set of electrodes, a caging mechanism and a charge management system, everything inside one vacuum enclosure.

2. *Optical Metrology System (OMS)*: This subsystem has as main objective the measurement of the main science output, i.e. the relative displacement between both test masses along the main measurement axis, i.e., the x-axis. At the same time, it will measure the position of test mass 1 with respect to the spacecraft. This readout will be redundant and it will test the optical readout technology with respect to the capacitive sensing (which also delivers this exact measurement). By performing wavefront sensing, the interferometer will also deliver angular motion readouts of test mass 1 relative to the spacecraft and those of test mass 2 relative to test mass 1. The sensitivity required for the interferometric system is 9 pm $\mathrm{Hz}^{-1/2}$ between 3 mHz and 30 mHz, relaxing as $1/f^2$ towards 1 mHz along the x-axis and of 400 nrad $\mathrm{Hz}^{-1/2}$ for the rotation axes (Heinzel et al., 2003). The system designed to do this is a heterodyne Mach-Zehnder interferometer. This design is based on four separate interferometers: two of them serve as references (phase and frequency reference) and the other two deliver the two outputs described above (Heinzel et al., 2004; Garcia-Marin, 2007). The complete interferometer system is based on an optical bench (OB), which is placed between the two GRSs and carry all the elements to perform the interferometry: the Laser Assembly, which contains

the laser source and the modulator unit and the Phasemeter Assembly, with the set of photodiodes and the processing unit. The readings coming from the phasemeter are processed by the Data Management Unit (DMU).

3. *Drag Free and Attitude Control System (DFACS)*: The control chain onboard LPF acts on the spacecraft to recreate a drag free environment and it is known as the DFACS unit. This controller has been designed by Astrium GmbH, based on the H-infinity technique (Ogata, 2001), to satisfy science requirements for each of the controlled coordinates (Schleicher, 2008; Brandt & et al., 2004). These controllers are modeled with sensor and actuation selection matrices, that allow to select different science/controlling modes. Each of these science modes use a certain and precise combination of sensors (and sensed variables) and actuators (and actuation variables). The main science control mode is Science Mode 1. This mode has two differentiated control loops, the drag-free loop and the low-frequency suspension loop. The drag free loop receives as reference signal the position of test mass 1 with respect to the spacecraft. Then, it commands actuation signals to the thrusters of the satellite to maintain the spacecraft centered with respect to test mass 1 (Schleicher, 2009). In this case, it shields the test mass from the multiple perturbations of the outer space and provides a free fall environment (geodesic motion) for test mass 1. The thrusters used in LPF are a set of 12 micro-Newton FEEP thrusters grouped in three different clusters (Bindel, 2008). The low-frequency suspension loop uses as reference signal the differential displacement between test mass 1 and test mass 2, and acts on test mass 2, forcing it to follow test mass 1. This actuation is done out of the measurement bandwidth, therefore in this band it recreates also a geodesic motion for the second test mass. Strictly speaking, TM_2 is not in geodesic motion, but the deviations thereof are out of the instrument band. Hence, in this situation we obtain a measurement of a relative distance between two free falling objects within the band from 1 mHz to 30 mHz. This actuation is done by means of the electrodes that surround test mass 2. The appropriate algorithms are stored in the Onboard Computer (OBC), which is the main mission computer.

4. *LTP core assembly (LCA)*: The central part of the spacecraft is where the LTP core assembly (LCA) is placed. The LCA is formed by two parts: the two gravitational reference sensors and the optical bench between them (Garcia-Marin, 2007). This grouping can be observed in Fig. 2.2. The LCA is fixed to a satellite cylindric wall located at a centered position in the spacecraft by means of 8 suspension struts (hyperstatic), see Figs. 2.3 and 2.4 .

5. *Data management and diagnostics subsystem (DDS)*: The DDS consists of two main parts: the data management unit (DMU) and the diagnostic elements (Cañizares et al., 2009; Lobo, 2005). The DMU is the computer for

Figure 2.3: General view of the spacecraft. The cylinder in the central part is thought for the LCA placement and the rest of the structure will allocate the remaining subsystems, such as front-end electronics, onboard computers or other units.

the LISA Technology package. It performs two main tasks: (1) drives and controls the diagnostics items, and (2) acquires and processes the phasemeter data. The other main part of the DDS is the set of diagnostic elements, sensors and actuators. The sensors are intended to monitor various physical disturbances happening inside the LTP and the actuators are meant to generate controlled disturbances to estimate the properties of the instrument. They are: (a) magnetometers and coils; (b) temperature sensors and heaters; and (c) the radiation monitor (Llamas, 2006). These diagnostic elements are described in section 2.3. The contribution of the Spanish LTP group, with researchers from UPC, ICE/CSIC and IEEC, to the LISA Pathfinder mission is mainly focused on this subsystem. Specifically, the work presented in this thesis is mainly devoted to the algorithms needed to process the data delivered by the magnetic diagnostic elements.

2.2 Noise measurement breakdown in LTP

The science objective of LISA Pathfinder is the verification of differential free-fall between two test masses. This verification will be done by measuring the differential displacement between these two test masses along the sensitive axis, which is the one connecting the centers of the test masses, conventionally the x-axis. In the main mode of the mission, i.e. Science Mode 1, the dynamics of the differential motion (coordinate Δx) are written in the Laplace domain as:

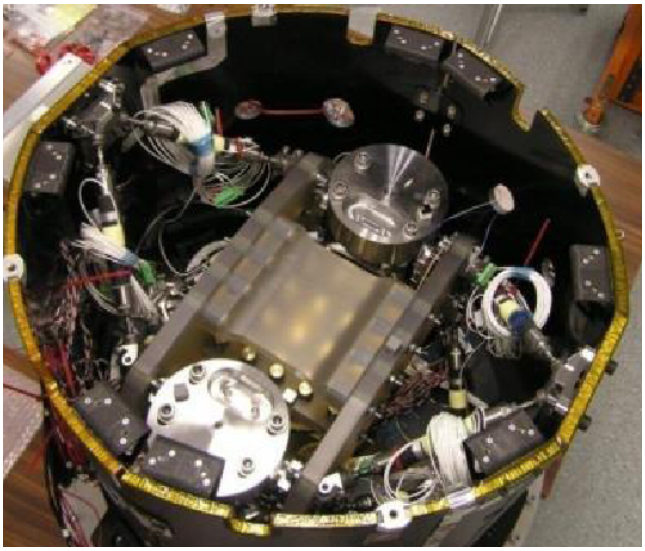

Figure 2.4: View of the LCA hardware already placed within the spacecraft. Each of the two GRSs cylinders are placed at the end of the optical bench, and the entire structure is mounted to the spacecraft walls by the struts.

$$\Delta x_{\rm m} = \frac{G(s)}{1+G(s)\,C_{\rm LFS}(s)}\,(-C_{\rm LFS}(s)\,n+\frac{f_2-f_1}{m}+(\omega_1^2-\omega_2^2)\,x_1+\omega_2^2\,(\delta x_2-\delta x_1)) \quad (2.2)$$

where $(f_2-f_1)/m$ are differential forces per unit mass along the sensitive axis, ω_1 and ω_2 are the stiffness parameters coupling the motion of each test mass to the motion of the spacecraft, and $(\omega_1^2-\omega_2^2)\,x_1$ is the acceleration due to differential stiffness. The transfer functions $G(s)$ and $C_{\rm LFS}(s)$ denote, respectively, the plant dynamics and the suspension controller transfer function. n is the optical readout noise output of the interferometer. The plant dynamics for the differential channel is essentially given by

$$G(s) \sim \frac{1}{s^2+\omega_2^2}.$$

The last term $\omega_2^2\,(\delta x_2-\delta x_1)$ denotes the coupling due to elastic distortion along the sensitive axis (Schleicher, 2009; Brandt & et al., 2004; Vitale, 2005; Brandt et al., 2010). s is the Laplace domain variable and the subindex "m" stands for *measured*.

In order to derive the acceleration data stream, on the ground, the transfer function

$$\frac{G(s)}{1+G(s)\,C_{\rm LFS}(s)}$$

must be known and inverted. Then, the measured differential displacement, Eq. (2.2),

should be multiplied by

$$\left(\frac{G(s)}{1+G(s)\,C_{\mathrm{LFS}}(s)}\right)^{-1}.$$

Hence, in an ideal case, the acceleration measurement is:

$$\Delta a_{\mathrm{m}} = \frac{f_2 - f_1}{m} + (\omega_1^2 - \omega_2^2)\,x_1 + \omega_2^2\,(\delta x_2 - \delta x_1) - C_{\mathrm{LFS}}(s)\,n \tag{2.3}$$

Any mismatch in the knowledge of

$$\frac{G(s)}{1+G(s)\,C_{\mathrm{LFS}}(s)}$$

affects the acceleration measurement. However, all acceleration terms are affected by the same amount. Note also that this mismatch can be frequency dependent because this operation is performed across the complete measurement bandwidth.

Similar equations can be obtained for other science modes, such as the Drift Mode or Science Mode 2. In Drift mode, the acceleration between test masses is measured only between control kicks, where no actuation noise is present in the interferometer reading (Grynagier, 2009), while in Science Mode 2, the second test mass is controlled taking the absolute position of test mass 2 instead of the differential reading as the main reference control variable (Schleicher, 2009). This thesis has been developed using Science Mode 1, as it is expected to be the main science mode for the majority of experiments (Vitale, 2005), nevertheless similar studies could be undertaken in other control modes.

2.2.1 Noise breakdown

The different noise contributions to the total acceleration measurements are classified into DC and in band contributions. The constant contributions are those type of effects that constantly disturb the test masses. They have to be counteracted by the control system to avoid secular drifts and the test masses colliding with the walls of the spacecraft. On the other hand, the contributions in the measurement bandwidth must be adequately identified and estimated to perform the noise subtraction process. These main sources are briefly described in the following sections.

DC differential forces and absolute torques

The test masses will suffer constant forces and torques mainly due to five effects:

- *Electric field*: The electric field in the surroundings of the test masses produces a force and a torque in each of the test masses because they behave as charged bodies. The force is the product of the charge of the test mass by the electric field at the charge position. Discharge mechanisms are envisioned to reduce this distortion.

- *Magnetic field*: The interaction of the magnetic field surrounding the test mass with any remanent or induced magnetism in the test mass will result in a force on the same test mass. The force is the product of the test mass magnetism (remanent or induced) and the gradient of the magnetic field in which the test mass rests. On the other side, the torques are mainly due to the vector product of the test mass remanent magnetic moment and the magnetic field existent at the location of the test mass.

- *Thermal distortions*: The thermal effects comprise the radiometer effect, the differential radiation pressure, and the outgassing. The radiometer effect happens in rarefield gas atmospheres, where the equilibrium condition is not reached at uniform pressure, but rather when the ratios of pressure to the square root of the temperature equal each other. The radiation pressure is the effect produced by the fact that any body at any absolute temperature emits thermal radiation. Finally, the outgassing is due to the presence of gas within the walls of the GRS.

- *Laser radiation pressure*: The laser beam of the optical metrology system impinges on the test mass and exerts a force proportional to its power. Because forces are exerted on both test masses, this causes the test masses to move in opposite directions, and the effect is considered to be correlated. This effect is proportional to the power of the laser beam.

- *Gravitational field*: The gravitational field of the spacecraft provides the largest DC force contribution. Its dominance is such that the DC field will need to be compensated by the careful placement of balance masses near the test masses. The gravitational compensation will aim to reduce the differential acceleration to zero. However, there may exist some errors in the knowledge of this field caused by alignment and mass distribution errors.

Along the $x-$axis, and according to Brandt et al. (2010), the apportioning to each of these DC contributions are listed in Table 2.1. Note that the main contribution is expected to be due to gravitational effects and that the contribution of the magnetic effects is, in this case, negligible.

Effects on the measurement bandwidth

The contributions to the total acceleration reading within the measurement bandwidth are grouped within five different types:

1. Direct forces: They represent the contribution of $(f_2 - f_1)/m$ in Eq. (2.3). This contribution can be sub-classified into the following contributions:

Table 2.1: Apportionment of the contribution of the DC force along the x-axis. In the table we show the budget prevision for each contribution. We also introduce the margin left up to the mission requirement.

Contribution	a_x [m s^{-2}]
Electric field	4×10^{-11}
Magnetic field	5×10^{-14}
Thermal distortion	2.78×10^{-12}
Laser radiation	2.04×10^{-11}
Gravitational field	3.71×10^{-10}
Total	4.34×10^{-10}
Margin	2.16×10^{-10}

- Internal forces: The internal forces contribution to the total acceleration noise are:
  - Thermal effects: they are due to all thermal fluctuations in the inertial sensors, such as the ones caused by the radiometer effect, the differential radiation pressure, the asymmetric outgassing and the thermal distortion of the IS housing.
  - Brownian noise: they are due to dielectric losses of the electrodes, residual gas damping, magnetic damping due to thermal dissipation due to eddy currents and, finally, brownian noise due to magnetic impurities — if the remanent magnetic moment of the test masses is not uniform (these effects are considered negligible when compared to the residual gas damping contribution).
  - Magnetic field effects: the determination of these effects in flight is the main purpose of this thesis, they will be examined in more detail in the following sections. Their total contribution is expected to be of 2.77×10^{-15} m s^{-2} Hz$^{-1/2}$. It represents the largest contributor among the internal direct forces.
  - Random charge fluctuations: charge fluctuations on the test masses and other voltage fluctuations may represent an acceleration noise contribution because the fluctuation in charge couples via any DC voltages into a force noise onto the test masses.
  - Laser radiation pressure: the optical metrology laser exerts forces on both test masses as the beam hits them. Fluctuations in the power of the beam produce fluctuations in the force on the test mass.
  - Self gravity noise: thermal distortions of the LTP and the SC platform structure are caused by fluctuations in the temperature of the whole

structure. These deformations will affect the local gravitational field of the structure at the test mass position, producing acceleration noise.

  - Stray voltage: under random charging effects it is shown that any charge fluctuation on the test mass couples via the integrated (effective average) stray DC voltage imbalance for the sensors' x-direction faces Δx into an acceleration noise on the test mass. Note, however, that not only the charge can fluctuate, but the stray DC voltage imbalance itself can fluctuate in the measurement bandwidth and thus create a force noise via the DC test mass charge.

- Sensitive axis Electrostatic Actuation: this contribution covers all effects on the direct forces due to actuation/sensing electrode voltage noise generated solely by the electrostatic actuation system. This also includes any quantization noise introduced due to the front-end electronics of the Inertial Sensors, the analog to digital converters and other noise sources not mitigated by the $\Sigma - \Delta$ loop (Dolesi et al., 2003).
- Cross-axes coupling: The cross-axes coupling considers direct acceleration effects along the sensitive axes due to control deviations or control actions along/around all cross axes coordinates. These are in particular: stiffness cross-coupling (contribution of the "off-diagonal terms of the stiffness") or electrostatic actuation cross-coupling (contribution of the "off-diagonal terms of the actuation matrix"[1] (Bortoluzzi et al., 2003).

2. Sensitive axis control: It corresponds to the term $(\omega_1^2 - \omega_2^2)\, x_1$ in Eq. (2.3). The sensitive axis control covers the differential acceleration noise contribution due to DC differential stiffness times the control jitter of test mass 1 along the sensitive axis in the measurement bandwidth.

3. Thermal distortion along the sensitive axis: It corresponds to the term $\omega_2^2\, (\delta x_2 - \delta x_1)$ in Eq. (2.3). The thermal distortion of the baseline between the two inertial sensor housing centers (actually the distance variation between the two electrostatic sensing nulls within the measurement bandwidth) has to be constrained, because it maps directly into a differential acceleration between the two test masses.

4. Optical Metrology System noise allocation: It corresponds to the term $C_{\mathrm{LFS}}(s)n$ in Eq. (2.3). This noise can be of two different natures: (1) the Optical Metrology System noise and (2) the alignment noise. The first is due to the measurement chain (electronics noise, laser frequency noise, laser power noise,...)

[1] Note that the coupling of the sensing system, i.e. distribution of sensing noise in different axes by parasitic coupling, has an indirect effect: it leads to control deviations and electrostatic actuation commands in each axis, depending on the multi-input-multi-output transfer function of the closed loop control system.

and external thermo-elastic induced errors. The second is due to the fact that whenever the x-faces of the test masses are not aligned, the Δx measurement may be degraded due to coupling of residual control jitter with other degrees of freedom.

5. Closed Loop uncertainty: The need of inverting

$$\frac{G(s)}{1 + G(s)\, C_{\mathrm{LFS}}(s)}$$

to obtain the acceleration measurement forces us to know this function within a given uncertainty. The science requirement document (Vitale, 2005) states that this closed loop transfer function must be known with 5% accuracy within the entire measurement bandwidth. This requirement is considered to be independent of all other requirements.

The contribution of each of the aforementioned different effects into the acceleration main reading (along the x-differential axis) are specified in Table 2.2. These contributions are extracted from the Experimental Performance Budget Document (Brandt et al., 2010). As can be seen in Table 2.2, the main noise contributor to the total acceleration reading is expected to be the contribution of the direct forces. More specifically, within the direct forces, the main contribution is apportioned to the internal forces. The residual gas damping effect together with the magnetic field effects are expected to be the most relevant noise sources with a contribution of around 5 m s^{-2} $Hz^{-1/2}$. In order of importance, it follows the contribution of the random charge fluctuation, the stray voltages, the thermal effects and finally the self gravity noise. These noises raise the necessity of monitoring each of their sources throughout the whole mission life time. Specifically, to monitor the magnetic effects, thermal effects and charging effects into the main science channel, the LISA Technology package is endowed with the Data Management and Diagnostics Subsystem (Cañizares et al., 2009).

2.3 The diagnostics subsystem onboard LISA Pathfinder

Among the internal forces acting on the test masses and not shielded by the drag free control system, there are three that are monitored by the Data Management and Diagnostics Subsystem (DDS). These three contributions are temperature fluctuations, presence of fluctuating magnetic fields within the spacecraft and the effect of random charging of the test masses due to cosmic and solar radiation. Therefore, the DDS is separated into three subsystems: Magnetic Diagnostics, Thermal Diagnostics and the Radiation Monitor.

Table 2.2: Apportionment of the contributions of different expected effects in the measurement bandwidth of the LTP instrument. We show the budget prevision for each contribution and the total margin up to the total requirement. Note that all requirements are expressed in acceleration terms and at 1 mHz, except for the Optical Metrology System requirement which is expressed at 30 mHz and in displacement terms. The requirement for the Optical Metrology System is expressed in displacement because this is the direct reading delivered by the interferometer and it is expressed at the highest frequency of the instrument band (30 mHz) because the high frequency noise of the measurement is the largest source of noise. This requirement is of 9 pm $\mathrm{Hz}^{-1/2}$ between 3 and 30 mHz along the sensitive axis and of 10 nrad $\mathrm{Hz}^{-1/2}$ for the alignment measurements (Heinzel et al., 2003, 2004).

Contribution in differential acceleration noise	a_x [m s^{-2} $\mathrm{Hz}^{-1/2}$] at 1 mHz
Direct forces	2.34×10^{-14}
Internal Forces	2.21×10^{-14}
Sensitive axis Electrostatic Actuation	6.95×10^{-15}
Cross Axes Coupling	3.35×10^{-15}
Sensitive axis control	1.25×10^{-16}
Thermal distortion	1.20×10^{-16}
Total	2.34×10^{-14}
Margin	1.83×10^{-14}
Contribution in differential displacement noise	x [m $\mathrm{Hz}^{-1/2}$] at 30 mHz
OMS, noise	6.37×10^{-12}
OMS-IS alignment	2.52×10^{-12}
Total	6.85×10^{-12}
Margin	5.83×10^{-12}

Magnetic diagnostics

This subsystem is conformed by four tri-axial magnetometers and two induction coils. These pieces of hardware are visible in Fig. 2.2. The four magnetometers are represented as floating boxes, and their actual physical support is the lateral wall of the larger cylinder which encloses the entire LTP (the LCA cylinder). Each of the induction coils are positioned next to each of the GRS towers, i.e., next to each of the test masses. The magnetometers are intended to sense with high precision the evolution of the magnetic field, acting then as pure passive hardware. The coils are capable of generating controlled magnetic field within the volume of the test masses, representing the active hardware of the subsystem. The specific characteristics of this subsystem are extensively presented in section 2.5, because it represents a key aspect for the development of this thesis.

Thermal diagnostics

The required temperature stability inside the LTP Core Assembly (LCA) is 10^{-4} K $\mathrm{Hz}^{-1/2}$. This will be monitored by a set of 24 high precision thermometers, positioned at different locations within the LCA (Cañizares et al., 2009; Sanjuán et al., 2008; Sanjuan, 2009). These thermometers will measure the temperature fluctuations and any temperature drift. Both have a direct effect on the dynamics of the test masses. They are the passive hardware of the thermal diagnostics subsystem. Additionally, this subsystem will be formed of 14 heaters that will allow to change the temperature dynamics and the temperature gradients at specific locations inside the LCA. These heaters represent the most critical hardware in terms of acceleration noise injection. The heaters are the active part of the thermal diagnostics subsystem.

The radiation monitor

LPF will be stationed in a Lissajous orbit around the Lagrange point L1, some 1.5 million km away from the Earth in direction to the Sun. There, the spacecraft will be exposed to various ionizing radiations coming from the Galaxy and from the Sun. Some of these charged particles, will hit the spacecraft structure surrounding the test masses, while others will make its way to them. The latter are particles having energies above a threshold of about 100 MeV. The excess charge deposited in the test masses depends on the primary energy of the incoming particle, since secondary particles are generated all the way of the primary particles across the spacecraft, most significantly (of course) in the electrode housing walls. Also, indeed, inside the test masses. The charge deposit is of course a random process which results in acceleration noise due to interactions with the electric system which monitors the position of the test masses in their enclosure. This results in fluctuations of the position of the test masses relative to the electrostatic center of the electrode housing, and in a Lorentz interaction with the environmental and interplanetary

magnetic field. The LTP is equipped with a system of ultraviolet lamps which are intended to purge (by photo-electric effect) the charge accumulated in the test masses. By accurately matching the discharge rates to the charging rates this noise can be minimized. However, the GRS can only track charging rates by averaging over certain periods of time. The Radiation Monitor (RM) is capable of measuring these charging rates over significantly shorter periods, thereby producing data which will be used to match the measured charging rates to the discharging rates, or else to clean LTP data by off-line analysis.

2.4 Magnetic acceleration noise in LTP

Magnetic noise in the LTP is allowed to be a significant fraction of the total mission acceleration noise requirement: $1.2 \times 10^{-14}\,\mathrm{m\,s^{-2}\,Hz^{-1/2}}$ can be apportioned to magnetism, i.e., 40 % of the total noise requirement, $3{\times}10^{-14}\,\mathrm{m\,s^{-2}\,Hz^{-1/2}}$. This noise occurs because the residual magnetization and susceptibility of the test masses couple to the surrounding magnetic field and its gradient.

From Ampere's Law, the elementary force on a current element $I\mathbf{dl}$ in the presence of a magnetic field $\mathbf{B}$ is given by $\mathbf{dF} = I(\mathbf{dl} \times \mathbf{B})$. Moreover, the total force on the current distribution $\mathbf{J}(\mathbf{x})$ in an external field $\mathbf{B}$ is calculated as (Jackson, 1999):

$$\mathbf{F} = \int \mathbf{J}(\mathbf{x}) \times \mathbf{B}\, dV. \tag{2.4}$$

This expression can be further manipulated to yield to the equation:

$$\mathbf{F} = \langle (\mathbf{M} \cdot \boldsymbol{\nabla})\mathbf{B} \rangle\, V \tag{2.5}$$

where $\mathbf{M}$ is the density of the magnetic moment of the test mass and $\mathbf{B}$ is the magnetic field at the test mass. In this expression, $\langle \cdots \rangle$ indicates test mass volume average of the enclosed quantity, therefore $\mathbf{M}$ and $\mathbf{B}$ are expressed at each test mass differential volume (dV). V is the volume of the test mass.

The magnetic moment comprises two terms: the first is known as the *remanent* magnetic moment, $\mathbf{M}_\mathrm{r}$, and it represents the natural value depending on the particle properties. The second is the *induced* magnetic moment, $\mathbf{M}_\mathrm{i}$, and it is originated when the test mass lies within a magnetic field. For the LTP test mass, the induced magnetic moment can be expressed linearly with respect to the magnetic field as a function of the magnetic susceptibility, i.e.:

$$\mathbf{M_i} = \frac{\chi}{\mu_0}\mathbf{B}.$$

The magnetic susceptibility, χ, is the degree of induced magnetization of a material in response to an applied magnetic field, whereas μ_0 is the vacuum magnetic constant, $4\pi \times 10^{-7}\,\mathrm{m\,kg\,s^{-2}\,A^{-2}}$. Therefore, the magnetic force expression is rewritten as:

$$\mathbf{F} = \left\langle \left[\left(\mathbf{M_r} + \frac{\chi}{\mu_0} \mathbf{B} \right) \cdot \boldsymbol{\nabla} \right] \mathbf{B} \right\rangle V. \tag{2.6}$$

In the above expressions it has been assumed that the derivative of the remanent magnetic moment is negligible. The magnetic field can be split into two contributions: the interplanetary magnetic field, $\mathbf{B}_{\mathrm{P}}$, and the magnetic field created by the subsystems of the spacecraft, $\mathbf{B}_{\mathrm{SC}}$. That is, we rewrite the magnetic field as:

$$\mathbf{B} = \mathbf{B}_{\mathrm{P}} + \mathbf{B}_{\mathrm{SC}} \tag{2.7}$$

Moreover, in order to assess the contribution of the magnetic effects within the measurement bandwidth of the LTP, we must consider the time varying components in each of the terms of Eq. (2.6). The fluctuations of the magnetic moment and the magnetic susceptibility have been considered negligible. Nevertheless, the effect of the fluctuations of the magnetic field and its gradient can not be neglected, and they are the reason for a fluctuating force in the LTP measurement bandwidth due to magnetic effects. Then, we write the magnetic field expressions as the sum of a constant DC part, $\mathbf{B}^{\mathrm{DC}}$, and a time varying component $\delta\mathbf{B}$. Note, that both components have an implied spatial dependence. This is done for the spacecraft and for the interplanetary field.

$$\mathbf{B}_{\mathrm{SC}} = \mathbf{B}_{\mathrm{SC}}^{\mathrm{DC}} + \delta\mathbf{B}_{\mathrm{SC}} \qquad \text{and} \qquad \mathbf{B}_{\mathrm{P}} = \mathbf{B}_{\mathrm{P}}^{\mathrm{DC}} + \delta\mathbf{B}_{\mathrm{P}} \tag{2.8}$$

For the spacecraft magnetic field gradient, we also have a DC part $\boldsymbol{\nabla}\mathbf{B}_{\mathrm{SC}}^{\mathrm{DC}}$ and a fluctuating part, $\delta\boldsymbol{\nabla}\mathbf{B}_{\mathrm{SC}}$, like we write in Eq. (2.9). However, the interplanetary field gradients (both DC and fluctuations) are negligible and therefore they are ignored. This is a safe assumption taking into account the small dimensions of the spacecraft in the interplanetary medium.

$$\boldsymbol{\nabla}\mathbf{B} = \boldsymbol{\nabla}\mathbf{B}_{\mathrm{SC}} = \boldsymbol{\nabla}\mathbf{B}_{\mathrm{SC}}^{\mathrm{DC}} + \delta\boldsymbol{\nabla}\mathbf{B}_{\mathrm{SC}} \tag{2.9}$$

Using this nomenclature, the magnetic force exerted on the test mass is rewritten as:

$$\begin{aligned}
\mathbf{F} &= \mathbf{F}^{\mathrm{DC}} + \delta\mathbf{F} = && (2.10)\\
&= \left\langle \left[\left(\mathbf{M}_{\mathrm{r}} + \frac{\chi}{\mu_0} \mathbf{B}_{\mathrm{P}}^{\mathrm{DC}} \right) \cdot \boldsymbol{\nabla} \right] \mathbf{B}_{\mathrm{SC}}^{\mathrm{DC}} \right\rangle V && (2.11)\\
&+ \left\langle \left[\left(\mathbf{M}_{\mathrm{r}} + \frac{\chi}{\mu_0} \mathbf{B}_{\mathrm{SC}}^{\mathrm{DC}} \right) \cdot \boldsymbol{\nabla} \right] \mathbf{B}_{\mathrm{SC}}^{\mathrm{DC}} \right\rangle V && (2.12)\\
&+ \delta\mathbf{F} && (2.13)
\end{aligned}$$

where the force fluctuation, $\delta\mathbf{F}$, is written as:

$$\delta\mathbf{F} = \left\langle \left[\frac{\chi}{\mu_0}\delta\mathbf{B}_{\rm P}\cdot\boldsymbol{\nabla}\right]\mathbf{B}_{\rm SC}^{\rm DC}\right\rangle V \tag{2.14}$$

$$+ \left\langle \left[\frac{\chi}{\mu_0}\delta\mathbf{B}_{\rm SC}\cdot\boldsymbol{\nabla}\right]\mathbf{B}_{\rm SC}^{\rm DC}\right\rangle V \tag{2.15}$$

$$+ \left\langle \left[\left(\mathbf{M}_{\rm r}+\frac{\chi}{\mu_0}\mathbf{B}_{\rm P}^{\rm DC}\right)\cdot\delta\boldsymbol{\nabla}\right]\mathbf{B}_{\rm SC}\right\rangle V \tag{2.16}$$

$$+ \left\langle \left[\left(\mathbf{M}_{\rm r}+\frac{\chi}{\mu_0}\mathbf{B}_{\rm SC}^{\rm DC}\right)\cdot\delta\boldsymbol{\nabla}\right]\mathbf{B}_{\rm SC}\right\rangle V \tag{2.17}$$

$$+ \left\langle \left[\frac{\chi}{\mu_0}\delta\mathbf{B}_{\rm P}\cdot\delta\boldsymbol{\nabla}\right]\mathbf{B}_{\rm SC}\right\rangle V \tag{2.18}$$

$$+ \left\langle \left[\frac{\chi}{\mu_0}\delta\mathbf{B}_{\rm SC}\cdot\delta\boldsymbol{\nabla}\right]\mathbf{B}_{\rm SC}\right\rangle V \tag{2.19}$$

being $\delta\mathbf{B}$ the fluctuation of the magnetic field, and $\delta\boldsymbol{\nabla}$ stands for the fluctuation of the gradient. Specifically, the constant terms are the one given by Eq. (2.11), which represents the constant force term due to the DC term of the interplanetary magnetic field, and that of Eq. (2.12), which represents the constant force term due to the DC term of the magnetic field created by the electric systems of the spacecraft. On the other hand, the fluctuating terms can be classified in terms due to the magnetic field fluctuation, terms due to the magnetic field gradient fluctuation, and second order terms, which represent the down converted AC contribution in the measurement bandwith. The first ones are given by Eq. (2.14), which represents the contribution of the fluctuation of the interplanetary magnetic field when it couples with the constant spacecraft magnetic field gradient, and that given by Eq. (2.15), which represents the contribution of the fluctuation of the spacecraft magnetic field when it couples with the constant spacecraft magnetic field gradient. The terms due to magnetic field gradient fluctuation are given by Eq. (2.16), representing the contribution of the fluctuation of the gradient of the magnetic field generated by the spacecraft when it couples with the constant interplanetary magnetic field, and that of Eq.(2.17) , representing the contribution of the fluctuation of the gradient of the magnetic field generated by the spacecraft when it couples with the constant spacecraft magnetic field. Finally, the second order terms are that given by Eq. (2.18), which represents the contribution of the fluctuation of the interplanetary magnetic field when it couples with the fluctuation of the gradient of the magnetic field generated in the spacecraft, and the one of Eq. (2.19), which represents the contribution of the fluctuation of the spacecraft magnetic field when it couples with the fluctuation of the gradient of the magnetic field generated in the spacecraft.

Table 2.3: Necessary test mass properties to proceed with the magnetic contribution calculation. Test mass conductance, susceptibility and remanent magnetic moment are requirements of the test masses (Vitale, 2005). On the other hand, the imaginary term of the susceptibility and its frequency break constant have been assessed after measurements performed at ESTEC (Trougnou, 2007; Fertin & Trougnou, 2007).

Property	Value
Mass (m)	1.96 kg
Edge (L)	0.046 m
Face aera (A)	$L^2 = 2.12 \times 10^{-4}$ m^2
Volume (V)	$L^3 = 9.73 \times 10^{-5}$ m^3
Electrical conductance (σ_0)	3.33×10^6 m$^{-1}\,\Omega^{-1}$
Magnetic susceptibility (χ_0)	2.5×10^{-5}
Imaginary susceptibility (δ_χ)	3×10^{-7}
Remanent magnetic moment (m_r)	2×10^{-8} A m^2
Susceptibility frequency break constant (τ_e)	$1/(2\,\pi\,630)$ s
Charge (DC) / electron charge (q_0)	1×10^7

2.4.1 Magnetic noise quantitative breakdown

In this section we perform a quantitative assessment of each of the aforementioned magnetic induced force noises within the measurement bandwidth. Prior to this analysis we need to know the value of the expected magnetic field and magnetic field gradient in the spacecraft during science operations. This information is listed in Table 2.5, which is extracted from tests done at Astrium Stevenage (Wealthy & Trenkel, 2010), assumptions reported in the Experimental Performance Budget (Brandt et al., 2010), experiments done by the University of Trento (Vitale, 2007), and documents reporting the magnetic testing campaign at ESTEC (Trougnou, 2007; Fertin & Trougnou, 2007, 2010). Moreover, we need to know the nominal test mass characteristics, thus they are listed in Table 2.3, whereas in Table 2.4, we list other necessary quantities to perform these calculations.

Magnetic field fluctuations

Using the equations presented in previous sections, we know that the acceleration noise contribution due to magnetic field fluctuations, $\delta\mathbf{B}$ coupled with the constant field gradient is computed as:

$$\delta\mathbf{F} \;=\; \left\langle \left[\frac{\chi}{\mu_0} \delta\mathbf{B} \cdot \boldsymbol{\nabla} \right] \mathbf{B}^{\mathrm{DC}} \right\rangle V \tag{2.20}$$

Table 2.4: Other constants needed for the calculation of the magnetic contributions. The characteristic length is the length used to convert magnetic field values into magnetic field gradients when the source of field and gradient are correlated. The magnetic frequencies are used to model the expected magnetic field spectrum and the shielding factor is the attenuation affecting the electric field that traverses the electrode housing (Vitale, 2005; Brandt et al., 2010).

Property	Value
Magnetic permeability (μ_0)	$4\pi 10^{-7}$ kg m s^{-2} A^{-2}
Electron charge (q_e)	1.602176487 $\times 10^{-19}$
Characteristic length (l_0)	3.5 m
Magnetic initial frequency constant (τ_i)	$1/(2\pi 10)$ s
Magnetic second frequency constant (τ_0)	$1/(2\pi 10^4)$ s
Shielding factor (α_S)	1×10^{-2}
Spacecraft speed in Sun fixed frame (v)	30 $\times 10^3$ m/s

Table 2.5: Magnetic field figures expected during mission operations. The values of the spacecraft units are those measured by Wealthy & Trenkel (2010), and the figures of the interplanetary magnetic field are reported in Brandt et al. (2010), which are confirmed by the values extracted from the ACE mission reported in Appendix B.

Magnetic Field Figures	Value
Spacecraft DC magnetic field component	$B_x = 144$ nT
Interplanetary DC magnetic field component	$B_x = 10$ nT
Spacecraft magnetic field fluctuation	$S_{B_x} = 21$ nT Hz$^{-1/2}$
Interplanetary magnetic field fluctuation	$S_{B_x} = 55$ nT Hz$^{-1/2}$
Spacecraft DC magnetic gradient	$\frac{\partial B_x}{\partial x} = 11\,500$ nT m^{-1}
Interplanetary DC magnetic gradient	0
Spacecraft magnetic gradient fluctuation	$S_{\frac{\partial B_x}{\partial x}} = 39$ nT m^{-1} Hz$^{-1/2}$
Magnetic field fluctuation above MBW	$S_{B_{x_{aboveMBW}}} = 0.3$ nT Hz$^{-1/2}$

If we consider that the three components of the magnetic field have the same value as B_x and we also consider that the gradients of B_x with respect to the three spatial components are equivalent, we can calculate the contribution to the acceleration noise along the sensitive axis (x-axis) as:

$$\delta a_{\delta\mathbf{B}} = \sqrt{2}\,\frac{\sqrt{3}}{m_\mathrm{TM}}\,\frac{\chi V}{\mu_0}\,\delta B_x \frac{\partial B_x}{\partial x}^{\mathrm{DC}} \tag{2.21}$$

where the $\sqrt{2}$ factor accounts for a worst case situation when computing differential acceleration, assuming that both test masses moved in opposite directions. If we consider the interplanetary magnetic field and the spacecraft fluctuations separately, we will obtain two terms, i.e., $\delta a_{\delta \mathbf{B}_{\mathrm{SC}}}$ and $\delta a_{\delta \mathbf{B}_{\mathrm{P}}}$

In these equations, the susceptibility χ is calculated as

$$\chi = \chi_0 + \frac{L^2 \mu_0 \sigma_0 \pi f}{12}, \tag{2.22}$$

where the nominal value χ_0 is modified by the frequency term observed in the torsion pendulum tests of the University of Trento (Vitale, 2007). In this equation, L is the side of the test mass, μ_0 is the magnetic permeability, σ_0 is the electrical conductance of the test mass, and f is set to 1 mHz.

Magnetic gradient fluctuations

With an analogous rationale to the previous sections, the fluctuations in the magnetic field gradients will contribute to the overall force according to:

$$\delta a_{\delta \boldsymbol{\nabla} \mathbf{B}} = \sqrt{2} \frac{\sqrt{3}}{m_{\mathrm{TM}}} V \left(M_r + \frac{\chi}{\mu_0} B_x^{DC} \right) \delta \frac{\partial B_x}{\partial x} \tag{2.23}$$

In this case, as the gradient of the interplanetary magnetic field is negligible, so we will obtain only one term due to the fluctuations of the gradients created by the electronics of the spacecraft, i.e., $\delta a_{\delta \boldsymbol{\nabla} \mathbf{B}_{\mathrm{SC}}}$.

Down converted AC magnetic fields

The final term of the force noise is due to the coupling of the fluctuations of both the magnetic field and the magnetic gradient, i.e.:

$$\delta \mathbf{F} = \left\langle \left[\frac{\chi}{\mu_0} \delta \mathbf{B} \cdot \delta \boldsymbol{\nabla} \right] \mathbf{B} \right\rangle V \tag{2.24}$$

From this equation it can be seen that if the time dependent component of the field has a sinusoidal form, it is plausible to generate a low frequency force by mixing two or more higher frequency AC fields that have frequencies close together. Assuming that the fluctuations in the spacecraft magnetic field will be caused by fluctuations in the current flowing through the different equipments, the component $\delta \mathbf{B}$ may be split into an spatial term (which does not vary with time) multiplied by an AC signal (a sinusoid in this case). Then the gradient of this field is expected to be a multiple of the field caused by the geometry of the unit with respect to the test mass, therefore we can write:

$$\delta\frac{\partial B_i}{\partial x} = \delta\frac{B_i}{l_0} \tag{2.25}$$

where l_0 is the characteristic length. Out of the results reported in (Trougnou, 2007), this characteristic length is fixed to 3.5 m. With the above assumption we write:

$$\delta F_x \;=\; \left(\frac{\chi(t)V}{\mu_0 l_0}|\delta\mathbf{B}|^2\right) \tag{2.26}$$

where the susceptibility is expressed as a time-dependent function ($\chi(t)$) because the magnetic fields on the test masses are time-dependent too (and have several frequencies at each time instant). If we want to perform this computation in the frequency domain, the time-varying susceptibility term can be modeled as (Vitale, 2007; Trougnou, 2007):

$$\chi(\omega) = A_0\left(\frac{-i\omega\tau_{\rm e}}{1+i\omega\tau_{\rm e}}\right), \tag{2.27}$$

and the linear spectral density of the field at high frequencies is modeled as[2]:

$$B(\omega) = B_0\left(\frac{1+i\omega\tau_{\rm i}}{i\omega\tau_{\rm i}(1+\omega\tau_0)}\right) \tag{2.28}$$

This spectrum has an initial $1/f$ behavior until a frequency value of 20 Hz (corresponding to the first breakpoint $\tau_{\rm i}$, then a plateau at $B_0 = 0.25$ nT Hz$^{-1/2}$ between 20 Hz up to 250 Hz. Finally, rolls-off as $1/f$, representing the high-frequency magnetic shielding due to the Vacuum Enclosure and also the Electrode Housing. This attenuation is quite considerable at high frequencies. For instance, at 10 kHz, this attenuation is approximately of 10^3. There is no onboard hardware to measure the field at high frequencies. Then, we expect to use this same model for data analysis procedures during mission operations. After some calculations, reported in (Vitale, 2007; Trougnou, 2007; Fertin & Trougnou, 2007), the value of the acceleration noise at low frequency, and specifically in the measurement bandwidth, due to AC magnetic fields is constant and can be shown to be:

$$\delta a_{\rm AC} = \left(\frac{V}{\mu_0\, l_0\, m_{\rm TM}}\right) A_0\, B_0 \sqrt{\frac{\tau_0\tau_{\rm e}(\tau_0^2+3\tau_0\tau_{\rm e}+\tau_{\rm e}^2)+\tau_{\rm i}^2(2\tau_0\tau_{\rm e}+\tau_{\rm i}^2)}{2\tau_0\left(1+\frac{\tau_0}{\tau_{\rm e}}\right)^3\tau_{\rm i}^4}} \tag{2.29}$$

where $\tau_{\rm i}$ and τ_0 are the breakdown points of the magnetic field model. The roll-off frequency of the gold-platinum test mass is 630 Hz (Trougnou, 2007), therefore we define $\tau_{\rm e} = 1/(2\,\pi\,630)$.

[2]The AC magnetic field has been measured for different units at Astrium Stevenage (UK). These tests are reported in Wealthy & Trenkel (2010)

Lorentz force contribution

A particle with charge q moving through an electro-magnetic field with velocity v experiences a force given by (Jackson, 1999):

$$\mathbf{F}_{\text{Lorentz}} = q(\mathbf{E} + \beta \times \mathbf{B}) \tag{2.30}$$

where E and B are, respectively, the electric field and the magnetic field. For the specific case of LISA Pathfinder, the satellite moves through the interplanetary magnetic field of the Sun. To do this calculation, we should obtain first the electromagnetic field in the rest frame. To this end, we use the Lorentz transformation in order to translate the interplanetary fields into the spacecraft frame. The general transformation stands that to transform the fields from a system S to a system S', which is moving at a velocity v relative to S, it can be written (Jackson, 1999):

$$\begin{aligned}
\mathbf{E}' &= \gamma(\mathbf{E} + \beta \times \mathbf{B}) - \frac{\gamma^2}{\gamma + 1}\beta(\beta \cdot \mathbf{E}) \\
\mathbf{B}' &= \gamma(\mathbf{B} - \beta \times \mathbf{E}) - \frac{\gamma^2}{\gamma + 1}\beta(\beta \cdot \mathbf{B})
\end{aligned}$$

Thus, we have:

$$\mathbf{E}' \simeq \gamma(\beta \times \mathbf{B}) \tag{2.31}$$

$$\mathbf{B}' \simeq \gamma\mathbf{B} \tag{2.32}$$

The speed of LISA Pathfinder in a Sun-fixed frame is about 30 km/s. Thus, the value of $|\beta|$, which is defined as $|\beta| = |\mathbf{v}|/c \sim 10^{-4}$, is small. As a consequence, $\gamma = 1/\sqrt{1 - |\beta|^2}$, is very close to 1. Hence, the Lorentz force is:

$$\mathbf{F}_{\text{Lorentz}} = q(\mathbf{E}' + \beta \times \mathbf{B}') \simeq q\gamma\beta \times \mathbf{B} \tag{2.33}$$

In this case, the fluctuation of the interplanetary magnetic field causes a fluctuating force on the test mass. However, the interplanetary magnetic field is now seen as an electric field, therefore it will be shielded by the electrode housing and inertial sensor surroundings. This shielding is represented by α_{S}, and is reported in Table 2.4. The magnetic fluctuation is expected to affect both test masses at the same time, however there will be a differential acceleration due to the different charge on each test mass. Assuming that the charge of both test masses will have the same sign, then the maximum differential force will be obtained assuming that we have maximum charge on one test mass and zero charge on the other. In this worst case scenario, the acceleration noise produce by this effect is computed as:

$$\delta a_{\text{Lorentz}} = \frac{\gamma\, Q\, \beta\, S_{B_{\text{P}}}^{1/2}}{m_{\text{TM}}\, \alpha_{\text{S}}} \tag{2.34}$$

Total magnetic contribution

The total contribution to acceleration noise of the different magnetic effects can be computed as a quadratic sum of the different terms. Specifically, the contribution due to fluctuation of the magnetic field and the fluctuation of the gradient of the magnetic field are considered as correlated sources as they are both originated by the spacecraft magnetic field. On the other hand, the contribution due to the fluctuation of the interplanetary magnetic field and the Lorentz effect are also correlated, since they are caused by the fluctuations of the interplanetary magnetic field. Thus, the final result is:

$$\delta a_{\text{Total}} = \sqrt{(\delta a_{\delta \mathbf{B}_{\text{SC}}} + \delta a_{\delta \boldsymbol{\nabla} \mathbf{B}_{\text{SC}}})^2 + \delta a_{\text{AC}}^2 + (\delta a_{\delta \mathbf{B}_{\text{P}}} + \delta a_{\text{Lorentz}})^2} \tag{2.35}$$

Considering the nominal mission values listed in Table 2.5, we compute the contribution of each term of the magnetic effects to the total budget. These results are listed in Table 2.6. The most relevant effect is the contribution of the fluctuations of the interplanetary magnetic field, followed by the contribution of the down-converted effects and the fluctuations of the gradient of the spacecraft magnetic fields. Note that all these calculations depend on the actual knowledge of the magnetic fields, the magnetic field gradients and their fluctuations at the test mass positions during mission operations. In this chapter we have assessed all contributions using expected values for each of these magnitudes, but for mission data analysis procedures we need to know the actual value of these fields. To this end, the spacecraft is equipped with four triaxial magnetometers. From these measurements, we should infer the magnetic field and its gradient at the test masses. This task is covered in chapters 5 and 6 of this thesis. On the other hand, note also that the other essential quantities are the magnetic characteristics of the test mass, such as their remanent magnetic moment and their susceptibility. These properties also need to be measured in flight. They will be measured by processing the response of the test masses to specific magnetic field injections created by the LTP induction coils. This task is covered in chapters 3 and 4. With all these ingredients, we expect to be able to subtract the magnetic effects from the main science data stream.

2.5 The LTP Magnetic diagnostic subsystem

The LTP Magnetic diagnostic subsystem is the hardware subsystem intended to deliver the necessary measurements to estimate the magnetic acceleration noise contribution to the total acceleration noise. It has 2 main goals: creating controlled magnetic field and gradients at the positions of the test masses, and measuring the DC magnetic field values and its fluctuations within the measurement bandwidth at different locations at the LCA. To this end, the Magnetic Diagnostic is endowed

Table 2.6: Contribution of the magnetic field effects to the total acceleration noise.

Contribution	Differential acceleration noise [m s^{-2} Hz$^{-1/2}$]
Spacecraft magnetic field fluctuation	$\delta a_{\delta \mathbf{B}_{\mathrm{SC}}} = 0.680 \times 10^{-15}$
Spacecraft magnetic field gradient fluctuation	$\delta a_{\delta \boldsymbol{\nabla} \mathbf{B}_{\mathrm{SC}}} = 1.097 \times 10^{-15}$
Down converted AC magnetic fields	$\delta a_{\mathrm{AC}} = 1.265 \times 10^{-15}$
Interplanetary magnetic field fluctuation	$\delta a_{\delta \mathbf{B}_{\mathrm{P}}} = 1.701 \times 10^{-15}$
Lorentz force	$\delta a_{\mathrm{Lorentz}} = 0.013 \times 10^{-15}$
Total of magnetic effects	$\delta a_{\mathrm{total}} = 2.775 \times 10^{-15}$
Requirement of magnetic effects	$\delta a_{\mathrm{requirement}} = 12\,000 \times 10^{-15}$

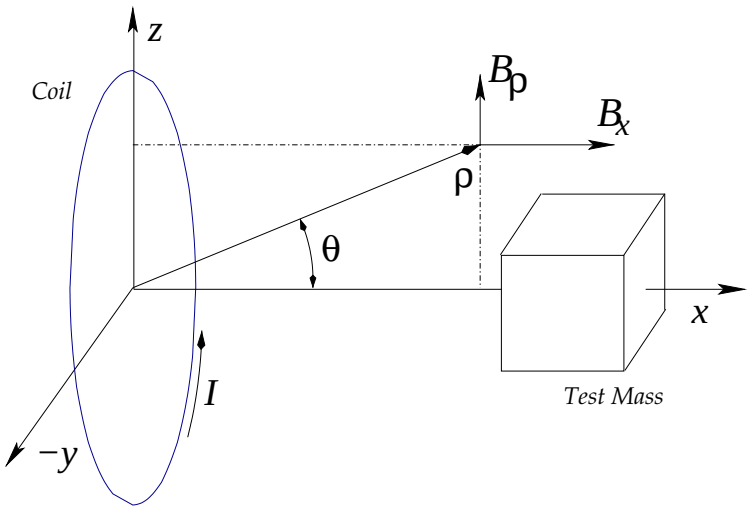

Figure 2.5: Coordinate reference frame centered at the position of the coils (see Appendix A). This reference frame is used for the magnetic field calculation, see text.

with two specific hardware: (1) the onboard magnetic coils, and (2) the onboard magnetometers.

2.5.1 Magnetic coils description

The two circular induction coils are made of a titanium alloy, specifically (Ti_6Al_4V), and have $N = 2\,400$ windings of mean radius $a = 56.5$ mm. They are placed 85.5 mm away from the center of their respective test mass. Their location within the complete LCA is shown in Fig. 2.2. The onboard coils are aligned with the x-axis of the test masses, thus, the magnetic field within the volume of the test masses

Table 2.7: Positions of the test masses referred to a coordinate system fixed to the spacecraft. This reference frame is the Magnetic Experiment Reference Frame and it is defined in Appendix A.

Test Mass	x [m]	y [m]	z [m]
1	-0.1880	0	0.6093
2	0.1880	0	0.6093

Table 2.8: Positions of the coils. They are referred to a coordinate system fixed to the spacecraft (Magnetic Experiment Reference Frame).

Coils	x [m]	y [m]	z [m]
1	-0.2735	0	0.6093
2	0.2735	0	0.6093

has axial symmetry. This geometric configuration is displayed in Fig. 2.5. For the sake of completeness, the positions of the test masses are listed in Table 2.7 and the positions of the center of the coils are listed in Table 2.8.

The magnetic field created by an induction coil is easily obtained from classical expressions. In particular, for slowly varying coil currents and short distances from them, radiative effects can be safely neglected (Jackson, 1999). Due to the symmetry, only the *parallel* (B_x) and *transverse* (B_ρ) components of the field $\mathbf{B}$ are different from zero. The definition of these field components are also shown in Fig. 2.5. The magnetic field is calculated by means of Ampère's induction law. Assuming a coil of negligible thickness, radius a, current I and a wire winding of N turns, we know that,

$$B_\rho(x,\rho) = \frac{\mu_0}{4\pi}\frac{N\pi a^2 I}{(a\rho)^{3/2}}\frac{k}{\pi}\frac{x}{a}\left[-K(k)+\frac{1-k^2/2}{1-k^2}E(k)\right] \tag{2.36a}$$

$$B_x(x,\rho) = \frac{\mu_0}{4\pi}\frac{N\pi a^2 I}{(a\rho)^{3/2}}\frac{k}{\pi}\left[\frac{1}{2}\frac{k^2}{1-k^2}E(k)\right]-\frac{\rho}{x}B_\rho(x,\rho) \tag{2.36b}$$

where

$$k=\sqrt{\frac{4a\rho}{x^2+(a+\rho)^2}}\,, \quad \rho^2=y^2+z^2 \tag{2.37}$$

In these expressions, as shown in Fig. 2.5, x, y and z are the coordinate triplet of the field point with respect to the center of the coils, and ρ is the distance to the x-axis. The result involves elliptic integrals of the first and second kind ($K(k)$ and $E(k)$, respectively),

$$K(k) = \int_0^{\pi/2} (1-k^2 \sin^2\phi)^{-1/2}\, d\phi \quad \text{and} \quad E(k) = \int_0^{\pi/2} (1-k^2 \sin^2\phi)^{1/2}\, d\phi \tag{2.38}$$

Once the transverse field B_ρ is known, it takes two multiplications to resolve it into its Cartesian components B_y and B_z, as shown in Eqs. (2.39).

$$B_y = \frac{y}{\rho} B_\rho = \frac{y}{\sqrt{y^2+z^2}} B_\rho \quad \text{and} \quad B_z = \frac{z}{\rho} B_\rho = \frac{z}{\sqrt{y^2+z^2}} B_\rho \tag{2.39}$$

In order to evaluate the force and torque contribution we also need to know the value of the gradient of the magnetic field created by the coils, i.e. the matrix

$$\boldsymbol{\nabla}\mathbf{B} \;=\; \begin{pmatrix} \dfrac{\partial B_x}{\partial x} & \dfrac{\partial B_x}{\partial y} & \dfrac{\partial B_x}{\partial z} \\ \dfrac{\partial B_y}{\partial x} & \dfrac{\partial B_y}{\partial y} & \dfrac{\partial B_y}{\partial z} \\ \dfrac{\partial B_z}{\partial x} & \dfrac{\partial B_z}{\partial y} & \dfrac{\partial B_z}{\partial z} \end{pmatrix} \tag{2.40}$$

Note that this matrix is symmetric and traceless. This is because of the properties of the induction field, i.e., $\boldsymbol{\nabla} \times \mathbf{B} = \boldsymbol{\nabla}\cdot\mathbf{B} = 0$. All these computations are cumbersome, thus they are detailed in Appendix C and in (Díaz–Aguiló et al., 2010). However, in order to partly verify the correctness of the field calculations, a specific and simple configuration can be used. For example, one can compute the on-axis field with the well known textbook expression:

$$B_x(x, \rho = 0) = \frac{\mu_0}{4\pi} \frac{2\pi a^2 N I}{(a^2+x^2)^{3/2}} \qquad \text{and} \qquad B_\rho(x, \rho = 0) = 0 \tag{2.41}$$

and this should reproduce the results obtained with Eqs. (2.36a) and (2.36b), in the appropriate limit. An additional check is the x-gradient of the longitudinal field B_x:

$$\frac{\partial B_x}{\partial x}(x, \rho = 0) = -\frac{\mu_0}{4\pi} \frac{6\pi a^2 N I\, x}{(a^2+x^2)^{5/2}} \tag{2.42}$$

As an example, the values of the magnetic field and its longitudinal gradients produced by the LTP hardware and the LTP geometry are shown in Table 2.9 for three different points on the closest test mass. These values are computed for a DC current of 1 mA.

Table 2.9: On-axis magnetic field and longitudinal gradient values at three points on the closest test mass for a 1 mA DC current fed to the 2 400 turn LTP coil. They are the closest point to the test mass, the test mass center and the farthest point along the x-axis.

	$x = 62.5$ mm	$x = 85.5$ mm	$x = 108.5$ mm
B_x [μT]	8.05	4.47	2.63
$\partial B_x/\partial x$ [μT/m]	−212.6	−109.2	−57.2

If the current fed to the coils is $I(t) = I_0 \sin \omega t$, the resulting magnetic field (and its gradient) will preserve the spatial dependence inferred from the previous formulae and will oscillate at the same frequency. Therefore, we can write,

$$\mathbf{B} = \mathbf{B}_0 \sin \omega t \quad \text{and} \quad \boldsymbol{\nabla}\mathbf{B} = \boldsymbol{\nabla}\mathbf{B}_0 \sin \omega t \tag{2.43}$$

where $\mathbf{B}_0$ and $\boldsymbol{\nabla}\mathbf{B}_0$ are the field vector and gradient matrix for a constant I_0. We will use these oscillating signals to estimate the magnetic properties, i.e. remanent magnetic moment and susceptibility — see chapters 3 and 4.

In the science requirement document (Vitale, 2005), the coils are required to produce a field at the test mass locations with no field noise in excess of 5 nT $\mathrm{Hz}^{-1/2}$ and the x-derivative of each field component in excess of 12 nT m^{-1} $\mathrm{Hz}^{-1/2}$. These values must be achievable at any frequency between DC and 30 mHz (Kahl, 2007; Lobo & Mateos, 2008). These requirements turn into an equivalent requirement in current stability of 110 nA $\mathrm{Hz}^{-1/2}$ at 1 mHz. These tests have been performed at IEEC and it has been demonstrated that the current satisfies these requirements for current amplitudes below 2 mA (Lobo & Mateos, 2008).

2.5.2 Magnetometers description

Measuring the magnetic field and gradient fluctuations at the location of the test masses is not possible. These must be estimated from the measurement at different selected locations. Previous studies (Vitale, 2005), led to place only 4 magnetometers within the LCA volume. Their specific positions are listed in Table 2.10. The onboard LTP magnetometers are fluxgate tri-axial magnetometers built by Billingsley. The specific model is TFM100G4-S (Billinglsey, Aerospace and Defense, 2007). By construction, these magnetometers consist of three different magnetic sensors, along the x-, y- and z-directions. For each of these axes, the fluxgate magnetometer consists of a sensing (secondary) coil surrounding an inner drive (primary) coil around high permeability magnetic core material.

The measurements delivered by these 4 magnetometers are not sufficient to infer accurate magnetic field values at the test mass locations with classical interpolation

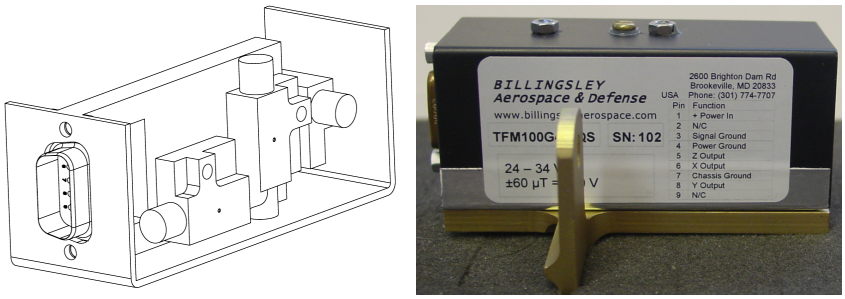

Figure 2.6: Onboard magnetometers. Left panel: technical drawing of the inner position of the sensing heads. Right panel: view of the caging of the engineering model of the magnetometer.

methods (see chapter 5). Nevertheless, we present alternative interpolation methods based on neural networks that, assuming that sufficient testing is performed, lead to promising results (see chapter 6).

Table 2.10: Positions of the magnetometers. They are referred to a coordinate system fixed to the spacecraft, consistent with Tables 2.7 and 2.8.

Magnetometers	x [m]	y [m]	z [m]
1	0.0758	−0.3694	0.6093
2	0.3765	0	0.6093
3	−0.0758	0.3694	0.6093
4	−0.3765	0	0.6093

Due to the large size of the sensing heads of these low-noise magnetometers, the spatial resolution in each of the directions is ~ 4.0 mm. On the other hand, the coils of the magnetometers have an orthogonality better than 1°. This angular error may be transformed to a linear uncertainty by multiplying by the longest distance inside the magnetometer caging, $l \simeq 82.5$ mm, resulting in an uncertainty of ~ 1.5 mm. The overall spatial uncertainty of the sensing position of the magnetometers can be computed by adding in quadrature the different contributions, and turns out to be $\Delta \sim 4.3$ mm. These magnetometers present a field measurement accuracy of 0.5% of its full scale, and have a linearity of 0.0035%. Their sensitivity is of 60 μV/nT. They have a temperature operating range from -55° to 80° and present a flat frequency response from DC up to 3.5 kHz. Other specifications are reported in its specification sheet (Billinglsey, Aerospace and Defense, 2007). The magnetometers are shown in Fig. 2.6.

As required in Vitale (2005); Kahl (2007), the magnetometers should have a

resolution of 10 nT $Hz^{-1/2}$ within the measurement bandwidth, their measurement range should lie between $-60\,\mu$T and $60\,\mu$T, and they should have a field measurement better that the 1% level. The tri-axial flight model magnetometers were tested at IEEC and satisfied all requirements (Lobo & Mateos, 2008).

Chapter 3

Magnetic experiments onboard LISA Pathfinder

In this chapter we describe the magnetic experiments that will be performed onboard the LISA Pathfinder spacecraft. These experiments are intended to estimate the remanent magnetic moment and susceptibility of the test masses. To this end, we present the magnetic forces and torques which will be injected in the onboard coils, we study their effects on the test masses, and we assess the magnitude of the kinematic excursions. Finally, we present preliminary results for the estimation of the magnetic characteristics of the test mass, that will be further expanded in chapter 4.

3.1 Introduction

The LTP is designed to measure relative accelerations between two test masses in nominal free fall (geodesic motion) with a differential acceleration noise budget

$$S^{1/2}_{\delta a,LPF}(\omega) \leq 3 \times 10^{-14} \left[1 + \left(\frac{\omega/2\pi}{3\ \mathrm{mHz}}\right)^2\right] \frac{\mathrm{m\ s^{-2}}}{\sqrt{\mathrm{Hz}}} \tag{3.1}$$

in the frequency band between 1 mHz and 30 mHz Vitale (2005); Antonucci et al. (2011b).

Magnetic noise in the LTP is allowed to be a significant fraction of the total mission acceleration noise: up to $1.2\times10^{-14}\,\mathrm{m\,s^{-2}\,Hz^{-1/2}}$ is apportioned to magnetic effects, i.e., 40 % of the total noise, $3\times10^{-14}\,\mathrm{m\,s^{-2}\,Hz^{-1/2}}$, see Eq. (3.1). This noise occurs because the residual magnetization and susceptibility of the test masses couple to the surrounding magnetic field, giving rise to a fluctuating force which is given by:

$$\delta\mathbf{F} = \left\langle \left[\left(\mathbf{M} + \frac{\chi}{\mu_0}\mathbf{B}\right)\cdot\delta\boldsymbol{\nabla}\right]\mathbf{B} + \frac{\chi}{\mu_0}\left[\delta\mathbf{B}\cdot\boldsymbol{\nabla}\right]\mathbf{B}\right\rangle V \tag{3.2}$$

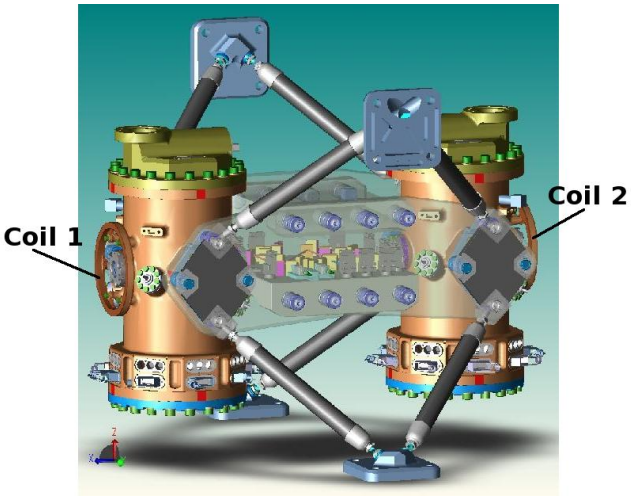

Figure 3.1: Artistic view of the LISA Technology Package. The two towers are the Gravitational Reference Sensors. They are connected by the optical bench (grey), where the interferometer is located. The induction coils are located next to the two towers.

in each of the test masses. In this expression $\mathbf{B}$ is the magnetic field in the test mass, χ and $\mathbf{M}$ are its magnetic susceptibility and residual density of magnetic moment, respectively, and V is the volume of the test mass, μ_0 is the vacuum magnetic constant, $4\pi \times 10^{-7}\,\mathrm{m\,kg\,s^{-2}\,A^{-2}}$, and $\langle \cdots \rangle$ indicates test mass volume average of the enclosed quantity. Finally, $\delta\mathbf{B}$ represents the fluctuation of the magnetic field, and $\delta\boldsymbol{\nabla}$ stands for the fluctuation of the gradient (Sanjuán et al., 2008).

This force noise stems from the fact that a magnetized body lying within a magnetic field suffers a force and torque expressed as (Jackson, 1999):

$$\mathbf{F} = \left\langle \left[\left(\mathbf{M} + \frac{\chi}{\mu_0}\,\mathbf{B} \right) \cdot \boldsymbol{\nabla} \right] \mathbf{B} \right\rangle V\,, \tag{3.3}$$

and a torque:

$$\mathbf{N} = \langle \mathbf{M} \times \mathbf{B} + \mathbf{r} \times [(\mathbf{M}\cdot\boldsymbol{\nabla})\ \mathbf{B}] \rangle\, V \tag{3.4}$$

In these expressions $\mathbf{r}$ denotes the distance to the center of the test mass. Thus, as can be readily seen in Eq. (3.2), to estimate and ultimately subtract the acceleration noise due to the magnetic interactions, the magnetic properties of the test masses must be determined.

In this chapter we describe the experimental setup and the data analysis needed to infer the values of the magnetic properties of the test masses on board the LTP, and we assess the feasibility of obtaining the magnetic characteristics of the test masses with good accuracy. Specifically, we present a set of simulations aimed at evaluating the response of the LTP hardware (coils and test masses) and control

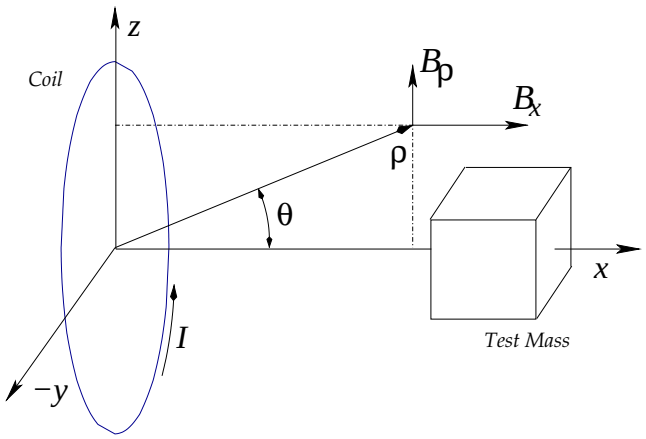

Figure 3.2: Coordinate reference frame of the experiment. This reference frame is centered at the position of the coils (see Appendix A).

architecture (drag free controllers and low frequency suspension controllers) when a controlled magnetic field is applied. We will show that using this procedure, both the magnetization and the magnetic susceptibility of the proof masses can be determined to the desired accuracy. The chapter is organized as follows: in section 3.2, we describe the main elements of the experimental setup. Section 3.3 is devoted to compute the forces and torques acting on the test masses. It follows section 3.4, where the different noise sources perturbing the experiment are presented. Finally, in section 3.5 we present our results, whereas in section 3.6 we summarize our main findings and we present our conclusions.

3.2 Experiment description

As mentioned, the basic approach to determine the magnetic properties of the test masses is to inject a controlled signal with the onboard coils and to study the dynamics of the proof masses. The two test masses are located at the center of each inertial sensor, and are the end mirrors of the OMS. In fact, one of the test masses will be the reference free floating body to perform the translation and rotation control of the spacecraft. The test masses are made of an alloy of Pt (27%) and Au (73%), their dimensions are $46 \times 46 \times 46$ mm and their weight is 1.95 kg. To comply with the top science requirements, the test masses must have certain properties. For the purpose of the present chapter the two most important ones are the magnetic moment and the susceptibility, which must be, respectively, $|\mathbf{m}| < 2.0 \times 10^{-8}$ A m^2 and $|\chi| < 2.5 \times 10^{-5}$ (Vitale, 2005). The volume of the test masses is $V = 0.0046^3$ m^3. The density of magnetic moment has to be then $|\mathbf{M}| < 9.451 \times 10^{-4}$ A/m, assuming homogeneity.

The controlled magnetic field will be produced by the onboard coils, which are placed next to each of the GRS towers — see Fig. 3.1. The two circular induction coils are made of a titanium alloy (Ti_6Al_4V), have $N = 2\,400$ windings of radius $r = 56.5$ mm. They are placed 85.5 mm away from the center of the respective test mass. The onboard coils are aligned with the x-axis of the test masses, thus, the magnetic field within the volume of the test masses has axial symmetry, see Fig. 3.2. If the current fed to the coils is $I(t) = I_0 \sin \omega t$, the resulting magnetic field (and its gradient) will oscillate at the same frequency. Thus, when the coils are switched on the test masses rotate and are displaced from their equilibrium positions. Typical values of I_0 and $\omega/2\pi$ are, respectively, 1 mA and 1 mHz.

Compared to other missions, LPF is very flexible in terms of the possible operation scenarios. Nevertheless, we characterize the magnetic experiment for a fixed operating mode, the main science mode (Schleicher, 2009). This mode is schematically shown in Fig. 3.3. **D** is a dynamical matrix which represents the dynamic response of the spacecraft and the test masses when they are affected by specific forces (**f**). This block consists of an 18 degree-of-freedom representation of the motion of these 3 bodies. The differential position of the test masses and their distance to the spacecraft are represented by **x** in this block-diagram.

The LTP is endowed with two different mechanisms to detect the motion and the actual position of the test masses. The first one is the interferometer, while the second is the electrode housing of each of the two gravitational reference sensors. The OMS in LTP is in charge of measuring the distance between one of the test masses and the optical bench, thus giving an absolute reference, and also the distance between both test masses, providing a differential reading. Due to its ability to perform wavefront sensing, the rotation angles of the test mass around the y- (η) and z-axis (ϕ) can also be measured (the y- and z-axis in the test mass coordinate frame are the same axis represented in Fig. 3.2 but centered at the test mass). The displacements are expected to be measured with a picometer accuracy while the rotation angles can be measured with an accuracy of $\sim$ 400 nrad (Heinzel et al., 2003, 2004). The electrode housing can also be used to determine the position of the test masses. However, this mechanism only offers readings with nanometer precision. It is, however, useful to determine the degrees of freedom the IFO cannot provide: y, z and θ (rotation about the x-axis). For our application only the readings of the interferometer will be used. The physical model of these sensing mechanisms is included in **S**, the sensing matrix (Fig. 3.3). $\mathbf{o_n}$ is the readout noise of the different sensors, and **o** is the actual measure delivered to the controller.

These kinematic measurements are processed by the controller block (**C**) and a feedback action is produced on the LTP dynamics by the actuators (**A**): the micropropulsion thrusters and the electrostatic actuators. They produce an additional set of forces ($\mathbf{f_a}$) with the following objectives. The drag-free controller acts on the spacecraft using the micropropulsion thrusters and forces it to follow test mass 1. The electrostatic actuators act on test mass 2 using the low frequency suspension,

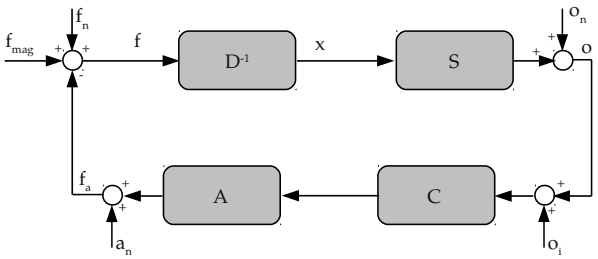

Figure 3.3: Control system architecture of LISA Pathfinder. **D** stands for the dynamical matrix, **S** represents the sensing matrix of the interferometer, i.e. the matrix translating the position of the test mass, **x**, into the interferometer readout, **o** ($\mathbf{o_n}$ stands for the readout noise) . **A** represents the physics of the FEEP and the electrostatic actuators, and finally **C**, is the controller matrix, implementing the drag free and low-frequency control loops. $\mathbf{o}_\mathrm{i}$ represents the displacement guidance signals. $\mathbf{a}_\mathrm{n}$ are the actuators noise and $\mathbf{f}_\mathrm{a}$ are the output forces of the actuators. $\mathbf{f}_\mathrm{mag}$ are the magnetic forces induced by the coils and $\mathbf{f}_\mathrm{n}$ are the environment force noises disturbing the spacecraft.

a specific control loop of very low gain in the LTP measurement bandwidth, that allows to control in band the differential acceleration between both test masses at the same time, avoiding secular drifts or stray motions of the second test mass.

Finally, $\mathbf{f}_\mathrm{n}$ represents the force noise on the test masses, and $\mathbf{f}_\mathrm{mag}$ represents the forces acting on the test masses due to the magnetic field created by the coils. The complete control architecture can be expressed by the following system of equations:

$$\begin{aligned} \mathbf{o} &= \mathbf{D}^{-1} \cdot \mathbf{S} \cdot \mathbf{f} + \mathbf{o}_\mathrm{n} \\ \mathbf{f} &= \mathbf{f}_\mathrm{mag} + \mathbf{f}_\mathrm{n} - \mathbf{A} \cdot \mathbf{C} \cdot (\mathbf{o} + \mathbf{o}_\mathrm{i}) - \mathbf{a}_\mathrm{n} \end{aligned} \tag{3.5}$$

where all the symbols have been already defined with the only exception of $\mathbf{o}_\mathrm{i}$ which represents the displacement guidance signals of the experiment and $\mathbf{a}_\mathrm{n}$ which are the actuators noise. Using Eqs. (3.5), we can calculate the transfer function from the magnetic forces ($\mathbf{f}_\mathrm{mag}$) to the interferometer readings ($\mathbf{o}$), which turns out to be:

$$\mathbf{o} = \frac{\mathbf{D}^{-1} \cdot \mathbf{S}}{1 + \mathbf{D}^{-1} \cdot \mathbf{S} \cdot \mathbf{A} \cdot \mathbf{C}} \cdot \mathbf{f_{mag}} \tag{3.6}$$

This transfer function characterizes the projection of the magnetic forces/torques into kinematic motion of the test masses. The controllers have been designed to deliver very sensitive readings of the differential motion of both test masses between 1 mHz and 30 mHz, the measurement bandwidth of the LTP mission. We would like to mention, however, that the system is better and more extensively described in chapters 4 and 7.

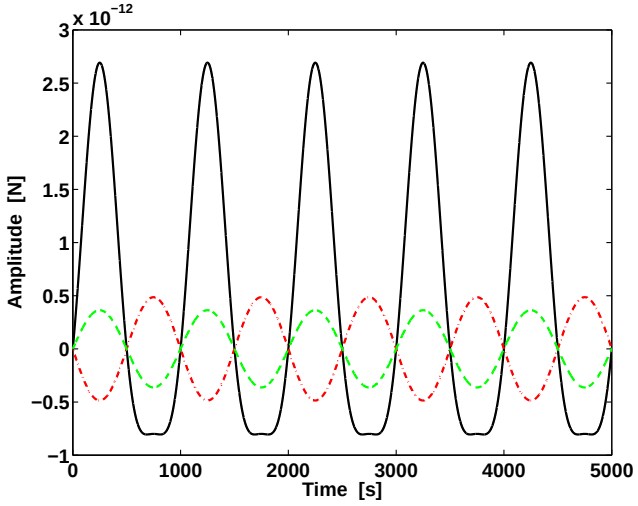

Figure 3.4: The three components of the force on test mass 1 when coil 1 is on. These forces depend on the values of χ and M_x, M_y and M_z. For this specific example we have adopted $M_x = 16.4\times10^{-5}$ A/m, $M_y = 9.1\times10^{-5}$ A/m, $M_z = -6.8\times10^{-5}$ A/m (a random orientation of the maximum $\mathbf{M}$) and $\chi = 2.5\times10^{-5}$. I_0 is 1 mA and ω is 1 mHz. The x-component of the force is shown as a solid black line, whereas the y-component is displayed as a dashed-dotted red line and the z-component is displayed as dashed green line.

3.3 Forces and torques

Using Eq. (3.3) and neglecting the environmental field (10 nT which is much smaller than the applied field, 500 nT), the x-component of the force acting on the test mass is

$$F_x = \langle \mathbf{M}\cdot\boldsymbol{\nabla} B_{0,x}\rangle\, V\, \sin\omega t + \frac{\chi V}{\mu_0}\, \langle \mathbf{B}_0\cdot\boldsymbol{\nabla} B_{0,x}\rangle\, \sin^2\omega t \tag{3.7}$$

where $\mathbf{B}_0$ is the field pattern produced by the coils. Thus, since $\sin^2\omega t = (1 - \cos 2\omega t)/2$, the linear acceleration of the test masses has two separate frequencies, one at ω and the other one at 2ω, and also a DC component. The force on test mass 1 is plotted in Fig. 3.4. The torque acting on the test mass also has a similar behavior. However, it must be noted that the torque only has one frequency component[1]:

$$\mathbf{N} = \langle \mathbf{M}\times\mathbf{B}_0 + \mathbf{r}\times[(\mathbf{M}\cdot\boldsymbol{\nabla})\,\mathbf{B}_0]\rangle\, V\, \sin\omega t \tag{3.8}$$

The resulting torques are displayed in Fig. 3.5. It is important to realize that only the y- and z-components of the torque can be measured with the interferometer, as N_x produces a rotation around the direction of the laser beam. Moreover,

[1]See chapter 4 for a specific explanation about the $2\omega_0$ component of the torque.

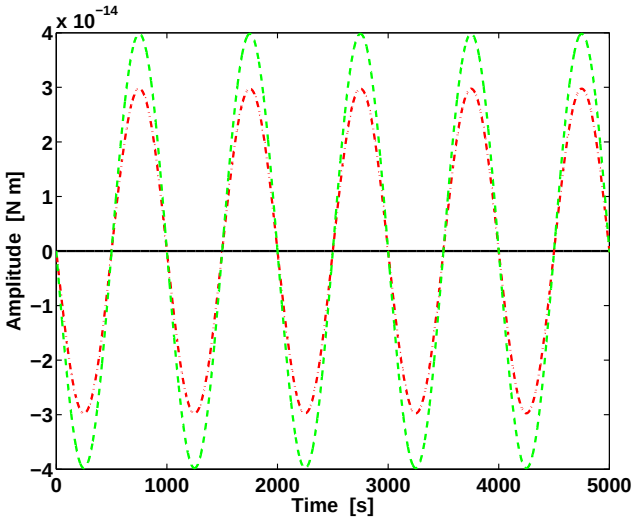

Figure 3.5: Torques on test mass 1 when coil 1 is on. The magnetic properties of the test mass are the same adopted in Fig. 3.4. The x-, y- and z-components of the torque are shown using black solid, red dashed-dotted and green dashed lines, respectively.

decomposing Eqs. (3.7) and (3.8), it is easy to show that the x-component of the force on the test mass (which can be obtained from its displacement) and the y- and z-components of the torque (which can be obtained from the rotation angles) can be cast in the form:

$$\begin{aligned} F_x &= \chi \cdot f_{x_{\rm DC}} + M_x \cdot f_{x_{1\omega}} + \chi \cdot f_{x_{2\omega}} \\ N_y &= M_z \cdot f_{y_{1\omega}} \\ N_z &= M_y \cdot f_{z_{1\omega}} \end{aligned} \tag{3.9}$$

where $f_{x_{\rm DC}}$ is a constant function, $f_{x_{1\omega}}$, $f_{y_{1\omega}}$ and $f_{z_{1\omega}}$ oscillate at ω and $f_{x_{2\omega}}$ oscillates at 2ω. Hence, N_y and N_z will be used to estimate M_z and M_y, respectively, while the differential displacement of the test masses will be used to measure M_x and χ.

3.4 Modeling of the noise sources

The forces and torques shown in Figs. 3.4 and 3.5 correspond to an ideal case. However, the real forces and torques acting on the test masses will not be noise-free. Additionally, the outputs detected by the interferometer will also be affected by several noise sources. Thus, to assess the feasibility of the experiment we need to model the noise sources. This section analyzes in detail the noise produced by the magnetic hardware of LTP. Other noise sources are detailed in chapter 7.

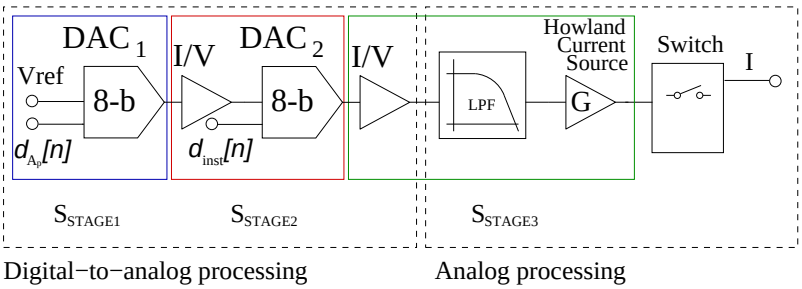

Figure 3.6: Block diagram of the current source of the coils.

3.4.1 Magnetic hardware noise

The stability of the magnetic field ($S_B^{1/2}$) produced by the coils at the position of the test masses and its gradient ($S_{\partial B_x/\partial x}^{1/2}$) must be, respectively, better than 5 nT Hz$^{-1/2}$ and 12 nT m^{-1} Hz $^{-1/2}$ (Vitale, 2005) within the measurement bandwidth (1 mHz $< f <$ 30 mHz). This can be translated into a requirement on the stability of the injected current. It turns out that the requirement on the magnetic field gradient is the more demanding one, and using Ampere's law it is straightforward to show that it is equivalent to a current fluctuation ($S_I^{1/2}$) requirement of 110 nA Hz$^{-1/2}$ within the measurement bandwidth.

In Fig. 3.6, we show a block diagram of the different hardware stages used to produce the current that feeds the coils. This block diagram has two parts: a digital-to-analog processing stage and an analog processing stage. The first block contains two digital-to-analog converters (DAC), followed by transresistance amplifiers (I/V) delivering low impedance output voltages. The first DAC sets the reference voltage of the second DAC and thus the peak amplitude of the sinusoidal current applied to the coil. The second one is configured with bipolar operation to generate the quantized signal with the previously selected amplitude. In the analog processing block the signal is low-pass-filtered and amplified with a Howland current source (Franco, 2002, 3rd edition). Finally, a switch is used to select one of the three possible states: short-circuit, open-circuit or connected. The noise of the current source chain for a DC signal, $S_{I_{\rm DC}}^{1/2}$, can be written as:

$$S_{I_{\rm DC}}^{1/2}(I,\omega) \simeq [G_2 G_3 S_{\rm STAGE_1} + G_3 S_{\rm STAGE_2} + S_{\rm STAGE_3}]^{1/2} \tag{3.10}$$

where $S_{\rm STAGE_1}$ is the noise density of the voltage reference and the first DAC, $S_{\rm STAGE_2}$ is the noise density of the transimpedance amplifier and the second DAC, $S_{\rm STAGE_3}$ is the noise density of the transimpedance amplifier, low-pass filter and Howland current source, and G_2 and G_3 are, respectively, the gains in the the second and third stages. The noise density of the first stage can be obtained as a contribution of the first DAC, $S_{\rm DAC_1}$, and of the reference voltage, $S_{V_{\rm ref}}$. However,

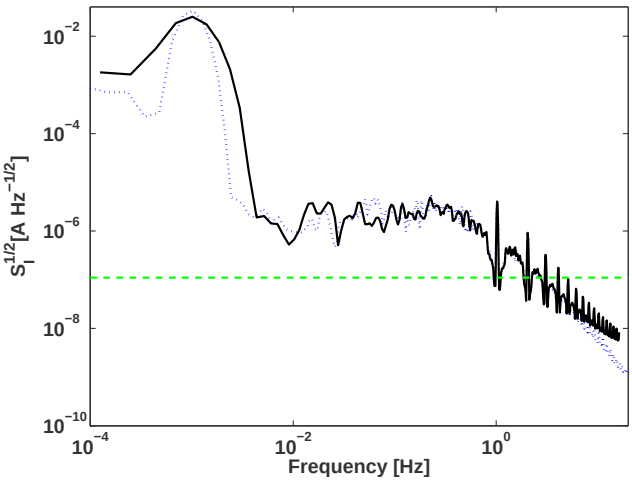

Figure 3.7: Noise density for a 1 mA sinusoidal current of 1 mHz nominal frequency. The dotted blue line shows the measured noise density, whereas the solid black line is our theoretical estimate (see text for details). The green dashed line represents the DC current fluctuations requirement.

the noise contribution of the first DAC is negligible with respect to that of the reference source, V_{ref}. Thus, if the DAC works at its full scale, $S_{\text{STAGE}_1} \sim S_{V_{\text{ref}}}$. Likewise, S_{STAGE_2} can be computed as a combination of two different sources S_{DAC_2} and $S_{\text{I/V}}$, being S_{DAC_2} the noise density of the second DAC and $S_{\text{I/V}}$ that of the transresistance amplifiers, and finally $S_{\text{STAGE}_3} = S_{\text{LPF}} + S_{\text{HCS}}$, where S_{LPF} and S_{HCS} are, respectively, the noise densities of the low-pass filter and of the Howland current source. These noise sources have been measured for a DC current of 1 mA. The values obtained are $S_{\text{STAGE}_1} = 9.6\,\text{nA}\,\text{Hz}^{-1/2}$, $S_{\text{STAGE}_2} = 0.03\,\text{nA}\,\text{Hz}^{-1/2}$, and $S_{\text{STAGE}_3} = 26.4\,\text{nA}\,\text{Hz}^{-1/2}$, respectively. The details of how these measurements were done are out of the scope of this thesis and will be provided elsewhere. However, we mention that although the previous analysis has been performed for DC currents, when we operate at 1 mHz the dominant noise source is the quantization noise of the second DAC. This means that the total current noise can be modeled as:

$$S_{I_{\text{AC}}}^{1/2} \simeq [G_3 S_{\text{DAC}_2}]^{1/2} \tag{3.11}$$

where the sole contributor is the quantization noise of the second stage, and thus the total noise assuming an uniform quantization and a signal amplitude greater than a quantization step is given by:

$$S_{I_{\text{AC}}}^{1/2} \simeq \frac{2I_0}{2^{N_{\text{b}}}} \frac{1}{\sqrt{12 \cdot f_{\text{s}}}} \tag{3.12}$$

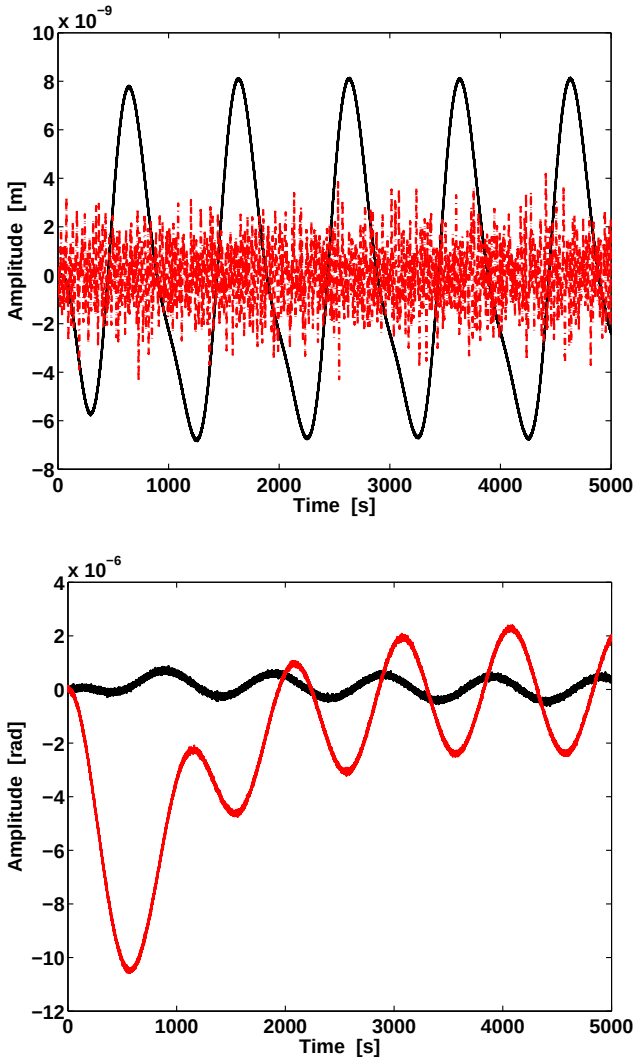

Figure 3.8: Top panel: relative displacement of the test masses measured using the differential channel of the interferometer (solid black line). The dashed red line shows the absolute displacement with respect to the optical bench. Bottom panel: rotation about the y-axis — black solid line — and the z-axis — red line. Both panels show the response of test mass 1 when only coil 1 is fed with a current of 1 mA and 1 mHz.

where f_s is the sampling frequency, $N_\mathrm{b} = 8$ is the number of bits of the onboard hardware, and the rest of the symbols have been already defined.

The DMU delivers the output at a rate of 1 024 samples per cycle. Thus, the 1 mHz sinusoidal signal will be sampled at a frequency $f_\mathrm{s} = 1.024$ Hz. Since the highest sinusoidal current used in the experiment will be 1 mA, the highest noise

will be 2.22 μA Hz$^{-1/2}$. This noise is 2 orders of magnitude larger than all other contributions and therefore will be the dominant noise. Fig. 3.7 shows the current noise for coil 1 for a signal of 1 mHz and 1 mA (which are the nominal values of the experiment). As can be seen, the quantization noise level is above the DC current stability requirement for the mission (dashed green line) but, as it will be shown below, it is still sufficiently small to allow a reliable estimation of the magnetic properties of the test masses. It is also interesting to note that the quantization noise (thus the total noise) can be reduced when a 16-bit DAC is used — see Eq. (3.12). Finally, note that our theoretical results nicely match the experimental results.

So far we have discussed the noise density of the onboard coils. However, the different electronic subsystems of the satellite produce magnetic fields, which are also noisy. The magnetic noise produced by these subsystems (~ 50) has been modeled considering the fluctuating values of their magnetic moments (Díaz-Aguiló et al., 2010). Other noise sources that affect the measurements are the readout noise of the Optical Metrology System, the noise induced by the Gravitational Reference Sensor and the noise from the Star Tracker. Moreover, the actuators noise (FEEP noise and the noise of the capacitive actuator) and external sources such as solar noise or infrared noise have also relevant impact in the total readout. These noise sources are described in section 7.3.6. Their effect in the parameter estimation quality is assessed in the following section.

3.5 Results

We have estimated the magnetic properties of the test masses using the readings provided by the mission telemetry. The telemetry corresponding to the magnetic experiments will consist of the commands sent to the coils, the displacement readings of the interferometer (namely, the absolute and differential readings) and the wavefront rotation readings about the y- (η) and z- axes (ϕ). For simplicity, we have assumed that the stiffness of the test masses, the actuators gains and the interferometer crosscoupling factors have already been determined (Monsky et al., 2009).

The simulated displacements and rotations measured by the onboard interferometer are displayed in Fig. 3.8. These displacements and rotations have been obtained by integrating numerically the equations of motion of a rigid solid, and including the drag free and low frequency controllers — see section 3.2. Note that the problem has 18 degrees of freedom. In particular, each of the two test masses has 6 degrees of freedom, and the spacecraft also has 6 degrees of freedom. The closed loop simulation is performed with appropriate simulation tools that will be used for mission operations[2]. As can be seen, the displacements of the test masses are below 8 nm, while in permanent regime the corresponding rotations have amplitudes of $\sim 4\,\mu$rad. The very long transient of about 3 000 s of the rotation excursions — see the bot-

[2] http://www.lisa.aei-hannover.de/ltpda/

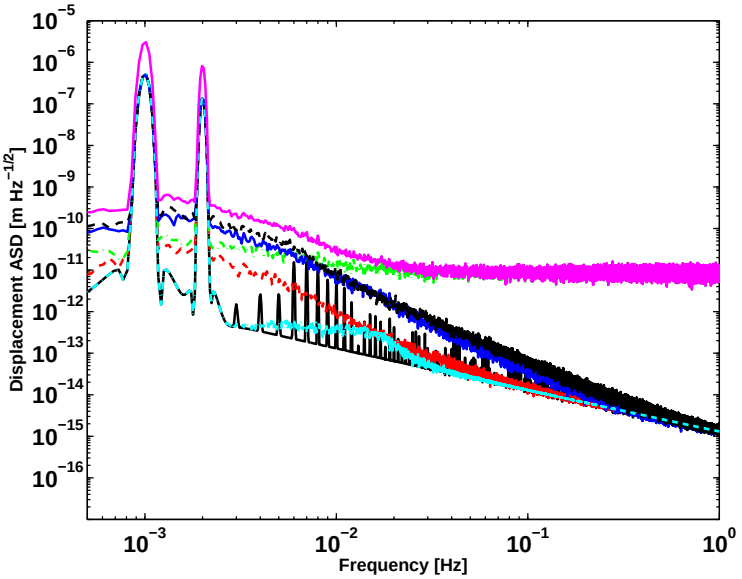

Figure 3.9: Noise breakdown of each of the noise sources to the differential displacement signal received when a 1 mA and 1 mHz current is circulating in coil 1. The black solid line shows the result of considering only the magnetic hardware noise. The red dashed line shows the result of considering only the environmental magnetic noise. The cyan dashed-dotted line only takes into account the solar and infrared emission noise. The green dotted green, the sensors contribution. The solid blue line the actuators noise, whereas the black dashed line shows the result of considering the test mass noise. Finally, in magenta solid line the result of considering all the noise sources together.

tom panel of Fig. 3.8 — is due to the effect of the low-frequency controller. This controller is designed to avoid drift excursions of the test masses with frequencies smaller than 1 mHz. Consequently, the transient is very long. A similar transient, although less evident, is present in the differential reading — see the top panel of Fig. 3.8. The reading of the displacement channel has two frequency components, ω and 2ω, however, these components are difficult to see in the time series shown in Fig. 3.8. Additionally, these two components are not in phase with the forces shown in Fig. 3.4 because the LPF dynamics and the controllers introduce a phase delay in each of the two components. Finally, it is worth mentioning that these displacements and rotations are within acceptable margins because they do not exceed the authority limits of the drag free and low-frequency controllers.

To further illustrate the feasibility of the experiment, in Fig. 3.9 we show the noise breakdown of the differential displacement reading of the interferometer. This figure has been obtained simulating the output of the entire instrument for each of the identified noise sources of the mission. We simulated 100 000 seconds for each source of noise. Then, we performed the spectral estimation with a smoothed

power spectral estimator based on the Welch estimator using a Blackman-Harris window (Welch, 1967). The time domain simulation and the spectral analysis have been performed using the `LTPDA` toolbox (Hewitson, 2011). This is the data analysis tool that will be used for mission operations — see chapter 7. As can be seen, in the frequency domain the signals at ω and 2ω are clearly visible. Note that the most important contribution is that of the sensors noise, which is mainly characterized by the high-frequency noise of the interferometer, the low-frequency contribution of the FEEP thrusters and the disturbance noise of the test masses. The environment noise, the magnetic hardware noise, and the solar and infrared emission contributions are totally negligible in the interferometer readings and do not represent any restriction in terms of parameter estimation quality.

We have already shown that the displacements and rotations of the test masses can be detected even in the case in which all the noise sources are considered. Now the question to be answered is to which accuracy the magnetic properties of the test masses can be estimated. To this end we have used a classical linear least squares procedure (Wolberg, 2005). The magnetic parameters are estimated in the following way. Let D_x be the differential displacement signals from the interferometer, and R_y and R_z the rotation excursions around the y- and the z-axis, respectively, we write then:

$$\begin{aligned} D_x &= \begin{pmatrix} d_{x_{1\omega}} & d_{x_{2\omega}} \end{pmatrix} \cdot \begin{pmatrix} M_x \\ \chi \end{pmatrix} + n_{d_x} \\ R_y &= M_z \cdot r_{y_{1\omega}} + n_{r_y} \\ R_z &= M_y \cdot r_{z_{1\omega}} + n_{r_z} \end{aligned} \tag{3.13}$$

where we have used Eq. (3.9), d and r are the signals in displacement and rotation matched to the expected waveforms in ω and 2ω, as obtained from Eq. (3.9), and n_{d_x}, n_{r_y} and n_{r_z} are the errors of the estimation model, namely, the displacement error, the η- and the ϕ- error, respectively. Then the estimated magnetic properties of the test masses ($\hat{M}_x$, $\hat{M}_y$, $\hat{M}_z$ and $\hat{\chi}$) applying least square techniques are computed as:

$$\begin{aligned} \begin{pmatrix} \hat{M}_x \\ \hat{\chi} \end{pmatrix} &= \left[\begin{pmatrix} d_{x_{1\omega}}{}^{\mathrm{T}} \\ d_{x_{2\omega}}{}^{\mathrm{T}} \end{pmatrix} \cdot \begin{pmatrix} d_{x_{1\omega}} & d_{x_{2\omega}} \end{pmatrix} \right]^{-1} \begin{pmatrix} d_{x_{1\omega}} \\ d_{x_{2\omega}} \end{pmatrix} D_x \\ \hat{M}_z &= \left[r_{y_{1\omega}}{}^{\mathrm{T}} \cdot r_{y_{1\omega}} \right]^{-1} r_{y_{1\omega}}{}^{\mathrm{T}} \cdot R_y \\ \hat{M}_y &= \left[r_{z_{1\omega}}{}^{\mathrm{T}} \cdot r_{z_{1\omega}} \right]^{-1} r_{z_{1\omega}}{}^{\mathrm{T}} \cdot R_z \end{aligned} \tag{3.14}$$

As can be seen, the values of M_x and χ can be disentangled from D_x because the dynamics of the test masses show two frequencies, while R_y and R_z can be directly used to estimate the values of M_z and M_y.

Table 3.1: Preliminary assessment of the errors in the estimates of the magnetic properties for each individual noise source and for all sources combined together.

	$\Delta\hat{M}_x$	$\Delta\hat{M}_y$	$\Delta\hat{M}_z$	$\Delta\hat{\chi}$
No noise	$10^{-13}\%$	$10^{-13}\%$	$10^{-13}\%$	$10^{-13}\%$
Hardware noise	0.13%	0.08%	0.09%	0.12%
Environmental noise	0.12%	0.26%	0.24%	0.10%
Sensors noise	0.87%	0.97%	1.05%	1.01%
Actuators noise	0.96%	0.99%	1.25%	1.17%
Solar and infrared noise	0.03%	0.02%	0.05%	0.06%
Test mass disturbance noise	0.82%	0.73%	0.75%	0.99%
All sources	1.15%	1.53%	1.72%	1.25%

We have examined the contribution of each of the noise sources in our estimation accuracy. The accuracy of the measurements of the magnetic properties of the test masses is mainly affected by the specific contribution of the noise source within the measurement bandwidth. For instance, if some noise source has a relevant contribution around 1 mHz in the rotation signals, the estimating algorithm can not disentangle this contribution from that of the injected torque. In Table 3.1 we list the accuracies of the estimated magnetic parameters obtained for each of the individual noise sources and that obtained when all the noise sources are present (last row). Rather naturally, the results for M_x and χ shown in this table are closely related to the noise contributions shown in Fig. 3.9 — note that Fig. 3.9, only shows the noise breakdown for the differential displacement channel. The largest contributions to the error budget are, as expected, the actuators noise, the interferometer noise and the test mass disturbances. Nevertheless, the overall quality of the estimate is fairly good, 1.43% (mean square error of the relative errors of all the estimated parameters). It is interesting to note as well that even if the rotations signals present signal to noise ratios around a factor of 3 smaller, we obtain errors of the same order of magnitude for the estimates of M_y and M_z. This follows from the fact that the signals from which they are obtained must not be disentangled.

3.6 Conclusions

In this chapter we have confirmed the feasibility of deriving the magnetic properties of the test masses of LISA Pathfinder. The magnetic experiment is based on injecting controlled sinusoidal currents through the on-board coils and studying the dynamics of the test masses, as measured with the optical metrology subsystem. In

our study we have performed numerical calculations that incorporate a full model of the dynamics of the test masses, realistic noise sources and up-to-date simulations of the interferometer and inertial sensors. In particular, all the degrees of freedom of the test masses have been appropriately analyzed and we have fully taken into account the control architecture of LISA Pathfinder. We have obtained that the displacements of the test masses along the x-direction are ~ 8 nm, while the rotation excursions are approximately $4\,\mu$rad. These findings confirm that the magnetic experiment is within the authority margins of the drag free and low frequency suspension controllers. Consequently, any damage to the entire experiment when the coils are excited can be safely discarded. Moreover, we have shown that the displacement and rotation signals can be processed and pipelined to an adequate estimation algorithm that allows to estimate both the magnetic moment and the magnetic susceptibility of the test masses to a good accuracy. Specifically, assuming that the remnant magnetic moment is homogenous within the entire volume of the test masses, the estimates have errors below the 2% level. We would like to emphasize that although in this chapter we have presented the basic setup and main characteristics of the experiment designed to determine the magnetic properties of the test masses, a simplified model was used. In subsequent chapters we introduce a more realistic approach to model and analyze the same experiment.

Chapter 4

Optimization of inflight magnetic estimations

In this chapter we present an expanded study of the magnetic experiments previously described in chapter 3. Particularly, we explain in detail the behavior of the force and torque signals. Moreover, we put forward the fact that the estimation quality of the remanent magnetic moment and susceptibility is frequency dependent. We also show how the best frequency for the estimation of these quantities can be obtained, and how the combined estimate using multiple frequencies should be calculated.

4.1 Introduction

The determination of the magnetic characteristics of the test masses (remanent magnetic moment and susceptibility) must be done in flight because their magnetic properties may change due to launch stresses and other circumstances. This will be done injecting controlled sinusoidal magnetic fields at the positions of the test masses and appropriately processing the resulting kinematics, which will be obtained from the readings delivered by the onboard interferometer. Although the basic design of the magnetic experiment is well settled — see Díaz-Aguiló et al. (2011a) and chapter 3 — due to the high complexity of the LTP experiment, more in-depth analyses based on a more realistic modeling are necessary to assess its feasibility and performance. The purpose of this chapter is, precisely, to fill this gap. In particular, we model in a realistic way the kinematics of the test masses and we evaluate the expected quality of the estimates of the magnetic moment and susceptibility. Specifically, we take into account several effects — like the cross-talks between some of the channels of the instrument, or the frequency behavior of the control loops governing the dynamics of the test masses — that previous analyses disregarded. All these effects depend on the frequency used to excite the test masses. Hence, the quality of the estimates of the magnetic data depends sensitively on the excitation frequency, since the satellite

does not behave equally across the complete measurement bandwidth. Therefore, it is important to determine the quality of the estimates across the complete measurement bandwidth, and the frequencies that deliver the best estimates of the magnetic parameters.

The chapter is organized as follows. In section 4.2 we give a brief description of the magnetic experiment intended to estimate the magnetic properties of the test masses. Then, in section 4.3 we present the dynamical model of the satellite. It follows section 4.4, where we discuss the estimation model and the estimation procedures used in this work. In this section we also present the whitening algorithms used in this estimation, and we show how the biases introduced by the cross-talk terms of the instrument can be corrected. In section 4.5 we present the sensitivity of this model to different hardware systems of the satellite and in section 4.6 we evaluate the frequency dependence of the experiment, and we optimize its performance with respect to the excitation frequency. Section 4.7 is devoted to analyze the robustness of our results. Finally, in section 4.8 we summarize our main findings, we discuss the significance of our results, and we draw our conclusions.

4.2 Experiment overview

The two test masses are located at the center of each inertial sensor — the two towers in Fig. 4.1 — and are the end mirrors of the Optical Metrology System, that senses the positions and attitudes of the test masses. The optical bench of the interferometer can be seen in Fig. 4.1 as well. In fact, one of the test masses is the reference free floating body to perform the translation and attitude control of the spacecraft. The x-axis of the experiment is the axis connecting the two test masses centers, and it goes from test mass 1 to test mass 2. The z-axis point towards the solar panel (parallel to the two inertial sensor towers and upwards in Fig. 4.1) and, finally, the y-axis closes the right-handed Cartesian coordinate system. The test masses are made of an alloy of Pt (27%) and Au (73%), their dimensions are $46 \times 46 \times 46$ mm and their weight is 1.95 kg. To comply with the top science requirements, the test masses must have certain properties. For the purpose of the present work the two most important properties are the remanent magnetic moment and the susceptibility. The remanent magnetic moment must be $|\mathbf{m}| < 2.0 \times 10^{-8}$ A m^2. Since the volume of the test masses is $V = 0.046^3$ m^3, the density of magnetic moment must be then $|\mathbf{M}| < 9.451 \times 10^{-4}$ A/m. The susceptibility of the test mass can be suitably represented by a complex number, $\chi = \chi_\mathrm{o} + i\chi_\mathrm{e}$, where χ_o is its real component and $\chi_\mathrm{e}(\omega)$ is a frequency-dependent imaginary term which is due to the eddy currents on the test mass (Vitale, 2005; Antonucci et al., 2011b). The value of the real component must be $\chi_\mathrm{o} < 2.5 \times 10^{-5}$.

As mentioned, to measure the remanent magnetic moment and the susceptibility of the test masses a controlled magnetic field will be injected at the position of

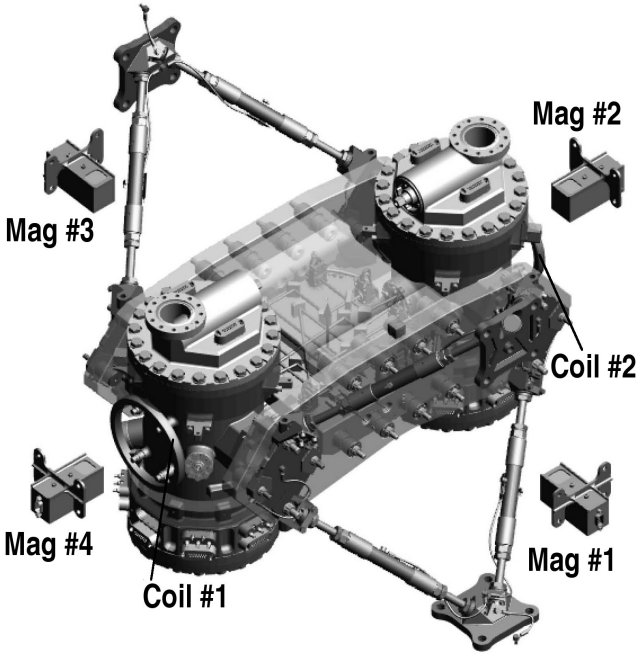

Figure 4.1: A schematic view of the payload of LISA Pathfinder, the LTP. The Inertial Sensors (two vertical towers) host the two test masses. The four floating boxes correspond to the tri-axial fluxgate magnetometers, and the two induction coils are placed next to each of the test masses. The optical bench of the interferometer is located on the horizontal plane between the Inertial Sensors.

the test masses. This magnetic field produces forces and torques which excite the kinematics of the test masses. Studying the motion of the test masses, namely their displacement and rotation, allows to estimate the three components of the magnetic moment and the susceptibilities of the test masses.

4.2.1 The injected magnetic fields

The magnetic field at the position of the test masses will be generated by the injection of sinusoidal currents to the onboard coils. These onboard coils are placed next to each of the inertial sensors towers, see again Fig. 4.1. The two circular induction coils are made of a titanium alloy (Ti_6Al_4V), and have $N = 2\,400$ windings of radius $r = 56.5$ mm (Antonucci et al., 2011b). They are placed 85.5 mm away from the center of the respective test mass. The onboard coils are aligned with the x-axis of the test masses, thus, the magnetic field within the volume of the test masses has axial symmetry. Given a current fed to the coils $I(t) = I_0 \sin \omega_0 t$, the resulting magnetic field (and its gradient) will oscillate at the same frequency. Therefore we write,

$$\mathbf{B}_{\text{app}} = \text{Re}\left\{\mathbf{B}_0\, ie^{-i\omega_0 t}\right\} = \mathbf{B}_0\, \sin\omega_0 t \tag{4.1}$$

$$\boldsymbol{\nabla}\mathbf{B}_{\text{app}} = \text{Re}\left\{\boldsymbol{\nabla}\mathbf{B}_0\, ie^{-i\omega_0 t}\right\} = \boldsymbol{\nabla}\mathbf{B}_0\, \sin\omega_0 t \tag{4.2}$$

The field produced by the coils at the center of the test mass is 4.47 μT, whereas the maximum environmental magnetic field expected during science operation is less than 100 nT. On the other hand, the magnetic field gradient along the x-axis produced by the coils is 109.2 μT/m, while the maximum magnetic field gradient required by the mission science specification is -5 μT/m. Therefore, it is a safe assumption to neglect the effects of the environmental magnetic field with respect to the applied field by the coils. Thus, the forces and torques exerted on the test masses are computed as (Jackson, 1999):

$$\mathbf{F} = \left\langle \left[\left(\mathbf{M} + \text{Re}\left\{ \frac{\chi_\text{o} + i\chi_\text{e}}{\mu_0}\, \mathbf{B}_0\, ie^{-i\omega_0 t} \right\} \right) \cdot \boldsymbol{\nabla} \right] \mathbf{B}_{\text{app}} \right\rangle V \tag{4.3}$$

and

$$\begin{aligned} \mathbf{N} &= \Big\langle \mathbf{M} \times \mathbf{B}_{\text{app}} + \mathbf{r} \times \Big([\mathbf{M} \cdot \boldsymbol{\nabla}]\mathbf{B}_{\text{app}} \\ &+ \left[\text{Re}\left\{ \frac{\chi_\text{o} + i\chi_\text{e}}{\mu_0}\, \mathbf{B}_0\, ie^{-i\omega_0 t} \right\} \cdot \boldsymbol{\nabla} \right] \mathbf{B}_{\text{app}} \Big) \Big\rangle V \end{aligned} \tag{4.4}$$

where $\mathbf{B}_{\text{app}}$ is the field produced by the coils, and $\mathbf{r}$ is the position vector that has the test mass center as origin. Note that the forces and torques depend on $\mathbf{M}$, χ_o and χ_e.

Considering Eqs. (4.1), (4.2) and (4.3), the x-component of the force acting on the test mass is

$$\begin{aligned} F_x &= \frac{\chi_\text{o} V}{2\mu_0}\, \langle \mathbf{B}_0 \cdot \boldsymbol{\nabla} B_{0,x} \rangle \\ &+ \langle \mathbf{M} \cdot \boldsymbol{\nabla} B_{0,x} \rangle\, V\, \sin\omega_0 t \\ &- \frac{\chi_\text{o} V}{2\mu_0}\, \langle \mathbf{B}_0 \cdot \boldsymbol{\nabla} B_{0,x} \rangle\, \cos\, 2\omega_0 t \\ &- \frac{\chi_\text{e} V}{2\mu_0}\, \langle \mathbf{B}_0 \cdot \boldsymbol{\nabla} B_{0,x} \rangle\, \cos(2\omega_0 t - \pi/2) \end{aligned} \tag{4.5}$$

where we have used that $\sin^2\omega_0 t = (1 - \cos 2\omega_0 t)/2$ and the $\pi/2$ rad phase due to the complex component of the susceptibility has been added as an argument in the corresponding cos term. As can be seen from this equation, the linear acceleration of the test masses along the x-axis has two separate frequencies, one at ω_0 and

the other at $2\omega_0$, and also a DC component. The $2\omega_0$ component presents an in-phase component proportional to χ_o and a quadrature component proportional to χ_e. Particularly, the ω_0 component can be more explicitly written as:

$$\langle \mathbf{M}\cdot\boldsymbol{\nabla} B_{0,x}\rangle = \left\langle M_x \frac{\partial B_{0,x}}{\partial x} + M_y \frac{\partial B_{0,x}}{\partial y} + M_z \frac{\partial B_{0,x}}{\partial z} \right\rangle \tag{4.6}$$

where M_x, M_y, M_z are the components of the density of the remanent magnetic moment. If the test mass is homogeneous we have the simplified expression

$$\langle \mathbf{M}\cdot\boldsymbol{\nabla} B_{0,x}\rangle = \left\langle M_x \frac{\partial B_{0,x}}{\partial x} \right\rangle \tag{4.7}$$

since the y and z components of $\boldsymbol{\nabla} B_{0,x}$ average to zero due to symmetry of the field of the coil. This leads to a force component along the x-axis that only depends on M_x, χ_o and χ_e.

On the other hand, the torque acting on the test mass also has a similar behavior:

$$\begin{aligned} \mathbf{N} &= \langle \mathbf{M}\times\mathbf{B}_0 + \mathbf{r}\times[(\mathbf{M}\cdot\boldsymbol{\nabla})\,\mathbf{B}_0]\rangle\, V\,\sin\omega_0 t \\ &+ \left\langle \mathbf{r}\times\frac{\chi_\mathrm{o}}{\mu_0}\,[\mathbf{B_0}\cdot\boldsymbol{\nabla}]\mathbf{B_0}] \right\rangle V\,\sin^2\omega_0 t \\ &- \left\langle \mathbf{r}\times\frac{\chi_\mathrm{e}}{\mu_0}\,[\mathbf{B_0}\cdot\boldsymbol{\nabla}]\mathbf{B_0}] \right\rangle V\,\sin\omega_0 t\,\cos\omega_0 t \end{aligned} \tag{4.8}$$

In this case, it must be noted that, because of the symmetry of the applied magnetic field, the terms multiplying $\sin^2\omega_0 t$ and $\sin\omega_0 t\,\cos\omega_0 t$ in Eq. (4.8) vanish. The two rotation excursions detected by the interferometer using wavefront sensing are the rotations about the y-axis and z-axis. The magnitude of the rotation about the x-axis is smaller, and cannot be detected by the interferometer because the axis of rotation is aligned with the laser beam. Taking this into account, the two relevant torques for the experiment are:

$$\begin{aligned} N_y &= \Big\langle M_z B_{0,x} - M_x B_{0,z} \\ &+ z\,(\mathbf{M}\cdot\boldsymbol{\nabla} B_{0,x}) \\ &- x\,(\mathbf{M}\cdot\boldsymbol{\nabla} B_{0,z})\Big\rangle V\,\sin\omega_0 t \end{aligned} \tag{4.9}$$

$$\begin{aligned} N_z &= \Big\langle M_x B_{0,y} - M_y B_{0,x} \\ &+ x\,(\mathbf{M}\cdot\boldsymbol{\nabla} B_{0,y}) \\ &- y\,(\mathbf{M}\cdot\boldsymbol{\nabla} B_{0,x})\Big\rangle V\,\sin\omega_0 t \end{aligned} \tag{4.10}$$

These equations can be further simplified in the case of a homogeneous test mass. In this case, due to the axial symmetry of the magnetic field, the terms $\langle B_{0,z}\rangle$ in

Eq. (4.9) and $\langle B_{0,y} \rangle$ in Eq. (4.10) vanish. Moreover, for the same reason the terms

$$\left\langle z \frac{\partial B_{0,x}}{\partial x} \right\rangle, \quad \left\langle z \frac{\partial B_{0,x}}{\partial y} \right\rangle,$$

and

$$\left\langle x \frac{\partial B_{0,z}}{\partial x} \right\rangle, \quad \left\langle x \frac{\partial B_{0,z}}{\partial y} \right\rangle$$

in Eq. (4.9) also vanish, as do the terms

$$\left\langle x \frac{\partial B_{0,y}}{\partial x} \right\rangle, \quad \left\langle x \frac{\partial B_{0,y}}{\partial z} \right\rangle,$$

$$\left\langle y \frac{\partial B_{0,x}}{\partial x} \right\rangle, \quad \left\langle y \frac{\partial B_{0,x}}{\partial z} \right\rangle$$

in Eq. (4.10). In these terms x, y and z are the three components of $\mathbf{r}$. Hence, the torque about the y-axis only depends on M_z and the torque about the z-axis only depends on M_y:

$$N_y = M_z \left\langle B_{0,x} + z \frac{\partial B_{0,x}}{\partial z} - x \frac{\partial B_{0,z}}{\partial z} \right\rangle V \sin \omega_0 t \tag{4.11}$$

$$N_z = M_y \left\langle -B_{0,x} + x \frac{\partial B_{0,y}}{\partial y} - y \frac{\partial B_{0,x}}{\partial y} \right\rangle V \sin \omega_0 t \tag{4.12}$$

Finally, we can cast Eqs. (4.5), (4.11) and (4.12) in the form:

$$\begin{aligned} F_x &= \chi_{\mathrm{o}} f_{x_{\mathrm{DC}}} + M_x f_{x_{1\omega_0}} + \chi_{\mathrm{o}} f_{x_{2\omega}} + \chi_{\mathrm{e}} f''_{x_{2\omega_0}} \\ N_y &= M_z n_{y_{1\omega_0}} \\ N_z &= M_y n_{z_{1\omega_0}} \end{aligned} \tag{4.13}$$

where $f_{x_{\mathrm{DC}}}$ is a constant function, $f_{x_{1\omega_0}}$, $n_{y_{1\omega_0}}$ and $n_{z_{1\omega_0}}$ oscillate at ω_0 and $f_{x_{2\omega_0}}$ and $f''_{x_{2\omega_0}}$ oscillate at $2\omega_0$.

4.3 Dynamic model

The LTP instrument will react to the injection of the aforementioned forces and torques inflicted upon the test masses. This will result in specific kinematic excursions in both test masses. These kinematic excursions will depend on the instrument dynamics and will be sensed by the onboard interferometer. The LTP is a very complex instrument but its full three-dimensional dynamical modeling can be split into 4 main parts (Schleicher, 2009; Brandt & et al., 2004):

1. The dynamical model (**D**) represents the evolution of the kinematic excursions of the two test masses placed inside the LTP and the kinematics of the spacecraft. This model takes into account the coupling of the motion of each of the test masses with the motion of the spacecraft and outputs the evolution of the 15 degrees of freedom of the instrument, i.e. 6 degrees of freedom for each of the test masses and 3 degrees of freedom for the spacecraft (only the attitude of the spacecraft is observable and not its linear displacement).

2. The sensing mechanisms (**S**) onboard LPF are the star tracker, the inertial sensors, and the interferometer. The star tracker measures the attitude of the spacecraft. The inertial sensors give accurate measurements of the position and attitude of the test masses with respect to the spacecraft by detecting differences in the capacitive sensors that surround the test masses (Vitale, 2005, 2002). Finally, the interferometer measures the differential distance between test mass 1 and the spacecraft and the differential distance between the two test masses (Heinzel et al., 2003, 2004).

3. The controller blocks (**C**) are in charge of calculating the appropriate commands to correct the positions of the test masses and the attitude of the spacecraft. In science mode, there are two main control loops applied by the instrument. The first one — the drag free loop — takes the absolute measurement of the distance between test mass 1 and the spacecraft as a reference. It then calculates which forces should be applied to the spacecraft in order to counteract all disturbances and recreate a drag free environment for test mass 1. The second loop — the low frequency loop — takes as a reference the differential measurement between both test masses and acts on the second test mass to avoid its collision with the spacecraft walls (Schleicher, 2008, 2009). The controllers have been designed to deliver very sensitive readings of the differential motion of both test masses between 1 mHz and 30 mHz, the measurement bandwidth of the LPF mission (Vitale, 2005). These two control loops are implemented inside the onboard computer of the LPF.

4. The actuators (**A**) are the physical systems that apply these commands to the test masses and to the spacecraft. The two actuator mechanisms existing in LPF are the satellite micropropulsion system, which is composed by 12 micro-newton FEEP thrusters (Field Emission Electric Propulsion), and the capacitive actuators which consist of a set of electrodes that surround the test masses and exert controlled forces on them.

This subsystem division is schematically shown in the block diagram of Fig. 4.2. For more detailed information of the system, the reader is referred to Díaz-Aguiló et al. (2011a), Schleicher (2009) and Nofrarias et al. (2010). This block diagram of the dynamical behavior allows to express for the interferometric readings as follows:

$$\mathbf{o} = \mathbf{D}^{-1} \cdot \mathbf{S} \cdot \mathbf{f} + \mathbf{o}_{\mathrm{n}} \tag{4.14}$$

where

$$\mathbf{f} = \mathbf{f}_{\mathrm{mag}} + \mathbf{f}_{\mathrm{n}} - \mathbf{A} \cdot \mathbf{C} \cdot (\mathbf{o} + \mathbf{o}_{\mathrm{i}}) - \mathbf{a}_{\mathrm{n}} \tag{4.15}$$

In these expressions the symbols are:

$\mathbf{o}$	:	the readings of the sensing devices,
$\mathbf{f}$	:	the forces or torques acting on the test masses,
$\mathbf{o}_{\mathrm{n}}$	:	the readout noises of the sensing devices,
$\mathbf{f}_{\mathrm{mag}}$	:	the forces or torques due to magnetic effects,
$\mathbf{f}_{\mathrm{n}}$	:	the force or torque noises,
$\mathbf{o}_{\mathrm{i}}$	:	the displacement guidance signals of the experiments,
$\mathbf{a}_{\mathrm{n}}$	:	the actuators noises.

For illustrative purposes, if we consider only the one-dimensional model, the different sub-blocks of Eq. (4.14) are:

$$\mathbf{D} = \begin{pmatrix} s^2 + \omega_1^2 & 0 \\ \omega_2^2 - \omega_1^2 & s^2 + \omega_2^2 \end{pmatrix}, \tag{4.16}$$

$$\mathbf{S} = \begin{pmatrix} 1 & 0 \\ \delta_{12} & 1 \end{pmatrix}, \tag{4.17}$$

$$\mathbf{C} = \begin{pmatrix} C_{\mathrm{DF}}(s) & 0 \\ 0 & C_{\mathrm{LFS}}(s) \end{pmatrix}, \tag{4.18}$$

$$\mathbf{A} = \begin{pmatrix} A_{\mathrm{FEEP}}(s) & 0 \\ 0 & A_{\mathrm{CA}}(s) \end{pmatrix} \tag{4.19}$$

where ω_1 and ω_2 are the stiffness parameters coupling the motion of each test mass to the motion of the spacecraft, δ_{12} is the cross-coupling factor between the two interferometer channels, $C_{\mathrm{DF}}(s)$ and $C_{\mathrm{LFS}}(s)$ are, respectively, the drag-free and the low-frequency suspension controller transfer functions and, finally, $A_{\mathrm{FEEP}}(s)$ and $A_{\mathrm{CA}}(s)$ are the physical models for the FEEP thrusters and the capacitive actuators, respectively. We normalize the transfer functions of the controllers and the actuators as a functions of their static gain (G):

$$C_{\mathrm{DF}}(s) = G_{\mathrm{DF}} \cdot C'_{\mathrm{DF}}(s) \tag{4.20}$$

$$C_{\mathrm{LFS}}(s) = G_{\mathrm{LFS}} \cdot C'_{\mathrm{LFS}}(s) \tag{4.21}$$

$$A_{\mathrm{FEEP}}(s) = G_{\mathrm{FEEP}} \cdot A'_{\mathrm{FEEP}}(s) \tag{4.22}$$

$$A_{\mathrm{CA}}(s) = G_{\mathrm{CA}} \cdot A'_{\mathrm{CA}}(s) \tag{4.23}$$

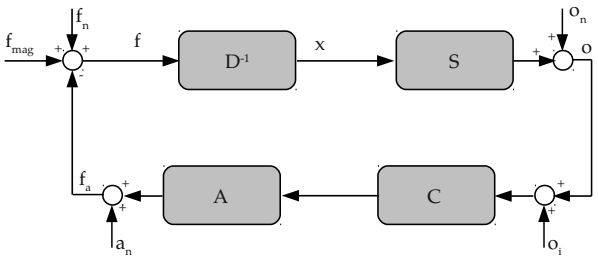

Figure 4.2: Control system architecture of LISA Pathfinder. **D** stands for the dynamical matrix, **S** represents the sensing matrix of the interferometer, i.e. the matrix translating the position of the test mass, **x**, into the interferometer readout, **o** ($\mathbf{o}_\mathrm{n}$ stands for the readout noise). **A** represents the physics of the FEEP and the electrostatic actuators, and finally **C**, is the controller matrix, implementing the drag free and low-frequency control loops. $\mathbf{o}_\mathrm{i}$ represents the displacement guidance signals. $\mathbf{a}_\mathrm{n}$ are the actuators noise and $\mathbf{f}_\mathrm{a}$ are the output forces and torques of the actuators. $\mathbf{f}_\mathrm{mag}$ are the magnetic forces and torques induced by the coils and $\mathbf{f}_\mathrm{n}$ are the environment force and torque noises disturbing the spacecraft.

where the G_DF, G_LFS, G_FEEP, and G_CA are constants and stand, respectively, for the static gain of the transfer functions of the drag free controller, the low frequency controller, the FEEP actuator, and the capacitive actuator. On the other hand, $C'_\mathrm{DF}(s)$, $C'_\mathrm{LFS}(s)$, $A'_\mathrm{FEEP}(s)$, and $A'_\mathrm{CA}(s)$ hold the frequency dependence of these transfer functions and have unit static gain.

In the magnetic experiment the input signals are the magnetic forces and torques ($\mathbf{f}_\mathrm{mag}$), and the outputs are the readings of the interferometer (**o**). Therefore, using Eqs. (4.14) and (4.15), we calculate the input/output transfer function, which results in:

$$\mathbf{o} = \mathbf{H} \cdot \mathbf{f_{mag}} \tag{4.24}$$

where

$$\mathbf{H} = \frac{\mathbf{D}^{-1} \cdot \mathbf{S}}{1 + \mathbf{D}^{-1} \cdot \mathbf{S} \cdot \mathbf{A} \cdot \mathbf{C}} \tag{4.25}$$

This transfer function depends on all the above described subsystems and represents the dynamical response of the instrument to the specific injected signals.

4.4 Estimation model

The estimation of the magnetic characteristics is performed processing the interferometer readings. To do so, we use the displacement of the differential channel ($o_{x_{12}}$), the rotation about the y-axis (o_{η_1}) and the rotation about the z-axis (o_{ϕ_1}). If cross talks are disregarded, the reading of the displacement channel stems only by the effect of the magnetic force acting along the x-axis, F_x. Analogously, something

similar occurs for the two torques in each of their respective axis. Thus, we can write:

$$\begin{aligned} o_{x12} &= M_x\, d_{x_{1\omega_0}} + \chi_{\mathrm{o}}\, d_{x_{2\omega_0}} + \chi_{\mathrm{e}}\, d''_{x_{2\omega_0}} \\ o_{\eta_1} &= M_z\, r_{y_{1\omega_0}} \\ o_{\phi_1} &= M_y\, r_{z_{1\omega_0}} \end{aligned} \tag{4.26}$$

where $d_{x_{1\omega_0}}$, $d_{x_{2\omega_0}}$ and $d''_{x_{2\omega_0}}$ are the respective transformations from force to displacement of the signals $f_{x_{1\omega_0}}$, $f_{x_{2\omega_0}}$ and $f''_{x_{2\omega_0}}$ in Eq. (4.13), and analogously for $r_{y_{1\omega_0}}$ and $r_{z_{1\omega_0}}$ for the case of $n_{y_{1\omega_0}}$ and $n_{z_{1\omega_0}}$. This is the model used in chapter 3. Nevertheless, because of the high complexity of the LTP instrument, this model is not sufficiently realistic. In particular, it turns out that the cross-talks cause important biases in the parameter estimates. This is because the effect of the x-force in the rotation readings and the effect of the torques in the x-axis readings are not negligible. As a consequence, we used the full three-dimensional model of the experiment:

$$\begin{pmatrix} o_{x12} \\ o_{\eta_1} \\ o_{\phi_1} \end{pmatrix} = \begin{pmatrix} H_{F_x\to x12} & H_{N_y\to x12} & H_{N_z\to x12} \\ H_{F_x\to \eta_1} & H_{N_y\to \eta_1} & H_{N_z\to \eta_1} \\ H_{F_x\to \phi_1} & H_{N_y\to \phi_1} & H_{N_z\to \phi_1} \end{pmatrix} \cdot \begin{pmatrix} M_x & \chi_{\mathrm{o}} & \chi_{\mathrm{e}} & 0 & 0 \\ 0 & 0 & 0 & M_z & 0 \\ 0 & 0 & 0 & 0 & M_y \end{pmatrix} \begin{pmatrix} f_{x_{1\omega_0}} \\ f_{x_{2\omega_0}} \\ f''_{x_{2\omega_0}} \\ n_{y_{1\omega_0}} \\ n_{z_{1\omega_0}} \end{pmatrix} \tag{4.27}$$

where the 3×3 matrix $\mathbf{H}$ is the transformation matrix from force/torque to displacement/rotation that represents the closed loop dynamics of the instrument — see Eq. (4.25). This matrix is not diagonal, as it is assumed in the model in which the cross-talks are neglected — namely, Eq. (4.26). For instance, the effect of the torque about the y-axis and the z-axis on the $o_{x_{12}}$ displacement channel is relevant, and thus non-zero transfer functions $H_{N_y\to x12}$ and $H_{N_z\to x12}$ need to be considered. Hence, to estimate M_x, M_y, M_z, χ_{o} and χ_{e}, these transfer functions have to be known. This model is still a simplification, because we do not include all the degrees of freedom, but it is certainly more realistic than that of Eq. (4.26), which is strictly one-dimensional.

4.4.1 Estimation procedure and bias correction

The estimation procedure has been already described in Díaz-Aguiló et al. (2011a) and in chapter 3. However, in this chapter we present an important modification to

correct for the biases introduced by cross-talks. The full three-dimensional estimation model given by Eq. (4.27) may be regrouped as:

$$\begin{aligned} o_{x12} &= (M_x + \alpha_{12} M_z + \alpha_{13} M_y)\; d_{x_{1\omega_0}} + \\ &+ \chi_{\mathrm{o}}\; d_{x_{2\omega}} + \chi_{\mathrm{e}}\; d''_{x_{2\omega_0}} \\ o_{\eta} &= (\alpha_{21} M_x + M_z + \alpha_{23} M_y)\; r_{y_{1\omega_0}} \\ o_{\phi} &= (\alpha_{31} M_x + \alpha_{32} M_z + M_y)\; r_{z_{1\omega_0}} \end{aligned} \tag{4.28}$$

where α are the cross-talks of the system (the matrix elements of $\mathbf{H}$ evaluated at the excitation frequency). If we introduce the quantities M'_x, M'_y, and M'_z, then Eq. (4.28) can be equivalently written as:

$$\begin{aligned} o_{x12} &= M'_x\; d_{x_{1\omega_0}} + \chi_{\mathrm{o}}\; d_{x_{2\omega_0}} + \chi_{\mathrm{e}}\; d''_{x_{2\omega_0}} \\ o_{\eta} &= M'_z\; r_{y_{1\omega_0}} \\ o_{\phi} &= M'_y\; r_{z_{1\omega_0}} \end{aligned} \tag{4.29}$$

and we estimate the values of $\hat{M}'_x$, $\hat{M}'_y$, $\hat{M}'_z$, $\hat{\chi}_{\mathrm{o}}$ and $\hat{\chi}_{\mathrm{e}}$ applying standard single output least square techniques (Díaz-Aguiló et al., 2011a; Wolberg, 2005) — see chapter 3. These values of $\hat{M}'_x$, $\hat{M}'_y$ and $\hat{M}'_z$ are biased, and do not correspond to the true magnetic moment components, M_x, M_y and M_z. Nevertheless, these biases can be corrected because we know the relation between them:

$$\begin{pmatrix} \hat{M}_x \\ \hat{M}_z \\ \hat{M}_y \end{pmatrix} = \begin{pmatrix} 1 & \alpha_{12} & \alpha_{13} \\ \alpha_{21} & 1 & \alpha_{23} \\ \alpha_{31} & \alpha_{32} & 1 \end{pmatrix}^{-1} \begin{pmatrix} \hat{M}'_x \\ \hat{M}'_z \\ \hat{M}'_y \end{pmatrix} \tag{4.30}$$

Note that Eq. (4.27) provides the values of the elements of this matrix, and that the matrix is invertible. Additionally, it is worth emphasizing that we only correct the components of the magnetic moment and no correction is considered for the susceptibility (χ_{o} and χ_{e}). This is because the magnetic susceptibility is not affected by any cross-talk at the $2\omega_0$ component. It turns out that the previously outlined procedure corrects biases of around 1% in each of the magnetic parameters, which are sizable. Finally, we also mention that during the lifetime of the mission some of the telemetry channels may fail. Thus, it is important to know beforehand that single channel estimation is still possible and that it introduces biases of $\sim 1\%$ — see section 3.5.

4.4.2 Whitening and splitting

Due to the low-frequency control architecture, the evolution of the reading of the differential channel and the absolute attitude variables of both test masses are con-

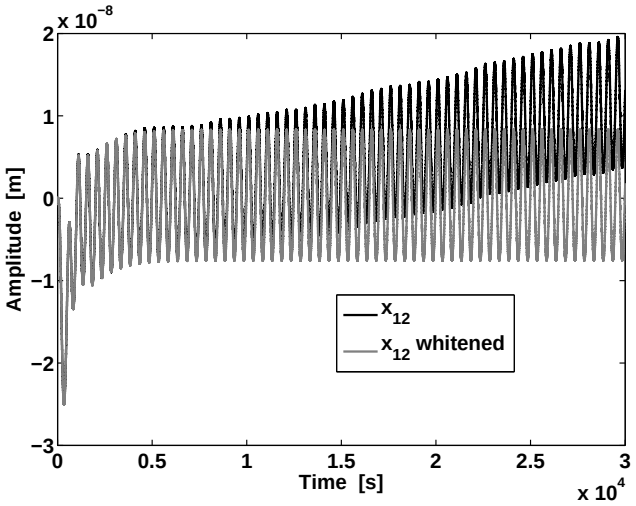

Figure 4.3: Amplitude of the differential displacement channel of the interferometer as a function of time, when a sinusoidal current of 1 mA and 2 mHz is injected to coil 1. The black curve is the raw output of the channel, while the gray curve shows the result after the whitening process that is performed before pipelining the telemetry readings to the estimation procedure.

trolled with a very low gain controller at low frequency. This avoids the collision of the test masses with the spacecraft walls at long time scales. Nevertheless, being a very slow controller, these kinematic excursions may suffer important low-frequency drifts between 1 000 and 10 000 s. This is because some low-frequency noise due to solar, infrared or other environmental factors is not filtered by the LTP controllers. This leads to a secular drift, like the one illustrated by the black curve in Fig. 4.3, where the differential displacement output shows a varying offset of approximately 5 nm. To avoid an undesirable impact on the estimation method, we whiten the interferometer output data. The whitening filter is obtained by fitting the noise spectra of each of the channels with a parallel filter bank. The tool used to obtain these filters is included in LTPDA toolbox (Antonucci et al., 2011a; Hewitson, 2011; Welch, 1967), the data analysis toolbox of the mission. After whitening the signal, the time series still presents a transient response at around 2 000 s, due to the response of the instrument to the initial conditions of the experiment. This can be observed in the gray curve of Fig. 4.3. Therefore, before pipelining the response to the estimation algorithms, we eliminate the first 5 000 s. This is the same to say that we only consider the permanent regime of the kinematic response.

4.5 An analysis of the uncertainties

The Experiment Master Plan of the mission is aimed at determining the physical parameters of the instrument, characterizing in this way the matrix elements of **H**. These transfer functions depend on several physical parameters. Amongst them we mention the stiffnesses of the test masses, the actuator gains, the interferometer cross-couplings, and the transfer function delays. In the end, this will result in a complete characterization of the main four blocks of the instrument. Detailed information on the Experiment Master Plan and on the accuracy of the estimates can be found in Nofrarias et al. (2010).

Nevertheless, for the calculations presented here it is important to realize that some of the parameters of the model may be poorly determined or have sizable uncertainties. Therefore, in our analysis we introduce uncertainties in each of the most relevant parameters of the mission. These uncertainties are represented as b, and the subscript "NOM" stands for the nominal value of the parameter:

$$\omega_1 = \omega_{1_{\mathrm{NOM}}}(1 \pm b_{\omega_1}) \tag{4.31}$$
$$\omega_2 = \omega_{2_{\mathrm{NOM}}}(1 \pm b_{\omega_2}) \tag{4.32}$$
$$\delta_{12} = \delta_{12_{\mathrm{NOM}}}(1 \pm b_{\delta_{12}}) \tag{4.33}$$
$$G_{\mathrm{FEEP}} = G_{\mathrm{FEEP}_{\mathrm{NOM}}}(1 \pm b_{G_{\mathrm{FEEP}}}) \tag{4.34}$$
$$G_{\mathrm{CA}} = G_{\mathrm{CA}_{\mathrm{NOM}}}(1 \pm b_{G_{\mathrm{CA}}}) \tag{4.35}$$

Clearly, the effects of these uncertainties on the estimation of the magnetic parameters need to be assessed. To this end, for each of the nine transfer functions of **H**, we have computed the effect of the uncertainties on each of the parameters of the system. We have done this analysis for values of b ranging from -0.2 to 0.2, and we have studied their effect on the modulus and on the phase of the transfer functions. We have found that the uncertainty on the capacitive actuator gain ($b_{G_{\mathrm{CA}}}$) is the only one that has a relevant impact, whilst the uncertainties on the other parameters have a negligible effect.

4.5.1 The capacitive actuator gain

In this section, we analyze the effect of the uncertainty of the capacitive actuator gain ($b_{G_{\mathrm{CA}}}$). To this end, for a specific value of $b_{G_{\mathrm{CA}}}$, we compute the absolute error of the modulus ($\mathbf{H}_{\mathrm{e}}{}^{\mathrm{b}}$) of the system transfer functions and the phase differences ($\mathbf{H}_{\psi}{}^{\mathrm{b}}$) across the measurement bandwidth (1 mHz to 30 mHz):

$$\mathbf{H}_{\mathrm{e}}{}^{\mathrm{b}} = |\mathbf{H}^{\mathrm{b}}| - |\mathbf{H}| \tag{4.36}$$
$$\mathbf{H}_{\psi}{}^{\mathrm{b}} = \measuredangle\mathbf{H}^{\mathrm{b}} - \measuredangle\mathbf{H} \tag{4.37}$$

where $\measuredangle$ stands for the matrix operator that calculates the phase of each of the elements of the matrix. In these expressions, the superscript "b" indicates that the specific transfer function has been calculated with a non-zero value of the parameter uncertainty. On the contrary, functions without superscript have been calculated with the nominal values of all the system parameters. Therefore, $\mathbf{H}_{\mathrm{e}}^{\mathrm{b}}$ calculates the absolute error of the modulus of each of the nine functions with respect to its nominal value for one specific value of uncertainty (b), and $\mathbf{H}_{\psi}{}^{\mathrm{b}}$ gives account for their phase differences. These two matrices give a quantitative assessment of the error of the model due to the uncertainties across the entire measurement bandwidth. Moreover, the most relevant contribution in the error of the model will be due to the error in the diagonal terms of the matrix. Therefore, we analyze mainly the effects on $H_{F_x \to x_{12}}$, $H_{N_y \to \eta_1}$ and $H_{N_z \to \phi_1}$.

Figure. 4.4 displays the results of this sensitivity analysis for $H_{F_x \to x_{12}}$, i.e the first element of matrices $\mathbf{H}_{\mathrm{e}}{}^{\mathrm{b}}$ and $\mathbf{H}_{\psi}{}^{\mathrm{b}}$ for several values of the uncertainty in the capacitive actuator gains, ranging from -0.2 to 0.2. The behavior as a function of the frequency of the other two elements of the diagonal are very similar. In the top panel of this figure it can be seen that the error of the modulus is especially relevant below 1 mHz, where the differences in amplitude increase up to 48% for 0.6 mHz, when the capacitive gain is 0.8 (instead of 1). The changes in modulus are also relevant between 1 mHz and 7 mHz. In the bottom panel, we examine the differences in the phase of the same transfer functions. It can be seen that there exist phase shifts of 15° for a capacitive actuator gain of 1.2 at a frequency of 1 mHz. These phase shifts are relevant between 0.4 mHz and 4 mHz. Such differences produce important biases in the estimates of the magnetic parameters. Moreover, the effect depends on the excitation frequency. Thus, the choice of the right excitation frequency (ω_0) is a crucial aspect in the experiment design. We postpone this analysis to section 4.6, where we will study which is the optimal excitation frequency. Finally, we also mention that similar analyses for the rest of the uncertainties on the nominal parameters have been performed, but are not shown here for the sake of conciseness.

4.6 The optimal frequency

Finding the optimal frequency of the sinusoidal currents injected in the coils to obtain the magnetic parameters is a crucial issue of the experiment. Actually, as it will be shown below, the optimal frequency can be obtained from a trade-off between the frequency range where the instrument presents a maximum of the signal-to-noise ratio (SNR) and the frequency range where the instrument is less sensitive to the uncertainties of the capacitive actuator gain — see section 4.5.1.

The SNR across the instrument measurement bandwidth for each of the channels — $o_{x_{12}}$, o_{η_1}, and o_{ϕ_1} — is shown in Fig. 4.5. The SNR reaches its maximum between 0.5 to 1.5 mHz for the displacement reading, and from 1 to 2 mHz for the rotation

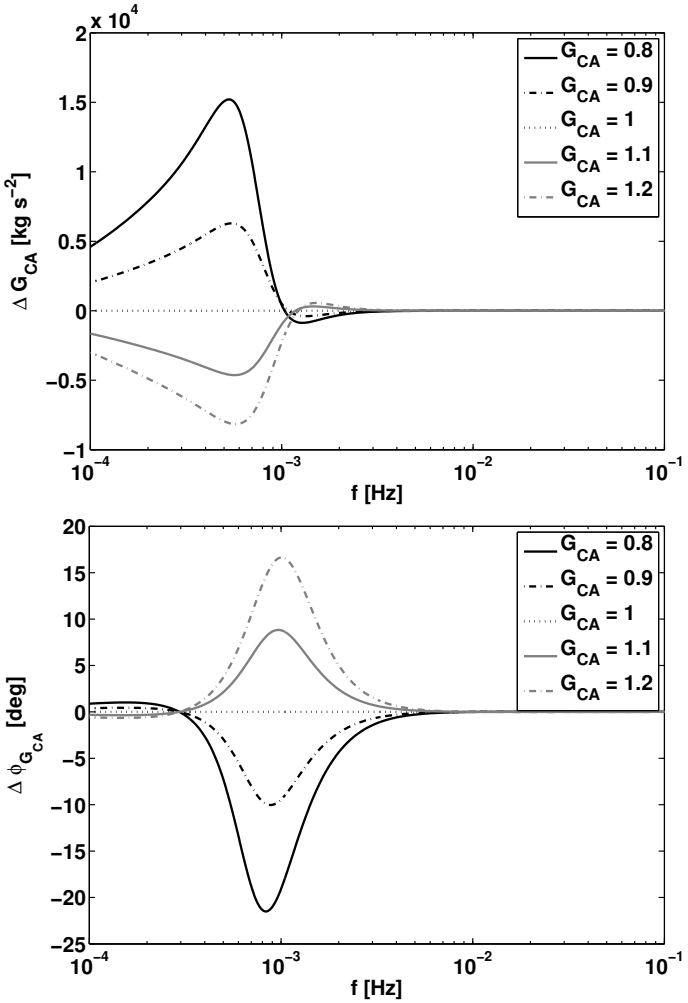

Figure 4.4: Top panel: error of the modulus of the transfer function $H^b_{F_x \to x_{12}}$ with respect to its nominal behavior. This frequency-dependent relative error is plotted for different capacitive actuator gain uncertainties ranging from -0.2 to 0.2. Bottom panel: phase differences in the $H^b_{F_x \to x_{12}}$ transfer function for different uncertainties of the gain of the capacitive actuator. The phase differences are also calculated for different relative gain uncertainties ranging from -0.2 to 0.2.

channels. This is the most sensitive band of the instrument. This is confirmed by inspecting Fig. 4.6, where we show the response of the system to the excitation by 4 different sinusoidal currents. All these sinusoidal currents have the same amplitude, 1 mA, but they oscillate respectively at 0.5 mHz, 2 mHz, 5 mHz and 9 mHz. In the left panel, we show the readings of the differential displacement channel to this set of four sinusoids. When exciting at 0.5 mHz the amplitude is $\sim$ 40 nm, whereas at

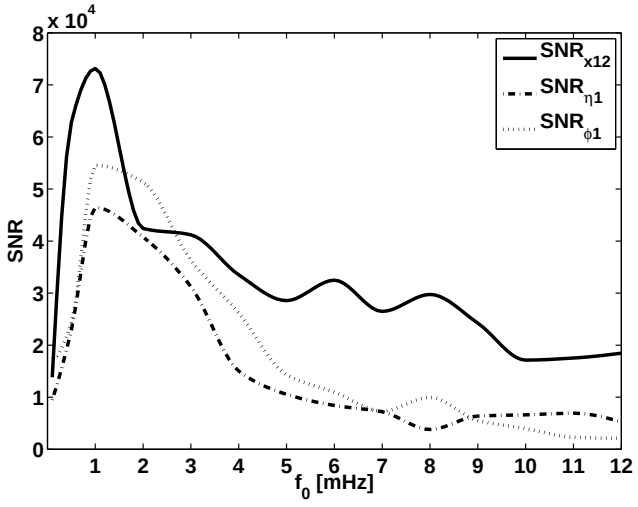

Figure 4.5: Signal-to-noise ratio as a function of frequency for each of the relevant signals of the magnetic experiment, the differential channel, x_{12} — solid line — the rotation about the y-axis, η_1 — dashed-dotted line — and the rotation about the z-axis, ϕ_1 — dotted line.

2 mHz drops to ~ 5 nm. Finally, when the frequency is 5 mHz the amplitude of the excursion is only ~ 1 nm. This same effect is observed in the right panel, where we show the Fourier analysis of these time series. As can be seen, each of the readings has a frequency component at ω_0 and a second one at $2\omega_0$, as expected. Note as well that the $2\omega_0$ components are highly attenuated with respect to the main component because they are located at higher frequencies. This simple analysis seems to indicate that the excitation frequency should be chosen around 1 mHz. However, this range of frequencies is where the uncertainty of the capacitive actuator has the largest impact on the estimates of the magnetic parameters — see Fig. 4.4 and section 4.5.1. Thus, the determination of the optimal excitation frequency should be the result of a joint optimization procedure, taking into account both the frequency dependence of the SNR and the uncertainties in the gain of the capacitive actuator.

To find the optimum excitation frequency we compute the estimation error of each of the magnetic parameters for different uncertainties of the gain of the capacitive actuator ranging from -0.2 to 0.2. We do this for different excitation frequencies across the entire measurement bandwidth. Thus, for each magnetic parameter, we compute an error function for each gain uncertainty, $e_b(\omega_0)$. Then we add quadratically each of these functions with their appropriate weight factor:

$$E(\omega_0) = \sum_b \left(\frac{1}{b} e_b(\omega_0) \right)^2 \tag{4.38}$$

where b is the uncertainty in the capacitive actuator gain, in percentage. In this way

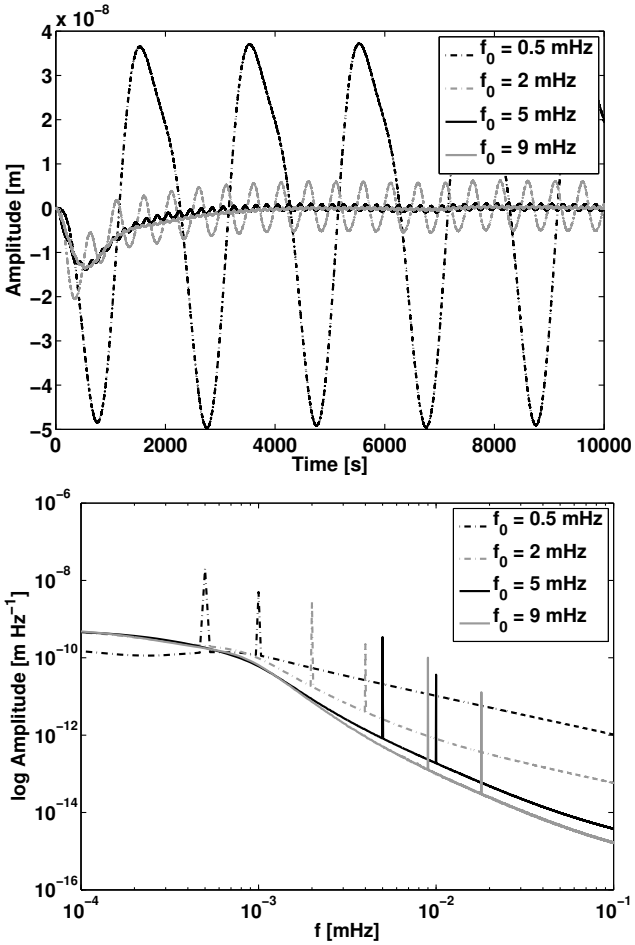

Figure 4.6: Top panel: time series of the responses detected at the differential channel of the interferometer when we inject 4 different sinusoidal signals in the onboard coils. The amplitude of these sinusoids in all the cases are 1 mA and the frequencies are respectively 0.5 mHz, 2 mHz, 5 mHz and 9 mHz. Bottom panel: Fourier analysis of the time series displayed in the left panel of this figure.

we compute a global error function for each of the magnetic parameters, $E_{M_x}(\omega_0)$, $E_{M_y}(\omega_0)$, $E_{M_z}(\omega_0)$, $E_{\chi_o}(\omega_0)$, and $E_{\chi_e}(\omega_0)$. The absolute minima of these functions correspond to the best excitation frequencies for each of the parameters.

The global error functions computed in this way are shown in Fig. 4.7 for frequencies from 0.1 mHz to 12 mHz. For the case of remanent magnetic moment the error function presents a very broad minimum between $\sim$ 5 mHz and $\sim$ 11 mHz, being the absolute minimum at $\sim$ 10 mHz. Note that at lower frequencies the global error function grows very abruptly. This occurs because, although the SNR of the experiment is larger at these frequencies, they are also very sensitive to the biases

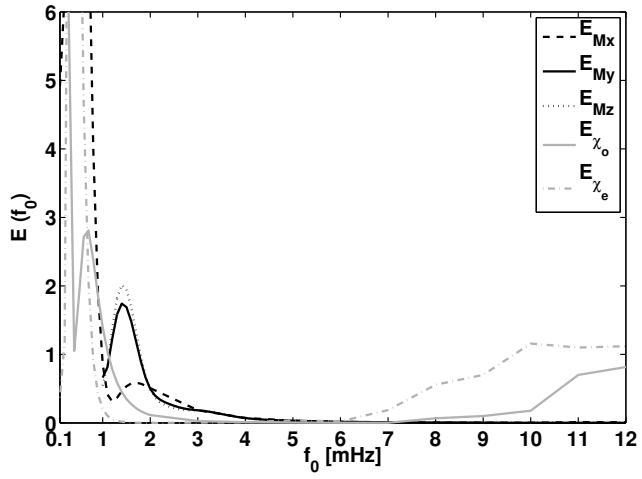

Figure 4.7: Global error functions of each of the magnetic parameters with respect to the excitation frequency. The dashed black line is the global error function for M_x — that is, $E_{M_x}(f_0)$ — the black solid line is $E_{M_y}(f_0)$, and the dotted black line corresponds to $E_{M_z}(f_0)$. Finally, the solid gray line corresponds to $E_{\chi_o}(f_0)$ and the dashed gray line to $E_{\chi_e}(f_0)$.

introduced by the actuator uncertainty. Note as well that the error functions have local minima at around 1 mHz, and also a local maximum between ~ 1.2 and ~ 2 mHz, following the sensitivity curve of the capacitive actuator — see Fig. 4.4. On the other hand, the optimal frequency needed to estimate χ_o and χ_e lies between 5 and 7 mHz. This is because these last two parameters are estimated with the $2\omega_0$ component of the x_{12} output, and higher frequencies are penalized by the larger attenuation on this frequency component. Finally, it is worth mentioning that the phase shift shown in Fig. 4.4 around 1 mHz penalizes the estimation at low frequencies, because the components at $2\omega_0$ suffer a different and unknown shift with respect to the ω_0 component. In summary, the best choice of excitation frequency is 5 mHz to estimate χ_o and χ_e and 10 mHz to estimate the three components of the magnetic moment. Nevertheless, if only one inflight experiment could be performed due to planning restrictions of the mission, the best frequency would be 5 mHz. This value is the result of minimizing the quadratic sum of the five error functions of the five parameters.

4.7 Robustness of the estimates

Finally, to conclude with our analysis we have studied the robustness of our findings. Specifically, we have tested the performance of our estimation algorithm under several circumstances. In order to model statistically its performance, we have estimated the magnetic parameters for 50 different simulated experiments and calculated the statistical distribution of the relative errors of each parameter. For example, for the

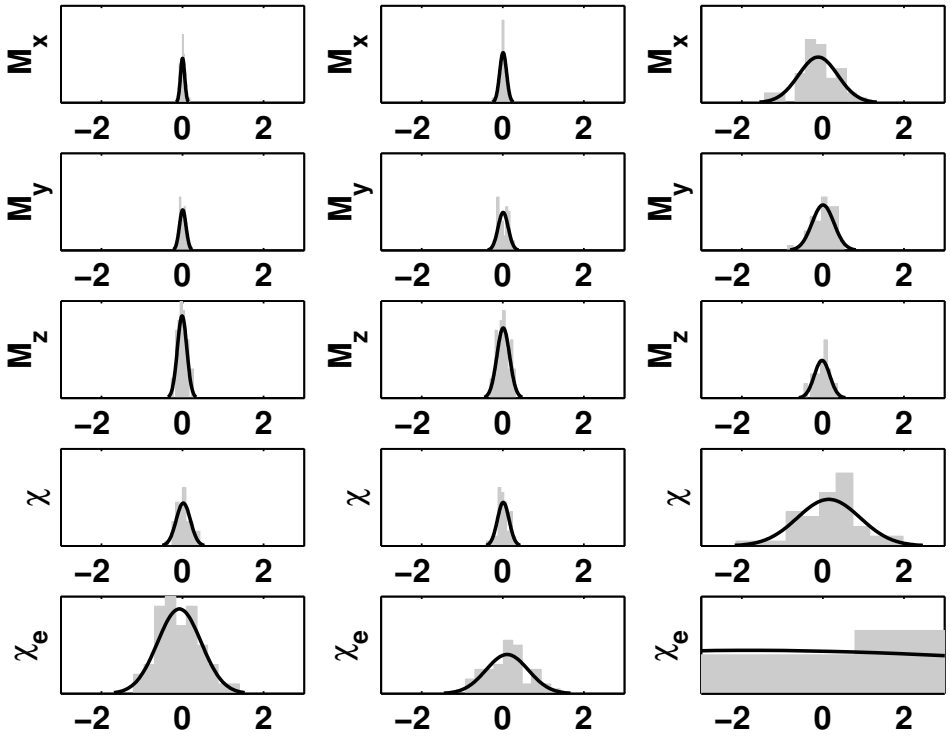

Figure 4.8: Statistical distributions of the estimates for the 5 magnetic parameters of the test masses for 3 different simulations. The left column shows the statistical distribution of these parameters when the capacitive actuator gain has no uncertainty. This simulation is done for an excitation frequency of 5 mHz. The second column shows the results when the uncertainties of the capacitive actuator gains of the principal axes are modeled with a normal distribution of zero mean and 0.01 standard deviation. This simulation is done for an excitation frequency of 5 mHz, too. Finally, the third column, shows the resulting parameter estimation for the same experiment as in the second column, but for 1 mHz. The x-axis of each subplot shows the relative error in the parameter (in percentage).

case of M_x the relative error is computed as:

$$e_{M_x} = \frac{(\hat{M}_x - M_x)}{M_x} \tag{4.39}$$

where $\hat{M}_x$ is the estimated parameter and M_x represents its true value.

Here we present the results of three different simulations. In the first simulation we excite the coils with a 5 mHz sinusoid and we consider that the gain of the capacitive actuator is the nominal one. In the second simulation we maintain the 5 mHz excitation frequency, but in this case the gains of the capacitive actuators of the three main axis are modeled with a normal random distribution of zero mean and of 0.01 standard deviation. Finally, the third simulation is only performed for

illustrative purposes. We maintain a random distribution of the uncertainty of the gain of the capacitive actuator, but we excite the coils at 1 mHz. Note that the analysis previously explained in section 4.4 concluded that this frequency should not be used. Consequently, this case clearly illustrates the effect of choosing a wrong excitation frequency.

The error distributions for each of the simulations previously described and for each of the magnetic parameters are displayed in Fig. 4.8, and their respective standard deviations are listed in Table 4.1. For consistency, these results are checked against the Cramér-Rao lower bound, which gives a lower limit for the variance of the estimated parameters (Wolberg, 2005). The Cramér-Rao bounds for each of the estimates of the magnetic parameters are listed the first row of Table 4.1. Moreover, for each of the simulations presented here we also compute the ratio of the standard deviation to the Cramér Rao lower bound. For the first simulation we obtain variances close to the Cramér-Rao lower bound, as expected due to the large SNR. In the second numerical experiment we obtain standard deviations smaller than 0.18% for all the magnetic parameters, except for χ_{e}, which is the one with the lowest SNR. In this experiment, we are still close to the optimal Cramér Rao bound because by acting at 5 mHz we minimize the effect of the capacitive actuator uncertainty. Finally for the third simulation we obtain an important degradation of the performance of the parameter estimation procedure. In particular, the standard deviations are increased by more than 1 order of magnitude. The ratio with respect to the Cramér-Rao lower bound is also clearly much larger. Particularly, the performance of the estimate of χ_{e} is totally unacceptable for this experiment, obtaining an estimation performance 25 times worse than the optimal one. Finally, comparing the second and third columns of Fig. 4.8 — and the second and third sections of Table 4.1 — we confirm that our estimation procedure delivers better results (and close to optimal) for an excitation frequency of 5 mHz than for 1 mHz, which was the frequency adopted in the preliminary design of the experiment. This clearly demonstrates the importance of choosing the appropriate excitation frequency.

However, this is not the most robust estimate that can be obtained. In particular, we suggest to use a multi-frequency estimation technique, where the properties of the test masses are computed using the results obtained at different frequencies. In this way the effects of spurious or non-modeled effects at a given specific frequency can be minimized. This can be done weighting the results obtained for each of the magnetic parameters at each frequency by the inverse of the corresponding total error function given by Eq. (4.38). For instance, for the x-component of the remanent magnetic moment we may write:

$$\hat{M}_x = \sum_{i=1}^{N} \frac{1}{E_{M_x}(\omega_i)} \hat{M}_{x_{\omega_i}} \tag{4.40}$$

where N is the total number of frequencies used, ω_i is the corresponding excitation

Table 4.1: Standard deviations of the estimated parameters for different estimation scenarios. For each of the different scenarios we calculate the ratio between the actual performance and the optimal Cramér Rao lower bound.

Run		$\Delta\hat{M}_x$	$\Delta\hat{M}_y$	$\Delta\hat{M}_z$	$\Delta\hat{\chi}_{\mathrm{o}}$	$\Delta\hat{\chi}_{\mathrm{e}}$
	CR bound	0.019%	0.046%	0.139%	0.083%	0.263%
1	σ	0.028%	0.067%	0.156%	0.084%	0.557%
	CR ratio	1.47	1.45	1.12	1.01	2.11
2	σ	0.123%	0.132%	0.162%	0.176%	0.632%
	CR ratio	6.47	2.86	1.17	2.12	2.40
3	σ	0.331%	0.215%	0.445%	0.553%	6.557%
	CR ratio	17.42	4.67	3.20	6.66	24.93

frequency, $\hat{M}_{x_{\omega_i}}$ is the estimate of M_x at ω_i and $\hat{M}_x$ is the final combined estimate. In this equation $E_{M_x}(\omega_i)$ are the weighting factors of Eq. (4.38) adequately normalized:

$$\sum_{1=1}^{N} \frac{1}{E_{M_x}(\omega_i)} = 1. \tag{4.41}$$

This estimation procedure provides an estimate of the magnetic characteristics of the test masses that takes into account all the limiting factors of the LTP instrument, and also delivers estimations which are robust to other unexpected (and not modeled) frequency dependent effects.

4.8 Summary and conclusions

In this chapter we have studied how the magnetic characteristics of the test masses onboard LISA Pathfinder can be determined. This is essential to estimate the magnetic noise contribution to the entire noise budget and, most importantly, to subtract this noise from the displacement reading. The estimation of M_x, M_y, M_z, χ_{o} and χ_{e} is done by injecting a controlled magnetic field at the position of the test masses. The field is generated by a sinusoidal current circulating through the two onboard induction coils placed at each side of both test masses. The induced magnetic field results in magnetic forces and torques on the test masses that excite their dynamics. We have shown that the force acting on the test masses has two frequencies, while the torques oscillate at single frequency, allowing to estimate the properties of the test masses by an adequate processing of three of the readings delivered by the interferometer. These readings are the differential displacement of both test masses ($o_{x_{12}}$), the rotation of test mass 1 about the y-axis (o_{η_1}) and that about the z-axis

(o_{ϕ_1}). We have also shown that the time series received from the satellite's telemetry need to be whitened and split to minimize the low-frequency effects inherent in the operation of the instrument. This way, the magnetic parameters can be estimated by a classical single-channel least-square technique once the effects produced by cross-talks are determined and corrected. Additionally, we have assessed the sensitivity of the estimation procedure to the uncertainty in the gain of the capacitive actuator of the instrument. This effect showed to be very relevant and, most importantly, it has been found to depend on the excitation frequency. Moreover, the SNR of the received signals also depends on the frequency of the injected signal. Accordingly, we have also presented a joint optimization analysis that takes into account these two factors, leading to the conclusion that the optimal excitation frequency for a joint experiment is 5 mHz. Performing the experiment at this frequency allows to estimate the magnetic characteristics without being affected by the likely uncertainty in the capacitive actuator gain. In this case we obtain parameter variances smaller than $\sim 0.18\%$ when the deviations of the gain of the capacitive actuator are $\sim 1\%$. Using all the previously explained steps and adopting this excitation frequency, the estimation turns out to be more accurate than that obtained using the preliminary design of the experiment, for which a frequency of 1 mHz was adopted. Moreover, we have suggested that a multi-frequency estimation technique could deliver estimates of the highest quality, enhancing the robustness of the experiment in front of non-modeled frequency-dependent effects. To conclude, we remark that our results provide useful insight on the design and analysis of the magnetic experiment onboard LISA Pathfinder.

Chapter 5

Interpolation of the magnetic field

In this chapter we present the studies developed to estimate the magnetic field and the magnetic field gradient inside the LTP Core Assembly (LCA) of LISA Pathfinder. In particular, we describe the characteristics of the problem, namely, we show how to infer the magnetic field at the test mass positions with measurements provided by the 4 magnetometers placed at the LCA walls. We argue that classical methods fail to perform this task and we present a new alternative based on neural networks (Díaz–Aguiló et al., 2009; Díaz-Aguiló et al., 2010)

Noise in the LTP arises as a consequence of various disturbances, mainly generated within the spacecraft itself, which limit the performance of the instrument. A number of these disturbances are monitored and dealt with by means of suitable devices, which form the so-called Diagnostics Subsystem (Araújo et al., 2007). In LPF, this includes thermal and magnetic diagnostics, plus the radiation monitor, which provides counting and spectral information on ionizing particles hitting the spacecraft. The magnetic diagnostics system will be the subject of our attention here.

One of the most important functions of the LTP magnetic diagnostics is the determination of the magnetic field and its gradient at the positions of the test masses. For this, it includes a set of four tri-axial fluxgate magnetometers, intended to measure with high precision the magnetic field at the positions they occupy in the spacecraft — see Fig. 5.1. Their readouts do not however provide a direct measurement of the magnetic field at the positions where the test masses are, and an interpolation method must therefore be implemented to calculate it. In the circumstances we face, this is a difficult problem, mostly because the magnetometers layout is such that they are too distant from the locations of the test masses compared with the typical scales of the distribution of magnetic sources in the satellite. Its solution is however imperative since magnetic noise can be as high as 40% of the total

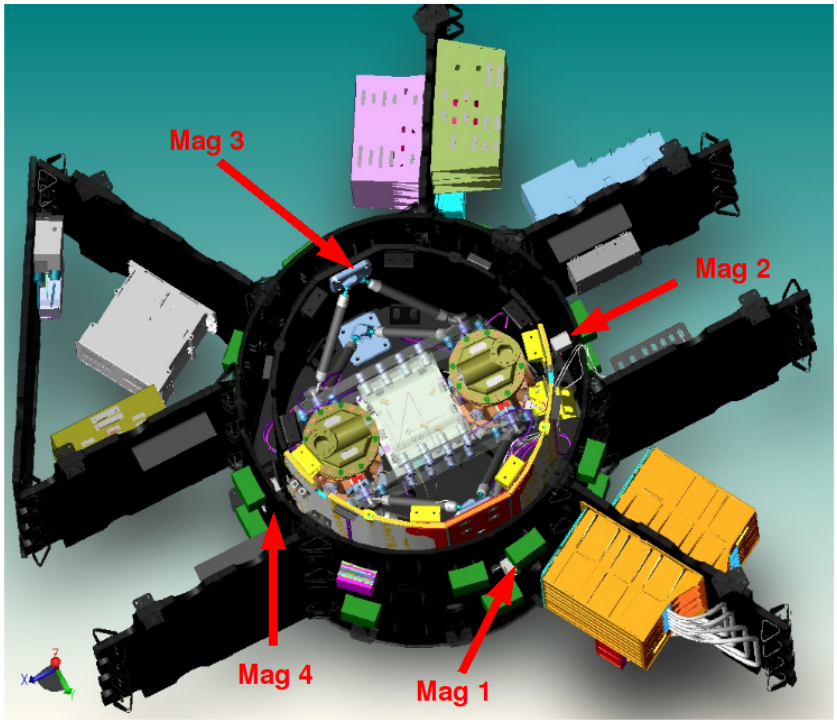

Figure 5.1: Artist view of the LPF science-craft. The LCA is in the center, surrounded by a double cylindrical shield. Outside it, a number of electronic boxes are represented, most of which are sources of magnetic field. The four magnetometers are the white little boxes indicated by the arrows (magnetometer #3 is however not visible), and are mounted on the outer cylindrical shell.

budget (Vitale, 2005) given by Eq. (2.1), and hence it must be properly quantified.

In order to design a suitable interpolation scheme, information on the actual distribution of magnetic sources is necessary. That is, we need to model the magnetic activity of each of the electronic boxes in the spacecraft and other magnetic sources such as FEEP, solar panels, batteries,... Data from the spacecraft manufacturer (EADS Astrium Stevenage, UK) have kindly been handed to us (Wealthy, 2006) for this purpose — see Appendix E. According to these data, magnetic sources can be characterized as magnetic dipoles, whose positions are known and whose magnetic moments are only known in modulus — not in orientation. Most of these dipoles are associated to electronic boxes, with a few genuinely magnetic elements, and to other spacecraft systems like the FEEP thrusters. An exception to this rule is the magnetic field of the solar panels, which cover the entire spacecraft and can hardly be considered as a dipole as seen by the magnetometers. They are however designed so that their cells are arranged to minimize magnetic effects by having their rim wires wound contiguous and in opposite senses.

Astrium data are based on system design, so validation with the real spacecraft must be done by means of experiment, which is of course included in the planned activities before launch. Actually, though, the structure of the magnetic source distribution and their properties will not be directly visible either to the magnetometers or to the interpolation algorithms, which will just work with magnetic field values no matter how they are generated. Nevertheless, we think that the information available so far, though not final, qualifies very well as a guide to the elaboration of a magnetic model which will be needed to define and verify the performance of the analysis algorithms which will eventually be applied to the data delivered by the satellite in flight.

In this chapter we will use a dipole model of the sources to assess the performance of two different types of interpolation methods: multipole interpolation and neural network algorithms. The first is the more immediate one to try, but as we will show below it is not as efficient as one might expect *a priori*. To overcome this problem we propose a novel method, based on neural networks. Based on the results obtained with the same dipole source model, our solution looks promising since the errors of the interpolated fields and gradients are significantly smaller than those obtained with the multipole approach. The chapter is structured as follows. In section 5.1 we provide a general description of the problem. It follows section 5.2, where we discuss the multipole interpolation, whereas in section 5.3 we explain our neural network approach. The results of applying these algorithms are presented in section 5.4, while in section 5.5 we summarize our major findings and we draw our conclusions.

5.1 General description of the problem

Magnetic noise in the LTP is allowed to be a significant fraction of the total mission acceleration noise: $1.2 \times 10^{-14}\,\mathrm{m\,s^{-2}\,Hz^{-1/2}}$ can be apportioned to magnetism, i.e., 40 % of the total noise, $3{\times}10^{-14}\,\mathrm{m\,s^{-2}\,Hz^{-1/2}}$, see Eq. (2.1). This noise occurs because the residual magnetization and susceptibility of the test masses couple to the surrounding magnetic field, giving rise to a force

$$\mathbf{F} = \left\langle \left[\left(\mathbf{M} + \frac{\chi}{\mu_0}\,\mathbf{B} \right) \cdot \boldsymbol{\nabla} \right] \mathbf{B} \right\rangle V \tag{5.1}$$

in each of the test masses. In this expression $\mathbf{B}$ is the magnetic field in the test mass, χ and $\mathbf{M}$ are its magnetic susceptibility and density of magnetic moment (magnetization), respectively, and V is the volume of the test mass; μ_0 is the vacuum magnetic constant, $4\pi \times 10^{-7}\,\mathrm{m\,kg\,s^{-2}\,A^{-2}}$), and $\langle \cdots \rangle$ indicates the test mass volume average of the enclosed quantity. Moreover, the magnetic field and its gradient randomly fluctuate in the regions occupied by the test masses, thus resulting in a randomly fluctuating force:

$$\delta\mathbf{F} = \left\langle \left[\left(\mathbf{M} + \frac{\chi}{\mu_0}\,\mathbf{B} \right) \cdot \delta\boldsymbol{\nabla} \right] \mathbf{B} + \frac{\chi}{\mu_0}\,\left[\delta\mathbf{B} \cdot \boldsymbol{\nabla} \right] \mathbf{B} \right\rangle V \tag{5.2}$$

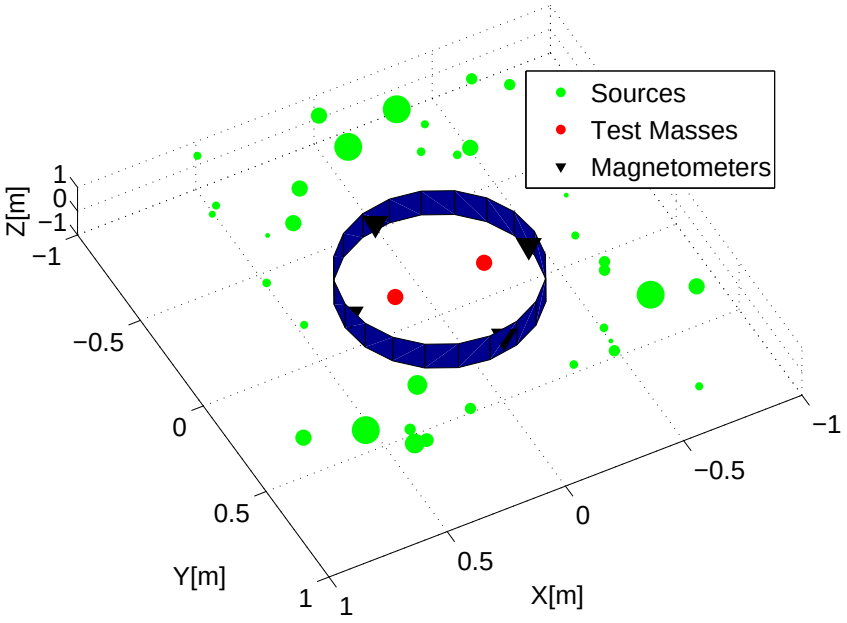

Figure 5.2: Conceptual diagram: magnetic sources (green dots, size proportional to the modulus of the magnetic moment of the source), test masses (red dots), and the four magnetometers (black triangles). Also represented (in dark blue) is the wall of the LCA.

where $\delta\mathbf{B}$ represents the fluctuation of the magnetic field, and $\delta\boldsymbol{\nabla}$ stands for the fluctuation of the gradient (Sanjuán et al., 2008).

Quantitative assessment of magnetic noise in the LTP clearly requires real-time monitoring of the magnetic field, which in LPF is done by means of a set of four tri-axial fluxgate magnetometers (Cañizares et al., 2009). These devices have a high-permeability magnetic core, which drives a design constraint to keep them somewhat far from the test masses (Lobo & Mateos, 2008). The price to be paid for this is that the measured field is not directly useful (we need to know it at the positions of the test masses). Hence, a procedure to estimate it at these positions, based on the data delivered by the magnetometers, must be set up.

As previously mentioned, the sources of magnetic field are essentially electronics boxes plus a few genuinely magnetic components inside the spacecraft. The interplanetary DC magnetic field is expected to be one order of magnitude weaker and spatially constant (see Appendix B). Their fluctuations are expected to be of similar magnitude — see Table 2.5. There are no sources of magnetic field inside the LCA, all being placed outside its walls. The number of Astrium identified sources is around 50, and can be modeled as point magnetic dipoles (Wealthy, 2006). Figure 5.2 gives an overview of the geometry, see caption for details.

5.2 Multipole interpolation

Perhaps the most immediate (and obvious) procedure to interpolate the magnetic field is to resort to its multipole structure. This is known to be the best option in some mathematical sense (Jackson, 1999). Consequently, we first describe the details of its implementation, and then we assess its practical merit.

We will treat the LCA region as a vacuum. This is a reasonable hypothesis, as the materials inside it are essentially non-magnetic. Accordingly, the magnetic field has zero divergence and rotational[1]:

$$\boldsymbol{\nabla}\cdot\mathbf{B}(\mathbf{x},t)=0 \qquad \boldsymbol{\nabla}\times\mathbf{B}(\mathbf{x},t)=0 \tag{5.3}$$

Since $\boldsymbol{\nabla}\times\mathbf{B}(\mathbf{x},t)=0$, we thus have

$$\mathbf{B}(\mathbf{x},t)=\boldsymbol{\nabla}\Psi(\mathbf{x},t) \tag{5.4}$$

where $\Psi(\mathbf{x},t)$ is a scalar function. Additionally, since $\boldsymbol{\nabla}\cdot\mathbf{B}(\mathbf{x},t)=0$, too, it immediately follows that $\Psi(\mathbf{x},t)$ is a harmonic function, or

$$\nabla^2\Psi(\mathbf{x},t)=0 \tag{5.5}$$

The solution to this equation can be expressed as an orthogonal series of the form

$$\Psi(\mathbf{x},t)=\sum_{l=0}^{\infty}\sum_{m=-l}^{l} M_{lm}(t)\, r^l\, Y_{lm}(\mathbf{n}) \tag{5.6}$$

where

$$r\equiv|\mathbf{x}|\ , \qquad \mathbf{n}\equiv\mathbf{x}/r \tag{5.7}$$

are the spherical coordinates of the field point $\mathbf{x}$, whose origin is by (arbitrary) convention assumed in the geometric center of the LCA. Eq. (5.6) could also contain terms proportional to r^{-l-1}, but these have been dropped because the field cannot diverge at the center of the LCA. Actually, the expansion of Eq. (5.6) is only valid in a region interior to the closest field source. Finally, the coefficients $M_{lm}(t)$, which will be called multipole coefficients in the sequel, depend on the sources of magnetic field.

To obtain the field components we take the derivative of Eq. (5.6) following Eq. (5.4):

$$\mathbf{B}(\mathbf{x},t)=\boldsymbol{\nabla}\Psi(\mathbf{x},t)=\sum_{l=1}^{\infty}\sum_{m=-l}^{l} M_{lm}(t)\,\boldsymbol{\nabla}[r^l\, Y_{lm}(\mathbf{n})] \tag{5.8}$$

[1] Given the distances in the spacecraft, in the order of 1 m, propagation effects will be neglected. Time dependence will therefore be purely parametric, i.e., the time variable will just label the value the field takes on at that time.

According to standard mathematics, the coefficients $M_{lm}(t)$ can be fully determined if the magnetic field is known at the boundary of the volume where the field equations are considered, in this case the LCA. This data is of course not available to us, since we only know $\mathbf{B}$ in four points of the boundary, where the magnetometers are. Therefore the question we need to address is: how many terms of the series can we possibly determine on the basis of the limited information available? Or, equivalently, how many multipole coefficients can we estimate, given the magnetometers readout data? Then, also, to which accuracy can we estimate the actual magnetic field after the maximum number of multipole coefficients have been calculated?

The answer to the first question above is actually not difficult: let us assume that the series in Eq. (5.8) is truncated after a maximum multipole index value $l = L$. The estimated field, $\mathbf{B}_\mathrm{e}$, is then given by:

$$\mathbf{B}_\mathrm{e}(\mathbf{x}, t) = \sum_{l=1}^{L} \sum_{m=-l}^{l} M_{lm}(t)\, \boldsymbol{\nabla}[r^l\, Y_{lm}(\mathbf{n})] \tag{5.9}$$

The number of terms in this sum is

$$N(L) = \sum_{l=1}^{L} (2l+1) = L(L+2) \tag{5.10}$$

which obviously equals the number of multipole coefficients needed to evaluate the sum. For example, we have $N(2) = 8$ and $N(3) = 15$. On the other hand, the number of magnetometer data channels is 12 — three channels per magnetometer, as the devices are tri-axial. This means we cannot push the series beyond the quadrupole ($l = 2$) terms. This means that since we only have 12 data channels we have some redundancy to determine the first eight $M_{lm}(t)$ coefficients up to $l = 2$, though we also lack information to evaluate the next seven octupole terms[2].

In order to make a best estimate of the $M_{lm}(t)$, a least-square method is set up as follows. Firstly, we define a quadratic error:

$$\varepsilon^2(M_{lm}) = \sum_{s=1}^{4} |\mathbf{B}_\mathrm{r}(\mathbf{x}_s, t) - \mathbf{B}_\mathrm{e}(\mathbf{x}_s, t)|^2 \tag{5.11}$$

where $\mathbf{B}_\mathrm{r}$ is the real magnetic field and the sum extends over the number of magnetometers, situated at positions $\mathbf{x}_s$ ($s = 1,\ldots,4$). We then find those values of M_{lm} which minimize the error:

$$\frac{\partial \varepsilon^2}{\partial M_{lm}} = 0 \tag{5.12}$$

[2] A clarification is in order here. The multipole coefficients $M_{lm}(t)$ are actually complex numbers, which may mislead one into inferring that actually fewer can be calculated. This is however not so because of the symmetry $M_{lm}(t) = (-1)^m M^*_{l,-m}(t)$, which ensures that $\mathbf{B}(\mathbf{x}, t)$ is actually a real number.

Once this system of equations is solved, the estimated coefficients $M_{lm}(t)$ are replaced back into Eq. (5.9) and then the spatial arguments $\mathbf{x}$ substituted by the positions of each test mass to finally obtain the interpolated field values. This process needs to be repeated for each instant t of time at which measurements are taken, thereby generating the magnetic field time series. The gradient is estimated by taking the derivatives of Eq. (5.9):

$$\left.\frac{\partial B_i}{\partial x_j}\right|_{\mathrm{e}}(\mathbf{x},t) = \sum_{l=0}^{L}\sum_{m=-l}^{l} M_{lm}(t)\,\frac{\partial^2}{\partial x_i \partial x_j}\left[r^l\, Y_{lm}(\mathbf{n})\right] \tag{5.13}$$

It is to be noted that Eq. (5.9) is a polynomial of degree $L-1$ in the space coordinates (x, y, z), hence its degree equals 1 when $L=2$. Since this is the most we can get of the magnetometer readout channels, the multipole expansion is actually equivalent to a *linear* interpolation of the field between its values at the boundary of the LCA and its interior. We may therefore not expect this method to produce excellent results, simply because the magnetic field inside the LCA is weaker than at its boundaries, the reason being that the magnetic field sources are outside the LCA. This valley structure of the magnetic field needs at least octupole (quadratic) terms to be approximated, but this would require at least one more vector magnetometer, which is not available. By the same argument, the field gradient can only be approximated by a *constant* value throughout the LCA — see Eq. (5.13).

5.2.1 Numerical simulations

In order to have a quantitative idea of the actual performance of the above interpolation scheme, we make use of the source dipole model. It has the following ingredients and assumptions:

1. The sources of magnetic field are point dipoles outside the LCA.

2. The sources are those identified by Astrium Stevenage, as already mentioned, whose positions in the spacecraft are known. The set itself, as well as the source magnetic parameters need to be updated, but the data used (which date back to November 2006) qualifies to verify the performance of the interpolation methods. The listing of these sources is shown in Appendix E.

3. The magnetic field created by the dipole distribution at a generic point $\mathbf{x}$ and time t is therefore given by

$$\mathbf{B}(\mathbf{x},t) = \frac{\mu_0}{4\pi}\sum_{a=1}^{n}\frac{3\left[\mathbf{m}_a(t)\cdot\mathbf{n}_a\right]\,\mathbf{n}_a - \mathbf{m}_a(t)}{\left|\mathbf{x}-\mathbf{x}_a\right|^3} \tag{5.14}$$

   where $\mathbf{n}_a = (\mathbf{x}-\mathbf{x}_a)/|\mathbf{x}-\mathbf{x}_a|$ are unit vectors connecting the a-th dipole $\mathbf{m}_a$ with the field point $\mathbf{x}$, and n is the number of dipoles.

4. Fluctuations of the dipoles, both in modulus and direction, are unknown, but this is not essential to assess the numerical performance of the algorithm.

We aim to compare interpolated magnetic field results with exact ones within the context and scope of the above model. To artificially simulate several possible scenarios, we will take advantage of the uncertainties in the source dipole orientations to randomly generate different magnetic field patterns, which we intend to reconstruct based on the multipole expansion. More specifically, the procedure is the following one:

1. Each dipole has a known fixed position in the spacecraft, and a fixed modulus, also known. The number of magnetic dipoles is also fixed to 46, which is the number in Astrium's list.

2. The orientations of the dipoles are instead unknown. An example scenario is characterized by a specific selection of the 46 dipole orientations.

3. In order to explore the behavior of the algorithm, a batch of examples are examined, each corresponding to a randomly generated set of dipole orientations.

4. In each case, Eq. (5.12) is solved for M_{lm}, and the field estimate at each test mass is then calculated with Eq. (5.9). In the last step, the result is compared with the theoretical one given in Eq. (5.14), and the differences annotated.

5. Finally, a statistical analysis of the differences (errors) is done.

The random character of the procedure may seem unrealistic, since the actual satellite configuration is not random. In this context, however, randomness is an efficient way of mimicking lack of knowledge. As we will see in the next section, numerical analysis based on this methodology sheds much light on the merits of the interpolation procedure — as it will also be the case when we come to neural networks performance in section 5.4.

Simulation results

In this section we summarize the most relevant results of the analysis of the multipole interpolation method. We use a batch of 1 000 example scenarios such as described above. Magnetic moment orientations were chosen by randomly picking values of the two defining spherical angles (θ, φ) from two independent uniform distributions.

Fig. 5.3 graphically represents a magnetic field map in the LCA region corresponding to an arbitrarily chosen example out of the 1 000 considered. The valley structure is very clear in the $|\mathbf{B}|$ plot, while the B_x component shows a saddle shape — see figure caption. B_y and B_z show qualitatively similar forms, and thus we do not show them. The elliptical forms in the estimate of $|\mathbf{B}|$ are due to the quadratic

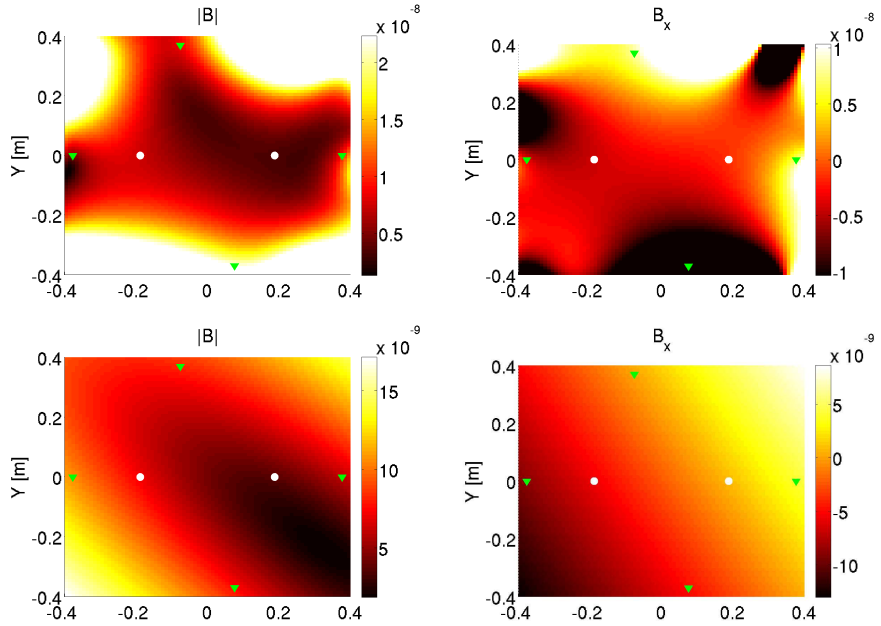

Figure 5.3: Magnetic field contour plots in the LCA region for a given source dipole configuration. x is the direction between the two test masses, and y is in the "horizontal" plane, which in the plot is at the test masses centers of mass altitude. Left panels: moduli of the magnetic field. The top panel displays the exact one, and the bottom one shows its multipole estimate. Right panels: same as in the left panels, but for one of the field components (B_x). The modulus of the magnetic field shows a complex structure in the central area, while B_x has a saddle structure there — see along the diagonals of the graph frame. The white dots mark the centers of the test masses, and the green triangles the positions of the magnetometers.

combination of the field components. The estimate of B_x shows instead a linear structure, with constant gradient in all directions. Naked eye inspection immediately reveals a poor resemblance between estimated and exact quantities, but let us elaborate some numerical data.

Fig. 5.4 displays the binned distribution of estimation errors, defined by

$$\varepsilon(|\mathbf{B}|) = \frac{|\mathbf{B}_\mathrm{e}| - |\mathbf{B}_\mathrm{r}|}{|\mathbf{B}_\mathrm{r}|} \ , \quad \varepsilon(B_x) = \frac{B_{x,\mathrm{e}} - B_{x,\mathrm{r}}}{|\mathbf{B}_\mathrm{r}|} \tag{5.15}$$

where we have used a denominator $|\mathbf{B}_\mathrm{r}|$ in $\varepsilon(B_x)$ to avoid meaningless infinities when B_x is close to zero. B_y and B_z show similar trends and are not displayed. As can be seen, errors average to zero, but have rms deviations well above 100%. Even worse, outliers are significant, as can be seen in Table 5.1, where averaged absolute values over the 1 000 simulated cases are displayed. Except, obviously, for the modulus error, we are around 500%, but detailed examination of individual data

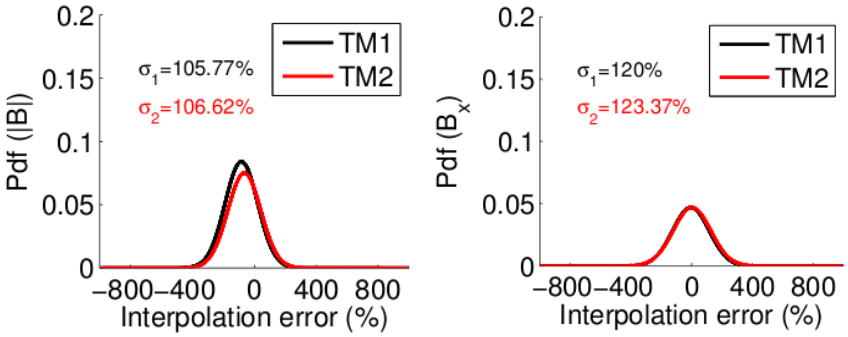

Figure 5.4: Binned errors of the estimated modulus of the magnetic field and of its x component. They are reported in percentage. Colors correspond to each of the LTP test masses, respectively. Inset values of σ indicate the r.m.s. half-width of the distributions. Solid lines are Gaussian fits to the histograms.

Table 5.1: Averaged absolute value of the estimation errors in the components of the magnetic field and of its modulus. They are reported in relative percent.

	TM1	TM2
$\varepsilon(B_x)$	493.7	640.4
$\varepsilon(B_y)$	330.5	543.1
$\varepsilon(B_z)$	359.5	368.2
$\varepsilon(\|\mathbf{B}\|)$	88.6	75.7

further shows that errors as high as 2 000% eventually happen.

The most salient features of the numerical analysis can be briefly summarized. Firstly we find that magnetic field estimation errors are very variable, ranging from very few percent to over 1 000 % and, secondly, these huge uncertainties happen in an utterly random and fully unpredictable way. The *a posteriori* conclusion is quite simple: the intrinsic linear character of the interpolation scheme is not capable of reproducing the field structure inside the LCA — hence at the positions of the test masses — and, therefore, can produce very good or very bad results just by accident. In addition to not being predictable, the average error is any case too large. The ultimate reason for such poor performance is the small number of magnetometers as well as their positioning: four magnetometers only allow for a field multipole expansion up to quadrupole terms, which means that the field values at the test masses are just linearly interpolated between magnetometer readouts at the boundary of the LCA. On the other hand, the magnetometers are closer to the magnetic field sources than they are to the test masses, which prevents resolution of the spatial field structure details inside the LCA with only linear terms in the space coordinates.

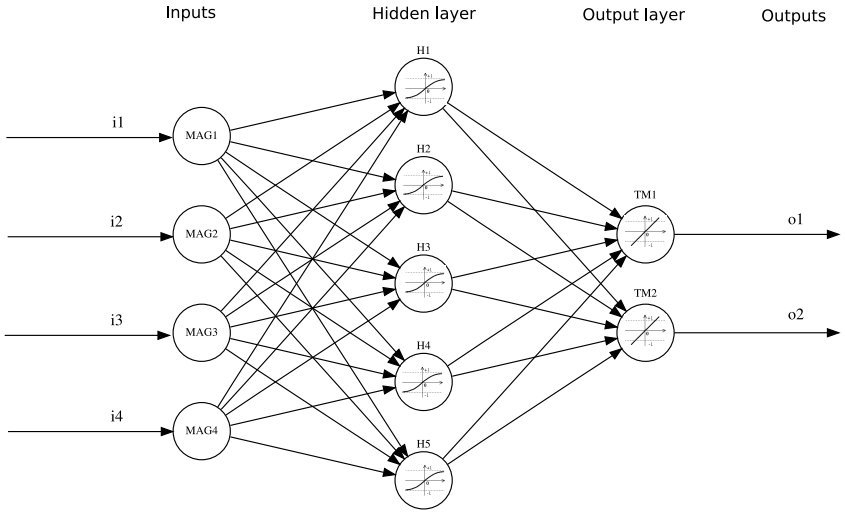

Figure 5.5: Feed-forward neural network architecture. Magnetometers readings are the system inputs, and estimates of the field and gradient at the positions of the test masses are the outputs of the system. In this architecture, only one intermediate, or hidden layer is assumed. Each of the circles represents one neuron and corresponds to the model of Eqs. (5.16) and (5.17).

5.3 A novel alternative approach: neural networks

Search for an alternative approach to the above interpolation schemes is imperative, otherwise the information provided by the magnetometers will hardly be useful for the main goal of the LTP magnetic diagnostics system, i.e., to quantify the contribution of the magnetic noise to the total system noise. Here some promising results are presented on the implementation of a completely different methodology: neural networks (Kecman, 2001).

Artificial neural networks are made up of interconnecting artificial neurons (programming constructs that mimic the properties of biological neurons) that have the capacity to learn from processing data. Neural networks are often used in solving nonlinear classification and regression tasks by learning from data, hence are worth trying with the present problem (Serpico & Visone, 1998).

There are four sets of tasks which need to be implemented when solving a problem with artificial neural networks:

1. Neuron model selection

2. Model and architecture selection

3. Learning paradigm and learning algorithm selection

4. Performance assessment

We next go through them, one by one.

5.3.1 Neuron model

The neuron is the basic unit of any neural network. It performs the following two operations:

- It collects the inputs from all other neurons connected to it and computes a weighted sum of the signals the latter inject into it, generally adding a bias as well. If we represent the inputs by a vector $\mathbf{x} \equiv (x_1, \ldots, x_n)$, and the weights by a $\mathbf{w} \equiv (x_1, \ldots, w_n)$ then this operation consists in calculating the sum

$$\Sigma = w_0 + \sum_{k=1}^{n} w_k x_k \equiv w_0 + \mathbf{w}^T \mathbf{x} \tag{5.16}$$

  where the superindex T stands for transpose matrix; in this case, $\mathbf{w}^T$ is a row vector while $\mathbf{x}$ is a column vector, so that $\mathbf{w}^T\mathbf{x}$ is the scalar product of $\mathbf{w}$ and $\mathbf{x}$. A term w_0 is added to form the most general linear function of the vector argument $\mathbf{x}$; it is called the bias.

- The above sum is used as the argument to the so-called activation function, $\varphi(\Sigma)$. The neuron's output, also known as its activation, is thus

$$o = \varphi(\Sigma) \tag{5.17}$$

  In general, $\varphi(\Sigma)$ can be selected in many different ways. Here, differentiable activation functions will be used, which suit well the gradient descent back-propagation learning algorithm — see sections below.

5.3.2 Neural network architecture

Artificial neural networks are software or hardware models inspired by the structure and behavior of biological systems, and they are created by a set of neurons distributed in layers. There are many different types of neural networks in use today, but the architecture of a so-called feed-forward network, where each layer of neurons is linked with the next by means of a set of weights, is the most commonly used, and will also be used here. The specific architecture adopted in this study is shown in Fig. 5.5. The data streams coming from the magnetometers will be considered the system inputs, while magnetic field results and their gradients at the positions of the test masses will be the system outputs.

5.3.3 Learning paradigms and learning/training algorithms

The investigation of learning algorithms is currently an active field of research. The design and implementation of an adequate training scheme is the essential ingredient for obtaining a good-quality estimate of the magnetic field and its gradient at the LTP test masses.

Learning paradigms

There are two major learning paradigms, each corresponding to a particular abstract learning task. These are *supervised learning* and *unsupervised learning*.

1. *Supervised learning*. The idea of this paradigm is quite clearly suggested by its very name. A set of examples is filed, each set consisting in a number of vector of inputs (the magnetometers' readouts in this case) and the corresponding values of the magnetic field and its gradient at the test masses for a given distribution of dipoles in the spacecraft. Let $\mathbf{x}$ represent a generic input vector, and $\mathbf{y}$ the associated vector output. These two vectors constitute an example. The set of filed examples for supervised learning is thus a set of pairs ($\mathbf{x}$,$\mathbf{y}$), where $\mathbf{x}\in X$ and $\mathbf{y}\in Y$, X and Y being some suitable sample spaces. The network is then fed the inputs $\mathbf{x}$ of one example and let it work out an output, $\mathbf{o}$, say. This output is then compared with the correct one, $\mathbf{y}$, and an error is calculated if $\mathbf{o}\neq\mathbf{y}$. Iterations are then triggered to adjust the weighting factors such that the error is minimized. These will however vary as different examples are run, so a cost function is defined which enables the network to optimize the set of weights which works best for the set of examples analyzed, based on some suitable criterion.

2. *Unsupervised learning*. In unsupervised learning a cost function is to be minimized as well, but this function can be any relationship between $\mathbf{x}$ and the network output, $\mathbf{o}$, but never taking into account the real expected target. The cost function is determined by the task formulation. Unsupervised learning is thus a form of self-adaptive system, whose guide is not an *a priori* knowledge of the final result but knowledge gained from experience.

In either case, the learning process is based on the architecture of the network, i.e., number of neurons and layers and their interconnections, as well as on the activation functions. These are parameters which, at least in the simplest cases, are tuned *ab initio* by the user based on observed performance of the network. In this study, supervised learning has been the implemented learning paradigm for the magnetic field interpolation, whereas unsupervised learning will be used in chapter 6 to discern between different operational modes.

Learning algorithms

There are many algorithms for training neural networks. When training feed-forward neural networks with supervised learning, a back-propagation algorithm is usually implemented. The error of the mapping at the output is propagated backwards in order to readjust the weights and improve the output error for the next iteration. The propagation can be implemented with different methods, the *Ideal Gradient Descent* being a classic which will also be used here, with slight modifications that make the algorithm convergence faster (see Appendix F for further details).

Iterations on the weights of the different neurons at the different layers proceed according to the following algorithm:

$$\mathbf{w}_{n+1} = \mathbf{w}_n - \eta \left.\frac{\partial E}{\partial \mathbf{w}}\right|_n \tag{5.18}$$

where n labels the current iteration step, and η is the learning rate, adjustable by the user. E is the sum over the set of training examples of the square errors of the outputs:

$$E = \sum_s (\mathbf{o} - \mathbf{y})^T (\mathbf{o} - \mathbf{y}) \tag{5.19}$$

where s stands for the number of examples, $\mathbf{o}$ is the (vector) output from the network, while $\mathbf{y}$ is the target, or correct output in the corresponding example. The quantity E can only be defined in supervised learning, of course, and the idea of the above procedure is to find that point in weight space where E is an absolute minimum. E can therefore be considered the cost function to be minimized in this particular supervised training scheme, also known as *batch mode* as the analysis is done across the entire set of training patterns in a single block.

There are a number of technical issues in pursuing the iterations in Eq. (5.18), such as the choice of the initial set of weights, the identification of local minima of E, the boundary effects, etc, which need to be addressed for each specific application. For further details, the reader is referred to Kecman (2001), Reed (1993) and Dreyfus (2005).

5.3.4 Performance assessment

In this last step, the trained network must be tested with examples which differ from those used in the learning process. This is needed to assess whether or not the trained neural network is able to generate the expected results when fed with previously unseen inputs, hence determine its usability for the specific purpose it is intended.

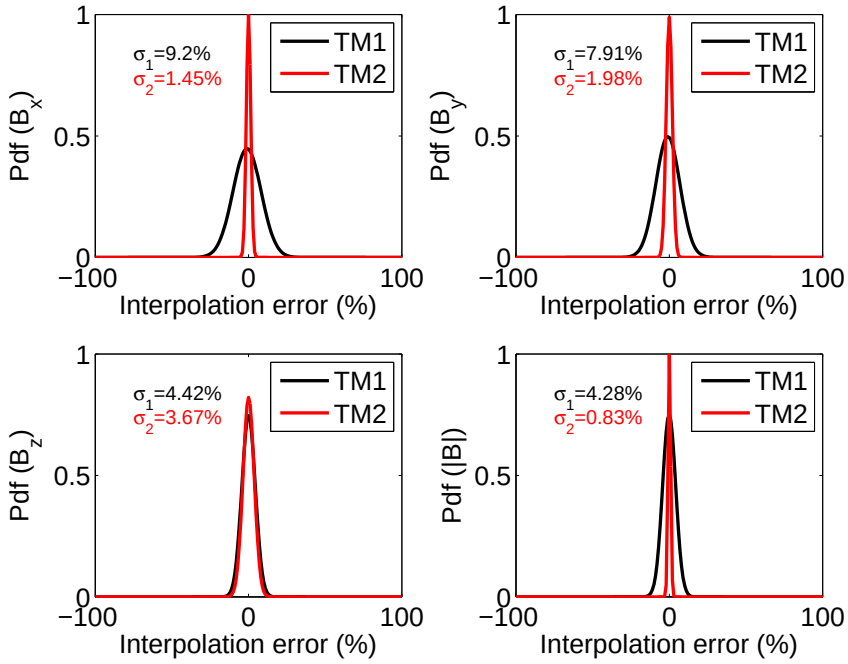

Figure 5.6: Error distributions for each field component at the position of test mass 1 (black line) and test mass 2 (red line). The top left panel displays the results for B_x, the top right panel shows the error distribution for B_y, while the bottom left panel depicts the distribution obtained for B_z and the bottom right panel that for $|\mathbf{B}|$.

5.4 Results

Training and testing have been done based on different field realizations, using the same model of sources and magnetic field described in section 5.2.1, i.e., each *example* will consist in the magnetic field at the magnetometers' positions, plus the magnetic field and gradient at the positions of the test masses, all of them corresponding to a given configuration of the 46 Astrium dipoles.

Two different batches of examples, each including 1 000 realizations of a possible magnetic environment, have been generated following the directives explained in section 5.2.1. The first batch has been used as the training set for a neural network with 12 inputs (3 inputs for each of the 4 vector magnetometers) and 16 outputs representing the field information at the position of the two test masses (3 field values plus 5 gradient components per test mass[3]). The second batch has been used for validation to assess the performance of the network in front of unseen magnetometers readings.

[3]Note that only 5 of the 9 gradient components $\partial B_i/\partial x_j$ are independent. This is because the conditions of Eq. (5.3) imply that $\partial B_i/\partial x_j$ is a traceless and symmetric matrix.

5.4.1 Field estimation

Fig. 5.6 shows the distribution of relative errors (in percentage) of the estimated components of the magnetic field at the positions of each test mass. The plot is based on the results of the 1 000 validation runs described in the previous section. As can be observed, the order of magnitude of the errors of the estimated fields are now within much more acceptable margins (below $\sim 10\%$). This represents a reduction of estimation errors of more than one order of magnitude in comparison with the multipole expansion method.

During the training process, the neural network eventually learns that the magnetic field at the test masses is generally smaller than the magnetometers read — with occasional exceptions due to the rich and complex structure of the field inside the LCA, see e.g. Fig. 5.3. The neural network is able to derive an inference procedure which is actually quite efficient, and it does so by proper adjustment of its weight matrix coefficients $\mathbf{w}$ as explained in section 5.3.3. In order to better understand the reaction of the trained neural network to the magnetometers' data, we found instructive and expedient to look into relationships between the data read by the magnetometers and the magnetic field estimates generated at the output of the neural network. We chose to calculate correlation coefficients between input and output data, and the results are displayed in Fig. 5.7. The following major features are identified:

- Each component of the field is basically estimated from the magnetometers reading of the same component. For example, the interpolation of the B_x component in test mass 1 is mostly dependent on the B_x readings of the magnetometers.

- The measurements of the magnetometers closer to the interpolation points have larger weights. For instance, when the field is estimated at the position of test mass 1, to which M4 is the closest magnetometer, the value it measures is the largest contributor to the interpolated field in test mass 1. At the same time, M1 and M3 being nearly equidistant from both test masses, their weights are almost identical.

5.4.2 Gradient interpolation

The magnetic field gradient can also be estimated. The 9 components $\partial B_i/\partial B_j$ of the gradient are not independent, since they must verify Eqs. (5.3), which reduce their number to 5. The remaining 4 components can be easily calculated thereafter. Another option is to estimate the 9 gradient components regardless of the previously mentioned constraint, in which case they are actually found not to satisfy them. Discrepancies are however within the estimation error range, so we do not adopt this

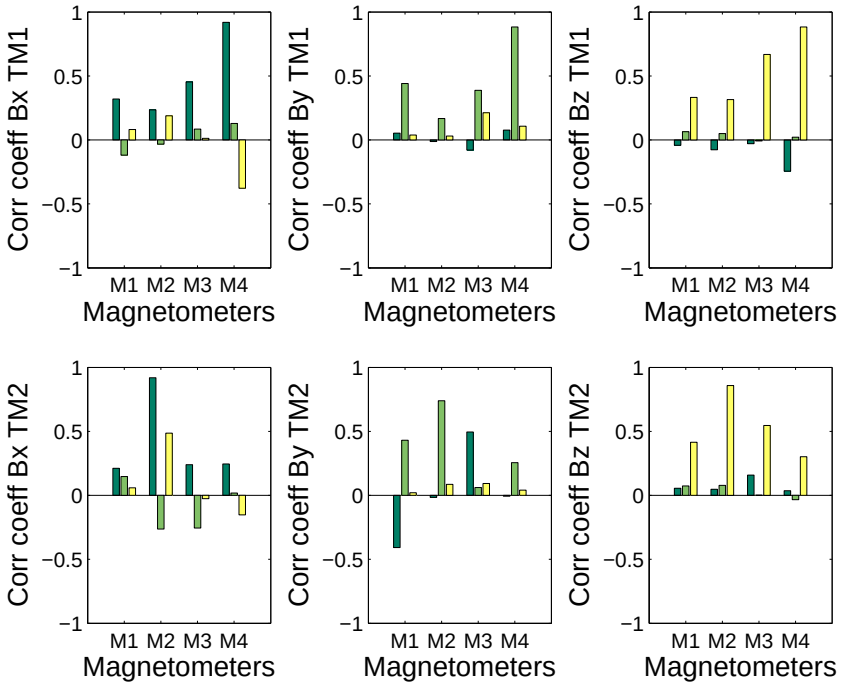

Figure 5.7: Correlation coefficient between the information entering the network (each magnetometer input) and the outputs provided by the trained network for the field estimates. Dark green bars correspond to the weights multiplying each of the x-component of the corresponding magnetometer reading, whereas light green bars and yellow bars correspond to the weights multiplying the y- and z- components respectively.

option here as it is slightly more cumbersome due to the correspondingly increased complexity of the network.

Results on gradient estimation are shown in Fig. 5.8 for $\boldsymbol{\nabla} B_x$ at the positions of both test masses. As can be observed, they are also within much more acceptable margins than the earlier interpolation approach could possibly produce. It is to be noted that no apparent or easily deductible physical relationship is found between the estimated gradient at the test mass positions and the magnetometer inputs, in contrast with what we have found for the field estimation.

5.4.3 Statistical analysis

In Table 5.2 we present a statistical comparison of the properties of the distribution of interpolated magnetic fields. For the sake of conciseness we only list the statistical properties of the interpolated modulus and x-component of the magnetic field. In particular, we show the standard deviation (σ) of the interpolating errors for both the multipole interpolation and the neural network estimate, the skewness

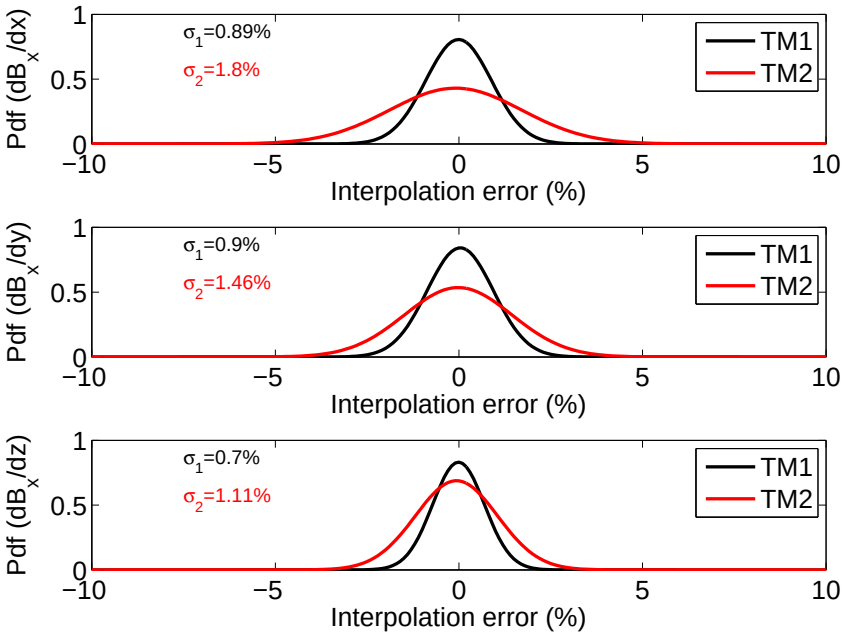

Figure 5.8: Probability density function of the errors distribution for the three components of $\boldsymbol{\nabla} B_x$. From top to bottom: $\partial B_x/\partial x$, $\partial B_x/\partial y$ and $\partial B_x/\partial z$ at the positions of the test masses. Errors are given in percentages, the black lines corresponding to test mass 1, and the red ones to test mass 2.

of the distribution (γ_1) and the corresponding kurtosis (γ_2). Clearly, and as already mentioned, the interpolating errors are very large for the case in which a multipole interpolating scheme is used, as clearly shown by the very large standard deviation obtained when using this method. Also interesting to note is that for the case of the x-component of the magnetic field both methods yield distributions which are almost symmetrical (low values of skewness). However, this is not the case for the modulus of the magnetic field when the multipole interpolating method is used. Finally, the kurtosis of the multipole interpolation is very large, revealing a large number of outliers. All in all, a look at Table 5.2 reveals that the neural network method presents much better statistical properties than the multipole interpolation.

5.5 Conclusions

The magnetic diagnostics sensor set in the LTP is such that to infer the magnetic field and gradient at the positions of the test masses based on the readouts of the magnetometers is far from simple. The more standard interpolation scheme, based on a multipole expansion of the magnetic field inside the LCA volume, cannot go beyond quadrupole order which, in practice, means that just a linear approximation

Table 5.2: Statistical properties of the distribution of errors of the interpolated magnetic field.

	σ	γ_1	γ_2
	Multipole interpolation		
B_x(TM1)	130.7583	-0.2782	19.3869
B_x(TM2)	128.3601	-0.1009	21.4974
$\|\mathbf{B}\|$(TM1)	105.5386	-3.6770	29.7343
$\|\mathbf{B}\|$(TM2)	102.1037	-4.4770	38.0686
	Neural network interpolation		
B_x(TM1)	1.5204	-0.0028	2.7746
B_x(TM2)	1.6260	-0.0008	2.8626
$\|\mathbf{B}\|$(TM1)	1.4464	-0.1014	2.9440
$\|\mathbf{B}\|$(TM2)	1.3682	-0.0969	2.9905

can be done, due to the reduced number of magnetometers available. This grossly fails to produce reliable results, with errors exceedingly large. This has motivated our search for better alternatives. Artificial neural networks have been presented as a more elaborate procedure to estimate the required field values at the positions of the test masses. In this chapter we have presented results which very significantly improve the performance of the multipole expansion technique by almost two orders of magnitude. This a very encouraging outcome which points to the use of the neural networks as the baseline tool to analyze LTP magnetic data.

One of the main problems of using the neural network to assess the magnetic field at the positions of the test masses is to find a training process adequate to the set of data that the magnetometers will deliver in flight. This underlines the need to characterize on ground to our best ability the magnetic field distribution across the LCA for as many as possible foreseeable working conditions, both regarding DC and fluctuating values. Reliable information on this is essential for a meaningful assessment of magnetic noise in the LTP. However, the neural network analyses presented in this chapter only apply to static fields. What they actually show is that neural networks work very well (always below $\sim 10\%$ accuracies and with standard deviations at the 2% level) no matter which the source dipole configuration is. We have performed a study of the underlying structures of the neural network and we have found that the ability of our interpolating scheme to recover the correct values of the magnetic field and gradients at the positions of the test masses is due to the fact that the neural network is able to learn from the readings of the magnetometers which are closest to the corresponding test mass, and that the most important contribution for each component field comes from the corresponding magnetome-

ter reading. Although very intuitive, this underlying relationship is not resolved by classical interpolation methods. A different issue is how to deal with time series of magnetometer readouts, which is of course the kind of data the satellite will transmit to ground. Features such as varying environmental conditions, field fluctuations, etc will likely happen during mission operations, and the neural network algorithm must be trained to properly deal with them. These results and a more in depth analysis of the robustness of the system are presented in the following chapter.

Chapter 6

The robustness of the magnetic field interpolation method

In this chapter we elaborate on the studies presented in chapter 5. Specifically, we analyze the accuracy, the precision and the robustness of the neural network used to interpolate the magnetic field and its gradient. In particular, we study if the architecture of the neural network is optimal. Moreover, we also assess its behavior under several circumstances of interest. Among other, we explicitly mention possible offsets in the magnetometer readings, small deviations from the nominal positions of the magnetometer heads, or varying environmental conditions (Díaz-Aguiló et al., 2011b). This is done in sections 6.1 to 6.6. Additionally, we also introduce a method to detect changes in the operational mode of the LTP. This method is thoroughly explained in section 6.7, where we present a hybrid architecture that allows the Magnetic Diagnostics Subsystem to act autonomously to choose the appropriate interpolation model and deliver accurate outputs for each operational scenario.

6.1 Introduction

We have already shown (Díaz-Aguiló et al., 2010) — see also chapter 5 — that the standard interpolation scheme, which is based in multipole expansion of the magnetic field inside the LCA volume, does not go beyond quadrupole order. Thus, its performance in estimating the magnetic field and its gradients is very poor. On the contrary, artificial neural networks have been shown to be a reliable alternative to estimate the required field and gradient values at the positions of the test masses. The reasons for this are multiple. Firstly, the multipole expansion only takes into account the readings of the magnetometers, whereas the artificial neural network also uses the actual value of the magnetic field at the position of the test masses to train the network. This is a crucial issue since the interpolation algorithm is fed with additional information. Secondly, the classical interpolation method seeks for

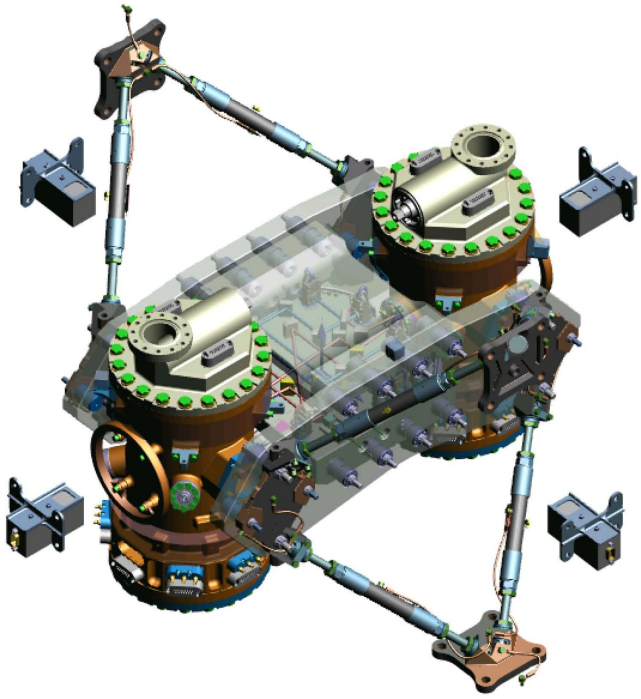

Figure 6.1: A schematic view of the payload of LISA Pathfinder, the LTP. The relative position of the 4 tri-axial magnetometers (the four grey floating boxes) with respect to the position of the test masses (located at the center of the two inertial sensors towers) is shown. Their exact positions are reported in Table 6.1.

a global solution of the magnetic field. That is, the multipole expansion models the magnetic field inside the entire volume of the LCA. Clearly, since the available information for the multipole expansion is rather limited, the quality of the global solution is very poor. In sharp contrast, the artificial neural network first finds and then uses the correlation between the magnetic field at the positions of the magnetometers and the test masses to obtain reliable values of the magnetic field for any magnetic configuration. As a matter of fact, the artificial neural network performs a point-to-point interpolation and it is not aimed at reproducing the highly non-linear magnetic field well at any arbitrary position within the volume of the LCA. Finally, artificial neural networks are trained using a large number of magnetic field realizations, thus the interpolating algorithm uses a statistically elaborated information. In this sense, it is important to realize that artificial neural networks have been shown to be a robust and easily implementable technique among numerous statistical modeling tools (Kecman, 2001). On the contrary, the multipole expansion does not use statistical information. Once the readings of the magnetometers are known, the theoretical solution for the magnetic field within the entire volume of the

LCA is determined in a straightforward way.

Nevertheless, an in depth study of how the results of the interpolation procedure depend on the specific characteristics of the neural network remains to be done. It also remains to further investigate why the neural network obtains such good results interpolating the value of the magnetic field at the positions of the test masses, which are well inside a deep well of magnetic field. Finally, an assessment of the robustness of the neural network interpolating scheme in front of the unavoidable errors in the positions of the magnetometers, or in front of low-frequency variations of the magnetic environment and, more importantly, in front of offsets in the readings of the magnetometers still is needed. These are precisely the goals of this chapter.

The chapter is organized as follows. In section 6.2 we discuss the appropriateness of our neural network approach to measure the magnetic field and its gradients at the positions of the test masses, and we discuss which are the accuracies obtained when different architectures of the neural network are adopted. It follows section 6.3, where we discuss how the unavoidable errors in the on-ground measurements of the magnetic dipoles of each electronic box affect the performance of the adopted neural network. In section 6.4 we evaluate the expected errors in the estimate of the magnetic field and its gradients due to a possible offset in the readings of the magnetometers due to launch stresses, whereas in section 6.5 we study how the mechanical precision of the positions of the tri-axial magnetometers and their spatial resolution affect the determination of the magnetic field and its gradients. Section 6.6 is devoted to assess the reliability of our neural network approach in front of a slowly varying magnetic environment, whereas section 6.7 presents the hybrid interpolation system thought for this application. Finally, in section 6.8 we summarize our main findings, we discuss the significance of our results and we draw our conclusions.

6.2 The neural network architecture

Although neural networks have been used in different space applications (Bullen et al., 2003; Loyola, 2006), to the best of our knowledge this is the first application of neural networks to analyze inflight outputs in space missions. Hence, studying the robustness of the neural network architecture proposed to estimate the magnetic field inside the LCA is a mandatory task.

6.2.1 The fiducial neural network architecture

Figure 6.2 shows a simplified version of the fiducial architecture of our neural network. As can be seen, the number of inputs is twelve — one for each magnetometer readout — corresponding to the four tri-axial magnetometers placed in the spacecraft. These readings are the only valuable information which can be used to estimate the magnetic field at the positions of the test masses, and constitute the input layer

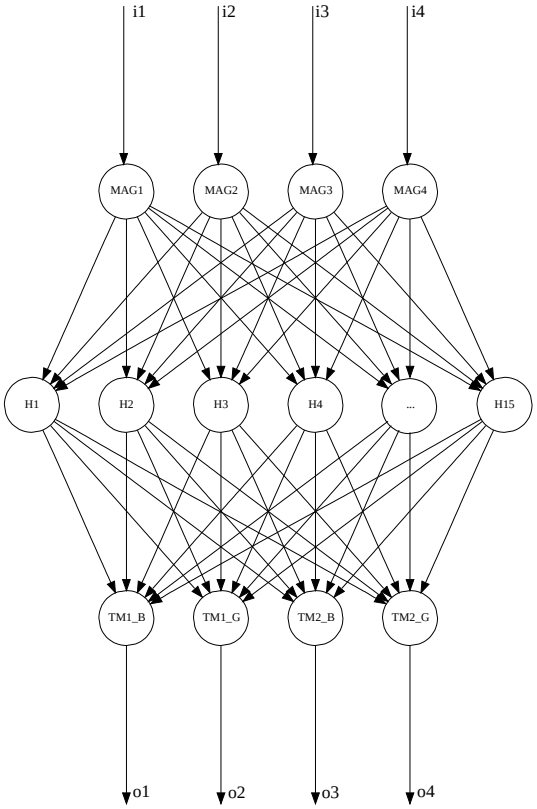

Figure 6.2: The fiducial feed-forward neural network architecture. The readings of the magnetometers are the system inputs (4 magnetometers, each one with 3 data channels). The outputs of the system are the magnetic field (3 field components per test mass) and gradient components (5 components per test mass) at the positions of the test masses. For the sake of simplicity, all the field and gradient channels have been grouped into a single neuron. Moreover, not all the neurons in the hidden layer are shown in this figure.

of the neural network. On the other hand, to estimate the magnetic field three outputs will be required — corresponding to the three field components per test mass — whereas to estimate the gradient only five additional outputs are needed. This is because the magnetic field has zero divergence and zero rotational. Thus, the gradient matrix $\partial B_i/\partial x_j$ is a traceless symmetric matrix, and therefore only 5 out of its 9 components are independent (Jackson, 1999). These outputs are the output layer of the neural network. In addition to the two previously described layers, there is only one intermediate layer, which constitutes the hidden layer. This layer, in our case, is made of 15 neurons. Using this architecture for the neural network the magnetic field estimates typically have standard deviations on the order of $\sim 5\%$ (Díaz-Aguiló et al., 2010), a value with which we compare the results of our analysis.

Table 6.1: Positions of the test masses and positions of the magnetometers referred to a coordinate system fixed to the spacecraft — see Appendix A. Their relative position can be seen in Fig. 6.1

Test masses	x [m]	y [m]	z [m]
1	−0.1880	0	0.6093
2	0.1880	0	0.6093
Magnetometers	x [m]	y [m]	z [m]
1	0.0758	−0.3694	0.6093
2	0.3765	0	0.6093
3	−0.0758	0.3694	0.6093
4	−0.3765	0	0.6093

6.2.2 Training and testing

Training and testing data sets were simulated using the most complete and up-to-date information about the magnetic configuration within the spacecraft. The complete magnetic configuration of the satellite has not been measured yet, because some units have not been delivered yet to the prime contractor. Nevertheless, the exact position of each unit in the spacecraft reference frame are already determined. On the other hand, the magnetic moments used in our simulations are those reported by the constructors of each subsystem — see Appendix E. Unfortunately, this data is not available yet for all units, and moreover although the moduli of the dipoles are known for all the subsystems their directions are not known yet for most of the units. The three-dimensional values of the magnetic dipoles of each unit will be accurately measured in the final testing campaign to be performed on each subsystem before assembling. This campaign is expected to be performed on the complete assembled spacecraft. The training and validation of the neural network using the measured values of the magnetic dipoles will be done after the campaign but the specific details of the processing algorithm are expected to remain unchanged. Moreover, the magnetic field inside the LCA is expected to vary substantially between the different operational modes. Accordingly, since the magnetic configuration of the spacecraft may have different characteristics for different operational modes, it is foreseen that a different neural network will be trained for each of these configurations.

Given the unknown orientations of the magnetic dipoles we generate several magnetic configurations assigning randomly the orientations of the 46 dipoles. An example scenario is thus characterized by a selection of the 46 dipoles with random orientations. It is worth mentioning that the produced sets are consistent with our

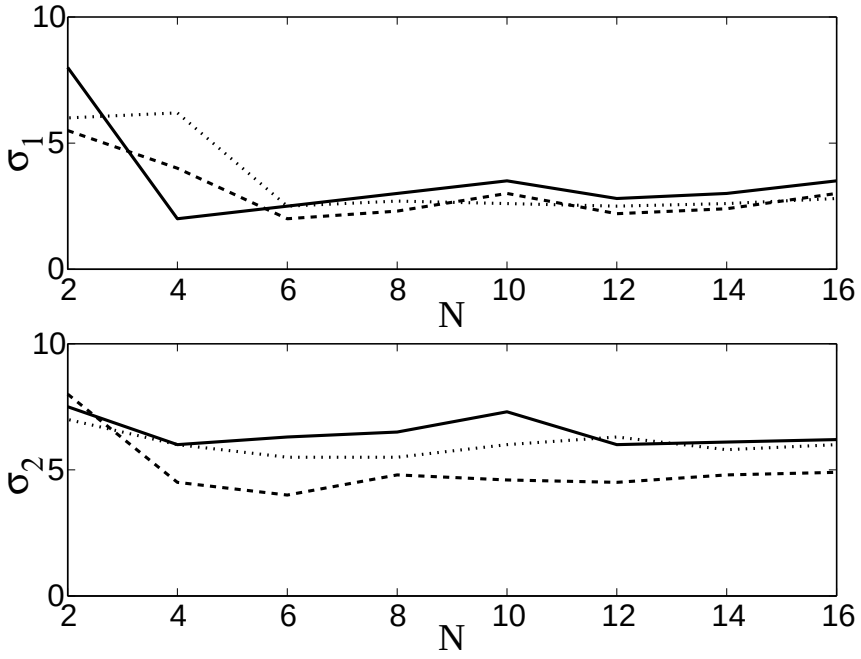

Figure 6.3: Quality of the estimate of the magnetic field as a function of the number of neurons in the hidden layer. The maximum interpolation error remains almost constant for neural networks larger than ~ 15 neurons in the hidden layer. The solid line corresponds to the standard deviation of the error obtained for the B_x-component, the dotted line for the B_y-component and, the dashed line for the B_z-component.

expectations and the mission requirements (LIST, 2008; Cañizares et al., 2009) since at the positions of the test masses we obtain magnetic fields ~ 200 nT, while the readings at the magnetometers are of the order of 4 to 10 μT. With this approach the magnetic field generated by the dipole distribution is given by Eq. (5.14). In order to simulate realistic magnetic environments, we compute the magnetic field at the positions of the magnetometers and at the positions of the test masses using Eq. (5.14) and the list of sources in Appendix E. The positions of the test masses and of the magnetometers are shown in Table 6.1. We recall that in order to train the network, we generate two different batches of 10^3 samples. The first batch was used as the training set for a neural network with the architecture of Fig. 6.2. This batch consists in 12 inputs (3 inputs for each of the 4 vector magnetometers) and 16 outputs representing the field information at the position of the two test masses (3 field plus 5 gradient components per test mass). The second batch has been used for validation to assess the performance of the neural network.

6.2.3 Varying the number of neurons

Assessing the correct choice of the number of neurons of a neural network is not a simple task. When the neural network is composed by only one hidden layer, the input layer contains as many input-neurons as the information we provide to the network and as many output-neurons as the target information we want to obtain. Nevertheless, as far as the number of neurons of the hidden layer is concerned, it is not guaranteed that the architecture of the selected neural network is optimal nor that there is an algorithm in the current literature to determine the optimal number of neurons (Reed, 1993; Dreyfus, 2005). Normally, to obtain good results, the smallest system obtained after pruning which is capable to fit the data should be used. Unfortunately, it is not obvious what size is best. A system with a small number of neurons will not be able to learn from the data, while one with a large number of neurons may learn very slowly and, moreover, it will be very sensitive to the initial conditions and learning parameters. Additionally, it should be taken into account that one of the biggest problems of large networks for some specific problems is the fact that in the early stages of training, the error on both the training and tests tends to decrease with time as the network generalizes for the examples to the underlying function. However, at some point, the error on the testing set reaches a minimum and begins to increase again as the network starts to adapt to artifacts and specific details in the training data, while the training error asymptotically decreases. This problem, known as overfitting, occurs more frequently in large networks due to the excessive number of degrees of freedom in comparison to the training set (Schittenkopf et al., 1997). To avoid this, we have used the early stopping technique, which overcomes this shortcoming.

In the early stopping technique the available data is divided into two subsets (Kecman, 2001). The first subset is the training set, which is used for computing the gradient and updating the network weights and biases. The second subset is the validation set. The error on the validation set is monitored during the training process. The validation error normally decreases during the initial phase of training, as does the training set error. However, when the network begins to overfit the data, the error on the validation set typically begins to rise. When the validation error increases for a specified number of iterations, the training is stopped, and the weights and biases at the minimum of the validation error are returned to the values obtained at the minimum. All these precautionary measures avoid overfitting. Therefore, the analysis of the number of neurons needed for the hidden layer can be made analyzing the evolution of the estimation error on the testing set as the number of neurons increases. The results of such an analysis are depicted in Fig. 6.3, which shows the standard deviation of the estimate for both test mass1, σ_1, and test mass 2, σ_2 as a function of the number of neurons in the hidden layer, N.

As can be seen in this figure, when a reduced number of neurons is used the model cannot accurately estimate the underlying function due to the lack of tunable

Table 6.2: Quality of the estimate for the most common neuron activation functions.

	TM_1			TM_2		
Function	σ_x	σ_y	σ_z	σ_x	σ_y	σ_z
Tangent sigmoid	4.1	3.8	2.5	5.9	5.2	4.5
Linear	3.8	3.5	2.3	5.7	5.4	4.2
Logarithmic sigmoid	4.2	3.8	2.5	6.2	5.1	4.5
Radial base	4.2	4.3	3.9	6.3	6.0	4.8
Step	7.5	7.6	4.9	12.3	8.2	7.9

parameters. As the number of neurons in the hidden layer is increased, the neural network performs better and for a number of neurons larger than 15 the error is not further reduced. Consequently, we conclude that for this specific application the adequate number of neurons for the hidden layer lies between 10 and 15. This choice ensures a network large enough to be capable of estimating the underlying relationship and not excessively large to consume excessive training time, learn slowly and be dependent on the learning algorithm and learning data. We have also checked that increasing the number of hidden layers of the neural network does not result in a better performance of the interpolating algorithm.

6.2.4 Changing the type of neuron

Most of the feed-forward networks are trained with the back-propagation algorithm and gradient descent techniques are used to minimize some specific cost function, and this has been the case for the training algorithm used here. This means that all activation functions within the network must be differentiable to be able to compute the network gradient for each learning step. Normally, the most commonly used type of functions are the tangent sigmoid or the logarithmic sigmoid (Kecman, 2001), which can model any non-linear function if properly trained (Dreyfus, 2005), whereas linear functions are usually employed for linear models with high dimensionality.

We have studied several possibilities and the results are listed in Table 6.2, where we show for the different types of neurons the standard deviations of the probability density functions of the estimates of the magnetic field for both test mass 1 and 2 (TM_1 and TM_2, respectively). In our case, and as borne out from Table 6.2, the linear function together with the tangent sigmoid and the logarithmic sigmoid are the most efficient choices, while the performance of the radial base function is slightly worse. Finally, the step function (the popular perceptron) does not yield good results because it is specifically designed to be used for classification problems.

Specifically, the linear neuron is the one for which we obtain the best results. This could be surprising given that our problem is highly non-linear. The reason is that for every magnetic configuration there exists a large and fairly stable difference between the value of the magnetic field at the location of the magnetometers (all of the components of the magnetic field are ~ 10 μT) and the field at the position of the test masses (all the components are on the 100 nT level). For this reason, the weights of the network happen to be the most relevant modeling factors. That is, the point-to-point interpolation can be understood in the linear case as a simple weighted sum of the magnetometers measurements. Accordingly, because of its simplicity and good results, we use the linear function as the basic unit in our regression study. It is worth noting at this point that similar results could be obtained using a high-dimensionality least squares analysis, but in our specific case we have found matrix inversion problems because some magnetometer channels present highly correlated signals.

6.2.5 Underlying structures

We have already shown that our neural network is highly reliable. Thus, it is pertinent to ask ourselves which is the ultimate reason of this behavior. The answer to this question is that during the training process, the neural network eventually learns that the magnetic field at the positions of the test masses is generally smaller than the magnetometers readouts — with occasional exceptions due to the rich and complex profile structure of the field inside the LCA. Moreover, the neural network is able to learn an inference procedure which is actually quite efficient. To better understand this, we found instructive to look into relationships between the data read by the magnetometers and the estimates of the magnetic field generated by the neural network. We chose to calculate correlation coefficients between input and output data, and the results are displayed in Table 6.3. The test masses are labeled as TM_1 and TM_2, respectively, whilst the four magnetometers are listed as M_i, $i = 1, \ldots, 4$.

The following major features can be easily identified. Firstly, each component of the field is basically estimated from the magnetometers reading of the same component. For example, the interpolation of the B_x-component in test mass 1 is mostly dependent on the B_x-readings of the magnetometers. Secondly, the measurements of the magnetometers closer to the interpolation points have larger weights. For instance, when the field is estimated at the position of TM_1, to which the magnetometer M_4 is the closest magnetometer, the value it measures is the largest contributor to the interpolated field in TM_1. At the same time, magnetometers M_1 and M_3 being nearly equidistant from both test masses, their weights are almost identical (see Table 6.1 for more details). Finally, no apparent or easily deductible physical relationship is found between the estimated gradient at the positions of the test masses and the magnetometer inputs.

Table 6.3: Input-output relationship learned by the network.

Output	B_x	B_y	B_z
B_x TM_1			
M_1	0.2177	−0.1060	0.0134
M_2	0.2581	−0.0185	0.1564
M_3	0.3754	0.0985	0.0054
M_4	0.9340	0.1528	−0.0501
B_y TM_1			
M_1	−0.0197	0.3556	−0.0682
M_2	0.0031	0.2240	0.0601
M_3	−0.0782	0.4249	0.1217
M_4	0.0668	0.9035	0.0102
B_z TM_1			
M_1	−0.0772	−0.0635	0.3090
M_2	−0.1343	0.0083	0.3377
M_3	−0.0180	−0.1027	0.5002
M_4	0.0493	0.0615	0.9041
B_x TM_2			
M_1	0.3506	0.1862	0.0840
M_2	0.9081	−0.2830	0.3782
M_3	0.1230	−0.2398	−0.0613
M_4	0.2502	0.0184	−0.0480
B_y TM_2			
M_1	−0.3662	0.3877	−0.0211
M_2	0.0184	0.8398	−0.1200
M_3	0.3722	0.2400	0.0927
M_4	−0.0040	0.2379	−0.0026
B_z TM_2			
M_1	0.1217	0.0267	0.4111
M_2	0.0144	−0.1222	0.8740
M_3	0.0333	0.0233	0.5054
M_4	0.0310	0.0141	0.2685

6.3 Variations in the magnetic dipoles

The numerical experiments done so far indicate that the neural network interpolating scheme offers good performances when properly trained, irrespective of its specific

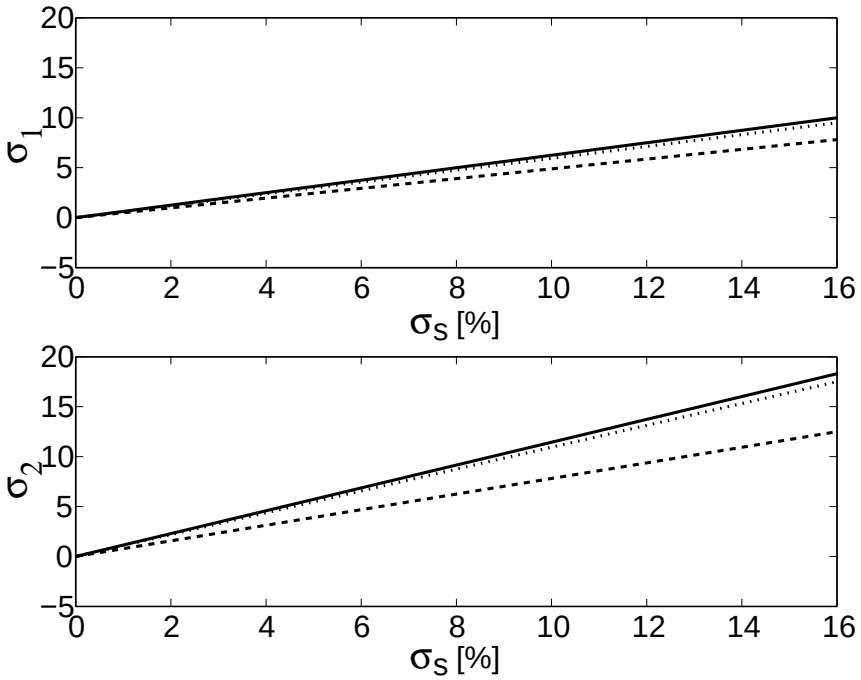

Figure 6.4: Quality of the estimate (standard deviation of the estimation) as a function of the difference between the real magnetic inflight measurements with respect to the on-ground measurements (in percentage). σ_{S} represents the standard deviation used to variate the components of the magnetic dipole moment of the sources. Again, the solid line corresponds to the B_x-component, the dotted line to the B_y-component and, the dashed line to the B_z-component.

architecture. However, we emphasize that the neural network has been trained using simulated data, while for the real spacecraft the neural network will be trained using on-ground measured data. This data, as already mentioned in section 6.2.2, is planned to be obtained in Spacecraft Magnetic Test Campaign. To assess how this could be done we have determined how many batches of samples need to be fed in the neural network to obtain the desired accuracies. We have found that for a proper training of the network, at least 10 batches of samples must be recorded from the real spacecraft with all the sources of magnetic field onboard. Only in this way can we be sufficiently confident on the trained neural network. Each of these batches will be constituted by 10^3 vectors of 28 values each, corresponding to 12 readings of the magnetometers (3 components for each of the 4 magnetometers), 6 magnetic field readings (3 components of the magnetic field measured at the positions of each test mass) and 10 readings of the gradients of the magnetic field (5 values for each test mass). This will allow us to choose a specific neural network model in a realistic case.

It is expected that the magnetic characteristics of each of the spacecraft units will not change due to launch stresses. However, the measurements taken on-ground may not be accurate enough to represent the real magnetic inflight characteristics of these units. For instance, some units would be missing during the on-ground measurement campaign or some others can change their magnetic characteristics during the lifetime of the mission or, finally, it could be as well that the system operation cannot be measured on-ground accurately. For all these reasons the predictions of the neural network may be biased. Hence, it is important to assess the robustness of the predictions of the neural network in front of changes in the magnetic dipoles of the electronic boxes. To do so we have adopted the following procedure. We varied randomly each of the components of the magnetic dipole moment of all the sources of magnetic field according to Gaussian distributions. The width of such Gaussians, σ_{S}, is our free parameter and corresponds to a given percentage of deviation of the specific component with respect to that of the training set. In this way we can simulate a difference between flight and ground data in a simple and realistic manner.

The results obtained using this procedure are shown in Fig. 6.4, where we show the standard deviation of the probability density function of the estimation of the three components of the magnetic field interpolated using the trained neural network as a function of the width of the Gaussians. As can be seen in this figure, the error of the estimate increases linearly for increasing widths of the Gaussian. Nevertheless, our simulations show that offsets of $\sim 15\%$ per component in each of the magnetic sources result in a global error of the estimate of $\sim 15\%$ for the magnetic field and of only $\sim 5\%$ for the gradient at the positions of the test masses, a very interesting result. Thus, we conclude that our interpolation scheme is fairly robust in front of small differences in the flight-ground data configuration.

6.4 Offsets in the magnetometers

It has been shown recently that the magnetometers readings may suffer from unpredictable offsets (Primdahl et al., 2006) due to launch stresses. In particular, this offset is most probably due to temperature changes during launch, and varies from $\Delta_B \sim 1$ nT to several nT. This, of course, may have important consequences on the estimate of the magnetic field at the positions of the test masses, as the interpolating algorithm presented here largely depends on the reading of the magnetometers.

To assess the robustness of the interpolation scheme to the offsets in the readings of the magnetometers we have simulated a random vector of offsets (a 12 valued-vector, 1 offset for each of the 12 magnetic channels), according to a Gaussian distribution of width Δ_B. This offset vector has been added to the inflight readings when performing the assessment of the results output by the interpolation network. Several simulations have been performed varying Δ_B from 1 nT to 200 nT. The results are shown in Fig. 6.5. As can be observed, the errors in magnetic field estimation are

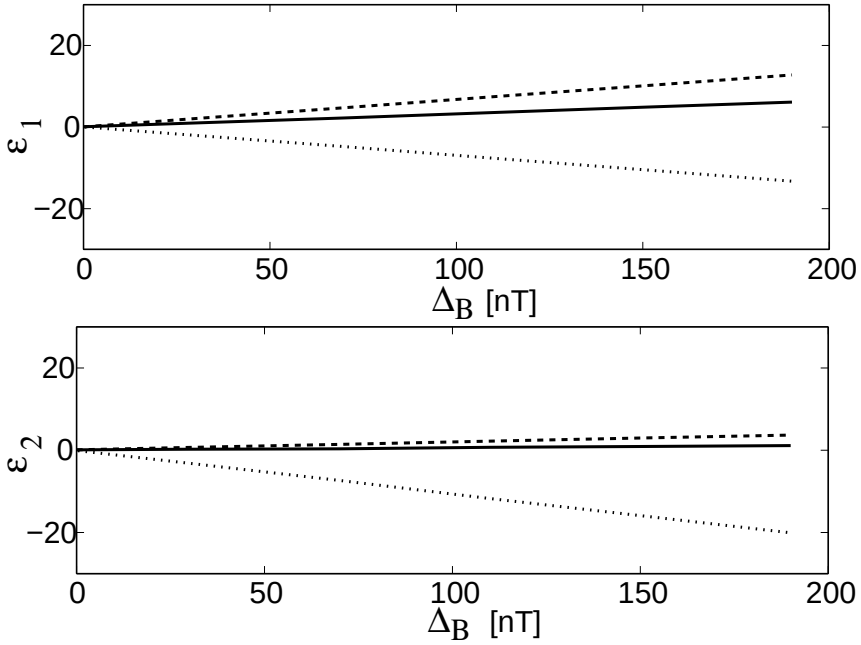

Figure 6.5: Quality of the estimate (mean error) as a function of the magnitude of the offset in all 4 magnetometers. The solid line corresponds to the B_x-component, the dotted line to the B_y-component and, the dashed line to the B_z-component.

below 10% up to an offset level at the magnetometers of 80 nT — which is one order of magnitude larger than the offset observed in other space missions (Primdahl et al., 2006). Consequently, we conclude that the magnetic data analysis of the mission will not be appreciably affected by the possible offset of the magnetometers readings.

6.5 Precision of the position of the magnetometers

Another aspect which may also be relevant for the determination of the magnetic field and gradients at the positions of the test masses is the uncertainty in the location of the heads of the magnetometers. Actually, the neural network is trained with the nominal position of the magnetometers, and the inflight training will be done with these nominal values. The uncertainty in these values may represent an important source of error because the neural network learns from the correlation between the field at the positions of the magnetometers positions and the field at the positions of the test masses. Therefore, if distances between those two locations are not accurate enough, they may affect the interpolation quality — see Fig. 5.7 and Table 6.3.

The onboard tri-axial magnetometers will be four TFM100G4-S. These are flux-gate magnetometers built by Billingsley. By construction, these magnetometers consist of three different magnetic sensors, along the x-, y- and z-directions. For

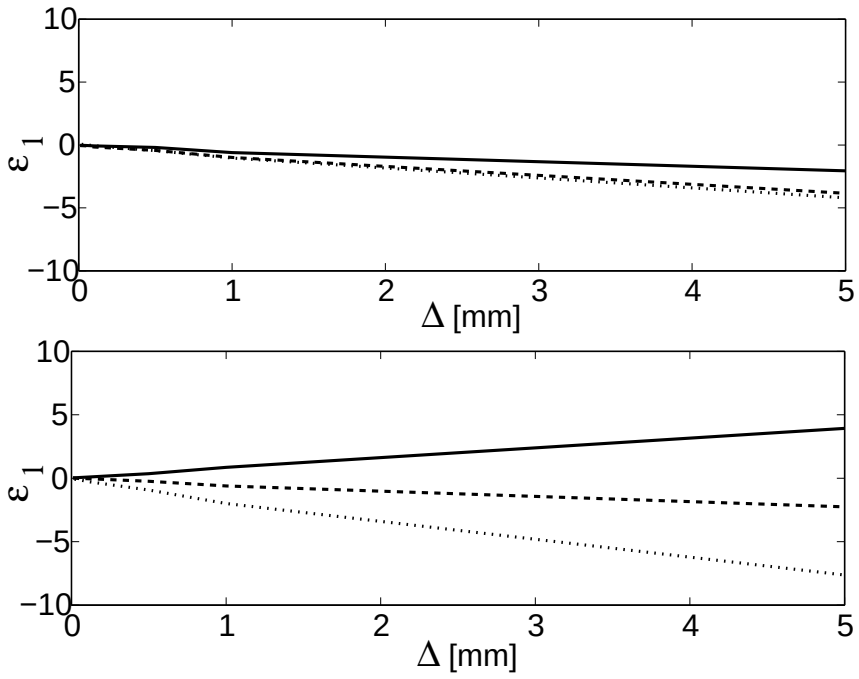

Figure 6.6: Quality of the estimate (mean error) due to the mechanical uncertainty in the precise position of the magnetometers.

each of these axes, the fluxgate magnetometer consists of a sensing (secondary) coil surrounding an inner drive (primary) coil around high magnetic permeability core material. Due to the large size of the heads of these low-noise magnetometers, the spatial resolution in each of the directions is ~ 4.0 mm. On the other hand, the coils of the magnetometers have an orthogonality better than 1°. This angular error may be transformed to a linear uncertainty by multiplying by the longest distance inside the magnetometer caging, $l \simeq 82.5$ mm, resulting in an uncertainty of ~ 1.5 mm. Finally, the exact placement of the satellite units onto the satellite walls may be imprecise. It is estimated that the mechanical precision will be on the order of the μm, and therefore it will be considered negligible in this analysis. The overall spatial uncertainty of the sensing position of the magnetometers can be computed by adding in quadrature the different contributions, and turns out to be $\Delta \sim 4.3$ mm. In view of these conundrums we performed an additional set of simulations in which the positions of the magnetometers where randomly changed within 5 mm. We then computed the error in the estimate of the interpolating neural network. The results are shown in Fig. 6.6. Clearly, the neural network outputs a mean error in interpolation below 6% if the mechanical uncertainty lies below 4.3 mm, which is the worst case expected in the mission. Therefore, the neural network is expected also to be very robust to this kind of uncontrollable situations.

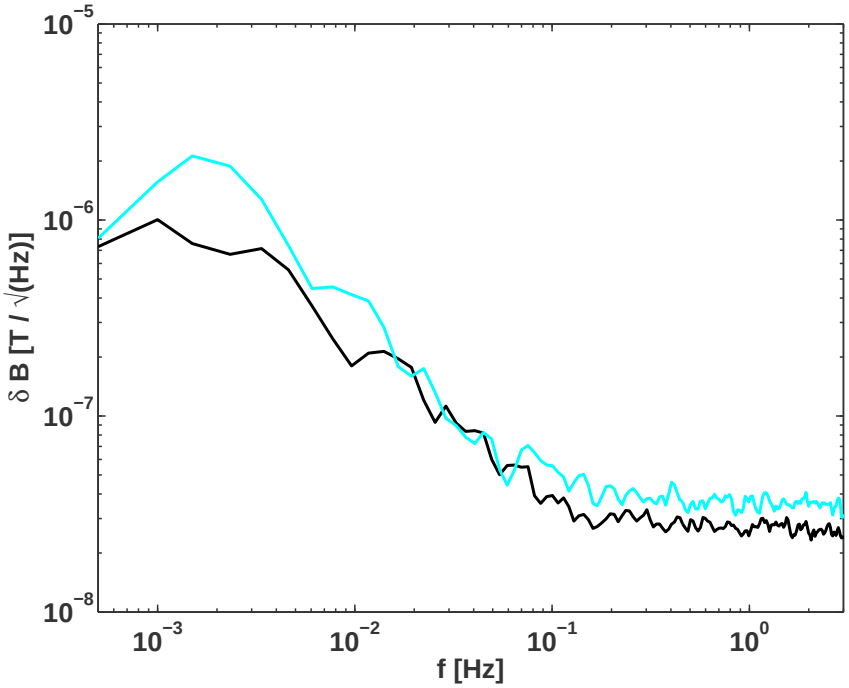

Figure 6.7: Spectrum of fluctuations of the magnetic field at the position of the test masses. The black line corresponds to the spectrum at the position of test mass 1 and the cyan one that at the position of test mass 2.

6.6 Varying environmental conditions

As can be seen in Eqs. (5.1) and (5.2), there is a non-linear dependence of the force on the magnetic field. This means that the acceleration depends on the temporal variations of the magnetic field and its gradient. Specifically, a coupling of the value of the magnetic field with the variations of its gradient (and vice versa) exists. In the previous sections we have shown that our neural network interpolating algorithm correctly retrieves the values of the magnetic field and its gradient at the positions of the test masses when they are assumed not to vary with time. However, these quantities are expected to be subject to small low-frequency fluctuations. Thus, we need to assess if our method is able to correctly follow a slow drift of the magnetic field and its gradient.

As previously mentioned, the magnetic field inside the LCA is a consequence of the electronic subsystems present inside the spacecraft. Almost all operational amplifiers (the most important source of noise of the electronics processing chain of each unit) are subject to a $1/f$ noise around 0.1 Hz or higher frequencies. Magnetic tests of every unit have not yet been performed, but it is foreseen that the spectrum of fluctuations of the magnetic field at the position of the test masses will be very similar

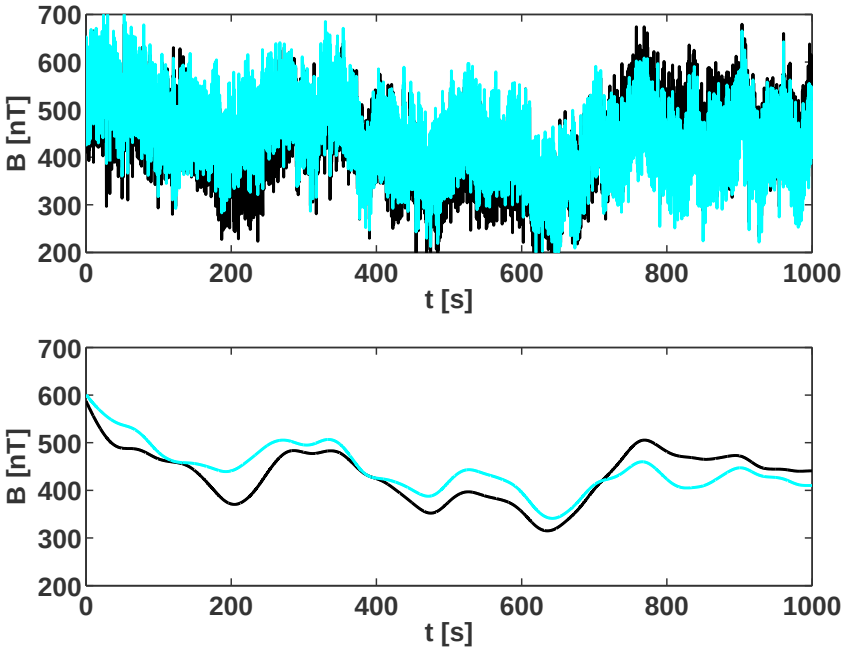

Figure 6.8: Top panel: temporal realization of the magnetic field at test mass 1 (black line) and interpolated magnetic field given by the trained network (cyan line). Bottom panel: same as the top panel, but filtered at 10 mHz with a first order low-pass filter (unitary gain).

to the noise spectrum of the amplifiers. In particular, it is expected that the spectrum will have a $1/f$ branch below a roll-off frequency of 0.1 Hz, and a white noise branch extending up to 10 Hz. The predicted spectrum, which has been obtained assuming a worst-case scenario — i. e., assuming an amplitude $5\mu\mathrm{Am}^2/\sqrt{\mathrm{Hz}}$ at 0.1Hz in the moduli of the magnetic moments of the source dipoles — is shown in Fig. 6.7. As will be shown below, one of the direct consequences of including the fluctuations given by the noise spectrum of Fig. 6.7 is the presence of low-frequency variations of up to 300 nT for each of the three magnetic components. These fluctuations may cause important errors in the magnetic field estimation if not considered in the training process. The magnetic field spectrum modeled in this section is expected to be one or two orders of magnitude larger than the real one, but testing our algorithms against such worst-case scenario gives valuable insights to an upper bound of the expected error of the interpolation algorithm.

Neural networks can be classified into dynamic and static categories. Static networks have no feedback elements and, consequently, contain no delays. Thus, the output is calculated directly from the input (and only the current input) through feedforward connections (Kecman, 2001). The training of static networks is performed with the well known and efficient backpropagation algorithm, as described in

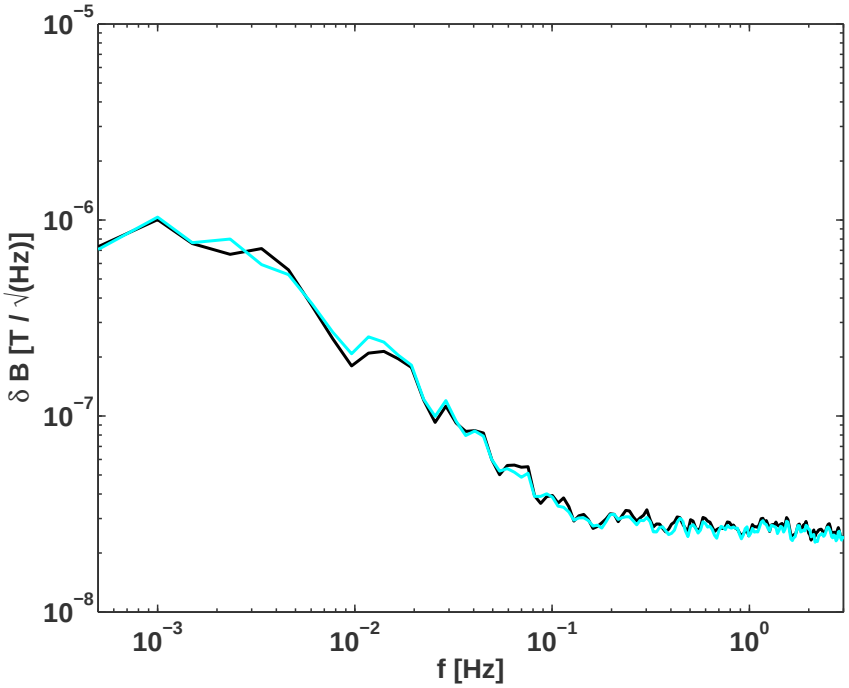

Figure 6.9: Spectral density of the magnetic field at the position of test mass 1 (black line) compared to the spectral density of the magnetic field retrieved by the neural network (cyan line).

section 5.3.3. In dynamic networks, the output depends not only on the current input to the network, but also on its previous inputs and outputs (Dreyfus, 2005; Kecman, 2001). Thus, for our case one might quite naturally think that we should be forced to choose a dynamic neural network. Nevertheless, as shown in Fig. 5.7, the most important feature of our interpolation scheme is the ability of the neural network to learn the underlying structures of the magnetic field inside the LCA. Since training a dynamic network is a hard task and, moreover, the learning rate is usually very slow it is worth exploring the possibility of using instead a static network with an adequate training procedure adapted to this new scenario. In other words, we have to let the network know during the training process that drifts may occur. To do this we use a simple and effective training procedure. We first generate 10 different time series using uncorrelated realizations. We then compute the dynamic range of the magnetic field for each of these realizations. Of these time series we select those five which have the widest dynamical range, and we concatenate them. These 5 time series are then used to train the network.

With this new training technique the interpolation results are remarkably good. To illustrate the goodness of our interpolation procedure in the top panel of Fig. 6.8

Table 6.4: Standard deviation of the error output by the network for both the case of a constant magnetic field and a fluctuating one.

	Constant **B**		Fluctuating **B**	
	σ_1	σ_2	σ_1	σ_2
B_x	2.68	3.28	8.75	14.75
B_y	2.71	3.27	4.86	8.46
B_z	3.15	3.82	2.92	13.16
$\|B\|$	2.13	3.15	5.85	16.30

we show the temporal evolution of the fluctuating magnetic field for test mass 1 (black line) and the interpolated result obtained using the neural network trained with the fluctuating examples (cyan line). As can be seen, although there are some differences, the result of the interpolation closely resembles the actual magnetic field. This can be better appreciated when both signals are filtered at 10 mHz using a low-pass filter (bottom panel of this figure). Clearly, the interpolated magnetic field follows very closely the real magnetic field. Moreover, the spectrum of the interpolated magnetic field is very similar to that of Fig. 6.7. This is borne out from Fig. 6.9, in which we compare both spectra. Clearly, the interpolated spectrum (cyan line) follows very closely the real one (black line), indicating that the neural network correctly describes the physical properties of the varying magnetic field. The only noticeable difference when a fluctuating magnetic field is analyzed is that in this case the neural network performs slightly worse. This can be seen in Table 6.4, where we show the standard deviations of the estimates for both a constant magnetic field and a fluctuating one, for all the field components and its modulus and for both test mass 1 (σ_1) and test mass 2 (σ_2). As can be seen, the estimation errors are larger for a fluctuating magnetic field, as it should be expected, but do not increase dramatically.

6.7 Hybrid interpolation system

As discussed in previous sections, the feed forward neural network yields very satisfactory results. However, this performance can only be achieved if sufficient and reliable training data exist. In other words, real measurements of the magnetic field produced by the onboard electronic systems at the positions of the test masses are needed. Moreover, we need such measurements for each of the different operation modes of the spacecraft. Here we define an "operation mode" as the status of the satellite when a specific list of hardware is switched on or is active at certain moment during the mission. These different operation modes lead to different magnetic configurations, and will produce a different magnetic imprint within the

LCA. However, as already mentioned, the neural network is only able to interpolate the magnetic field within the learned input space, but cannot infer values beyond this space. This means that the neural network can infer the magnetic field at the positions of the test masses if it has been trained with magnetic data corresponding to the adequate operation mode. If this is not the case, and the magnetic model used to interpolate does not coincide with the spacecraft magnetic configuration of the new magnetometers inputs, the performance of the interpolation algorithm will be worse — see section 6.3. This shortcoming can be overcome using a model database corresponding to each of the expected magnetic configurations of the spacecraft and adding a decision layer in the interpolator architecture. These blocks conform the hybrid interpolation system presented in this section.

The hybrid algorithm described here takes full advantage of the interpolation power of the feed-forward network discussed in previous sections. In addition, a higher level decision level using a self-organizing map (Kohonen, 2001) to decide which trained magnetic model should be used at any given moment, is incorporated. As can be seen in Fig. 6.10, the self-organizing map processes the magnetometer inputs and determines the best suitable magnetic model from the database by means of clustering techniques (Dreyfus, 2005). Then, it pipelines this decision to the neural network interpolation algorithm and the algorithm updates the weights of the neural network model with those selected from the database. Finally, the interpolation algorithm behaves as described in previous sections and delivers the estimates of magnetic field and gradient at locations of the test masses.

6.7.1 Architecture of the hybrid interpolation system

The architecture of the hybrid interpolation system presented in this section is shown in Fig. 6.10. It consists of three main blocks:

- *Magnetic model database.* This database collects different magnetic models and also the input vectors used for training them. Currently, the database is only composed by simulated data sets. However, real magnetic data will be available after the magnetic test campaign, which will be done at Astrium Stevenage (England, UK).

- *SOM network.* A self-organizing map (SOM) compares the different input vectors and classifies them into groups or clusters — see Appendix F for additional details about self-organizing maps.

  When a new input vector is fed to the network for training, its Euclidean distance to all weight vectors is computed. The Euclidean distance from vector $\mathbf{p}$ to vector $\mathbf{q}$ is defined as in Cartesian coordinates:

$$d(\mathbf{p},\mathbf{q}) = \sqrt{\sum_{i=1}^{N}(p_i - q_i)^2}, \tag{6.1}$$

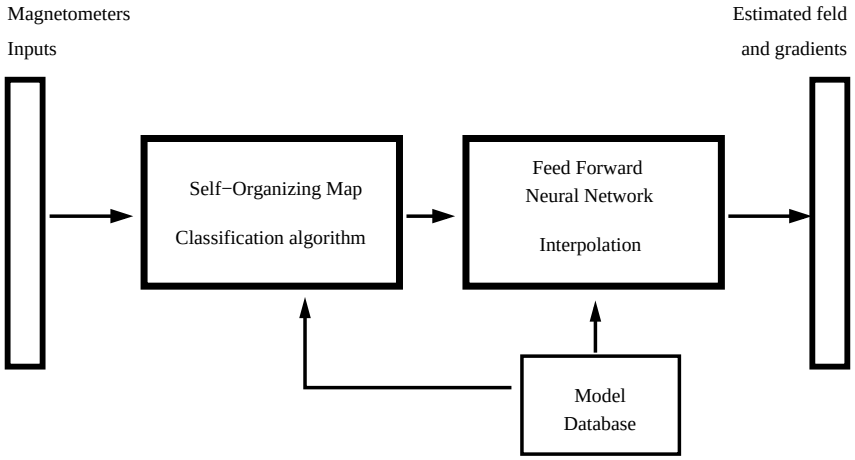

Figure 6.10: Hybrid interpolation system consisting in a magnetic model data base, a self-organizing map for autonomous classification and decision and a feed-forward network for interpolation.

where N are the number of components of each vector. The neuron with weight vector most similar to the input is called the best matching unit (BMU). The weights of the BMU and neurons close to it in the SOM lattice are adjusted with the input vector. The magnitude of the change decreases with time and with distance from the BMU. A neuron with weight vector $\gamma(t)$ is updated using the expression:

$$\gamma(t+1) = \gamma(t) + \Theta(n,t)\Delta(t)\left(I(t) - \gamma(t)\right), \tag{6.2}$$

where $\Delta(t)$ is a monotonically decreasing learning coefficient and $I(t)$ is the input vector. The neighborhood function — typically, a Gaussian is a common choice — $\Theta(v,t)$ depends on the lattice distance between the BMU and neuron n. This neighborhood function shrinks with time. That is, during the first iterations this function is broad, and self-organization takes place on a global scale, and after a sufficient number of iterations the neighborhood shrinks to just a couple of neurons, and the weights converge to local estimates. With this iterative process, the network ends up associating output nodes with groups or patterns in the input data set (Dreyfus, 2005).

In our application we have used this ability of SOMs to split the magnetic readings time series in subsets where the same satellite magnetic configuration was present. By comparison with the existent database models, we are able to discern which magnetic configuration is onboard and which magnetic model from the trained magnetic model database should be used. If no configuration is sufficiently correlated, an alarm in the diagnostics subsystem is raised. This

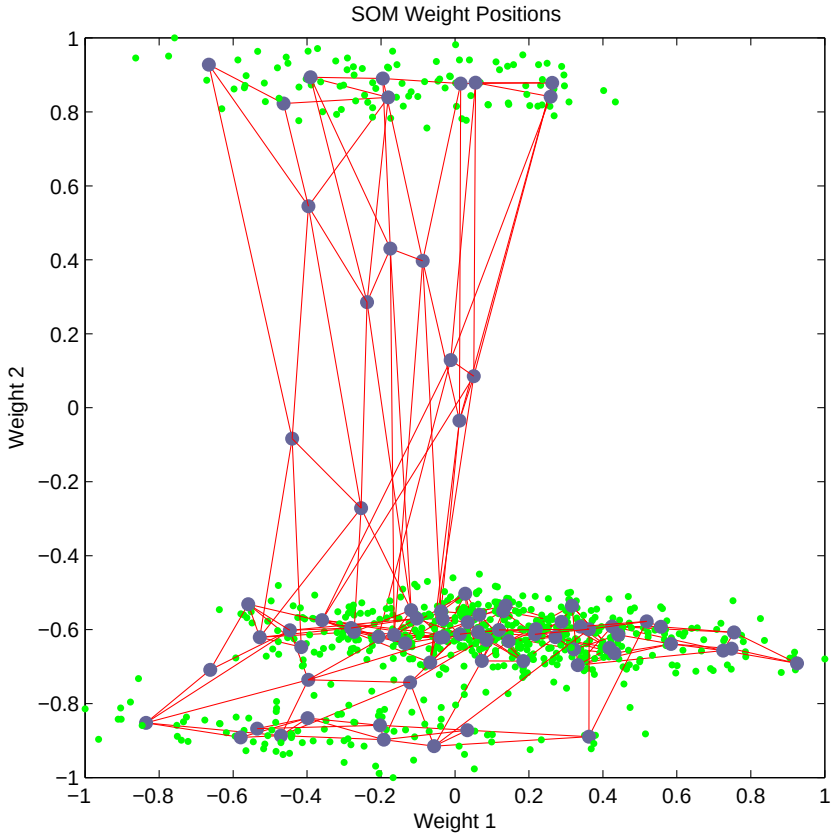

Figure 6.11: SOM output, showing that the classification algorithm is able to discern three different magnetic configurations. The intermediate set of points corresponds to the nominal configuration, whilst the upper set of points corresponds to a reduced FEEP thrusters activity and, finally, the bottom set of points is obtained when there is both a reduced FEEP and cold gas thrusters activity.

alarm informs that a not catalogued magnetic configuration is present on the spacecraft, and no interpolated field will be output.

- *Feed-forward neural network.* The feed forward network adopts the weights from the trained model pointed out by the SOM layer, and interpolates the magnetic field and its gradient at the positions of the test masses.

6.7.2 Results of the hybrid interpolation architecture

To show the ability of SOMs to classify the input data we have done a simulation in which different operation modes were introduced. Specifically, we have generated a time series of 7 000 s with the 12 readings of the magnetometers. From time 0 until

time 4 000 s, the nominal magnetic configuration was present. From time 4 000s to 5 500s, the magnetic activity of the three FEEP thrusters clusters were reduced to 50% (that is, the corresponding modulus of the magnetic moment was reduced to 50% of its value). Finally, from 5 500s to 7 000s, the activity of the cold gas thrusters was also reduced to 50%. These 12 simulated time series have been fed to the SOM. As can be seen in Fig. 6.11, with an appropriately tuned SOM network of 8 and 10 neurons in the inner hidden layers and trained for 1 000 epochs, the algorithm is able to discern three different clusters of neurons, which correspond to the three different magnetic configurations. This identification enables the decision layer to decide which magnetic model should be used at each time. For this simulation, this method reduces the interpolation error from 15% — when the decision layer is not activated and only one magnetic model is used — to 5% — when the decision layer is activated and the model data base is integrated. We consider that this global hybrid system delivers reliable and robust inflight magnetic field and gradient interpolations, and provides a large degree of autonomy to the interpolation procedure.

6.8 Summary and conclusions

The diagnostic system of LISA Pathfinder will monitor with unprecedented accuracy the disturbances of the motion of the test masses. An essential part of this subsystem is the magnetic diagnostics subsystem, which will be in charge of measuring the magnetic noise. To this end, this subsystem has four tri-axial magnetometers, which due to design constraints are placed far from the positions of the test masses. Thus, measuring the magnetic field at these positions is not an easy task. To overcome this problem a novel approach in which neural networks are used was recently proposed (Díaz-Aguiló et al., 2010) and it is described in chapter 5. The initial results obtained using this technique were encouraging but a full assessment of its reliability was still lacking.

Accordingly, we have studied how different alternatives for the architecture of the neural network affect the precision of the interpolation of the magnetic field and its gradients at the position of the test masses. We have performed a study of the underlying structures of the neural network and we have found that the ability of our interpolating scheme to recover the correct values of the magnetic field and gradients at the positions of the test masses is due to the fact that the neural network is able to learn from the readings of the magnetometers which are closest to the corresponding test mass, and that the most important contribution for each component field comes from the corresponding magnetometer reading. We have also found that the number of neurons in the hidden layer originally proposed is the optimal one, and that a larger number of neurons in this layer does not improve the quality of the interpolation. Also, the results are not sensitive to the choice of the transfer function, and consequently the simplest choice, a linear transfer function, is the best

option. Finally, we have also found that the optimal number of hidden layers is just one.

We have also discussed how the neural network must be trained with real data. In particular, we stress the importance of finding a training process adequate to the set of data the magnetometers will deliver in flight. This underlines the need to characterize on ground to our best ability the magnetic field distribution across the LCA for as many as possible foreseeable working conditions. This information will be obtained from the Magnetic Test Campaign, to be performed during 2011. Reliable information on the magnetic characteristics is essential for a meaningful assessment of magnetic noise in the LTP, and may lead to model various networks for different magnetic configurations. Our results indicate that when typical variations in the magnitudes of the magnetic dipoles of the electronic units are fed into our neural network algorithm the quality of the estimates of the magnetic field and its gradients degrade linearly with increasing departures from the on-ground measurement, although the measurements of the magnetic field degrade faster than those of the gradient components. However, the quality of the estimates does not degrade dramatically.

We have also studied which would be the effect in the in-flight measurements of an offset in the readings of magnetometers caused by temperature changes during launch, and we have found that, for typical offsets, the interpolating algorithm works reasonably well. The same can be said about the uncertainty in the position of the heads of the magnetometers.

Finally, we have also assessed the accuracy of the magnetic field interpolation when a low-frequency drift of the magnetic characteristics is present, concluding that with an appropriate training procedure, good results are obtained. Additionally, we have presented a hybrid interpolation system, that is able to discriminate between different magnetic configurations and deliver the most accurate result. We want to stress once more that the methods presented in these sections highly depend on the on-ground measurements as they represent the sole mechanism to calibrate our interpolation system. Nevertheless, we conclude that the neural network interpolating algorithm is robust enough to obtain a good estimate of the magnetic field at the positions of the test masses under most foreseeable circumstances.

Chapter 7

LISA Pathfinder simulator

This chapter describes the effort done by the LTPDA science team to develop a complete, accurate and fast simulator of the LISA Technology Package dynamics. This is not an easy task as it requires the modeling, validation, and simulation of multiple subsystems that exist in the instrument and influence its behavior. Thus, the simulator and each of its submodels presented in this chapter is the result of an important collaborative effort within the LTPDA science team. It is important to realize that this piece of work it is framed in a large collaborative effort and it is presented here because it is of relevance for the simulation of the instrument dynamics when magnetic signals are injected. However, by no means it is attempted to present this work as an individual achievement, although we have contributed to its development.

As made clear in the previous chapters, the LTP features many new technologies that have never been tested on-orbit. Besides, the mission is constrained to 90 days of operations for each partner (ESA and NASA). This poses a challenge in terms of mission data-analysis, investigation and diagnosis during the in-orbit operations. With this perspective, the science team developed the LTP Data Analysis toolbox (Hewitson, 2011), also known as LTPDA, which shall allow to use a repository, process the datasets in different ways, keeping track of all manipulations, conduct parameter estimation procedures, or even produce simulated datasets. Data analysis procedures and the definition of specific investigations strongly depend on the models of the system. Therefore each subsystem must be modeled and characterized within the LTPDA toolbox. To this end, a complete set of the LTP subsystems ready for data analysis are included as instances of the `ssm` class (State Space Model class) in the toolbox. They provide with error-proof, modular, multidimensional and scalable models for the user to conduct various operations. The content is separated from the usage so the same model may be used for various operations: retrieve a transfer function, estimate a state, estimate the covariance, or even serve as a template generator for a parameter fitting algorithm.

This chapter will focus on the presentation of the architecture of this important modeling effort for the LISA Pathfinder mission. It is organized as follows: in section 7.1, we introduce the LTPDA toolbox, its main goal and characteristics, whereas in section 7.2, we present the architecture of the State Space Model class. It follows section 7.3, where we briefly describe all subsystems on-board the LPF and how they have been modeled. In section 7.4, we present one example of analysis that can be performed with the toolbox built-in functionalities and finally we conclude in section 7.5.

7.1 LTPDA toolbox: Data Analysis toolbox for LISA Pathfinder

The LISA Technology Package Data Analysis toolbox is a MATLAB© free toolbox for accountable and reproducible data analysis. It uses an object-oriented approach to data analysis. LTPDA objects are processed through a data analysis pipeline that outputs *analysis objects*. This is done in order to give traceability and reproducibility to all the analyses performed within the mission. This means that any user, when receiving an analysis object, will be able to find out all steps that were involved in the production of the final result. This is important because the result of any data analysis procedure should encapsulate not only the numerical result, but also which raw data was involved (date, channel, time segment, time of retrieval, units,...) Also, a complete history of which algorithms were used in producing the result, and all details of how each algorithm was configured (its input parameters), as well as the details of the software version used in the processing, should be available. Additionally, details of when the processing took place and on which machine, should also be given. Finally, this is needed for all channels of a multi-channel result. As a consequence, any user will be perfectly able to re-do all operations, provided access to the raw data is granted, and will also be able to re-plot the results with different plot properties or highlighting specific parts of the plots.

This is achieved by a specific recording of all the operations performed on a specific data stream. At each analysis step, we record exactly what algorithm was applied to which object and with which parameters. In this way, the result of a particular data analysis is one or more objects, each containing the final result as numerical data together with a full processing history of how the result was achieved (Antonucci et al., 2011a).

In order to build up a complete data analysis toolbox, in addition to the aforementioned *analysis object*, the LTPDA toolbox contains the following objects:

1. *pzmodel* objects, that represent physical systems out of its pole-zero representation,

2. *rational* objects, that represent systems defined as a ratio between two Laplace polynomials,

3. *parfrac* objects, which correspond to the representation of a system as a combination of partial fractions,

4. *miir* objects, that correspond to Infinite Impulse Response (IIR) filters (Oppenheim & Schafer, 1975)),

5. *mfir* objects, that correspond to FIR (Finite Impulse Response) filters (Oppenheim & Schafer, 1975)).

Finally, to model high dimensionality multi-input, multi-output (MIMO) systems, the LTPDA toolbox includes the State Space Model objects (*ssm* objects). These objects are well suited for modeling the high dimensionality of the LTP instrument and allow to perform fast and precise simulations, template generation or implement parameter estimation algorithms with a complete model of the LISA Pathfinder mission. The state space model architecture and its built-in model library are the subject of the following sections of this chapter.

7.2 State Space Model class

7.2.1 State space representation

Linear, time invariant, dynamic systems can be expressed in state-space form with time-independent coefficient matrices. In this case, a set of first order of differential equations are expressed in matrix form. The classical state space representation is (Kirk, 1970):

$$\begin{aligned} \dot{\mathbf{x}}(t) &= \mathbf{A}\cdot\mathbf{x}(t) + \mathbf{B}\cdot\mathbf{u}(t) \\ \mathbf{y}(t) &= \mathbf{C}\cdot\mathbf{x}(t) + \mathbf{D}\cdot\mathbf{u}(t) \end{aligned}$$

where $\mathbf{x}$ are the states, $\mathbf{u}$ represents the inputs, and $\mathbf{y}$ are the outputs of the system. $\mathbf{A}$ is the state matrix of the system, $\mathbf{B}$ is the input matrix, $\mathbf{C}$ is the output matrix and $\mathbf{D}$ is the feedthrough matrix. State-space modeling is well suited to high-dimensionality MIMO systems due to its matrix architecture. Moreover, matrix algebra eases the interconnection of multiple systems.

7.2.2 Requirements on the state space architecture

The LTP instrument is very complex and has several subsystems. Each of these subsystems has different models, however each of them has to be indistinguishably

used within the entire architecture. Therefore, the main feature of the modeling of the *ssm* objects is its modularity. This characteristic makes easier to understand the building of high-dimensionality systems, and simplifies the process of validating the model, which in turn becomes modular too. Moreover, the models should be scalable. This means that the most simplified models should be obtained by building a reduced version of a 3-dimensional model on which we select the inputs/outputs or states of interest. In this way code maintenance is reduced, because parallel versions of each of the models are avoided. On the other hand, the models should be parametrized, that is, they are built using symbolic matrices, where symbolic parameters can be introduced. This allows the definition and simulation of dynamical systems that are not constant and depend on one parameter (or on several parameters) that we want to estimate, or for which we want to study their sensitivity dependance. Dealing with symbolic objects reduces the computational speed. Thus, specific tools to *numerize* these models are also required. Finally, these parameters have to be stored with all relevant information including units, physical meaning and their default values.

To enhance physical representation and meaning of the system, all inputs, outputs and state variables are associated to a name and to a physical description and have the appropriate units. Moreover, the input, state and output variables are grouped into blocks with high level descriptions and global names. In this respect, the matrices and vectors involved in the definition of the `ssm` class are block-defined. These blocks regroup together variables which are of similar nature. Examples of these groups are the group of output signals from the interferometer or the commands output by the controller. Matrices are then split according to the grouping of variables into the so-called *blocks*. As an illustrative example, for a specific case the input matrix $\mathbf{B}$ may look like:

$$\begin{aligned} \mathbf{B} &= \begin{pmatrix} \mathbf{B}_{1,1} & \mathbf{B}_{1,2} & \mathbf{B}_{1,3} \\ \mathbf{B}_{2,1} & \mathbf{B}_{2,2} & \mathbf{B}_{2,3} \\ \mathbf{B}_{3,1} & \mathbf{B}_{3,2} & \mathbf{B}_{3,3} \end{pmatrix} \\ &= \begin{pmatrix} (5\times 3) & \cdot & (5\times 7) \\ (2\times 3) & (2\times 1) & \cdot \\ \cdot & (4\times 1) & (4\times 7) \end{pmatrix} \end{aligned} \tag{7.1}$$

In this example, our system has 3 *blocks* of inputs, and each of these blocks has 3, 1 and 7 input *ports* respectively. At the same time, we can figure out that the system is characterized by 3 states and each of the states has a dimension of 5, 2 and 4 respectively. Note that the size of the outputs can not be extracted from this example because they are defined by the $\mathbf{C}$ and $\mathbf{D}$ matrices.

Using the naming infrastructure combined with this block-structured architecture, two subsystems should be able to be easily interconnected when the output block names coincide with the input block names. The appropriate matrix reordering should be performed when doing this *assembling* of subsystems. To visualize

these interconnections, various display functions are available to the user, providing with Matlab© console display or dot-generated graphs. The operation and manipulation of *ssm* models should be programmed to deliver a high-level language to the user. As a consequence of a higher level programming, error messages should be very explicit. Finally, during the building process of the model library and the characteristics of the class, important emphasis should be placed on documentation. This documentation, references and origin of the model should also be stored in the *ssm* object.

7.2.3 Model library and class methods

The `ssm` class represents each system storing its state matrix (**A**), the input matrix (**B**), the output matrix (**C**) and the feed-through matrix (**D**). Additionally, it stores the sampling time (`timestep`) of the model, the information concerning the `inputs`, the `states` and the `outputs`), and the information concerning the symbolic and substituted parameters.

The *ssm* class was conceived with 3 different ingredients: (1) a basic class constructor, (2) a library of models, and (3) a series of class methods to operate on these models. The class constructor builds up the models. The library model contains already hard-coded models available to the user, such as text-book models as the harmonic oscillator. On the other hand, as the LTPDA toolbox is the data analysis toolbox for data analysis of the LISA Pathfinder mission, there exists a library of only LPF-related models. The science team of the mission is developing and testing one model (and some times several versions of the same model) for each of the subsystems that exist in the LISA Technology Package. This modeling effort is necessary to understand the behavior of the complete system. Moreover, during science operations several parameter estimation experiments will be performed in orbit. In these experiments, specific signals will be injected and the corresponding telemetry will be recorded. To this end, and in order to determine the specific characteristics or parameters of the experiment, a complete symbolic model of the satellite is needed (see section 7.3).

The ultimate goal of building a data analysis toolbox leads to the need of building a set of high level functions to operate and investigate the properties of the systems. These functions range from the obtention of the input or output names of the system to the possibility of running complete time domain simulations. These sets of high level functions that can operate on *ssm* objects are organized by functionality in Table 7.1. Their usage and specific functionality may be extracted from the documentation in Hewitson (2011). From the list in Table 7.1, we highlight functions that enable conversion to various LTI representations (e.g. `ssm2pzmodel`), provide a time-response of the system (`resp`), a frequency response (`bode`), state estimates (`kalman`), run simulations (`simulate`), generate a random state (`initialize`) or power spectral estimates (`cpsd`, `psd`), differentiates the states and outputs with re-

Functionality	Method
Constructor/Conversion	`ssm`
	`ssm2ss`
	`double`
	`ssm2pzmodel`
	`ssm2miir`
	`ssm2rational`
	`ssm2dot`
Transformation operator	`sMinReal`
	`simplify`
	`reorganize`
	`modifyTimeStep`
	`assemble`
System analysis	`isStable`
	`settlingTime`
	`steadyState`
	`bode`
	`cpsd`
	`psd`
	`simulate`
	`resp`
	`kalman`
	`parameterDiff`
Parameter management	`getParameters`
	`addParameters`
	`setParameters`
	`subsParameters`
	`findParameters`
Setters and plotters	`setName`
	`setDescription`
	`setParams`
	`setBlock-Properties`
	`setPort-Properties`
	`Dotview`
	`displayProperties`
	`display`
	`report`
	`viewHistory`
	`setPlotinfo`
Repository management	`csvexport`
	`submit`
	`save`
	`retrieve`

Table 7.1: Principal *ssm* methods grouped by functionality.

spect to a parameter (`parameterDiff`). Many other functions complete the class to provide with a thorough data analysis environment. Emphasis was placed on the velocity of the routines, and profiling sessions helped to reach a speed that allows for parameter estimation in few minutes. This feature will be very useful for live mission data analysis tasks, where fast analysis should be performed on the telemetered data in order to assure the good behavior of the instrument.

7.3 LISA Technology Package subblock modeling

The LTP dynamical closed loop is schemed in Fig. 7.1. Its dynamical equations can be written in the following form:

$$\begin{aligned} \mathbf{o} &= \mathbf{D}^{-1} \cdot \mathbf{S} \cdot \mathbf{f} + \mathbf{o}_{\mathrm{n}} \\ \mathbf{f} &= \mathbf{f}_{\mathrm{ext}} + \mathbf{f}_{\mathrm{n}} - \mathbf{A} \cdot \mathbf{C} \cdot \mathbf{T} \cdot (\mathbf{o} + \mathbf{o}_{\mathrm{i}}) - \mathbf{a}_{\mathrm{n}} \end{aligned} \tag{7.2}$$

where:

$\mathbf{x}$	:	are the kinematic variables of the experiment, i.e., position and velocities of the test masses and spacecraft,
$\mathbf{o}$	:	are the readings of the sensing mechanisms,
$\mathbf{o}_{\mathrm{n}}$	:	are the readout noises of the sensing mechanisms,
$\mathbf{o}_{\mathrm{i}}$	:	are the displacement guidance signals of the experiments,
$\mathbf{a}_{\mathrm{n}}$	:	are the actuators noises,
$\mathbf{f}_{\mathrm{a}}$	:	are the force/torques commands from the actuators,
$\mathbf{f}$	:	are the forces or torques acting on the test masses,
$\mathbf{f}_{\mathrm{ext}}$	:	are the forces or torques due to external effects, and
$\mathbf{f}_{\mathrm{n}}$	:	are the force/torque noises.

In this same figure, the main subsystems are:

D	:	the *Equations of Motion*,
S	:	the *Sensing mechanisms*,
T	:	the *Delay models*,
C	:	the *Controllers*,
A	:	the *Actuators*,
Force Noise	:	the different force/torque noise sources,
Sensing Noise	:	the different sensing noise sources, and
Actuators Noise	:	the different actuators noise sources,

7.3.1 Equations of motion

LISA Pathfinder is a three-body system composed of one spacecraft (SC) and two test masses (TM_1 and TM_2). Thus, 15 degrees of freedom need to be considered. The state vector is composed of the spacecraft attitude and rotation rate, followed by the position, velocity, attitude and rotation rate for both test masses. The coordinates are defined using many reference frames with tunable linear and angular offsets — inertial frame, body frames, instrument frames... — see Appendix A. The equations of motion were derived using the Euler-Lagrange and d'Alembert equations (Grynagier & Weyrich, 2008). Once the equations of motion are written, the variables corresponding to the spacecraft inertial motion can be removed as they are not observable, yielding 30 states. A basis change is then operated to express the state coordinates of TM_2 relatively to TM_1.

The equations of motion also model the linear stiffness caused by self-gravity and electrostatic forces, and by the linear drag. The input variables of this model are the actuation forces and torques from the actuators as well as the disturbance forces (or torques) from the space environment. This model returns the attitude and position of the test masses and spacecraft. The simplified equations of motion for a 1 dimensional system, only along the x-axis, where we only represent the position of TM_1 with respect to the spacecraft and the differential position between the two test masses are expressed in the Laplace domain as

$$\mathbf{D} = \begin{pmatrix} s^2 + \omega_1^2 + \frac{m_1}{m_{SC}}\omega_1^2 + \frac{m_2}{m_{SC}}\omega_2^2 & \frac{m_2}{m_{SC}}\omega_2^2 + \Gamma_x \\ \omega_2^2 - \omega_1^2 & s^2 + \omega_2^2 - \Gamma_x \end{pmatrix} \tag{7.3}$$

where ω_1 and ω_2 are the stiffness parameters coupling the motion of each test mass to the motion of the spacecraft, Γ_x represents the gravitational coupling between the two test masses, and s is the Laplace domain variable. m_1, m_2, and m_{SC} are, respectively, the masses of TM_1, TM_2 and the spacecraft. Since the equation of motion involves a second derivative we need up to 30 states for the 3-dimensional case where we want to represent 15 degrees of freedom and only 4 states for the example shown above with only 2 degrees of freedom. In this particular case, the states of the system would be the position and speed of TM_1 with respect to the spacecraft and the position and speed of the differential channel.

7.3.2 Sensing mechanisms

The sensors chains model how the real displacements and rotations are sensed or detected by the onboard instruments. The existing sensing mechanisms in LPF are the star tracker (Vitale, 2005), the inertial sensor (Dolesi et al., 2003; Hueller, 2003) and the interferometer (Heinzel et al., 2003). The star tracker delivers a measurement of the attitude of the satellite. The inertial sensors measure the position and

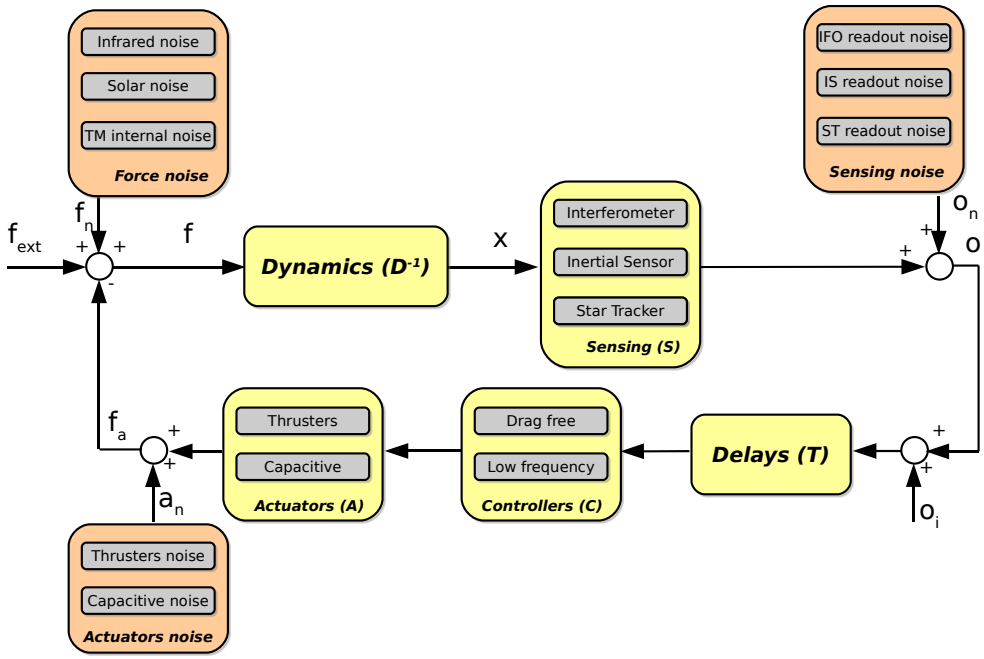

Figure 7.1: Control system architecture of LISA Pathfinder. **D** stands for the dynamical matrix, **S** represents the sensing matrix of the interferometer, i.e. the matrix translating the position of the test mass, **x**, into the interferometer readout, **o**, and $\mathbf{o_n}$ stands for the readout noise. **T** represents the processing delay transfer functions. **A** represents the physics of the FEEP and the electrostatic actuators, and finally **C**, is the controller matrix, implementing the drag free and low-frequency control loops. $\mathbf{o}_\mathrm{i}$ represents the displacement guidance signals. $\mathbf{a}_\mathrm{n}$ are the actuators noise and $\mathbf{f}_\mathrm{a}$ are the output forces of the actuators. $\mathbf{f}_\mathrm{ext}$ are the magnetic forces induced by the coils and $\mathbf{f}_\mathrm{n}$ are the environment force noises disturbing the spacecraft.

attitude of the test masses with respect to the electrode housing reference frame (see Appendix A) by measuring the change in capacity of the electrodes surrounding the test masses. Finally, the interferometer provides picometer precision measurements of the relative position between the two test masses and also delivers a redundant measurement of the absolute position of test mass 1. At the same time, it delivers differential attitude angles of the test masses by means of the measurements resulting from differential wavefront sensing (Heinzel et al., 2004). The interferometer is based on a non-polarizing heterodyne Mach-Zehnder design using a Nd:YAG laser (1064 nm) with a power of approximately 25 mW. The interferometer system has its own power and frequency stabilization loop (Heinzel et al., 2003). The LTP interferometer design contains four separate interferometer signals: (1) *x1* – *x2*, this

interferometer provides the main measurement, namely the distance between the two test masses and their alignment, (2) *x1*, this signal provides the distance between one test mass and the optical bench and the alignment of that test mass, (3) *reference*, this signal provides the reference phase for the above two measurements, and (4) *frequency*, this signal uses basically the same interfering beams as the *reference* signal, but with intentionally unequal path lengths so as to measure laser frequency fluctuations (Heinzel et al., 2004). This system is located between the two inertial reference sensors within the optical bench.

The outputs delivered by the differential channel of the interferometer are three orders of magnitude less noisy than the inertial sensor readings. As these systems have a much faster dynamics than the 10 Hz simulation we aim for, they were modeled with only a gain matrix D. That is, we did not include dynamics in the model. In this case the input to the sensing mechanisms are the real position and attitude variables of the test masses and the spacecraft, and their outputs are their actual readings (including errors and readout noise). To carry on with the one-dimensional example introduced in the previous section, the implementation of the sensing mechanisms and in particular of the interferometer is:

$$\mathbf{S} = \begin{pmatrix} 1 & 0 \\ \delta_{12} & 1 \end{pmatrix} \tag{7.4}$$

where δ_{12} is the interferometer channel cross-coupling. Thus, according to Eq. (7.4), the interferometer reading equations are:

$$o_1 = x_1 + o_{n1} \tag{7.5}$$

$$o_{12} = \delta_{12} \cdot x_1 + x_{12} + o_{n12} \tag{7.6}$$

where o_1 and o_{12} are the actual readings of the absolute and the differential channels delivered by the interferometer, respectively. x_1 and x_{12} are the real physical variables and o_{n1} and o_{n12} are the readout noises. These readout noises and their models are detailed in section 7.3.6

7.3.3 Delays

The readings delivered by the interferometer or the inertial sensors are processed by the Data Management Unit (DMU) (Anza et al., 2005; Cañizares et al., 2009), and by the Onboard Computer (OBC). This processing introduces delays in the readings before they reach the controller unit (see Fig. 7.1). These delays affect the stability of the control loop dynamics, therefore their modeling is essential to mimic the real behavior of the instrument. These delay systems take as input the readings of the three sensing mechanisms and deliver their delayed version as output. The theoretical functions modeling these delays for the one-dimensional example are:

$$\mathbf{T} = \begin{pmatrix} \mathrm{e}^{-\tau_1 s} & 0 \\ 0 & \mathrm{e}^{-\tau_{12} s} \end{pmatrix} \tag{7.7}$$

where τ_1 and τ_{12} are the processing delays affecting each of the channels under examination. The exponential function $\mathrm{e}^{-\tau s}$ is how a pure delay is modeled in Laplace domain. Actually, it is the Laplace domain transform of $\delta(t-\tau)$, where $\delta(t)$ is the Dirac function. The modeling of these delays within the *ssm* framework are introduced as Padé-approximants of order 2 or 3 (to be chosen by the user) (Kirk, 1970). Specifically, the transfer functions used to model these delays are:

$$\mathrm{e}^{-\tau s} \simeq \frac{12 - 6s\tau + (s\tau)^2}{12 + 6s\tau + (s\tau)^2} \tag{7.8}$$

for order 2 and

$$\mathrm{e}^{-\tau s} \simeq \frac{120 - 60s\tau + 12(s\tau)^2 - (s\tau)^3}{120 + 60s\tau + 12(s\tau)^2 + (s\tau)^3} \tag{7.9}$$

for order 3. These models imply 2 or 3 states, respectively, for each delayed signal. For instance, in the one-dimensional case, the usage of the second order approximation would imply 4 states for delay modeling (2 per degree of freedom).

7.3.4 Controllers

The control chain acts on the spacecraft to create a drag free environment. The Drag-Free and Attitude Control System (DFACS) is modeled using the transfer functions provided by Astrium GmbH. This model is the block C in Fig. 7.1. These controllers were derived based on the H-infinity technique (Ogata, 2001) and to satisfy the science requirements on all axis (Schleicher, 2009, 2008). These controllers are modeled along with sensor and actuation selection matrices, that allow to select different science/controlling modes. Each of these science modes uses a certain and precise combination of sensors (and sensed variables) and actuators (and actuation variables). The input variables to this model are the delayed readings of the three onboard sensing mechanisms. The outputs are the commands to the two onboard actuators. For the specific case of Science Mode 1, and particularly for the one-dimensional example, the reference variable to control the x-axis of the spacecraft is the reading of the first channel of the interferometer. This reading is processed by the Drag Free controller and sends the appropriate commands to the satellite thrusters in order to isolate TM_1 from the outer space perturbations and place the test mass in geodesic free fall. On the other hand, the differential reading of the interferometer is used by the low frequency suspension to control the position of test mass 2. This second control chain avoids the collision of TM_2 with the satellite walls. Moreover, it has very low gain within the measurement bandwidth in order

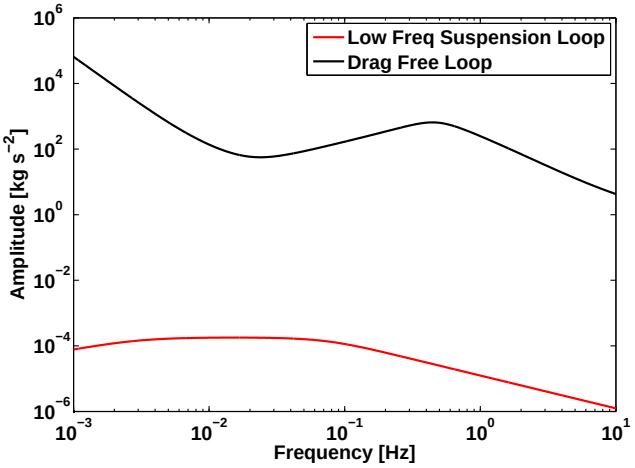

Figure 7.2: Transfer functions of the Low Frequency Suspension controller (red) and the Drag Free controller (black).

to minimize the interference of the controllers in the differential channel. The one dimensional model is written as:

$$\mathbf{C} = \begin{pmatrix} C_{\mathrm{DF}}(s) & 0 \\ 0 & C_{\mathrm{LFS}}(s) \end{pmatrix} \tag{7.10}$$

where $C_{\mathrm{DF}}(s)$ and $C_{\mathrm{LFS}}(s)$ are the drag free and the low frequency suspension controller transfer functions respectively. Their frequency responses are shown in Fig. 7.2 These transfer functions are 5 order polynomials in the Laplace domain, therefore for their state space representation we use 10 states for the entire one-dimensional controller. At the same time, it is interesting to note that this model incorporates various types of inputs such as guidance inputs, guidance acceleration signals, or force commands that enable the user to analyze the behavior of the system in specific circumstances.

7.3.5 Actuators

The actuators are the transfer function between the commanded forces/torques output by the controller blocks and the real forces/torques applied to the spacecraft or to the test masses. The two onboard actuation systems are the capacitive actuators (Vitale, 2005), which act on the test masses by applying specific electric currents to the electrodes that surround the test masses, and the FEEP thrusters (Bindel, 2008), which act on the spacecraft to create the drag free environment for TM_1. The capacitive actuator has faster dynamics than 10 Hz. Therefore, it is modeled with a simple gain matrix D. Nevertheless the microthrusters have been modeled with a

first order actuation response with a characteristic time of 0.06 s. This implies that their time response is delayed approximately 0.2 s, approximately 3τ (Kirk, 1970). The inputs of these models are the commands coming from the controllers and their outputs are forces/torques signals applied onto the test mass and spacecraft. These actuators, in the one-dimensional example, can be expressed as a diagonal matrix of Laplace functions:

$$\mathbf{A} = \begin{pmatrix} A_{\mathrm{FEEP}}(s) & 0 \\ 0 & A_{\mathrm{EA}}(s) \end{pmatrix} \tag{7.11}$$

where

$$A_{\mathrm{FEEP}}(s) = \frac{1/\tau}{s + 1/\tau} \qquad \text{and } \tau = 0.06\mathrm{s} \tag{7.12}$$

$A_{\mathrm{EA}}(s)$ is constant (no states required), are the physical models for the FEEP thrusters and the electrostatic actuators, respectively. Therefore, for the 1 dimensional model we only need 1 state to characterize the actuators.

7.3.6 Noise sources

The LPF mission goal is to demonstrate that the noise environment and the noise reduction techniques are compatible with the detection of gravitational waves (Vitale, 2005). Therefore, the science team and the industry have invested relevant efforts on characterizing and modeling different expected noise sources (Monsky et al., 2009; Brandt et al., 2010; Armano et al., 2009). The noise sources modeled in the `ssm` class can be classified into three categories: the actuators noise, the sensors noise and the external noise.

The actuators noise is expressed as a_n in Fig. 7.1 and it is composed of the thruster noise and the capacitive actuator noise. The micro-propulsion system of LISA Pathfinder is composed of 12 FEEP thrusters. The force noise of each individual thruster is modeled as (Schleicher, 2008):

$$|N_{\mathrm{thrusters}}(f)| = \left(\frac{f + 10^{-2}}{f + 10^{-3}}\right)^2 \tag{7.13}$$

where f is the frequency in Hz. Their contribution in the differential readout channel is not relevant but they represent the main disturbance source on the channel x_1 — the reading of the distance of test mass 1 to the spacecraft (Vitale, 2005). Specifically, in terms of acceleration noise, after including the dynamics and the control loops of the instrument, their contribution at 1 mHz in channel x_1 is 2×10^{-8} m s^{-2} Hz$^{-1/2}$ (see Fig. 7.3). The capacitive actuator noises are the most relevant instrument noise source in the differential channel at low frequency. Their modeling results from the hardware characterization of the electrode housing (Dolesi et al., 2003). System

identification techniques led to a fifth order degree transfer function used as noise shaping filter in our model. They contribute with up to 2×10^{-14} m s^{-2} Hz$^{-1/2}$ at 1 mHz. Due to their important contribution at low frequency in the differential channel in nominal science mode, alternative control modes are being developed within the mission, such as the Drift Mode (Grynagier, 2009), where the actuators noise is not existent.

The sensor noises are due to the readout noises of the three onboard mechanisms, namely the interferometer, the inertial sensors and the star tracker. They act on the LTP dynamics as additive noise to the reading outputs and are specified by o_n in Fig. 7.1. The most relevant noise source among these three in the differential axis is the contribution of the interferometer noise, as it is the most relevant disturbance at high frequency. Its noise shape filter is modeled as:

$$|N_{\mathrm{IFM}}(f)| = \left(\frac{f + 2 \times 10^{-2}/(2\pi)}{f + 2 \times 10^{-4}/(2\pi)} \right)^2 \tag{7.14}$$

where f is expressed in Hz. Taking into account the dynamics and the control loops of the instrument, this represents a contribution of 2×10^{-13} m s^{-2} Hz$^{-1/2}$ on the differential channel at 30 mHz but below requirement at 1 mHz (see Fig. 7.3). The contribution of the Inertial Sensor and the Star Tracker in the differential reading are negligible.

Finally, the third category of noise comprises the noise produced by external sources. These are force/torque noises that act on the test masses due to spacecraft sources or that act differentially between the spacecraft and the test masses due to exogenous sources, such as infrared noise or solar noise. These forces are represented as f_n in Fig. 7.1. Solar disturbances are due to the solar flux fluctuations impacting on the surfaces of the spacecraft. Infrared disturbances are due to the infrared emission from the spacecraft external surfaces. These two noise sources are the most important disturbance contributions on the spacecraft coordinates but they are highly attenuated by the control architecture and they turn out to be completely negligible in the interferometer readings. Finally, the test mass spacecraft disturbance noises are expected to be the most relevant sources at low frequency on the differential interferometer channel: their detection would imply the success of the mission. Their contribution has been estimated to be $\sim 3 \times 10^{-14}$ m s^{-2} Hz$^{-1/2}$ at 1 mHz.

These models characterize the noise filters that shape the white noise entering the simulator. These noise shaping filters are assembled as well with the entire system automatically, and reside in the model library with different options and parameters allowing the user to customize the noise model during mission science activities. To finish with the one-dimensional model, the complete model contains 23 states (4 from the equation of motions, 4 from the delay of the interferometer output model, 4 from the delay of the inertial sensors, 1 from the FEEPS actuators and 10

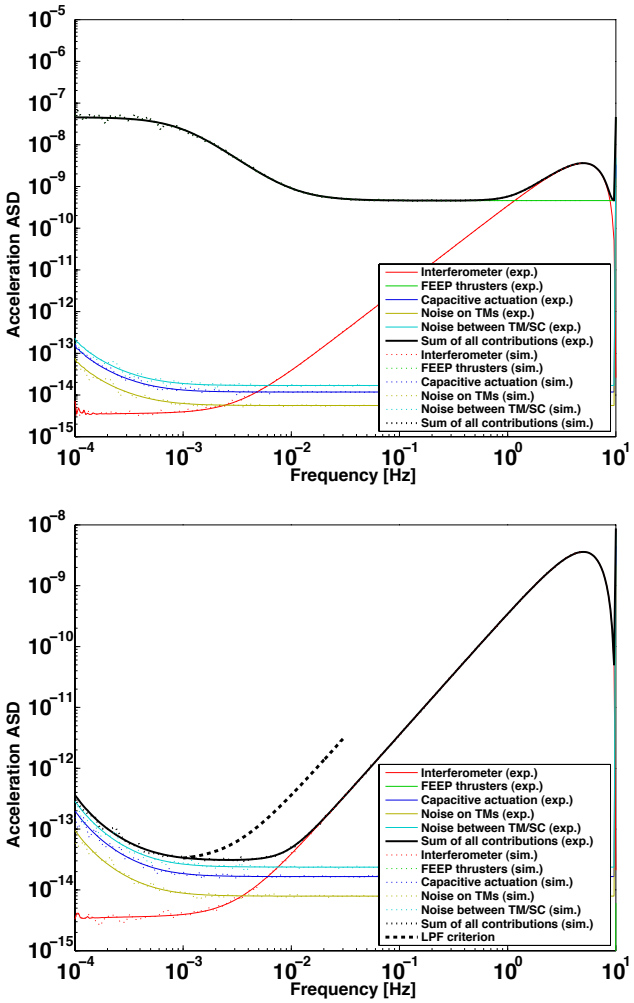

Figure 7.3: Top panel: acceleration noise breakdown for channel 1 (observed along the sensitive axis of the spacecraft to TM_1). Bottom panel: acceleration noise breakdown for the differential channel (from TM_1 to TM_2 along the sensitive axis). Values were derived using the `psd` function on one side, and using `simulate` and `spsd` on the other side.

from the DFACS controllers. The modeling of the noise shape filters represent 27 extra states. Thus, in total we obtain a complete one-dimensional model (dynamical model and noise sources) with 50 states. To give an order of magnitude, the full three-dimensional LISA Pathfinder model (with noise shape filters) is composed of 532 tunable parameters, 27 input blocks, 20 state blocks (containing 615 state variables) and 32 output blocks.

7.4 Simulations

The characterization of each of the submodels of LISA Pathfinder individually, and their codification within the `ssm` framework, enables the possibility of using all these subblocks to build a complete LPF simulator. The result yields a high-dimensionality state space object where the user can perform several data analysis operations, as if the science team was simulating mission operations. This complete `ssm` object contains the physics of all its subsystems. The user can perform 10 000 s time domain simulations of the three-dimensional dynamics of the spacecraft in less than 1 minute computation time in a standard 1 GHz computer. Previously developed techniques within the mission, based on Laplace transfer function did not allow to easily implement a complete system with more than one dimension (Monsky et al., 2009). On the other hand, the only available three-dimensional simulation is the one delivered by Astrium (Brandt & et al., 2004). Their simulator is based on `Simulink` and runs only 2 times faster than real time, thus excessively slow for data analysis purposes. Moreover, parametric or symbolic systems are not accepted in this simulator.

We have done a noise breakdown simulation of the mission to test the agreement of the model with theoretical results. In this simulation we have used a complete 3 dimensional LISA Pathfinder model including all its sub-models and noise sources. We have then obtained the time domain simulations of the kinematic readings and the accelerations of the absolute and differential channel. Fig. 7.3 shows the theoretical and simulated power spectral densities of each noise contribution in each of these channels. This figure illustrates that the noise projection output by the simulator agrees with the results expected in the science requirement document of the mission (Vitale, 2005). In the differential channel (main scientific channel of the mission), the overall acceleration noise projection is below the 3×10^{-14} m s^{-2} Hz$^{-1/2}$ requirement at 1 mHz — see Fig. 7.3, bottom plot. At the same time, it can be seen that the most prominent source in the absolute channel is the FEEP thrusters, as expected. In the differential channel the most relevant noise sources are the test-mass noises at low frequency (Vitale, 2005) and the interferometer noise at high frequency (Vitale, 2005; Armano et al., 2009).

7.5 Conclusions

We have presented the state space model class for LISA Pathfinder within the LTP Data Analysis toolbox (LTPDA). This class will play a major role in data analysis procedures as it represents a fast and accurate methodology to model the complete instrument. The `ssm` class takes advantage of the mathematical characteristics of the state space representation to model MIMO systems preserving the physical information of the system, i.e., its input names, units of its parameters, physical description of its internal states,... All subsystems identified in the LTP instrument have been

modeled and validated independently, making this tool highly flexible and modular, therefore suitable for mission operations. We have described the main characteristics of each of the main sub-models in the mission library. We have shown that the LTPDA tool allows the user to build a complete LISA Pathfinder three-dimensional system in a single `ssm` object by automatic assembling of the relevant submodels. The user can perform fast, accurate and realistic data analysis procedures with this complete model. The modeling approach adopted here and presented in this chapter has been shown to be successful and can be applied to other space missions or other modeling frameworks. Moreover, it has been extensively used in the design and preparation of all the magnetic experiments studied throughout this thesis.

Chapter 8

Summary and Conclusions

In this last chapter we summarize the most important results reported in this thesis and we draw the main conclusions. We also suggest some plausible future investigation lines to be undertaken in the future.

8.1 Summary of the thesis

This thesis has been structured in four different blocks:

- *Introductory chapters to Gravitational Waves, LISA and LISA Pathfinder (LPF) (Chapters 1 & 2)*: We describe the physics of gravitational waves, their origin and their main characteristics. We introduce as well the present status of the most relevant gravitational wave ground detectors, such as LIGO and VIRGO. We introduce LISA as the mission expected to be the first space gravitational wave detector, thus we present here its characteristics and objectives. The need for a technological demonstrator leads us to LISA Pathfinder, LISA's precursor mission. We describe its status, its characteristics and its main goals. Finally, we put forward the role of the Data management and Diagnostics Subsystem in LPF, and we highlight the importance of the Magnetic Diagnostics Subsystem. In this respect we present the different magnetic contributions to the total differential acceleration reading of the LISA Technology Package (LTP).

- *Design of the inflight magnetic experiment and its data analysis procedures for the estimation of the magnetic properties of the test masses of LPF (Chapters 3 & 4)*: We present the magnetic experiment that will be performed in orbit to determine the value of the three components of the remanent magnetic moment of the test masses and their susceptibility. To this end, we present the hardware and the characteristics of the signals involved in the experiments, and we report its expected results.

- *Data analysis algorithms to infer the magnetic field and its gradient at the locations of the test masses (Chapters 5 & 6)*: We introduce the magnetic field interpolation problem, which implies the estimation of the magnetic field and its gradient at the location of the test masses using the measurements delivered by the onboard magnetometers. We present several interpolation methods, we assess their performance, and we choose neural networks as our preferred method.

- *Description of the LTP simulator built-in within the LTPDA toolbox (Chapter 7)*: We describe the LTP Data Analysis tool that is being developed for data analysis operations. Specifically, we focus on the LTP dynamics simulator developed within the State Space Model framework of the LTPDA tool.

8.2 Conclusions

This thesis has focused on the estimation of the contribution of the magnetic effects to the total differential acceleration measurement between the two onboard test masses. The main objective of the thesis has been the determination of an upper bound for the uncertainty of this estimate. To do this we used specific data analysis to address two different problems: (1) the design and analysis of the magnetic experiments to estimate the remanent magnetic moment and susceptibility of the test masses of LTP, and (2) the analysis and processing of the data streams delivered by the onboard magnetometers to estimate the magnetic field and its gradient at the locations of the test masses.

With respect to the estimation of the magnetic remanent magnetic moment and susceptibility of the test masses we have contributed to:

- The design of the inflight experiment that will estimate the magnetic properties of the test masses. This experiment will consist in the processing of the kinematic excursions of the test masses when they are excited by the magnetic forces and torques produced by the onboard coils.

- Studying the magnetic force along the x-direction (the sensitive axis connecting both test masses). We have found that the force presents a double-frequency behavior when a sinusoidal current circulating through the onboard coils is injected. On the other hand, the torques acting on the test masses present a single frequency response.

- Characterizing the estimation of the magnetic parameters of the test masses (the remanent magnetic moment and the susceptibility). We found that they can be estimated with three single measurements obtained from the onboard interferometer, i.e. the x-axis displacement, and the rotations about the y-

and z-axes (the z-axis points to the solar panel). The kinematic excursion detected along the sensitive axis (x-axis) between the two test masses is below 8 nm while the corresponding rotations have amplitudes of ~ 4 μrad. These displacements and rotations do not exceed the authority limits of the *drag-free* and *low-frequency* controllers. Therefore, we confirmed that the usage of the coils will not produce harmful effects on the LTP instrument and will provide sufficient signal-to-noise ratio (SNR) for parameter estimation.

- Determining the cross-couplings between rotations and displacement axes. We found that they are not negligible in the LTP instrument. Therefore, in order to estimate the susceptibility and magnetic moment of the test masses we needed a three-dimensional analysis model. We discarded the one-dimensional approach because it induces constant biases of more than 1% in the estimates.

- Quantifying the effect of the uncertainty in the capacitive actuator gain in the *force-to-displacement* LTP transfer function. We concluded that this uncertainty is critical for the accuracy of the estimates and that it depends on the excitation frequency of the coils.

- Computing the SNR of the readings of the interferometer, x-, y-, and z-readings, which we found to be also frequency dependent.

- Conducting a joint optimization of these two frequency-dependent effects. We showed that excitation currents through the coils at 5 mHz, instead of 1 mHz, deliver more robust and accurate results. We also found that the estimates of the magnetic characteristics of the test masses have a zero bias and a standard deviation of $\sim$1% of relative error. Moreover, we also demonstrated that a robust estimation can be achieved combining the estimations at different frequencies. This approach ensures robustness in front of non-modeled frequency-dependent effects.

Concerning the estimation of the magnetic field at the location of the test masses we found that:

- Classical interpolation methods with only 4 tri-axial magnetometers (12 independent measurements) allow us to perform only a *linear* interpolation. For this particular application these methods are not sufficient since they deliver averaged estimation errors on the order of up to 400% for each of the field components.

- These limitations can be overcome with a novel approach based on neural networks. We showed that extensive ground testing data will allow to perform an appropriate training of the network model, and that the magnetic field at

the locations of the test masses can be inferred with a standard deviation of only 5%.

- The statistical outputs delivered by the neural network model are better than those delivered by the classical method, as the classical methods leads to high skewness and kurtosis values. This shows that these estimates are not symmetrical and have an important number of outliers. This behavior is not observed with the neural network interpolation model.
- The interpolation model is robust at the 10% error level, with respect to the error in the training vectors (on ground measured data). Moreover, the interpolation model is robust with respect to plausible offsets in the magnetometers readings.
- The uncertainty in the mechanical precision of the heads of the magnetometers propagates into the magnetic field estimates below the 5% error level.
- Appropriate training enables to estimate low-frequency drifts in the magnetic field time evolutions.
- A hybrid interpolation algorithm presents a quasi-autonomous magnetic field interpolation framework for LPF. Nevertheless, we stress the need for having extensive ground test data to build the magnetic model data base.
- In summary, neural network interpolation algorithms are a valid alternative to process the magnetic readings delivered by the magnetometers onboard LISA Pathfinder, since they are expected to deliver estimates with uncertainties below the 10% level in any mission scenario.

Finally, once these two separate tasks are performed, a remaining goal consists in assessing how their uncertainties project into the precision of our estimate of the magnetic contribution to the total differential acceleration reading in LPF. To do this, we propagated the errors of the determination of the magnetic characteristics and the magnetic field and gradient into the calculation of the magnetic acceleration noise. The error propagation is computed as:

$$\sigma_{\text{total}} = \sqrt{\sum_{i=1}^{N} \left(\frac{\partial f}{\partial s_i} \sigma_{s_i} \right)^2},$$

where f is the total function of the magnetic effects and s_i are the several sources of error. In our case, these sources of error are (1) the uncertainty on the magnetic field and gradient determination and (2) the uncertainty on the estimation of the remanent magnetic moment and susceptibility of the test masses. The results of this error propagation are shown in Table 8.1.

Table 8.1: Budget of the contribution of the magnetic field effects to the total acceleration noise and their uncertainties. These uncertainties are computed using the expected error of the magnetic characteristics, which were computed in chapters 3 and 4, and using the expected error of the magnetic field determination reported in chapters 5 and 6.

Contribution	Differential acceleration noise [m s^{-2} Hz$^{-1/2}$]
Fluctuation of the spacecraft magnetic field	$(0.680 \pm 0.096) \times 10^{-15}$
Fluctuation of the spacecraft magnetic field gradient	$(1.097 \pm 0.108) \times 10^{-15}$
Down converted AC magnetic fields	$(1.265 \pm 0.254) \times 10^{-15}$
Interplanetary magnetic field fluctuation	$(1.701 \pm 0.241) \times 10^{-15}$
Lorentz force	$(0.013 \pm 0.001) \times 10^{-15}$
Total of magnetic effects	$(2.775 \pm 0.425) \times 10^{-15}$
Requirement of magnetic effects	12.0×10^{-15}

To put it in short, the data analysis algorithms presented in this dissertation determine the total magnetic contribution with an standard deviation of 0.425×10^{-15} m $^{-2}$ Hz$^{-1/2}$. Thus, using neural networks and optimized magnetic experiments, the magnetic contribution is determined within the 15% relative error level. In comparison, using the formerly disregarded data analysis methods, i.e. the multipole interpolation scheme and the non-optimized magnetic experiments, this contribution could only be determined with errors at the 130% level. Therefore, using the techniques presented in this thesis, the overall performance of the estimate has been enhanced by one order of magnitude.

8.3 Future work

Following the investigations described in this dissertation, a number of studies can be undertaken, and most of them could be of interest for LISA. Specifically, the experience gained from the design, definition and implementation of the data analysis algorithms for the Magnetic Diagnostics Subsystem of LISA Pathfinder will be of great value for LISA or other gravitational waves missions. For instance, the need for placing the magnetometers closer to the test mass and changing its technology from fluxgate to AMR is already under investigation now. Moreover, useful insights can be provided to define the position of the future LISA coils or other active magnetic hardware used to infer the properties of the LISA test masses.

Concerning the estimation of the magnetic characteristics of the test masses in LPF, the effect of non-homogeneities of the magnetic moment in the overall estimation can also be assessed. The magnetic moment of the test mass is due to the specific distribution of its inner dipoles throughout the entire volume, which are normally grouped in so-called magnetic domains (Jackson, 1999). This distribution is not expected to be homogenous. Thus, new studies are needed to assess this circumstance in the estimation of the properties of the test masses. Also, excitations at higher frequencies or differential excitations with both coils could be the subject of further investigations.

Last but not least, a straightforward future line of work to be performed concerns the inference of the magnetic field using a calibrated interpolation model with the available measured data. Particularly, all data recorded in the magnetic test campaign performed at Astrium Stevenage should be used and a complete magnetic model database should be built. This calibration is essential to deliver good quality data out of our neural network interpolation algorithm. Furthermore, even if the neural network approach has been presented as one valid alternative, several other supervised techniques, such as bayesian approaches or clustering techniques, could also be investigated.

Appendix A

Reference frames and coordinate definitions for LTP

This appendix describes briefly the main reference coordinate frames defined for LISA Pathfinder. These conventions have been used throughout the entire volume.

A.1 Reference Frames

Geodesic Reference Frame (J)

The Earth centered geodesic J2000 (true date) reference frame is defined as follows:

- JO: The origin is defined as the center of the Earth.
- JX: Is defined in the direction of the vernal equinox on January 1, 2000 at 12 noon.
- JY: Completes the right hand system.
- JZ: Is defined in the direction of the Earth's North Pole on January 1, 2000 at 12 noon.

Mechanical Reference Frame (M)

The mechanical reference frame is the Science Spacecraft principal reference frame. It is defined as follows:

- MO: The origin is at the separation plane between the Science Spacecraft and the Propulsion Module, on the centerline of the cylinders.
- MX: Is defined parallel to the LTP centerline with the positive direction towards test mass 1.

- MY: Completes the right hand system.
- MZ: Is pointing up towards the solar array.

Body Reference Frame (B)

The body reference frame is defined as the science spacecraft AOCS control frame. It is defined as follows:

- BO: The origin is at the predicted nominal (or real, measured) center of mass of the Science Spacecraft.
- BX: Is defined parallel to the LTP centerline with the positive direction towards test mass 1.
- BY: Completes the right hand system.
- BZ: Is pointing up towards the solar array.

Optical Bench Reference Frame (O)

The optical bench frame is defined as follows:

- OO: The geometrically derived center of the optical bench.
- OX: Along the geometrically derived x-axis, pointing from origin towards test mass 1.
- OY: Completes the right hand system.
- OZ: Perpendicular to OX, pointing away from (and with no intersection with) the optical bench plane.

Magnetic Experiments Reference Frame (MEF)

The magnetic experiments described in this thesis have been referenced to the Magnetic Experiments Reference Frame. This frame is defined as follows:

- OO: The center point of the line connecting the two test mass centers translated 0.6093 m away from the solar array along the OZ axis of O frame.
- OX: Along the geometrically derived x-axis (axis connecting test mass 1 and test mass 2), pointing from origin towards test mass 2.
- OY: Completes the right hand system.
- OZ: Perpendicular to OX, pointing towards the solar array (parallel to the OZ axis of the O frame).

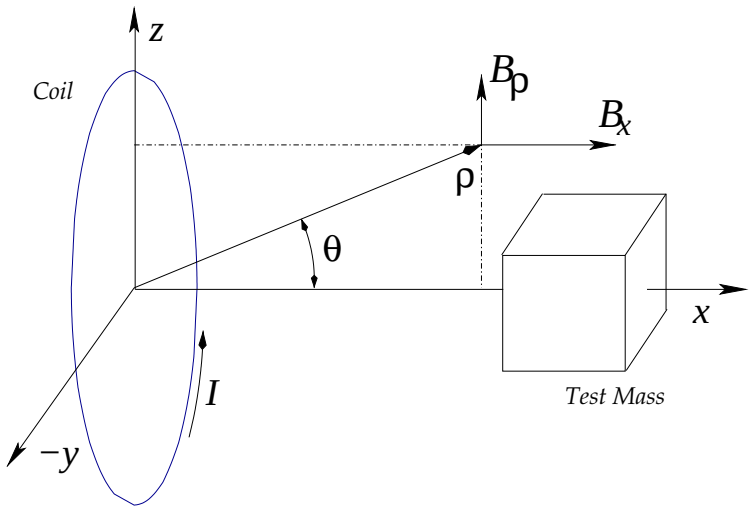

Figure A.1: The coils reference frame (CF) is a coordinate reference frame centered at the center of the induction coils. This reference frame is used for magnetic field calculation, therefore we represent I as the current circulating through the coil, B_ρ is the perpendicular component of the field and B_x is the longitudinal component.

Coils Reference Frame (CF)

The calculation of the magnetic field generated by the onboard coils is done with respect to a reference frame centered at each of the coils (see Fig. A.1):

- OO: The center point of the induction coil.
- OX: Along the geometrically derived x-axis (axis connecting the coil with the test mass), pointing from origin towards the test mass.
- OY: Completes the right hand system.
- OZ: Perpendicular to OX, pointing towards the solar array (parallel to the OZ axis of the O frame).

Electrode Housing Frames (H1, H2)

The two test masses are numbered in such a way that the test mass that is closer to the fiber injectors is called test mass 1. This is the test mass whose distance is measured with respect to the optical bench. The other test mass is denoted test mass 2. The housing frame test mass 1 or H1-frame is defined as follows:

- H1O: Center of electrode housing of test mass 1. The center is defined as the nominal position of test mass 1 during science measurements.

- H1X: Along the geometrically derived x-axis of the electrode housing, pointing away from the optical window.
- H1Y: Completes the right hand system.
- H1Z: Along the geometrically derived x-axis of the electrode housing pointing up.

The housing frame of test mass 2 or H2-frame is defined as follows:

- H2O: Center of electrode housing of test mass 2. The center is defined as the nominal position of test mass 2 during science measurements.
- H2X: Along the geometrically derived x-axis of the electrode housing, pointing towards the optical window.
- H2Y: Completes the right hand system.
- H2Z: Along the geometrically derived x-axis of the electrode housing pointing up.

Test Mass Frames (T1,T2)

The body reference frame of test mass 1 or T1-frame is defined as follows:

- T1O: Center of mass of test mass 1.
- T1X: Principal axis of test mass 1, nominally aligned with H1X.
- T1Y: Principal axis of test mass 1, nominally aligned with H1Y.
- T1Z: Principal axis of test mass 1, nominally aligned with H1Z.

The body reference frame of test mass 2 or T2-frame is defined as follows:

- T2O: Center of mass of test mass 2.
- T2X: Principal axis of test mass 2, nominally aligned with H2X.
- T2Y: Principal axis of test mass 2, nominally aligned with H2Y.
- T2Z: Principal axis of test mass 2, nominally aligned with H2Z.

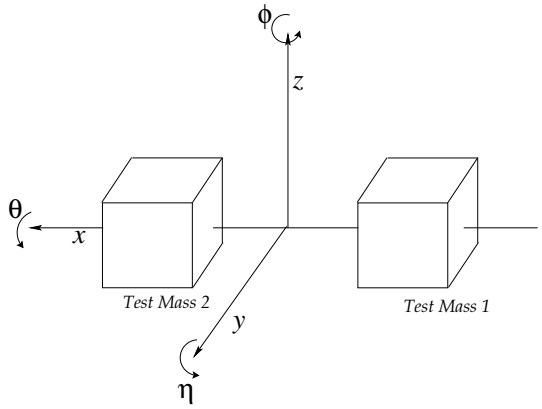

Figure A.2: Attitude parametrization.

A.2 Coordinate Definitions

Attitude parametrization

Whenever attitude is parameterized as a rotation sequence, the following convention of a 1-2-3 rotation sequence is used.

1. First rotation around the x-axis, angle θ.
2. Second rotation around the new y-axis, angle η.
3. Third rotation around the new z-axis, angle ϕ.

For the test mass attitude with respect to the housing frames, lower case Greek letters are used, whereas upper case Greek letters are used for the spacecraft attitude with respect to the inertial frame.

Test Mass coordinates

For each test mass, the relative coordinate is defined as the relative displacement and relative attitude of the test mass fixed frames (T1 and T2) with respect to the respective housing frames (H1 and H2). The relative coordinates are:

$$\begin{aligned} \mathbf{q_1} &= (x_1, y_1, z_1, \theta_1, \eta_1, \phi_1) \\ \mathbf{q_2} &= (x_2, y_2, z_2, \theta_2, \eta_2, \phi_2) \end{aligned} \tag{A.1}$$

Inertial attitude

The inertial attitude is defined as the attitude of the B-frame with respect to the J-frame. The attitude is denoted by the angles Θ, H and Φ.

Appendix B

Magnetic data from the ACE mission

This appendix briefly describes the main results obtained by the magnetometer operated in the Advanced Composition Explorer (ACE) mission. This instrument delivers magnetic field measurements at the first lagrangian point (L1) of the Earth-Sun system, exactly where LISA Pathfinder is planned to be located. Thus, the ACE Magnetic Field Experiment will establish the time-varying, large-scale structure of the interplanetary magnetic field at this point as derived from continuous measurement of the local field at the spacecraft.

B.1 ACE magnetic experiment description

The magnetic field experiment on ACE provides continuous measurements of the local magnetic field in the interplanetary medium (Smith et al., 1998). The experiment consists of a pair of twin, boom-mounted, triaxial fluxgate sensors which are located 4.19 m from the center of the spacecraft on the opposite solar panels. The electronics and Digital Processing Unit is mounted on the top deck of the spacecraft. The two triaxial sensors provide a balanced, fully redundant vector instrument and allow an enhanced assessment of the properties of the magnetic field at L1 (the first Lagrangian point of the Earth-Sun system). Data recorded by this instrument is available online[1]. Moreover, real-time observations with a resolution of 1 second are provided continuously to the Space Environmental Center (SEC) of the National Oceanic and Atmospheric Administration (NOAA) for near-instantaneous, world-wide dissemination as a free service to pursue space weather studies. The ACE experiment uses fully redundant systems and extremely conservative designs. Data processing for the instrument is led by the University of New Hampshire.

[1] `http://www.ssg.sr.unh.edu/mag/ACE.html`

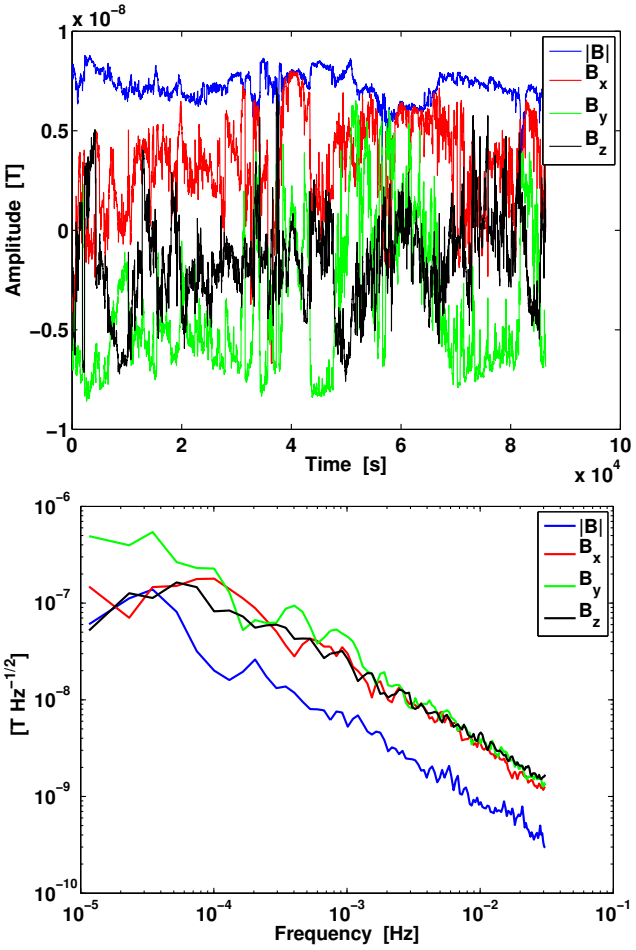

Figure B.1: a) Magnetic field time series of day 67 in year 2000 (March 2000, month of the last solar maximum up to the date of writing.) b) Amplitude spectral density of the magnetic field components for the same data series.

As mentioned, the results of the ACE experiment are particularly interesting for LISA Pathfinder, as its orbit is also designed to be around the same Lagrangian point. In the present study we have adopted that the interplanetary DC magnetic field was 10 nT, whereas its fluctuation was 55 nT $\mathrm{Hz}^{-1/2}$. These are reasonable values, but we can use the ACE magnetic data to validate them. To this end, we processed two sets of data. The first one corresponds to data from October 2010, while for the second one we picked up data from the last solar maximum, which took place in March, 2000. In Fig. B.1 we plot the time evolution of the three components and the modulus of the magnetic field for the second set of data along with their amplitude spectral density. In this way we can obtain the maximum DC

field values and the maximum fluctuations at 1 mHz. For the B_x component, the maximum magnetic field value is of 12 nT (day 296, year 2010) and the maximum fluctuations are of 31 nT $Hz^{-1/2}$ (day 67, year 2000), somewhat lower than assumed. However, this study, even if not exhaustive, shows that the order of magnitude of the interplanetary magnetic field at L1 adopted here is correct.

Appendix C

Calculation of the magnetic field produced by the LTP coils

This appendix details the calculations of the magnetic field and the gradient of the magnetic field produced by the coils onboard the LISA Technology Package.

C.1 Magnetic field calculation

Consider a circular coil of radius a and of N loops of metallic wire through which an electric current I flows. Reference coordinates are shown in Fig. C.1. Specifically, they can be made explicit:

$$x = x \ , \quad y = \rho\cos\theta \ , \quad z = \rho\sin\theta \tag{C.1}$$

so that $\rho = (x^2+y^2)^{1/2}$. The angle θ is an azimuthal angle around x, which increases in the direction of I — see Fig. C.1.

From geometrical considerations it is obvious that the magnetic field $\mathbf{B}$ has axial symmetry, i.e., only the x- and ρ- components are different from zero, and do not depend on θ. They are given by

$$B_\rho(x,\rho) = \frac{\mu_0}{4\pi}\frac{N\pi a^2 I}{(a\rho)^{3/2}}\frac{k}{\pi}\frac{x}{a}\left[-K(k)+\frac{1-k^2/2}{1-k^2}E(k)\right] \tag{C.2a}$$

$$B_x(x,\rho) = \frac{\mu_0}{4\pi}\frac{N\pi a^2 I}{(a\rho)^{3/2}}\frac{k}{\pi}\left[\frac{1}{2}\frac{k^2}{1-k^2}E(k)\right] - \frac{\rho}{x}B_\rho(x,\rho) \tag{C.2b}$$

where

$$k^2 = \frac{4a\rho}{x^2+(a+\rho)^2} \tag{C.3}$$

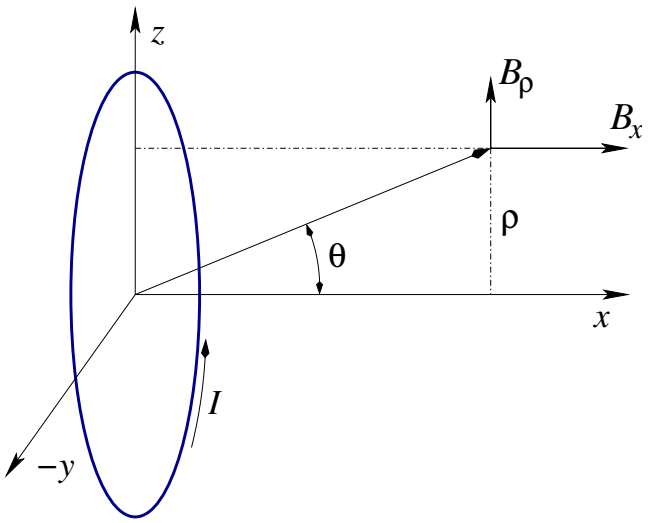

Figure C.1: Coordinate reference frame for the magnetic field calculation.

and

$$K(k) \equiv \int_0^{\pi/2} (1 - k^2 \sin^2 \phi)^{-1/2}\, d\phi \ , \qquad E(k) \equiv \int_0^{\pi/2} (1 - k^2 \sin^2 \phi)^{1/2}\, d\phi \quad \text{(C.4)}$$

are elliptic integrals of the first and second kind, respectively (Abramowitz, 1972). The Cartesian components of the field are given by:

$$B_x(x,\rho) = B_x(x,\rho) \ , \qquad B_y(x,\rho) = \frac{y}{\rho} B_\rho(x,\rho) \ , \qquad B_z(x,\rho) = \frac{z}{\rho} B_\rho(x,\rho) \quad \text{(C.5)}$$

C.2 Gradient calculation

We are now interested in the gradient components of the field. To the effect, we recall that

$$\boldsymbol{\nabla} \times \mathbf{B} = \boldsymbol{\nabla} \cdot \mathbf{B} = 0 \quad \text{(C.6)}$$

i.e., the derivatives matrix $\partial B_i / \partial x_j$ is symmetric and traceless. Hence, only 5 of its 9 components are independent. We can choose them arbitrarily, and the choice we make is the following:

$$\frac{\partial B_x}{\partial x} \ , \quad \frac{\partial B_y}{\partial x} \ , \quad \frac{\partial B_z}{\partial x} \ , \quad \frac{\partial B_y}{\partial y} \ , \quad \frac{\partial B_y}{\partial z} \quad \text{(C.7)}$$

Because of the symmetry of the field, all of these components are expressible as linear combinations of the four derivatives

$$\frac{\partial B_x}{\partial x}\,, \quad \frac{\partial B_x}{\partial \rho}\,, \quad \frac{\partial B_\rho}{\partial x}\,, \quad \frac{\partial B_\rho}{\partial \rho} \tag{C.8}$$

In fact, the relationships between Eqs. (C.7) and (C.8) can be easily established, and is the following:

$$\frac{\partial B_x}{\partial x} = \frac{\partial B_x}{\partial x} \tag{C.9a}$$

$$\frac{\partial B_y}{\partial x} = \frac{y}{\rho}\frac{\partial B_\rho}{\partial x} \tag{C.9b}$$

$$\frac{\partial B_z}{\partial x} = \frac{z}{\rho}\frac{\partial B_\rho}{\partial x} \tag{C.9c}$$

$$\frac{\partial B_y}{\partial y} = \frac{y^2}{\rho^2}\frac{\partial B_\rho}{\partial \rho} + \frac{z^2}{\rho^2}\frac{1}{\rho}B_\rho \tag{C.9d}$$

$$\frac{\partial B_y}{\partial z} = \frac{yz}{\rho^2}\left(\frac{\partial B_\rho}{\partial \rho} - \frac{1}{\rho}B_\rho\right) \tag{C.9e}$$

We now recast Eqs. (C.2) in the handier form

$$B_\rho(x,\rho) = A_\rho \frac{x}{\rho^{3/2}} F(k) \tag{C.10a}$$

$$B_x(x,\rho) = A_x\,\rho^{-3/2}\,G(k) - \frac{\rho}{x}B_\rho(x,\rho) \tag{C.10b}$$

where

$$A_\rho \equiv \frac{\mu_0}{4\pi}\frac{N\pi a^2 I}{\pi a^{5/2}}\,, \qquad A_x \equiv \frac{\mu_0}{4\pi}\frac{N\pi a^2 I}{2\pi a^{3/2}} = \frac{a}{2}A_\rho \tag{C.11}$$

are quantities not depending on either x or ρ, and where abbreviations are defined by

$$F(k) = k\left[\frac{1-k^2/2}{1-k^2}E(k) - K(k)\right] \tag{C.12a}$$

$$G(k) = \frac{k^3}{1-k^2}E(k) \tag{C.12b}$$

We can now proceed to evaluate the four quantities given in Eq. (C.8). For that we note that

$$\frac{\partial F}{\partial x} = \frac{\partial k}{\partial x}\frac{dF}{dk}\,, \qquad \frac{\partial F}{\partial \rho} = \frac{\partial k}{\partial \rho}\frac{dF}{dk} \tag{C.13}$$

and likewise with $G(k)$. The following is easily found:

$$\frac{\partial k}{\partial x} = -\frac{x}{4a\rho}k^3\,, \qquad \frac{\partial k}{\partial \rho} = \frac{x^2+a^2-\rho^2}{8a\rho^2}k^3 \tag{C.14}$$

To calculate the derivatives $F'(k)$ and $G'(k)$ requires expressions for the derivatives of the elliptic functions. It can be proved that

$$\frac{dE}{dk} = \frac{E(k) - K(k)}{k} \tag{C.15a}$$

$$\frac{dK}{dk} = \frac{1}{k}\left[\frac{E(k)}{1-k^2} - K(k)\right] \tag{C.15b}$$

A bit of algebra shows that

$$F'(k) \equiv \frac{dF}{dk} = \frac{1-k^2+k^4}{(1-k^2)^2}\,E(k) - \frac{1-k^2/2}{1-k^2}\,K(k) \tag{C.16a}$$

$$G'(k) \equiv \frac{dG}{dk} = \frac{k^2}{1-k^2}\left[\frac{4-2k^2}{1-k^2}\,E(k) - K(k)\right] \tag{C.16b}$$

We can now finally express the four derivatives in Eq. (C.8):

$$\frac{\partial B_\rho}{\partial x} = A_\rho\,\rho^{-3/2}\left[F(k) - \frac{x^2}{4a\rho}\,k^3F'(k)\right] \tag{C.17a}$$

$$\frac{\partial B_\rho}{\partial \rho} = A_\rho\,\frac{x}{\rho^{5/2}}\left[-\frac{3}{2}\,F(k) + \frac{x^2+a^2-\rho^2}{8a\rho}\,k^3F'(k)\right] \tag{C.17b}$$

$$\frac{\partial B_x}{\partial x} = -A_x\,\frac{x}{4a\rho^{5/2}}\,k^3G'(k) - \frac{\rho}{x}\left[\frac{\partial B_\rho}{\partial x} - \frac{1}{x}\,B_\rho\right] \tag{C.17c}$$

$$\begin{aligned}\frac{\partial B_x}{\partial \rho} &= \frac{A_x}{\rho^{5/2}}\left[-\frac{3}{2}\,G(k) + \frac{x^2+a^2-\rho^2}{8a\rho}\,k^3G'(k)\right] \\ &- \frac{\rho}{x}\left[\frac{\partial B_\rho}{\partial \rho} + \frac{1}{\rho}\,B_\rho\right]\end{aligned} \tag{C.17d}$$

These expressions suffice to determine (analytically) all five gradient components in Eq. (C.7), thanks to the equalities provided by Eqs. (C.9). The final expressions are, however, a bit cumbersome.

Appendix D

Estimation of parameters using linear least squares

This appendix reviews the basic procedures needed to estimate parameters using a least squares technique. It also gives the resulting expression to estimate one and two amplitude parameters from a single channel measurement.

D.1 Least square theory

In linear regression using least squares (Wolberg, 2005), we fit the data to a linear model. For the sake of clarity, in this appendix we use upper case bold letters to represent matrices and lower case bold letter to represent vectors. Thus, a regression equation can be written as:

$$\mathbf{y} = \mathbf{X} \cdot \boldsymbol{\beta} + \mathbf{e} \tag{D.1}$$

where $\mathbf{y}$ are the measurements, which are assumed to be a $T \times 1$ vector (it can be considered a single channel output with T samples), $\mathbf{X}$ are our regressors, which are assumed to be a $T \times K$ matrix, $\boldsymbol{\beta}$ is the parameter vector, which is assumed to be a $K \times 1$ vector, $\mathbf{e}$ are the errors, which are considered vector of $T \times 1$. We want to minimize the sum of the squared errors:

$$S(\boldsymbol{\beta}) = \mathbf{e}' \cdot \mathbf{e} = (\mathbf{y} - \mathbf{X} \cdot \boldsymbol{\beta})' (\mathbf{y} - \mathbf{X} \cdot \boldsymbol{\beta}) . \tag{D.2}$$

Thus, we take derivatives and equal them to 0, or

$$\frac{\partial S(\boldsymbol{\beta})}{\partial \boldsymbol{\beta}} = \mathbf{X}'\mathbf{X}\boldsymbol{\beta} - \mathbf{X}'\mathbf{y} = 0 \tag{D.3}$$

and we obtain the estimator for our parameters as:

$$\hat{\boldsymbol{\beta}} = (\mathbf{X}'\mathbf{X})^{-1}\mathbf{X}'\mathbf{y} \tag{D.4}$$

if $\mathbf{X}'\mathbf{X}$ has full rank, or

$$\hat{\boldsymbol{\beta}} = (\mathbf{X}'\mathbf{X})^{-}\mathbf{X}'\mathbf{y} + [I - (\mathbf{X}'\mathbf{X})^{-}\mathbf{X}'\mathbf{X}]w \tag{D.5}$$

if $\mathbf{X}'\mathbf{X}$ has not full rank. In this case $(\mathbf{X}'\mathbf{X})^{-}$ is the generalized inverse (Wolberg, 2005) and w is an arbitrary vector. Therefore, in the first case, our model is estimated as follows:

$$\hat{\mathbf{y}} = \mathbf{X}\hat{\boldsymbol{\beta}} = \mathbf{X}(\mathbf{X}'\mathbf{X})^{-1}\mathbf{X}'\mathbf{y} = P\mathbf{y} \tag{D.6}$$

The errors are assumed to be originated by a random variable (ε) with the following statistical properties:

$$E(\varepsilon) = 0 \qquad E(\varepsilon\varepsilon') = \sigma^2\mathbf{I} \tag{D.7}$$

Under these assumptions, the estimator of Eq. (D.4) is the minimum variance unbiased estimator. This means that if $\boldsymbol{\beta}_0$ is the true value for the parameter vector, $E(\hat{\boldsymbol{\beta}}) = \boldsymbol{\beta}_0$. Moreover, the variance of the parameter vector is minimal. That is, the uncertainty of the estimated parameters is the minimum that can be obtained with the existent data. This variance can be computed as:

$$\begin{aligned}
\mathbf{D}(\hat{\boldsymbol{\beta}}) &= E[(\hat{\boldsymbol{\beta}} - \boldsymbol{\beta}_0)(\hat{\boldsymbol{\beta}} - \boldsymbol{\beta}_0)'] \\
&= \begin{pmatrix} \mathrm{var}(\hat{\beta}_1) & \dots & \mathrm{cov}(\hat{\beta}_1\hat{\beta}_{k-1}) & \mathrm{cov}(\hat{\beta}_1\hat{\beta}_k) \\ \vdots & \dots & \cdots & \mathrm{cov}(\hat{\beta}_2\hat{\beta}_k) \\ \mathrm{cov}(\hat{\beta}_k\hat{\beta}_1) & \dots & \dots & \mathrm{var}(\hat{\beta}_k) \end{pmatrix}
\end{aligned} \tag{D.8}$$

which in our specific case turns out to be:

$$\begin{aligned}
\mathbf{D}(\hat{\boldsymbol{\beta}}) &= E\left[(\hat{\boldsymbol{\beta}} - \boldsymbol{\beta}_\mathbf{0})(\hat{\boldsymbol{\beta}} - \boldsymbol{\beta}_\mathbf{0})'\right] = E(\hat{\boldsymbol{\beta}}^2) - \boldsymbol{\beta}_\mathbf{0}\boldsymbol{\beta}_\mathbf{0}'\mathbf{I} = \\
&= E\left[\left((\mathbf{X}'\mathbf{X})^{-1}\mathbf{X}'\mathbf{y}\right)\left((\mathbf{X}'\mathbf{X})^{-1}\mathbf{X}'\mathbf{y}\right)'\right] - \boldsymbol{\beta}_0\boldsymbol{\beta}_0'\mathbf{I} = \\
&= (\mathbf{X}'\mathbf{X})^{-1}\mathbf{X}'E[\mathbf{y}\mathbf{y}']\mathbf{X}(\mathbf{X}'\mathbf{X})^{-1} - \boldsymbol{\beta}_0\boldsymbol{\beta}_0'\mathbf{I} = \\
&= (\mathbf{X}'\mathbf{X})^{-1}\mathbf{X}'E\left[(\mathbf{X}\boldsymbol{\beta}_0 + e)(\mathbf{X}\boldsymbol{\beta}_0 + e)'\right]\mathbf{X}(\mathbf{X}'\mathbf{X})^{-1} - \boldsymbol{\beta}_0\boldsymbol{\beta}_0'\mathbf{I} = \\
&= (\mathbf{X}'\mathbf{X})^{-1}\mathbf{X}'\left[(\mathbf{X}\boldsymbol{\beta}_0\boldsymbol{\beta}_0'\mathbf{X}' + \sigma^2\mathbf{I}\right]\mathbf{X}(\mathbf{X}'\mathbf{X})^{-1} - \boldsymbol{\beta}_0\boldsymbol{\beta}_0'\mathbf{I} = \\
&= (\mathbf{X}'\mathbf{X})^{-1}\sigma^2
\end{aligned} \tag{D.9}$$

In this equation, σ^2 is the variance of errors. The unbiased estimator for this variance is:

$$s^2 = \frac{1}{T-K}\mathbf{e}' \cdot \mathbf{e} \tag{D.10}$$

where K is the number of parameters and T is the number of samples in the single channel.

D.2 One amplitude parameter and one single channel reception

We assume that the signal is received merged with additive Gaussian noise. Then, at the receiver output we have:

$$r[n] = \alpha \cdot x[n] + w[n] \tag{D.11}$$

where $r[n]$ is the detected signal, α is the unknown amplitude parameter, $x[n]$ is the known part of the signal, and $w[n]$ is the additive noise. In this case, the estimator for α is obtained as:

$$\hat{\alpha} = \frac{\sum_{i,j=1}^{N} \mu_{ij} r_i x_j}{\sum_{i,j=1}^{N} \mu_{ij} x_i x_j} \tag{D.12}$$

where μ is the covariance matrix of the noise, which is defined as:

$$\mu_{ij} = E[(w_i - m)(w_j - m)], \tag{D.13}$$

where m is the mean of the noise. In the case of additive white Gaussian noise, where the covariance matrix is diagonal this calculation can be further simplified to obtain:

$$\hat{\alpha} = \frac{\sum_{i=1}^{N} r_i x_i}{\sum_{i=1}^{N} x_i x_i} \tag{D.14}$$

and its minimum variance is calculated as $D(\hat{\alpha}) = (\rho^2)^{-1}$, where ρ is:

$$\rho^2 = \sum_{i,j=1}^{N} \mu_{i,j} x_i x_j \tag{D.15}$$

D.3 Two amplitude parameters and one single channel reception

In this case, the received signal is:

$$r[n] = \alpha \cdot x[n] + \beta \cdot y[n] + w[n] \tag{D.16}$$

and the estimator for α and β, in its matrix form is:

$$\begin{pmatrix} \hat{\alpha} \\ \hat{\beta} \end{pmatrix} = \begin{pmatrix} \sum_{i,j=1}^{N} \mu_{i,j} x_i x_j & \sum_{i,j=1}^{N} \mu_{i,j} x_i y_j \\ \sum_{i,j=1}^{N} \mu_{i,j} x_i y_j & \sum_{i,j=1}^{N} \mu_{i,j} y_i y_j \end{pmatrix}^{-1} \begin{pmatrix} \sum_{i,j=1}^{N} \mu_{i,j} r_i x_j \\ \sum_{i,j=1}^{N} \mu_{i,j} r_i y_j \end{pmatrix} \tag{D.17}$$

The covariance matrix of the parameters is the inverse of the Fisher matrix , i.e. $\mathbf{D}(\hat{\alpha}, \hat{\beta}) = (\mathbf{F})^{-1}$, and the Fisher matrix is obtained as:

$$\mathbf{F} = \begin{pmatrix} \sum_{i,j=1}^{N} \mu_{i,j} x_i x_j & \sum_{i,j=1}^{N} \mu_{i,j} x_i y_j \\ \sum_{i,j=1}^{N} \mu_{i,j} x_i y_j & \sum_{i,j=1}^{N} \mu_{i,j} y_i y_j \end{pmatrix} \tag{D.18}$$

Appendix E

Magnetic moments of satellite subsystems

In this appendix we list the subsystems of the LISA Technology Package that have been considered for the simulation of the magnetic field of the spacecraft. We report the positions of these units and their respective magnetic moments.

Table E.1: List of the positions of the subsystems that have been considered for this study. Their magnetic dipole moment is also listed. These values of magnetic field are not the only spacecraft units that have to be considered in a realistic simulation, but it can be considered as a representative set. These sources were communicated by David Wealthy, to whom we thank for his help (Wealthy, 2006).

Subsystem	Moment [mA m^2]	x [m]	y [m]	z [m]
On-board computer	50	0.2891	−0.5258	0.4454
PCDU	100	−0.2826	0.5637	0.4812
Solar Array	3	0.0000	0.0000	0.8497
Battery	100	−0.1094	0.6040	0.7071
Transponder 1	100	−0.6415	0.0615	0.6104
Transponder 2	100	−0.6790	0.2923	0.6004
Solid State Power Amplifier 1 + Isolator	75	−0.9166	0.0700	0.3044
Solid State Power Amplifier 2 + Isolator	75	−0.9166	0.0700	0.5900
Filter 1	25	−0.6820	0.1330	0.3219
Filter 2	25	−0.6570	0.2259	0.3019
SPDT 1 (RF switch)	25	−0.8399	0.2026	0.5296
SPDT 2 (RF switch)	25	−0.8754	0.2571	0.6328
DPDT 1 (RF switch)	25	−0.6198	0.1942	0.6803
DPDT 2 (RF switch)	25	−0.5319	0.1707	0.6810

Continued on next page...

Table E.1 — Continued

Coupler	75	−0.5305	0.1580	0.4807
Medium Gain Antenna (MGA)	50	−0.9243	0.3793	0.4642
Omni directional antenna 1	50	−0.2231	1.0370	0.4755
Omni directional antenna 2	50	0.2227	−1.0373	0.4755
Digital Sun sensor 1	50	−1.0122	0.0462	0.8672
Digital Sun sensor 2	50	0.6143	0.8076	0.8672
Digital Sun sensor 3	50	0.4233	−0.8580	0.8672
Gyro Pack 1	25	0.4159	0.3770	0.6614
Gyro Pack 2	25	−0.4127	−0.3657	0.6384
Star Tracker head 1	50	0.0549	−0.8550	0.3275
Star Tracker head 2	50	0.0545	−0.8565	0.6275
Star Tracker Electronics 1	50	−0.5671	−0.2495	0.2905
Star Tracker Electronics 2	50	−0.5671	−0.2495	0.6500
FEEP Cluster 1	100	−0.9365	−0.2512	0.4781
FEEP Cluster 2	100	0.2507	0.9367	0.4787
FEEP Cluster 3	100	0.6853	−0.6851	0.4786
FEEP PCU 1	300	−0.8044	−0.1540	0.4779
FEEP PCU 2	300	−0.0149	0.8496	0.4779
FEEP PCU 3	300	0.5972	−0.5579	0.4779
Neutralizer 1	0	−0.9956	−0.2670	0.4782
Neutralizer 2	0	0.2666	0.9957	0.4786
Neutralizer 3	0	0.6424	−0.6426	0.4784
Micropropulsion electronics	300	−0.7752	−0.3460	0.3128
Cold Gas PCU 1	300	−0.6685	0.4654	0.3420
Cold Gas PCU 2	300	0.8006	0.1101	0.6217
Cold Gas PCU 3	300	−0.1565	−0.7893	0.5550
Cold Gas Cluster 1	100	−0.6456	0.6456	0.4784
Cold Gas Cluster 2	100	0.8819	0.2363	0.4784
Cold Gas Cluster 3	100	−0.2363	−0.8819	0.4784
Cold Gas Tank	20	−0.2470	−0.5540	0.3265
Cold Gas PEPRE	50	−0.2066	−0.5646	0.6606
Cold Gas FEED Assembly	100	−0.2707	−0.5005	0.6606

Appendix F

Neural network principles: theory and application

In this appendix we briefly describe the principles of neural networks as a statistical modeling tool. We explain the concept of neural networks, and we also review the architecture used in this work. Additionally, we also provide a brief overview of the back-propagation algorithm to find the optimal weights of the neural network, and we show as well how to estimate the variances of these weights. Nevertheless, we emphasize that our aim is only to give a brief introduction to the basic concepts used in this manuscript and not to be complete whatsoever. Consequently, the reader is referred for further details to the excellent works of Kecman (2001), Dreyfus (2005), and Rumelhart et al. (1985).

F.1 Introduction to feedforward neural networks

Artificial neural networks are made up of interconnecting artificial neurons (programming constructs that mimic the properties of biological neurons) that have the property of learning from processing data. Neural networks are often used in solving nonlinear classification and regression tasks. The Parsimonius approximation states (Dreyfus, 2005) that any bounded, sufficiently regular function can be approximated uniformly with arbitrary accuracy in a finite region of variable space, by a neural network with a single layer of hidden neurons having the same activation function and a linear output neuron. In order to model the function correctly, we ought to choose the model with the smallest number of parameters.

The utility of artificial neural network models lies in the fact that they can be used to infer a function from observations. This is particularly useful in applications where the complexity of the data or task makes analytical approximations impractical. The neural network can predict values of the quantity of interest for points that lie between the measured points. This ability is termed *statistical inference* or

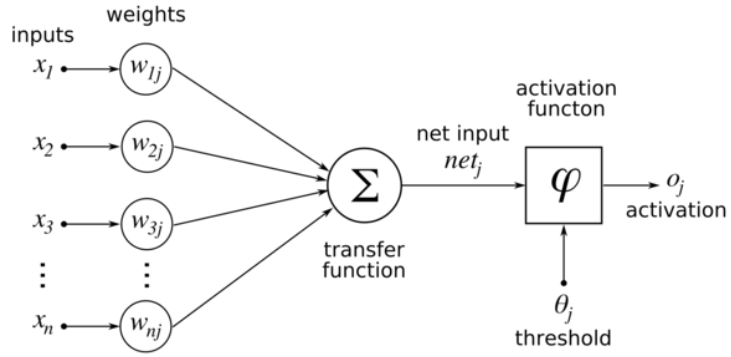

Figure F.1: Schematics of the operations performed by an artificial neuron.

generalization in neural network parlance. However, it has to be understood that this generalization is limited and cannot be extended beyond the boundaries of the region of the input space. This is a key aspect when using these models. In order to infer a model based on neural networks we need a set of examples that sample the input space (for unsupervised training) and also the output space (for supervised training). Moreover, for this approach to be robust, we need a number of examples larger than the number of parameters and they ought to be representative of the process we want to model. Generally speaking, if the dimension of the input space is larger than 3, neural networks are advantageous to polynomials or other classical methods. When solving a problem with artificial neural networks we need to define the neuron type, the neural network architecture, select the appropriate inputs to the model and choose the learning process. Finally, in order to validate the model, its performance should also be assessed. These concepts are developed in the following sections.

F.2 Neuron model

The *neuron* is the basic unit of any neural network. It performs two operations — see Fig. F.1. Firstly, it collects the inputs from all other neurons connected to it and computes a weighted sum of the signals the latter inject into it, generally adding a *bias* as well. If we represent the inputs by a vector $\mathbf{x} \equiv (x_1, \ldots, x_n)$, and the weights by a $\mathbf{w} \equiv (w_1, \ldots, w_n)$, this operation consists in calculating the sum

$$\Sigma = w_0 + \sum_{k=1}^{n} w_k x_k = w_0 + \mathbf{w}^{\mathrm{T}}\mathbf{x} \tag{F.1}$$

where the superindex T stands for the transpose matrix. In this case, $\mathbf{w}^{\mathrm{T}}$ is a row vector while $\mathbf{x}$ is a column vector, and thus $\mathbf{w}^{\mathrm{T}}\mathbf{x}$ is the scalar product of $\mathbf{w}$ and $\mathbf{x}$.

Finally, w_0 is the bias. In second term, this sum is used as the argument to the so called *activation function*, $\varphi(\Sigma)$. The output of the neuron is thus

$$o = \varphi(\Sigma) \tag{F.2}$$

In general, $\varphi(\Sigma)$ can be selected in many different ways. Here, differentiable activation functions will be used, which suit well the gradient descent back-propagation learning algorithm — see section F.5 below.

F.3 Neural network architecture

Artificial neural networks are software or hardware models inspired by the structure and behavior of biological systems, and they are built using a set of neurons distributed in layers. There are many different types of neural networks in use today, but the architecture of a so-called *feed-forward network*, where each layer of neurons is linked with the next by means of a set of weights, is the most commonly used, and will also be used here. A feed-forward network with N_i inputs, N_c hidden neurons, and N_o output neurons computes N_o nonlinear functions of its N_i inputs variables as composition of the N_c functions computed by the hidden neurons.

In this study we adopt the architecture shown in Fig. F.2, where i_1, i_2, i_3 and i_4 are the inputs of the system and o_1 and o_2 are its outputs. This figure has been restricted to 4 inputs and 2 outputs because for the application under study in

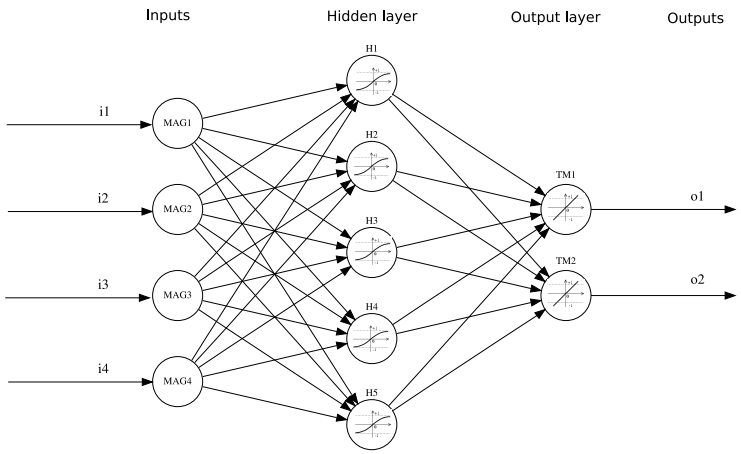

Figure F.2: Feed-forward neural network architecture. For the application presented in this thesis, the readings of the magnetometers are the system inputs and the estimates of the field and gradient at the positions of the test masses are the outputs of the system. Note that in this architecture, one only intermediate, or *hidden* layer is assumed. Each of the circles represents one neuron and corresponds to the model shown in Fig. F.1.

this thesis, the information coming from the 4 magnetometers will be considered the system inputs, while the magnetic field results at both test masses will be considered the outputs.

F.3.1 What is the best network architecture?

Finding the optimal neural network architecture for an specific regression problem is not a a trivial task, and has not been solved yet, since there is no systematic solution to the general problem (Kecman, 2001; Dreyfus, 2005). This is because the problem of *generalization* is an ill-posed problem. Specifically, if the network has too many parameters (that is, too many neurons), the model is over-parametrized and, normally, has a tendency to learn from noise. This behavior is known as "overfitting" (Schittenkopf et al., 1997). On the other hand, if it has too few parameters, the network is not flexible enough to learn the hidden function between inputs and outputs. Moreover, when choosing the best architecture the so-called *bias-variance* dilemma is faced (Dreyfus, 2005). In practice this means that if a high number of neurons in the network is adopted, the solution has less bias but more variance, whereas if an insufficient number of neurons is adopted, interpolation errors with more bias and less variance are obtained. Consequently, there is a trade-off between learning and generalization capacity. Additionally, note that increasing the complexity of the system leads to an important number of parameters. If the problem is non-linear, several minima of the cost function are often found. Thus, to find the global minimum, all them should be carefully analyzed. This task is normally difficult as it depends highly on initialization. On the other hand, if the problem is linear, only one unique solution exists, but these problems are usually quite rare.

F.4 Selection of input data

In order to find a proper regression model with neural networks, input data has to be carefully selected. This is so because not relevant inputs may increase complexity and add uncertainty to the determination of the weights of the network, and thus increase model error. This reduction of the input-space size can be performed with classical methods such as Principal Component Analysis (PCA) for linear systems or Curvilinear Component Analysis (CCA) for non-linear systems (Dreyfus, 2005). However, the scientific community has developed other interesting techniques to solve this problem such as those based on the Akaike's criterion (Akaike, 1973, 1974). These techniques try to minimize both the number of inputs and the obtained mean square error of the model. Other techniques can be found in McQuarrie & Tsai (1997), and Guyon et al. (2005). On the other hand, input data should be normalized and centered in order to compact the input space. In our application, this is done by application of simple `mapminmax` functions (Kecman, 2001).

F.5 Learning paradigms and learning-training algorithms

In neural network parlance, learning algorithms are understood as the iterative processes to find the best weights for each of the neurons of the model. The investigation of learning algorithms is currently an active field of research. The design and implementation of an adequate training scheme is the essential ingredient for a good quality estimation of the model.

F.5.1 Learning paradigms

There are two major learning paradigms, each corresponding to a particular abstract learning task. These are *supervised learning* and *unsupervised learning* (Rumelhart et al., 1985). Training is the algorithmic procedure whereby the parameters of such a model are sought, for a family given of functions. In statistical modeling, the best model is the model whose parameters are estimated with the best accuracy. In machine learning, the best model is the one that generalizes best, and the statistical properties of the network parameters are of less interest.

1. **Supervised learning.** The idea of this is quite clearly suggested by its very name: a set of *examples* is filed, which consists in a number of vector of inputs and a number of outputs, and the network learns from these specific examples.

   Let x represent a generic input vector, and y the associated vector output. These two vectors constitute an example. The set of filed examples for supervised learning is thus a set of pairs (x, y), where $x \in X$ and $y \in Y$, X and Y being some suitable sample spaces. The network is then fed the inputs x of one example and let it work out an output, o, say. This output is then compared with the correct one, y, and an error is calculated if $o \neq y$. Iterations are then triggered to adjust the weighting factors such that this error is minimized. These will however vary as different examples are run, so a *cost function* is defined which enables the network to optimize the set of weights which works best for the set of examples analyzed, based on some given criterion. See section F.5.2 for specific details on the learning algorithms.

2. **Unsupervised learning.** In unsupervised learning a cost function is to be minimized as well, but generally this function is a relationship between the inputs of the system (and normally not the output — which is some times not available). These schemes are often used to perform inputs space classification and discrimination (Kohonen, 2001). In this work they are used to discriminate different groups of inputs, namely magnetometer readings corresponding to different operating modes of the satellite.

In either case, the learning process is based on the architecture of the network. That is, with the adopted number of neurons, layers and their interconnections, as

well as on the chosen activation functions.

F.5.2 Learning algorithms

There are many algorithms for training neural networks. When training feed-forward neural networks with supervised learning, a back-propagation algorithm is usually implemented. The error of the mapping at the output is propagated backwards in order to readjust the weights and improve the output error for the next iteration. The weight computation can be implemented with different methods, the *Ideal Gradient Descent* being a classic, which will also be used here. The method is widely used in the field of soft computing, and is a variant of the method of steepest descent (Rumelhart et al., 1985; Press et al., 1992).

Iterations on the weights of the different neurons at the different layers proceed according to the following algorithm:

$$\mathbf{w}_{n+1} = \mathbf{w}_n - \eta \left.\frac{\partial E}{\partial \mathbf{w}}\right|_n \tag{F.3}$$

where n labels the current iteration step, and η is the learning rate, adjustable by the user. E is the sum over the set of training examples of the square errors of the outputs:

$$E = \sum (\mathbf{o} - \mathbf{y})^{\mathrm{T}} (\mathbf{o} - \mathbf{y}) \tag{F.4}$$

where $\mathbf{o}$ is the (vector) output from the network, while $\mathbf{y}$ is the *target*, or correct output in the corresponding example. This E can only be defined in supervised learning, of course, and the idea of the above procedure is to find that point in weight space where E is the minimum possible. E can therefore be considered the cost function to be minimized in this particular supervised training scheme.

This has to be done for all layers in the network, therefore, the algorithm to update the weights across the entire network is:

1. Initialization of the weights. This can be done randomly or using other techniques.
2. Computation of the outputs of the network with the initial weights (forward phase).
3. Computation of the error in the last layer.
4. Computation of the weight update of the last layer of neurons.
5. Computation of the error in the penultimate layer.
6. Compute the weight update of the penultimate layer.
7. Iterate successively until the first layer.

8. Repeat the forward phase.

9. If the goal has not been achieved, iterate the backward process from point 3 for a new epoch.

This is why this technique is known as the back-propagation error technique. To implement the Gradient Descent algorithm several mathematical tools can be chosen. Levenberg-Marquardt (Marquardt, 1963) is a second order gradient descent method which performs very good for small networks because it is very demanding in memory size. The BFGS technique is also a second order method, however it is less memory demanding. Thus, it is suitable for large networks (Press et al., 1992). There are a number of technical issues in pursuing the aforementioned steps, such as the choice of the initial set of weights, identification of local minima of E, boundary effects,... which need to be addressed in each specific application.

F.5.3 Learning rate

True gradient descent requires infinitesimal steps to be taken. A learning rate factor may increase the evolution of the algorithm. but nevertheless it may cause computational problems too. The larger the learning rate, the larger the changes of the weights. Therefore, the learning rate should be as large as possible without leading to oscillations (Rumelhart et al., 1985).

F.5.4 The early stopping technique

Frequently, to avoid overfitting, namely, to do not let the neural network learn the noise artifacts present in the data, training software implement techniques such as the early stopping technique. In this technique, the data provided to the training algorithm is divided into two sets: the training data and the validation data. For each of these two sets we define the training mean square error (T_{MSE}):

$$T_{\text{MSE}} = \sqrt{\frac{1}{N_t}\sum_{k=1}^{N_t}[y^k - g(x^k, w)]^2} \tag{F.5}$$

and the validation mean square error (V_{MSE}):

$$V_{\text{MSE}} = \sqrt{\frac{1}{N_v}\sum_{k=1}^{N_v}[y^k - g(x^k, w)]^2} \tag{F.6}$$

In these equations k is the index of each of the examples fed to the algorithm, y are the outputs of our data, x are the inputs, w the neural network weights, and $g(x, w)$ is the network model. The training set is composed of N_t examples, and the

validations set of N_v examples, thus the total data provided to the early stopping technique is conformed by $N_t + N_v$ examples. The learning algorithm described in the previous sections is performed on the training data, in order to minimize the T_{MSE}. At the same time, during the learning process the value of the V_{MSE} is monitored. Both values start decreasing when the training starts. Nevertheless, there is a moment when the T_{MSE} keeps decreasing with respect to previous epochs while the V_{MSE} starts increasing. This is when the early stopping technique stops the learning procedure and sets the weights of the network to the set of weights existing when the V_{MSE} started to increase. This avoids the network to learn from the existing noise particularities in the training data. In order to obtain a good generalization and avoid overfitting, we want that T_{MSE} and V_{MSE} to be of the same order of magnitude of the noise expected for the specific application.

F.5.5 Estimating variances of the weights of neural networks

To estimate the variance of the neural network weights, the same approach used in Appendix D can be used. There, the variance of the parameters for a linear model was defined as $D(\hat{\beta}) = (\mathbf{X}'\mathbf{X})^{-1}\sigma^2$. For a non-linear model, the variance of the estimated parameters is calculated using the linearized model. If the non-linear model is $o = g(\mathbf{x}, \mathbf{w})$, the linearized model is then:

$$o = \frac{\partial g(\mathbf{x}, \mathbf{w})}{\partial \mathbf{w}} \cdot \mathbf{w} + e = \mathbf{L} \cdot \mathbf{w} + e \tag{F.7}$$

where $\mathbf{L}$ is a matrix of $T \times K$, being T the number of samples and K the number of parameters of the model. Specifically, $\mathbf{L}$ is given by:

$$\mathbf{L} = \left[\frac{\partial g(\mathbf{x}, \mathbf{w})}{\partial w_1} \frac{\partial g(\mathbf{x}, \mathbf{w})}{\partial w_2} \cdots \frac{\partial g(\mathbf{x}, \mathbf{w})}{\partial w_K} \right] \tag{F.8}$$

Hence, the variances of the weights estimated by the learning algorithms may be approximated by $\mathbf{D}(\hat{\mathbf{w}}) = (\mathbf{L}'\mathbf{L})^{-1}\sigma^2$. In this equation, σ^2 stands for the variance of the errors obtained by the trained model.

Bibliography

Abramovici, A., Althouse, W. E., Drever, R. W. P., Gursel, Y., Kawamura, S., Raab, F. J., Shoemaker, D., Sievers, L., Spero, R. E. & Thorne, K. S., 1992. LIGO - The Laser Interferometer Gravitational-Wave Observatory. *Science*, **256**, 325–333.

Abramowitz, M., 1972. *Handbook of Mathematical Functions*. NBS Applied Mathematics Series 55.

Acernese, F., Amico, P., Alshourbagy, M., Antonucci, F., Aoudia, S. et al., 2007. Status of Virgo detector. *Class. & Quantum Grav.*, **24**, 381–392.

Advanced LIGO team, 2008. Advanced LIGO reference design. Technical report. Tech. Rep. LIGO-060056-08-M, Caltech, MIT, LIGO Hanford, LIGO Livingstone.

Aguiar, O. D., Andrade, L. A., Camargo Filho, L., Costa, C. A., de Araujo, J. C. N. et al., 2002. The Gravitational Wave Detector "Mario Schenberg": Status of the Project. *Brazilian J. of Phys.*, **32**, 866–868.

Akaike, H., 1973. Information theory and an extension of the maximum likelihood principle. *2nd International Symposium on Information Theory, Akademia Kiado*, 267.

Akaike, H., 1974. A new look at the statistical model identification. *IEEE Transactions on Automatic Control*, **19**, 716.

Antonucci, F., Armano, M., Audley, H., Auger, G., Benedetti, M. et al., 2011a. LISA Pathfinder data analysis. *Class. & Quantum Grav.*, **28**, 094006.

Antonucci, F., Armano, M., Audley, H., Auger, G., Benedetti, M. et al., 2011b. LISA Pathfinder: mission and status. *Class. & Quantum Grav.*, **28**, 094001.

Anza, S., Armano, M., Balaguer, E., Benedetti, M., Boatella, C. et al., 2005. The LTP experiment on the LISA Pathfinder mission. *Class. & Quantum Grav.*, **22**, 125–148.

Araújo, H., Boatella, C., Chmeissani, M., Conchillo, A., García-Berro, E., Grimani, C., Hajdas, W., Lobo, A., Martínez, L., Nofrarias, M., Ortega, J. A., Puigdengoles, C., Ramos-Castro, J., Sanjuán, J., Wass, P. & Xirgu, X., 2007. LISA and LISA PathFinder, the endeavour to detect low frequency GWs. *Jour. of Phys. Conf. Ser.*, **66**, 012003.

Armano, M., Benedetti, M., Bogenstahl, J., Bortoluzzi, D., Bosetti, P. et al., 2009. LISA Pathfinder: the experiment and the route to LISA. *Class. & Quantum Grav.*, **26**, 094001.

Astone, P., Bassan, M., Bonifazi, P., Carelli, P., Castellano, M. G. et al., 2002. The EXPLORER gravitational wave antenna: recent improvements and performances. *Class. & Quantum Grav.*, **19**, 1905–1910.

Astone, P., Bassan, M., Bonifazi, P., Carelli, P., Coccia, E. et al., 1997. The gravitational wave detector NAUTILUS operating at T = 0.1 K. *Astroparticle Phys.*, **7**, 231–243.

Bender, P., 1998. LISA for the detection and observation of gravitational waves. Pre-phase A. Tech. Rep. LISA Technical Report 244, Max Planch fur Quantenoptik.

Berti, E., Buonanno, A. & Will, C. M., 2005. Testing general relativity and probing the merger history of massive black holes with LISA. *Class. & Quantum Grav.*, **22**, 943–951.

Billinglsey, Aerospace and Defense, 2007. TFM100G4 Triaxial Fluxgate Magnetometer. Tech. Rep. TFM100G4 Users Manual, Billinglsey.

Bindel, D., 2008. FEEP Simulink Model for LISA Pathfinder End-2-End Simulator. Tech. Rep. S2-ZAR-TN-2007, ZARM, Germany.

Blair, D. G., Ivanov, E. N., Tobar, M. E., Turner, P. J., van Kann, F. & Heng, I. S., 1995. High Sensitivity Gravitational Wave Antenna with Parametric Transducer Readout. *Phys. Rev. Lett.*, **74**, 1908–1911.

Bortoluzzi, D., Bosetti, P., Carbone, L., Cavalleri, A., Ciccolella, A. et al., 2003. Testing LISA drag-free control with the LISA technology package flight experiment. *Class. & Quantum Grav.*, **20**, 89–93.

Brandt, N. & et al., 2004. End-to-end modelling for drag-free missions with application to LISA Pathfinder. Tech. Rep. Proceedings of the 16th IFAC Symposium on Automatic Control in Aerospace, Astrium Gmbh. Germany.

Brandt, N., Hirth, M., Fichter, W., Schubert, R., Warren, C. & Wealthy, D., 2010. Experiment performance budget, LISA Pathfinder Project Documentation. Tech. Rep. S2-ASD-TN-3036, Astrium Gmbh. Germany.

Bullen, R. J., Cornford, D. & Nabney, I., 2003. Outlier detection in scatterometer data: neural network approaches. *Neural Networks*, **16**, 419.

Cañizares, P., Conchillo, A., García-Berro, E., Gesa, L., Grimani, C., Lloro, I., Lobo, A., Mateos, I., Nofrarias, M., Ramos-Castro, J., Sanjuán, J. & Sopuerta, C. F., 2009. The diagnostics subsystem on board LISA Pathfinder and LISA. *Class. & Quantum Grav.*, **26**, 094005.

Danzmann, K., 1992. Interferometric gravitational wave detectors become reality. In *Astronomische Gesellschaft Abstract Series*, vol. 7, 58–78.

Danzmann, K. & Rüdiger, A., 2003. LISA technology - concept, status, prospects. *Class. & Quantum Grav.*, **20**, 1–22.

de Waard A., 2005. Mini Grail progress report. Tech. rep., Universiteit Leiden.

Díaz–Aguiló, M., García-Berro, E. & Lobo, A., 2009. Neural Network algorithms for magnetic diagnostics in the LTP. Tech. Rep. S2-IEC-TN-3052, IEEC.

Díaz–Aguiló, M., Lobo, A. & García-Berro, E., 2010. Algorithm specification for the Magnetic Diagnostics onboard LPF. Tech. Rep. S2-IEC-TN-3071, IEEC.

Díaz-Aguiló, M., García-Berro, E. & Lobo, A., 2010. Theory and modelling of the magnetic field measurement in LISA PathFinder. *Class. & Quantum Grav.*, **27**, 035005.

Díaz-Aguiló, M., Lobo, A. & García-Berro, E., 2011a. Design of the magnetic diagnostics unit onboard LISA Pathfinder. *Aerospace Science Technology*, accepted.

Díaz-Aguiló, M., Lobo, A. & García-Berro, E., 2011b. Neural network interpolation of the magnetic field for the LISA Pathfinder Diagnostics Subsystem. *Exp. Astron.*, 7–18.

Dolesi, R., Bortoluzzi, D., Bosetti, P., Carbone, L., Cavalleri, A. et al., 2003. Gravitational sensor for LISA and its technology demonstration mission. *Class. & Quantum Grav.*, **20**, 99–105.

Dreyfus, G., 2005. *Neural Networks: Methodology and Applications*. Springer.

Fafone, V., 2004. Resonant-mass detectors: status and perspectives. *Class. & Quantum Grav.*, **21**, 377–386.

Fertin, D. & Trougnou, L., 2007. LisaPF Test Masses Acceleration Noise due to Eddy Currents. Tech. Rep. S2-EST-TN-2016, ESTEC.

Fertin, D. & Trougnou, L., 2010. Low frequency force due to amplitude modulated AC magnetic field. Tech. Rep. S2-EST-TN-3044, ESTEC.

Folkner, W. M., Buchman, S., Byer, R. L., DeBra, D. B., Dennehy, C. J., Gamero-Castaño, M., Hanson, J., Hruby, V., Keiser, G. M., Kuhnert, A., Markley, F. L., Houghton, M., Maghami, P., Miller, D. C., Prakash, S. & Spero, R., 2003. Disturbance reduction system: testing technology for precision formation control. In *Society of Photo-Optical Instrumentation Engineers (SPIE) Conference Series*, vol. 4860, 221–228.

Franco, S., 2002, 3rd edition. *Design with operational amplifiers and analog integrated circuits*. McGraw-Hill.

Frossati, G., 2003. Ultralow-temperature resonant gravitational wave detectors, present state and future prospects. *Adv. in Space Res.*, **32**, 1227–1232.

Gair, J. R., Barack, L., Creighton, T., Cutler, C., Larson, S. L., Phinney, E. S. & Vallisneri, M., 2004. Event rate estimates for LISA extreme mass ratio capture sources. *Class. & Quantum Grav.*, **21**, 1595–1603.

Garcia-Marin, A., 2007. *Minimisation of optical pathlength noise for the detection of gravitational waves with the spaceborne laser interferometer LISA and LISA Pathfinder*. Ph.D. thesis, AEI, Hannover.

Grynagier, A., 2009. The Drift Mode for LISA Pathfinder. Tech. Rep. S2-IFR-TN-3005, Institute of Flight Mechanics and Control, University of Stuttgart.

Grynagier, A. & Weyrich, M., 2008. The SSM class: Modelling and Anlyses of the LISA Pathfinder Technology Experiment. Tech. Rep. SSM-iFR, Institute of Flight Mechanics and Control, University of Stuttgart.

Guyon, I., Gunn, S. & Zadeh, L., 2005. *Feature extraction, foundations and applications*. Springer.

Heinzel, G., Braxmaier, C., Schilling, R., Rüdiger, A., Robertson, D., te Plate, M., Wand, V., Arai, K., Johann, U. & Danzmann, K., 2003. Interferometry for the LISA technology package (LTP) aboard SMART-2. *Class. & Quantum Grav.*, **20**, 153–173.

Heinzel, G., Wand, V., García, A., Jennrich, O., Braxmaier, C., Robertson, D., Middleton, K., Hoyland, D., Rüdiger, A., Schilling, R., Johann, U. & Danzmann, K., 2004. The LTP interferometer and phasemeter. *Class. & Quantum Grav.*, **21**, 581–601.

Heng, I. S., Daw, E., Giaime, J., Hamilton, W. O., Mchugh, M. P. & Johnson, W. W., 2002. Allegro: noise performance and the ongoing search for gravitational waves. *Class. & Quantum Grav.*, **19**, 1889–1895.

Hewitson, M., 2011. LTPDA user manual and help. Tech. Rep. LTPDA toolbox: Matlab help. http://www.lisa.aei-hannover.de/ltpda/, AEI Hannover. Germany.

Hobbs, G., 2010. Pulsars as gravitational wave detectors. *ArXiv e-prints*.

Hobbs, G., Archibald, A., Arzoumanian, Z., Backer, D., Bailes, M. et al., 2010. The International Pulsar Timing Array project: using pulsars as a gravitational wave detector. *Class. & Quantum Grav.*, **27**, 084013.

Hueller, M., 2003. *Geodesic motion of LISA test masses: development and testing of drag-free position sensors.*. Ph.D. thesis, Universita degli Studi di Trento.

Hughes, S. A., 2003. Listening to the universe with gravitational-wave astronomy. *Annals of Phys.*, **303**, 142–178.

Hulse, R. A. & Taylor, J. H., 1975. Discovery of a pulsar in a binary system. *ApJ*, **195**, L51–L53.

Jackson, J. D., 1999. *Classical Electrodynamics*. John Wiley & Sons.

Janssen, G. H., Stappers, B. W., Kramer, M., Purver, M., Jessner, A. & Cognard, I., 2008. European Pulsar Timing Array. In *40 Years of Pulsars: Millisecond Pulsars, Magnetars and More*, vol. 983, 633–635.

Jenet, F., Finn, L. S., Lazio, J., Lommen, A., McLaughlin, M. et al., 2009. The North American Nanohertz Observatory for Gravitational Waves. *ArXiv e-prints*.

Kahl, G., 2007. DDS Subsystem Specification. Tech. Rep. S2-ASD-RS-3004, ASD.

Kecman, V., 2001. *Learning and soft computing*. The MIT Press.

Kirk, D. E., 1970. *Optimal Control Theory: An Introduction*. Prentice Hall Inc. Englewood Cliffs.

Kohonen, T., 2001. *Self-Organizing Maps*. Springer series in Information Sciences. Berlin: Springer Verlag.

Lange, B., 1964. *The control and use of drag-free satellites*. Ph.D. thesis, SUDAER.

LIST, 2008. The *LISA* International Team 2008 ESA-NASA Report. Tech. Rep. LISA-SCRD-Iss5-Rev1, ESA-NASA.

Llamas, X., 2006. DDS design specification. Tech. Rep. S2-NTE-DS-3001, NTE.

Lobo, A., 2005. DDS Science Requirements document. Tech. Rep. S2-IEEC-RS-3002, IEEC.

Lobo, A. & Mateos, I., 2008. Test Report for LTP FM Diagnostics. Tech. Rep. S2-IEC-TN-3071, IEEC.

Lobo, J. A., 1992. Effect of a weak plane GW on a light beam. *Class. & Quantum Grav.*, **9**, 1385–1394.

Loyola, D. G., 2006. Applications of neural network methods to the processing of Earth observation satellite data. *Neural Networks*, **19**, 168.

Lück, H., Hewitson, M., Ajith, P., Allen, B., Aufmuth, P. et al., 2006. Status of the GEO600 detector. *Class. & Quantum Grav.*, **23**, 71–92.

Lyons, T. T., Regehr, M. W. & Raab, F. J., 2000. Shot Noise in Gravitational-Wave Detectors with Fabry Perot Arms. *Appl. Optics*, **39**, 6761–6770.

Marquardt, D., 1963. An algorithm for least-squares estimation of nonlinear parameters. *Journal of the Society of Industrial and Applied Mathematics*, **11**, 431.

McQuarrie, A. & Tsai, C., 1997. *Regression and Time Series Model Selection*. World Scientific.

Meers, B. J., 1988. Recycling in laser-interferometric gravitational-wave detectors. *Phys. Rev. D*, **38**, 2317–2326.

Misner, G., Thorne, K. S. & Wheeler, J. A., 1973. *Gravitation*. W. H. Freeman & Co.

Monsky, A., Hewitson, M., Ferraioli, L., Wanner, G., Nofrarias, M. et al., 2009. The first mock data challenge for LISA Pathfinder. *Class. & Quantum Grav.*, **26**, 094004.

Nofrarias, M., Röver, C., Hewitson, M., Monsky, A., Heinzel, G., Danzmann, K., Ferraioli, L., Hueller, M. & Vitale, S., 2010. Bayesian parameter estimation in the second LISA Pathfinder mock data challenge. *Phys. Rev. D*, **82**, 122002.

Ogata, K., 2001. *Modern Control Engineering*. Prentice Hall Inc. Englewood Cliffs.

Oppenheim, A. & Schafer, R., 1975. *Digital Signal Processing*. Prentice Hall Inc. Englewood Cliffs.

Press, W., Teukolsky, S., Vetterling, W. & Flannery, B., 1992. *Numerical Recipes in C: The Art of Scientific Computing*. Cambridge University Press.

Primdahl, F., Risbo, T., Merayo, J. M. G., Brauer, P. & Tøffner Clausen, L., 2006. In-flight spacecraft magnetic field monitoring using scalar/vector gradiometry. *Meas. Sci. & Tech.*, **17**, 1563–1569.

Reed, R., 1993. Prunning algorithms – A survey. *IEEE Trans. on Neural Networks*, **4**, 740–747.

Rumelhart, D., Hinton, G. & Williams, R., 1985. *Learning internal representations by error propagation*. University of California, San Diego. Institute for Cognitive Science.

Sanjuan, J., 2009. *Development and Validation of the thermal diagnostics instrumentation in LISA Pathfinder*. Ph.D. thesis, UPC.

Sanjuán, J., Lobo, A., Nofrarias, M., Mateos, N., Xirgu, X., Cañizares, P. & Ramos-Castro, J., 2008. Magnetic polarization effects of temperature sensors and heaters in LISA Pathfinder. *Rev. of Sci. Instruments*, **79**, 084503.

Schittenkopf, C., Deco, G. & Brauer, W., 1997. Two strategies to avoid overfitting in feedforward networks. *Neural Networks*, **10**, 505.

Schleicher, A., 2008. DFACS User Manual. Tech. Rep. S2-ASD-MA-2004 Issue 1, Astrium Gmbh. Germany.

Schleicher, A., 2009. DFACS General Design. Tech. Rep. S2-ASD-TN-2001 Issue 3, Astrium Gmbh. Germany.

Schumaker, B. L., 2003. Disturbance reduction requirements for LISA. *Class. & Quantum Grav.*, **20**, 239–245.

Schutz, B. F., 1984. Gravitational waves on the back of an envelope. *Amer. J. of Phys.*, **52**, 412–419.

Serpico, C. & Visone, C., 1998. Magnetic hysteresis modeling via feed-forward neural networks. *IEEE Trans. on Magnetics*, **34**, 623–628.

Sigg, D. & the LIGO Scientific Collaboration, 2008. Status of the LIGO detectors. *Class. & Quantum Grav.*, **25**, 114041.

Smith, C. W., L'Heureux, J., Ness, N. F., Acuña, M. H., Burlaga, L. F. & Scheifele, J., 1998. The ACE Magnetic Fields Experiment. *Space Sci. Rev.*, **86**, 613–632.

Stroeer, A. & Vecchio, A., 2006. The LISA verification binaries. *Class. & Quantum Grav.*, **23**, 809–826.

Takahashi, R. & the TAMA Collaboration, 2004. Status of TAMA300. *Class. & Quantum Grav.*, **21**, 403–432.

Taylor, J. H., Fowler, L. A. & McCulloch, P. M., 1979. Measurements of general relativistic effects in the binary pulsar PSR 1913+16. *Nature*, **277**, 437–440.

Taylor, J. H. & Weisberg, J. M., 1982. A new test of general relativity - Gravitational radiation and the binary pulsar PSR 1913+16. *ApJ*, **253**, 908–920.

Tinto, M., Shaddock, D. A., Sylvestre, J. & Armstrong, J. W., 2003. Implementation of time-delay interferometry for LISA. *Phys. Rev. D*, **67**, 122003.

Trougnou, L., 2007. AC Magnetic Susceptibility of LisaPF Test Masses, issue 2. Tech. Rep. S2-EST-TN-3013, ESTEC.

Vitale, S., 2002. The Lisa Technology Package on board SMART-2. LISA Technology Package Architect. Tech. Rep. UNITN-INT-10-2002, Department of Physics, University of Trento, Italy.

Vitale, S., 2005. Science Requirements and Top-level Architecture Definition for the Lisa Technology Package (*LTP*) on Board LISA Pathfinder (SMART-2). Tech. Rep. LTPA-UTN-ScRD-Iss003-Rev1, Department of Physics, University of Trento, Italy.

Vitale, S., 2007. Effect of eddy currents on down-conversion of magnetic noise. Tech. Rep. Memo, LISA Technology Package, Department of Physics, University of Trento.

Wealthy, D., 2006. Magnetic sources on-board the LPF. Private communication.

Wealthy, D. & Trenkel, C., 2010. Prediction of Spacecraft Magnetic Field Based on Recent Testing. Tech. Rep. S2-ASU-TN-2523 Issue 3, Astrium Gmbh. Germany.

Weber, J., 1960. Detection and Generation of Gravitational Waves. *Phys. Rev. D*, **117**, 306–313.

Weber, J., 1969. Evidence for Discovery of Gravitational Radiation. *Phys. Rev. Lett.*, **22**, 1320–1324.

Welch, P. D., 1967. The Use of Fast Fourier Transform for the Estimation of Power Spectra: A Method Based on Time Averaging Over Short, Modified Periodograms. *IEEE Trans. Audio Electroacoust.*, **15**, 70–73.

Wolberg, J., 2005. *Data Analysis Using the Method of Least Squares*. Springer Verlag.

Yardley, D. R. B., Hobbs, G. B., Jenet, F. A., Verbiest, J. P. W., Wen, Z. L., Manchester, R. N., Coles, W. A., van Straten, W., Bailes, M., Bhat, N. D. R., Burke-Spolaor, S., Champion, D. J., Hotan, A. W. & Sarkissian, J. M., 2010. The sensitivity of the Parkes Pulsar Timing Array to individual sources of gravitational waves. *MNRAS*, **407**, 669–680.

Zendri, J., Baggio, L., Bignotto, M., Bonaldi, M., Cerdonio, M. et al., 2002. Status report and near future prospects for the gravitational wave detector AURIGA. *Class. & Quantum Grav.*, **19**, 1925–1933.